End-of-Study Internship Report:

Turbulence in Porous Media

Turbulence analysis of TPMS materials using DNS simulations with the JAGUAR code

Student: **Adrian RUSNAK**

Office national d'études et de recherches aérospatiales (ONERA)
Internship Tutor: **Rémi RONCEN**

Institut Supérieur de l'Aéronautique et de l'Espace (ISAE-Supaero)
Internship Supervisor: **Jérôme FONTANE**

Politecnico di Torino (PoliTo)
Internship Supervisor: **Francesco AVALLONE**

Academic year: 2023 - 2024
Internship period: 1st april 2024 - 15th september 2024

Abstract

Porous media have a wide range of applications across industries such as energy, chemical processing, and environmental engineering, due to their ability to enhance heat and mass transfer, improve mixing, and optimize fluid flow. Their potential for advancing turbulent combustion systems is especially significant, offering the possibility of ultra-low emission technologies through enhanced turbulent mixing and flame stabilization. However, understanding the complex flow dynamics within porous structures remains a challenge. The intricate geometry of porous media—characterized by high curvature and small-scale features—combined with high Reynolds numbers (Re), introduces significant numerical and experimental complexities. Extremely fine meshes and small time steps, dictated by the Courant–Friedrichs–Lewy (CFL) condition, often result in prohibitive computational costs. Recent efforts to study these materials in the turbulent regime have utilized either macroscopic simulations—sacrificing pore-scale details—or pore-resolved DNS using Finite Volume Method (FVM) or Lattice Boltzmann Method (LBM) on simpler geometries like arrays of bars, spheres, or grids of cubes.

Among the various types of porous media, **Triple Periodic Minimal Surfaces (TPMS)** have gained particular attention due to their superior thermal, structural, and diffusive properties. TPMS structures not only enhance transport processes but are also relatively easy to fabricate and parametrize, allowing for precise control over pore sizes and surface areas. These features, coupled with their accessibility for experimental setups, make TPMS ideal candidates for applications requiring finely tuned porous structures to optimize performance.

This research investigates the turbulence characteristics of TPMS materials using **Direct Numerical Simulation (DNS)** through the **JAGUAR code**, which employs the **Spectral Difference Method (SDM)**, **Immersed Boundary Conditions (IBC)**, and the **Pressure Gradient Scaling (PGS)** technique. PGS enhances simulation efficiency by enabling larger time-steps, reducing computational costs while maintaining accuracy. Additionally, turbulence is injected using the **Synthetic Random Fourier Method (SRFM)**, providing controlled and realistic turbulence spectrum—a novel approach compared to the usual method of generating turbulence through triply periodic boundary conditions and a forcing pressure gradient.

First we validated the PGS method, demonstrating that even in coarser, lower-resolution simulations, the mean errors in velocity magnitude and turbulent kinetic energy (TKE) remain below 4% and 5%, respectively.

Key findings reveal that in high-porosity TPMS configurations, such as the Gyroid with a structural factor of 1.20 (porosity $\phi = 90\%$), larger injected turbulence scales are reduced to the pore size as the flow passes through. The TPMS acts as a **scale reducer**, diminishing both the length scales and time scales of turbulence, which slowly begin to increase again after exiting the porous medium. TKE increases at a rate of about 4% per pore, following an initial steep increase of 600% upon entering the media. The ability of TPMS to isotropize the flow was confirmed through power spectral density (PSD) analyses, showing behavior similar to that of turbulent grids.

Additionally, we compared two Gyroid TPMS configurations with different porosities—structural factors of 1.20 ($\phi = 0.90$) and 0.75 ($\phi = 0.72$). Reducing the porosity from 0.90 to 0.72 increased TKE by up to 65%, with a corresponding rise in dissipation rates by a factor of 10. The characteristic turbulent length scales adapt to the pore size, consistent with the **Pore-Scale Prevalence Hypothesis (PSPH)**. This adaptation occurs almost immediately within the first pore in low-porosity structures, whereas in high-porosity configurations, it takes about three pores to fully adjust. In particular, the low-porosity configuration showed a blocking effect that increased the time-scale before entering in the PM of around 15%. This effect is not observed in the high-porosity case.

These results underscore the capacity of TPMS geometries to control turbulence intensity and energy dissipation, making them highly effective for applications such as heat exchangers and combustion systems.

In conclusion, this study highlights the potential of TPMS geometries as a powerful tool for advancing the understanding of turbulent flows in porous media. By injecting a controlled turbulence spectrum and validating the PGS method, we provide novel insights into the development of turbulence models for future low-emission combustion technologies and enhanced energy efficiency applications.

Acknowledgments

Thanks to everybody, especially to my internship supervisors - Rémi, François and José - and to you, my dear reader.

Contents

Nomenclature

Acronyms

AM Additive Manufacturing

CDF Cumulative Distribution Function

CFD Computational Fluid Dynamics

CFL Courant-Friedrichs-Lewy condition

CPU Central Processing Unit

DFT Discrete Fourier Transform

DNS Direct Numerical Simulation

DoF Degrees of Freedom

EOS Equation of State

ERC European Research Grant

ERK Explicit Runge-Kutta scheme

FD Finite Difference

FE Finite Element

FFT Fast Fourier Transform

FP Flux Points

FR Flux Reconstruction

FV Finite Volume

GENCI Grand équipement national de calcul intensif (ENG: Large national computer intensive equipment)

GPM Generic Porous Matrix

HIT Homogeneous and Isotropic Turbulence

HLLC Harten Lax and van Leer Contact Riemann Solver

HO High Order

HPC High Performance Computing

IBC Immersed Boundary Condition

IBM Immersed Boundary Method

IRK Implicit Runge-Kutta scheme

JAGUAR proJect of an Aerodynamic solver using General Unstructured grids And high ordeR schemes

LBM Lattice Boltzmann Method

LES Large Eddy Simulation

LO Low Order

MPI Message Passing Interface

NS Navier-Stokes

ONERA Office national d'études et de recherches aérospatiales (ENG: National Office of Aerospace Studies and Research)

PDF Probability Density Function

PDF Probability Distribution Function

PIV Particle Image Velocimetry

PP Passot-Pouquet

PSD Power Spectral Density

PSPH Pore Scale Prevalence Hypothesis

PT Post-Treatment

RANS Reynolds Averaged Navier-Stokes

REV Representative Elementary Volume: REV-L (in Laminar regime), REV-T (in Turbulent regime)

RK Runge-Kutta

RMS Root Mean Square

RST Reynolds Stress Tensor

SD Spectral Difference

SDM Spectral Difference Method

SP Solution Point

SRFM Synthetic Random Fourier Method, a type of STI

STI Synthetic Turbulence Injection

SV Spectral Volume

TKE Turbulent Kinetic Energy

TPMS Triply Periodic Minimal Surface

TVD Total Variation Diminishing

VKP von Kármán-Pao

VTK Visualization ToolKit (Python library and/or file format)

VTU Visualization ToolKit for Unstructured meshes (file format)

Greek Symbols

α [m^2/s] Thermal diffusivity

α_{PGS}^{-2} [-] PGS factor

α_{PGS} [-] PGS coefficient

$\bar{\tau}_{ij}$ [s] Integral time-scale, defined as $\int_0^\infty \rho_{ij}(\tau)d\tau$

β [1/K] Thermal expansion coefficient

η_k [m] Kolmogorov's length-scale

$\gamma = \frac{C_v}{C_p}$ [-] Ratio of specific heats

$\Lambda_{ij,k}(\mathbf{x})$ [m] Energy-containing length-scale, computed as the peak of the energy spectrum function $E_{ij,k}(\mathbf{x}, \kappa_k)$ along direction $\hat{e_k}$

$\Lambda_{ij}(\mathbf{x})$ [m] Energy-containing length-scale, computed as the peak of the energy spectrum function $E_{ij}(\mathbf{x}, \mathbf{k})$

μ [kg$\frac{}{m \cdot s}$] Dynamic viscosity

$\nu = \frac{\mu}{\rho}$ [m$^2/s$] Kinematic viscosity

$\omega = 2\pi f$ [rad/s] Angular frequency, where f is the frequency [Hz]

ϕ [-] Porosity

ϕ_c [-] Critical porosity, beyond which the PSPH is no more true

ρ [kg/m^3] Density

$\rho_{ij}(\tau)$ [-] Two-points time-correlation, defined as $\frac{R_{ij}(\tau)}{R_{ij}(0)} = \frac{\langle u_i(t) u_j(t+\tau) \rangle}{\langle u_i(t) u_j(t) \rangle}$

τ_η [s] Kolmogorov's time-scale

Kolmogorov's velocity-scale

Roman Symbols

ΔT [K] Temperature difference across the fluid layer

$\mathbf{u_i} = \frac{\mathbf{u_{Darcy}}}{\phi}$ [m/s] Intrinsic average velocity

$\mathbf{u_{Darcy}}$ [m/s] Darcy's velocity

$\mathbf{u}(\mathbf{x}, t) \equiv \{u_1, u_2, u_3\} \equiv \{u(\mathbf{x}, t), v(\mathbf{x}, t), w(\mathbf{x}, t)\} = \mathbf{U} - \bar{\mathbf{U}}$ [m/s] Velocity fluctuation field

$\mathbf{U}(\mathbf{x}, t) \equiv \{U_1, U_2, U_3\} \equiv \{U(\mathbf{x}, t), V(\mathbf{x}, t), W(\mathbf{x}, t)\}$ [m/s] Velocity field

$\mathcal{L}_{ij,k}$ (or$L_{ij,k}$) [m] Integral length-scale, computed using the spatial correlation function $R_{ij,k}$

$\{x, y, z\} \equiv \{x_1, x_2, x_3\}$ [m] Coordinates in the frame of reference

$\{\hat{e_1}, \hat{e_2}, \hat{e_3}\}$ [-] Unit vectors in the frame of reference

$c = \sqrt{\gamma r T}$ [m/s] Speed of sound

C_p [J/kg·K] Specific heat at constant pressure

C_v [J/kg·K] Specific heat at constant volume

d_H [m] Hydraulic diameter

$E(\mathbf{x}, \kappa)$ [m^3/s^2] Isotropic energy spectrum function at point $\mathbf{x}$

$E_{ij,k}(\mathbf{x}, \kappa_k)$ [m^3/s^2] Energy spectrum function at point $\mathbf{x}$ along direction $\hat{e_k}$

$E_{ij}(\mathbf{x}, \kappa)$ [m^3/s^2] Energy spectrum function at point $\mathbf{x}$

$E_{ij}(\omega)$ [m^2/s^2/(rad/s)] Energy spectrum in the angular frequency domain ω, defined as $\frac{1}{\pi} \int_{-\infty}^{\infty} R_{ij}(\tau) \exp(-i\omega\tau) d\tau = \frac{1}{\pi} \int_0^{\infty} R_{ij}(\tau) \cos(\omega\tau) d\tau$

$E_{ij}(f)$ [m^2/s^2/Hz] Energy spectrum in the linear frequency domain f

f [Hz] Frequency

$g = 9.80665$ [m/s^2] Gravitational acceleration

h [W/(m$^2 K$)] Heat transfer coefficient or mesh size [m]

$K = \frac{\rho g k}{\mu}$ [m/s] Hydraulic conductivity

k [m^2] (Intrinsic) Permeability

k [W/(m K)] Thermal conductivity

$Kn = \frac{\lambda}{l}$ [-] Knudsen number

L [m] Characteristic length

$L_0 = \sqrt{L_{0,x}^2 + L_{0,y}^2 + L_{0,z}^2}$ [m] Isotropic integral length-scale

$L_{0,k} = \frac{1}{2}(\mathcal{L}_{11,k} + \mathcal{L}_{22,k} + \mathcal{L}_{33,k})$ [m] Integral length-scale along direction $\hat{e_k}$

$M = \frac{m}{N}$ [kg/mol] Molar mass

m [kg] Mass

$Ma = \frac{V}{c}$ [-] Mach number

N [mol] Number of moles

$Nu = \frac{hL}{k}$ [-] Nusselt number

p Polynomial degree in SDM [-], Pressure [Pa], or pore size [m]

$R = 8.314462$ [J/(mol·K)] Universal gas constant

$r = \frac{R}{M}$ [J/(kg·K)] Specific gas constant

$R_{ij,k}(\mathbf{x}, r\hat{e_k})$ [$\mathrm{m^2/s^2}$] Spatial correlation at point $\mathbf{x}$ along direction $\hat{e_k}$

$R_{ij}(\mathbf{x}, \mathbf{r})$ [$\mathrm{m^2/s^2}$] Spatial correlation at point $\mathbf{x}$

$R_{ij}(\tau)$ [$\mathrm{m^2/s^2}$] Two-points time-covariance, defined as $\langle u_i(t)u_j(t+\tau)\rangle$

$R_{ij}(x, t, \tau)$ [$\mathrm{m^2/s^2}$] Two-points time-covariance function
(for a statistically stationary random process, simplified as $R_{ij}(x, \tau)$)

$Ra = \frac{g\,\beta\,\Delta T\,L^3}{\nu\,\alpha}$ [-] Rayleigh number

$Re = \frac{\rho U D}{\mu}$ [-] Reynolds number

$Re_p = \frac{\rho|\mathbf{u_i}|p}{\mu}$ [-] Reynolds number

s (or p)[m] Pore size

struct [-] Structural factor (used in the mathematical definition of a TPMS)

Overline Symbols

$\hat{(.)}$ Quantity in the iso-parametric domain

$\overline{(.)}$ Time-average or resolved filtered quantity

$\tilde{(.)}$ Reconstructed quantity using correction functions, Roe's average, Favre time-average, or resolved Favre-filtered quantity

Mathematical Operators

$\frac{\partial(.)}{\partial t} \equiv (.)_{,t} \equiv \dot{(.)}$ Partial derivative with respect to time

$\frac{\partial(.)}{\partial x_i} \equiv (.)_{,x_i} \equiv (.)'$ Partial derivative with respect to space

$\frac{\partial(.)}{\partial x} \equiv \partial_x(.) \equiv (.)_{,x}$ Partial (prime) derivative with respect to x

$\frac{D(.)}{Dt} \equiv \frac{\partial(.)}{\partial t} + \mathbf{U} \cdot \nabla(.)$ Material derivative

$\mathcal{F}\{\}$ (Continuous) Fourier Transform operator

$\nabla(.)$ Gradient

$\nabla \cdot (.)$ Divergence operator

$\nabla \times (.)$ Curl operator

$\nabla^2(.) \equiv \nabla \cdot \nabla(.)$ Laplacian operator

$dft\{\}$ Discrete Fourier Transform operator

$fft\{\}$ Fast Fourier Transform operator

$Tr()$ Trace operator

F(.) CDF

f(.) PDF

1 Introduction

Porous media are not merely static materials; they are dynamic participants in both natural and engineered systems. Whether it's the Earth's soil, acting as a highway for water and nutrients, or the intricate network of air sacs in human lungs facilitating gas exchange, porous materials have been integral to life and technology for eons. Nature has long used porous structures, offering inspiration for engineering applications across diverse fields (see Figure 1).

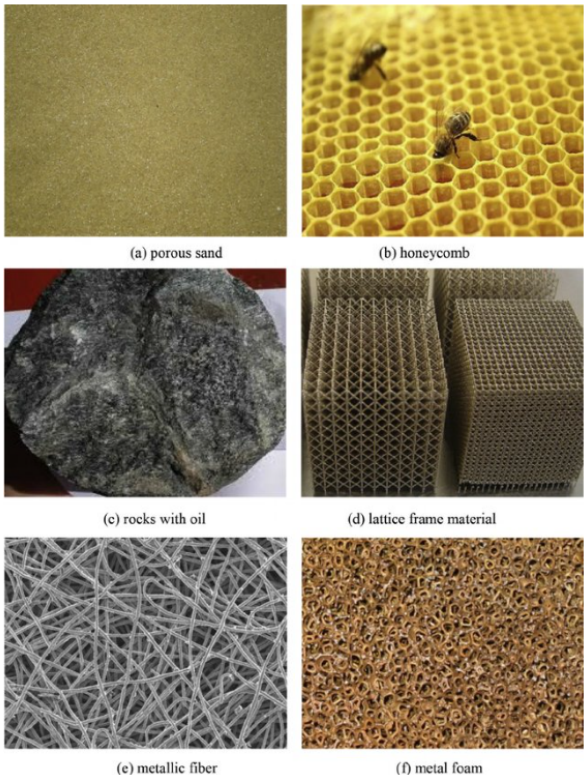

Figure 1: Some common examples of porous media in nature and engineering. (ref:[195])

Porous media are defined by their network of interconnected voids, which gives them a high surface area-to-volume ratio and a tunable pore structure. These characteristics enable effective mass transfer, adsorption, and fluid flow, making porous materials indispensable for filtration, catalysis, and heat transfer applications. Their permeability dictates fluid behavior, while properties like thermal conductivity and mechanical robustness make them valuable for thermal management and structural uses.
Across various industries, porous media find critical applications. In filtration systems, they remove contaminants from fluids in water purification and air filtration ([62], [201], [114]). They also serve as catalyst supports in chemical reactions, from petroleum refining [1] to environmental remediation ([137], [100]). Heat exchangers ([149], [186], [139]), biomedical implants and tissues ([3]), and acoustic insulation systems ([197]) all utilize porous materials for their exceptional properties in mass and heat transfer, chemical processes, and noise attenuation.
In aerospace and industrial domains, porous media are pivotal due to their impact on fluid dynamics and acoustic behavior, particularly in combustion chambers and liners [14], [115]. Within combustion systems, these materials optimize the interaction between fuel and oxidizer, enhancing mixing, stabilizing flames, and improving safety and, most of all, the efficiency, leading to a leaner combustion with estimated reductions in NO_x and CO_x emissions by up to 50% and an increase in the efficiency of a thermal (Brayton cycle) engine by a factor of around 1.2 ([160], [126]). Their use as flame stabilizers is especially crucial for mitigating combustion instabilities, increasing the lean flammability limit, and ensuring operational safety ([113], [120]). An example of application is heterogeneous combustion shown in Figure 2. In Figure 4 is also an example of porous media samples adopted in combustion research.
In the realm of acoustics, porous media excel in noise reduction and vibration control. By dissipating acoustic energy through mechanisms such as viscous and thermal losses, they help meet stringent regulatory standards in aerospace propulsion systems, industrial machinery, and beyond ([21], [196]). One

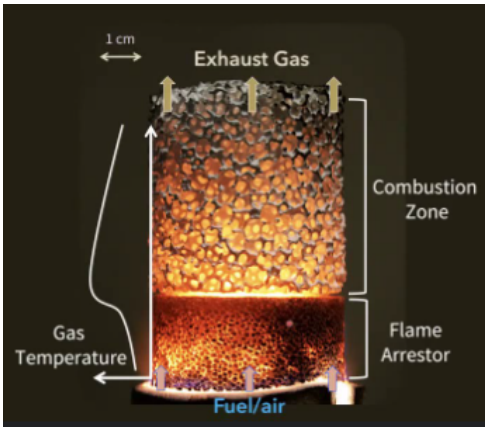

Figure 2: Example of state-of-the-art application: heterogeneous combustion in porous media ring foams for ultra-low emissions. The ongoing study is mainly directed by Prof. Ihme at the Research Department of Mechanical Engineering, Stanford University.([44], [24])

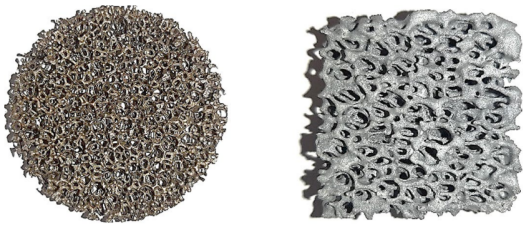

Figure 3: Typical ceramic (left) and metallic (right) PM structures used for combustion or noise reduction applications in engineering.

particularly interesting application in recent decades is the broadband noise reduction of a wing trailing edge through porous wing surfaces ([169], [170]).

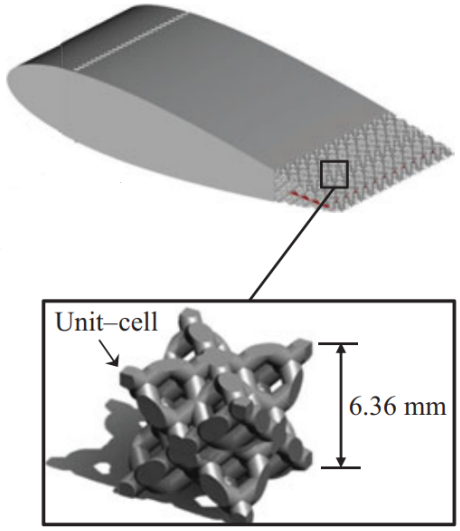

Figure 4: Example of state-of-the-art application: porous media trailing edge for broadband noise reduction. ([169])

Despite their widespread use in diverse applications, understanding the flow inside porous media remains a significant challenge. Their geometric complexity and unique physical behaviors, particularly in turbulence and combustion, make accurate simulation difficult, even with high-performance computing resources. Moreover, experimental studies are equally demanding due to the difficulty of accessing

internal pore structures without compromising the natural flow behavior. As a result, most historical studies have focused on laminar flow regimes and simplified geometries, such as packed spheres or randomly generated porous structures [70], [71]. While several models have been proposed to address these challenges ([176], [96], [89]), our understanding of turbulence in porous media remains limited.
However, recent advances in computational power, along with the advent of 3D printing technology, have paved the way for more detailed and accurate studies of porous media, especially in critical regimes like the transition from laminar to turbulent flow and fully developed turbulence itself ([194], [73]). These developments provide the perfect opportunity to deepen our understanding of the complex flow dynamics in porous structures, moving beyond the simpler models of the past.
In this context, our contribution aims to explore the lesser-known field of turbulence in porous media using state-of-the-art numerical approaches. Specifically, this work investigates the turbulence behavior within a class of porous materials known as Triple Periodic Minimal Surfaces (TPMS) through Direct Numerical Simulations (DNS). By leveraging high-performance computing (HPC) and modern simulation techniques, we hope to shed light on the intricate turbulence mechanisms within TPMS, offering new insights and potential applications in fields ranging from aerospace to energy systems.

- **Why turbulent regime in porous media?**
  Turbulence in porous media is more exciting than the laminar regime because it enhances mixing, heat transfer, and overall efficiency in processes like combustion and filtration. Its complexity and unpredictability push the boundaries of fluid dynamics, offering potential breakthroughs in engineering and technology. Moreover, certain applications inherently operate in turbulent regimes, making it crucial to deepen our understanding for future optimization of these systems.

- **Why TPMS materials?**
  For a systematic study, we required a class of materials with well-defined geometries, easy parametrization of properties such as porosity, and ease of reproduction via additive manufacturing (AM) and 3D printing techniques ([45], [200], [77]) for future experiments and applications. TPMS materials fulfill all these criteria and offer additional advantages. Recent studies have demonstrated that this class of materials, with its high surface-to-volume ratio and constant mean curvature, possesses excellent mechanical ([145], [77]), thermal ([186], [198]), and turbulence-enhancement properties, significantly increasing scientific interest.

- **Why DNS?**
  Given the uncertainty surrounding turbulent behavior in porous media and the lack of extensive literature on the subject, assumptions cannot be made at this stage. Traditional modeling approaches are insufficient, making Direct Numerical Simulation (DNS) the ideal tool for accurately capturing the flow properties and underlying dynamics in this complex regime.

This work represents just the first step in a broader research journey, which will continue through my PhD within the POROLEAF project (ERC Starting Grant 2023, led by Remi Roncen at ONERA). The future phases of this research will focus on the practical development of turbulence models, building upon the fundamental understanding of turbulence in porous media. In parallel, the project will investigate combustion in porous media, particularly in TPMS materials. We will begin with laminar regimes to establish a solid foundation, before progressing toward turbulent combustion, where my contribution will be key in advancing our understanding of turbulence. After all, one cannot study turbulence in combustion without first understanding turbulence in non-reactive air.
As we venture into this exploration, it's worth noting that research is often a long and challenging journey. Yet, the fire of curiosity, knowledge, and human potential drives us forward. *Sapere aude*—dare to know, to delve deep into the unknown, and to uncover the truths that propel our world forward. This is the spirit in which this research is presented, and it is our hope that this work ignites the same passion in its readers.

In this introductory section, we begin with an overview of the state of the art in the field of turbulence in porous media in Section 1.1, highlighting the connected challenges (Section 1.2). This leads us to present the objectives and motivations of this work in Section 1.3. Finally, we conclude by explaining the structure of the manuscript in Section 1.4.

1.1 Overview of turbulence in porous media

Turbulent flows in porous media occur in a wide variety of applications as shown in Table 1. A common way to describe the flow features and its regime is using the Reynolds number, that in this case is defined based on the pore size p and the velocity mean velocity through the pore (called intrinsic velocity $\mathbf{U_i}$): $Re_p = \frac{|U_i|p}{\nu}$. Over the last century, various authors have attempted to understand and model these flows across all regimes, within different types of porous media, ranging from foams and honeycombs to packed beds and highly inhomogeneous and anisotropic materials.

Table 1: Example applications of high-$Re_p = \frac{|U_i|p}{\nu}$ (pore Reynolds number) flows in porous media.

Application	Re_p **range**	**Typical value**	**Reference(s)**
Packed bed catalysis	1.5×10^2 – 1.0×10^4	3.0×10^3	Lucci et al. (2017) [106], Shams et al. (2014) [156]
Heat transfer operations in packed beds	3.0×10^2 – 6.0×10^4	5.0×10^2	Chandesris et al. (2013) [34], Dixon et al. (2012) [41]
Catalytic steam reforming	4.0×10^2 – 2.3×10^4	5.0×10^3	Shayegan et al. (2008) [158], Zhang et al. (2018) [202]
Dense fluidized beds/sprouted beds	1.0×10^2 – 1.0×10^4	3.0×10^2	Deen et al. (2012) [40], Link et al. (2005) [99]
Nuclear pebble bed reactors	6.0×10^2 – 6.5×10^4	4.6×10^4	Lucci et al. (2017) [106], Dave et al. (2018) [39], Shams et al. (2013) [157]
Fluid–porous interface/dams zone	1.0×10^2 – 1.9×10^5	3.0×10^2	Blois et al. (2014) [22], Packman et al. (2004) [135]
Porous burners	2.0×10^2 – 1.3×10^4	2.5×10^2	de Lemos et al. (2009) [98], Nimvari et al. (2014) [131]
Oil–air separations	1.5×10^2 – 3.5×10^3	1.0×10^3	de Carvalho et al. (2015) [31]
Produce cooling	2.3×10^2 – 4.4×10^3	1.0×10^3	Irvine et al. (1993) [68], Vigneault et al. (2004) [182]
Rotating packed beds	3.0×10^3 – 3.5×10^4	3.6×10^3	Burns et al. (2000) [27], Larsson et al. (2017) [91]
Near-surface atmospheric flows (e.g., forest canopies, urban landscapes)	1.0×10^2 – 1.0×10^6	NA	Belcher (2005) [17], Lucci et al. (2017) [106], Belcher et al. (2012) [18]

In porous media, two types of turbulence can be observed, as described by Jin et al. (2024) [73] in a recent publication: high-Re_p turbulence (the classical form) and high-Ra turbulence (referred to as "pseudo-turbulence"), which can occur even at low Re_p than traditionally observed.

- **Classical turbulence in porous media:**

  Regarding classical turbulence, when Re_p approaches or exceeds approximately 100, the flow within the pores can transition to a turbulent state. This phenomenon is particularly relevant in applications such as thermal energy storage systems, where rocks or bricks are used for heat retention [134]. In these systems, the heat charging and discharging processes are often governed by mixed convection—a combination of forced and natural convection. Due to the low thermal conductivity of materials like rocks or bricks, the efficiency of heat transfer is limited, resulting in slow charging and discharging rates. To improve this process, the porous element size and fluid velocity may be adjusted to induce fully turbulent flow, as demonstrated by [34] in their DNS studies of heat transfer in porous domains, which showed improved efficiency under turbulent conditions.

  When considering porous media as analogous to a bank of tubes, the relationship between the Nusselt number Nu and the Reynolds number Re_p shifts from $Nu \sim Re_p^{0.36}$ for $Re_p < 300$ to Nu

$\sim Re_p^{0.64}$ for fully turbulent flow ($Re_p > 300$), as reported by the Engineering Sciences Data Unit ([174]). This transition significantly enhances heat transfer efficiency due to the onset of turbulence. This has been further validated in packed bed reactors, a field thoroughly investigated by [156, 39, 106], where pore-scale turbulence is crucial in optimizing chemical reactions. For instance, the pore-scale Reynolds number in nuclear pebble bed reactors can reach up to 10^5 [39], exceeding the laminar-turbulent transition threshold by several orders of magnitude.

Additionally, systems such as catalyst-packed beds, where Re can reach as high as 10^4 [106], and urban canopy flows [118] exhibit significant turbulent effects, particularly in scenarios with high porosity values, ϕ, often exceeding 90% [53]. For instance, turbulence within plant canopies can attain pore-scale Reynolds numbers (Re_p) as high as 10^5 in the upper regions of well-ventilated canopies [18]. Tree canopies are frequently modeled as porous media, and a detailed understanding of their turbulent behavior is crucial for studying the exchange processes between the soil and atmosphere (e.g. CO_2 budget [18]).

- **Pseudo-turbulence in porous media:**

  In addition to classical turbulent flows, natural convection in porous media at high Rayleigh numbers (Ra) can lead to flow instabilities. These flows, which occur at large Ra, are transient, chaotic, and random, exhibiting characteristics akin to classical turbulence. However, unlike classical turbulence, these transient natural convection flows can occur at very low Re_p, a phenomenon termed "pseudo-turbulence." Studies such as [65] and [54] highlight how pseudo-turbulence impacts CO_2 sequestration and geothermal energy extraction, with implications for enhancing oil and gas recovery [50].

1.1.1 Multiscale Modeling and Simulation of Turbulent Flows in Porous Media

The study of turbulent flows in porous media has gained significant attention in recent years, driven by the need to address industrial challenges and better understand natural processes. CFD has emerged as a critical tool in this endeavor. Depending on the time and length scales of the motions under study, CFD simulations of convection in porous media can be categorized into microscopic and macroscopic simulations.

- **Microscopic Simulations**:
  Microscopic simulations resolve motions at scales smaller than the Representative Elementary Volume (REV, i.e. the smallest sub-volume of the porous matrix that shows the same flow behavior), necessitating detailed consideration of the porous elements' geometry. A prominent example is Pore-Scale-Resolved Direct Numerical Simulation (PSR-DNS), where the microscopic governing equations (typically the NS equations) are solved directly without additional modeling. PSR-DNS offers high accuracy but is computationally expensive, limiting its application until recent advances in computational power [34, 72, 175, 36, 148, 187, 188, 163]. In particular, the work of [175] showed how DNS could be applied to simulate turbulence within porous structures, reinforcing the Pore-Scale Prevalence Hypothesis (PSPH) [70] which is presented in the next paragraph.

- **Macroscopic Simulations**:
  In contrast, macroscopic simulations are more computationally efficient, derived by time and volume averaging (or sometimes just volume averaging) of the microscopic governing equations. These simulations are widely used in engineering applications due to their lower computational demands [94, 143, 88, 76, 86, 97]. However, macroscopic simulations often rely on strong assumptions to close the averaged momentum equations, which can lead to inaccuracies and uncertainties in the results, as shown in studies such as [96].

1.1.2 The Pore-Scale Prevalence Hypothesis (PSPH)

The possibility of macroscopic turbulence surviving in porous media has been a subject of intense study and debate in recent years. Two distinct perspectives have emerged in the literature regarding the feasibility of macroscopic turbulence within such media:

- **First View: Possibility of Macroscopic Turbulence**
  The first school of thought, supported by researchers such as Lee and Howell [94] and Antohe and Lage [5], contends that macroscopic turbulence in porous media is indeed possible. According

to this view, when macroscopic turbulence is present, the transport of turbulent kinetic energy must be considered. Several macroscopic turbulence models have been developed incorporating this transport mechanism, including models by Prescott and Incropera [143] and de Lemos [96].

- **Second View: Impossibility of Macroscopic Turbulence**
  In contrast, the second perspective argues that macroscopic turbulence is fundamentally impossible within porous media due to the constraints imposed by the pore scale on the size of turbulent eddies. Prominent proponents of this view include Nield [130] and Nakayama and Kuwahara [128]. Studies such as [167] suggested that only turbulent eddies with mixing length scales greater than the cylinder diameter contribute significantly to dispersion.

  DNS studies by Jin et al. [71, 72] (Figure 5) reinforced this view by showing that turbulent eddies are generally confined by the pore size, leading to the "Pore-Scale Prevalence Hypothesis" (PSPH). Uth et al. [175] further validated this hypothesis, confirming the restriction of turbulent eddies across different geometries.

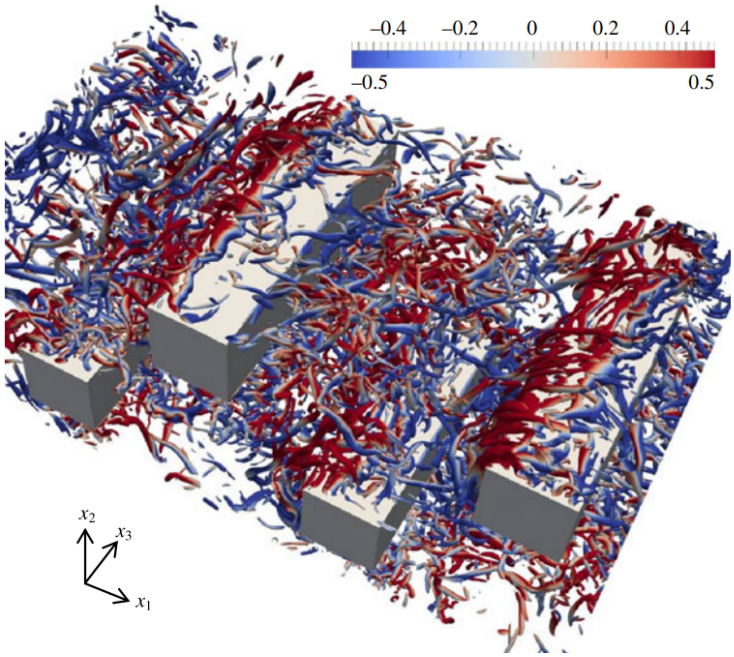

Figure 5: A visualization of vortex structures (isosurfaces of $Q \cdot d^2/u_m^2 = 1$, color-coded by the instantaneous vertical velocity u_2, where Q represents the Q-criterion) based on Jin et al. (2015) [72]. The flow is simulated around a 2D configuration of regularly arranged square bars ($Re_p = 1000$, $\phi = 0.82$). This study provides significant evidence supporting the PSPH for mid-to-high porosity porous matrices.

What are the conclusions about the PSPH?
While the PSPH provides a strong argument for the limitation of turbulence to the pore scale, recent studies suggest that this hypothesis has a boundary of validity. As porosity approaches unity, the influence of the porous matrix on the flow diminishes, potentially allowing macroscopic turbulence to survive. Rao, Kuznetsov, and Jin [147] developed a macroscopic model based on the PSPH, which effectively captures microscopic turbulence. However, they acknowledged limitations, particularly when the porosity becomes high enough that the porous matrix's impact diminishes (see Figure 6). In fact they defined a critical value of the porosity ϕ_c, after which value the macroscopic turbulence can survive. Its value is material-dependent and is slightly influenced by the magnitude of Re_p. For example for arranged spheres $\phi_c \simeq 0.92 - 0.96$ while for a mix of arranged spheres and bars it is higher ($\phi_c \simeq 0.95 - 0.97$) [148].
Further work by Uth et al. [175] demonstrated that introducing larger-scale elements in the porous matrix could stimulate strong, large-scale turbulence. Chu, Weigand, and Vaikuntanathan [35], as well as Srikanth et al. [163], also observed the presence of large turbulent structures in high-porosity flows, suggesting that PSPH may not universally preclude macroscopic turbulence in all porous media configurations.

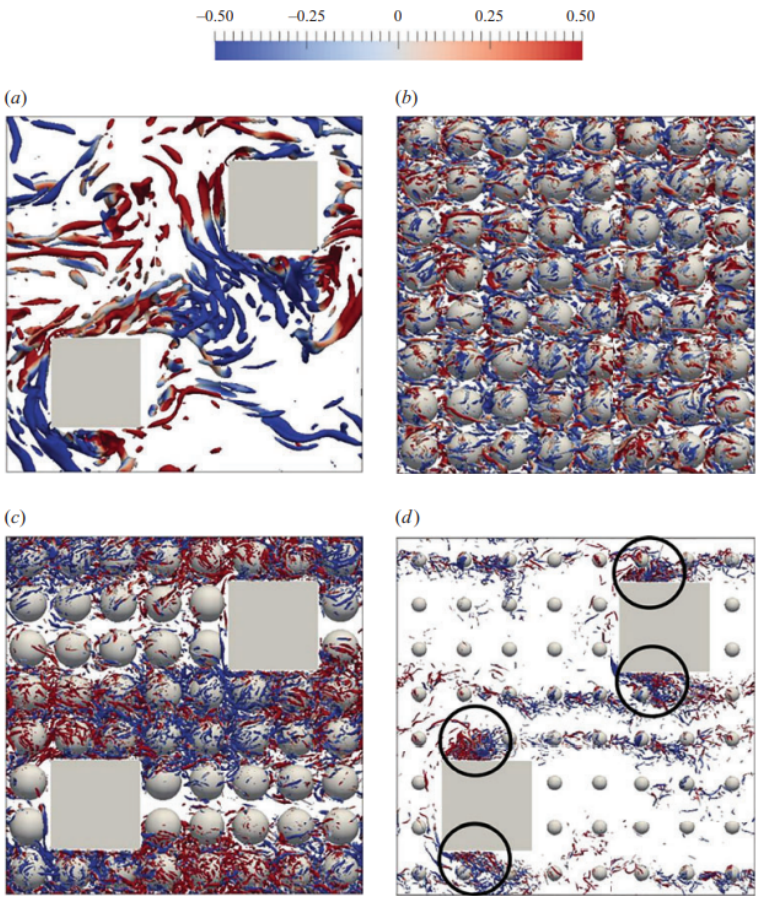

Figure 6: The 4 types of porous media geometry studied recently by Rao, Jin et al. (2022) [148]. Instantaneous turbulence structures are represented, with a colour coding showing the instantaneous value of the vertical velocity u_2, $Q/Q_M = 2 \times 10^{-2}$, where Q_M is the maximum value of Q:Q-criterion.

1.2 Challenges in Turbulence in Porous Media

In Table 2 we resume the main articles on the subject of the turbulence in porous media.
Despite significant advancements, both microscopic simulation and macroscopic modeling of turbulent flows in porous media remain challenging due to the high complexity of the phenomena and the difficulty in validation. Future research should focus on addressing these challenges, particularly in refining multiscale modeling techniques and improving the accuracy of simulation methods. The consolidation and systematic analysis of existing knowledge, as well as the identification of unresolved issues, will be crucial in advancing this field.
Turbulence in porous media presents several significant challenges for current research:

1. **Limited bibliographical foundation**: The study of turbulence in porous media has only gained substantial attention in the past few decades, primarily in fields like combustion and acoustics, where advanced engineering applications are prominent.

2. **Complexity of modeling the Navier-Stokes (NS) equations**: The application of models such as Reynolds-Averaged Navier-Stokes (RANS) and Large Eddy Simulation (LES) in porous media presents significant challenges due to the complex fluid-solid interactions that are not fully understood. This complexity makes Direct Numerical Simulation (DNS) an indispensable tool for advancing our understanding of turbulence in porous materials. However, DNS itself faces internal limitations, particularly when modeling solid boundary conditions. Capturing the intricate geometries of porous media typically requires highly refined meshes, which substantially increase computational costs. Furthermore, these fine meshes necessitate smaller time steps to maintain stability, as dictated by the CFL condition. This constraint on the time step adds to the computational burden, making DNS simulations both time-consuming and resource-intensive.

3. **High computational demands**: The intricate geometry of porous media, characterized by high curvature and small-scale features, necessitates extremely fine meshes and correspondingly small time steps due to the CFL condition. Additionally, turbulence at smaller scales, which are inversely proportional to the Reynolds number, further escalates computational costs, especially in high-Reynolds-number turbulent applications.

4. **Statistical complexity**: The rapidly varying geometry along flow paths in porous media prevents the assumption of statistical independence along the fluid-solid interface, a simplification often used in simpler geometries like pipes or ducts.

5. **Challenges in manufacturing complex geometries**: The production of porous media with small pore sizes and intricate geometries necessitates advanced manufacturing techniques, such as Additive Manufacturing, Inkjet Printing, Electrohydrodynamic (EHD) Jet Printing, or Screen Printing. Specifically, for Triply Periodic Minimal Surfaces (TPMS) materials, which are of interest in our work, additive manufacturing is a crucial technology [200], [77], [45].

Article Name	**Numerical Method**	**Porous Media Type**	Re_p **Range**	**Porosity**
Jin et al. (2024) [73]	Review of methods	NA	NA	NA
Jin et al. (2015) [72]	DNS-FVM and DNS-LBM	Regularly arranged squared cylinders	500 - 1000	0.78 - 0.94
Jin et al. (2017) [70]	DNS-LBM	Regularly arranged spheres	250-500	0.69 - 0.80
Liu et al. (2023, 2021) [103, 101]	DNS-LBM	Square pores connected by rectangular throats	NA	0.33
Chandesris et al. (2013) [34]	DNS-FVM	Regularly arranged cubes	5500 - 6000	0.88
Uth et al. (2016)	DNS-LBM [175]	Squared and circular cylinders, regularly arranged spheres	400 - 600	0.78 - 0.94
Chu et al. (2019) [36]	DNS-FVM	Squared cylinders	500 - 1500	0.56 - 0.75
Rao et al. (2021) [148]	DNS-FVM	Arranged spheres, squared cylinders and mix	500 - 750	0.70 - 0.98
He et al. (2018, 2019) [60, 61]	DNS-LBM	Arranged bed of spheres	300-1000	0.26
Srikanth et al. (2021) [163]	LES-FVM and DNS-FVM	Circular cylinders	100 - 1000	0.50
Shams et al. (2014) [156]	LES-FVM	Randomly stacked bed of spheres	9000	0.40
Lucci et al. (2017) [106]	DNS-FVM	Foams	10 - 1000	0.82-0.88
Breugem et al. (2005) [25]	DNS-FVM	Regularly arranged cubes	0 - 1000	0.88
Kuwahara et al. (2006) [87]	LES-LBM	Arranged spheres, arranged squared cylinders	3600	NA
Suga (2016) [164]	LES-LBM	Arranged spheres, arranged squared cylinders	500 - 1000	NA

Table 2: Summary of numerical methods, porous media types, Reynolds number ranges, and porosity studied in various articles.

1.3 Motivations and Objectives of this work

This study employs Direct Numerical Simulations (DNS) using the JAGUAR code, developed by ONERA-CERFACS in Toulouse. The simulations were executed on GENCI's supercomputers, the French National High-Performance Computing Facility, through a challenge secured by my supervisor, R. Roncen.
GENCI (Grand Équipement National de Calcul Intensif) plays a crucial role in providing access to the high-performance computing resources needed for advanced research, including those at the Très Grand Centre de Calcul (TGCC). TGCC is a state-of-the-art facility designed to host petascale supercomputers, offering immense computational power for scientific research. One of the key systems used in our project at TGCC is Irene, part of the Joliot-Curie supercomputer. Irene's Skylake (SKL) partition, with 1656 dual-processor Intel Skylake 8168 nodes running at 2.7 GHz and 24 cores per processor, contributes 79488 cores to the system, delivering 6.86 Pflops/s of computational power. Each node is equipped with 192 GB of DDR4 memory, and the partition is connected via Infiniband EDR, ensuring fast communication for parallel processing. This amazing computation power, made possible by GENCI's support, enabled us the execution of the DNS simulations required for this study.
The JAGUAR code integrates several advanced features to enhance accuracy and efficiency, including the Spectral Difference Method (SDM) solver for precise turbulence resolution, an Immersed Boundary Conditions (IBC) method to handle complex geometries of porous media, and a Pressure Gradient Scaling (PGS) technique to improve computational efficiency. DNS, by resolving all turbulence scales, allows for a detailed analysis of flow structures that are often averaged out in other simulation approaches like RANS, LES, or Volume Averaged Theory (VAT) models.
This thesis aims to achieve two primary objectives:

1. **Validation of the Numerical Setup**: While the JAGUAR code with IBC has already been validated [38], the integration of the PGS method and its interaction with IBC require validation, particularly for simulating turbulence in porous media. This study focuses on ensuring the reliability and accuracy of these methods within this context.

2. **Systematic Turbulence Analysis**: The second objective is to systematically investigate the turbulent behavior in porous media by exploring the effects of key parameters such as porosity, Reynolds number, and inlet turbulence conditions. In this preliminary stage, the study focus was on three specific analyses:

   (a) **Post-treatment of big-data from DNS simulations**: We first needed to develop a strategy to extract only the most essential portion of the data as efficiently as possible, without compromising valuable information needed for turbulence analysis. The main challenge was managing simulations with high Degrees of Freedom (DoF), fine meshes, small time-steps and relatively large time-spans required for the convergence of the flow. In this stage, it was crucial to strike a balance between computational cost, accuracy, and storage constraints.

   (b) **Turbulence Analysis in a Gyroid with struct=1.20**: This analysis delves into the turbulent flow within a *Gyroid* structure with a structural parameter of 1.20 ($\phi = 0.9$). A comprehensive examination of flow patterns, turbulence intensity, and energy dissipation will be conducted using both temporal and spatial turbulence analysis methods to identify key characteristics relevant to TPMS (Triple Periodic Minimal Surface) materials.

   (c) **Turbulence Comparison Based on Different TPMS Structures**: A comparative study between two Gyroid structures with parameters struct=1.20 ($\phi = 0.9$) and struct=0.75 ($\phi = 0.72$) will be performed. This comparison will assess the impact of geometric parameters on flow behavior and turbulence characteristics, laying the groundwork for future optimization and application.

This research is conducted within the broader framework of the ERC (European Research Council) Starting Grant 2023, awarded to my supervisor, R. Roncen, a researcher at ONERA, Toulouse, for the POROLEAF project. POROLEAF focuses on understanding the interactions between flames, turbulence, and waves in porous materials. The key objectives of the project are to investigate turbulence in TPMS structures through both numerical simulations and experimental methods. DNS will be used to capture the detailed turbulence dynamics in these complex geometries, while experimental techniques such as Particle Image Velocimetry (PIV) will provide crucial validation of the numerical results. Additionally, the project aims to develop turbulence models for predicting fluid behavior in porous media and combustion models for flame propagation in both laminar and turbulent regimes. By integrating

these approaches, POROLEAF seeks to advance our understanding of multiphysics interactions within porous materials, with potential applications in energy systems and materials science.

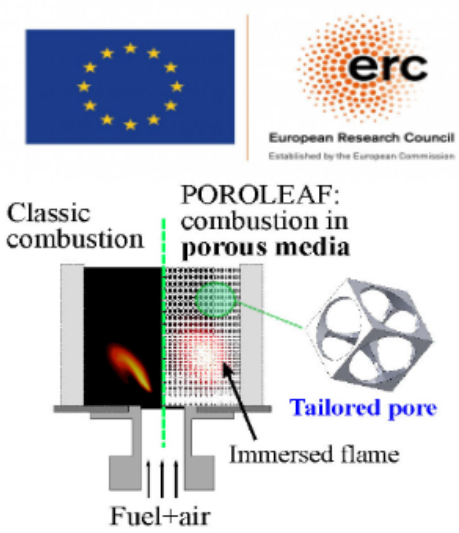

Figure 7: In 2023, Rémi Roncen was awarded a prestigious European Research Council (ERC) grant for his project POROLEAF, focusing on turbulence and flame interactions in porous materials. Selected from 2,696 applicants with a 14.8% success rate, his recognition highlights the importance of his research and the support provided by ONERA's scientific environment.

During my 6-month internship titled "Turbulence in Porous Media," I developed the work presented in this manuscript. **My contribution to POROLEAF project has been to develop a post-treatment analysis and strategy of the data derived from DNSs run by my supervisor R. Roncen**. Inspired by the subject's complexity and future potential, I have chosen to continue researching this area as part of my PhD, which will start in December 2024. The aim of my doctoral research will be to build upon the foundational work of this thesis, contributing to the critical exploration of multiscale modeling and simulation of turbulent flows in porous media, integrating an experimental approach as well. This ongoing effort is part of the broader scientific challenge of understanding and optimizing turbulence in porous structures—an area that, despite its chaotic appearance, holds immense promise for energy and material applications.

1.4 Manuscript Overview

This manuscript is organized as follows:

- **Section 2** introduces the fundamental concepts of porous media, with a focus on the class of materials central to this study: the TPMS (Triply Periodic Minimal Surfaces) matrices. This section provides the necessary background to understand the specific geometries analyzed in the simulations.
- **Section 5** provides a comprehensive review of classical turbulence literature, covering foundational theories. It also introduces the primary turbulence analysis tools, ranging from established methods to advanced approaches, including those developed specifically for the unique requirements of this study.
- **Section 6** outlines the numerical approach used in this research. It describes the JAGUAR code, which employs the Spectral Difference Method (SDM) to directly solve the compressible Navier-Stokes equations. Additionally, this section explains how solid boundaries are modeled using the Immersed Boundary Conditions (IBC) method and how computational efficiency is enhanced through the Pressure Gradient Scaling (PGS) method.
- **Section 7** presents the results of the Direct Numerical Simulations (DNS) conducted in three parts:
  1. Analysis of turbulence in a Gyroid structure with struct=1.20.
  2. Comparative analysis between Gyroid structures with struct=1.20 and struct=0.75.
- **Section 8** provides a discussion of the key findings of this study, synthesizing the results and their implications. Additionally, this section outlines potential avenues for future research based on the insights gained from the simulations.

Happy reading!

2 Porous media properties

With the rapid advancements in material science and manufacturing engineering, complex structures are increasingly being developed and utilized across various engineering fields. These structures, whether made from metals, inorganic non-metals, polymers, or other complex materials, are generally classified as solid structures, where porosity is typically negligible. In fact, internal pores are often viewed as defects resulting from poor manufacturing quality. However, many porous structures found in nature, such as bones, corals, honeycombs, and wood, exhibit exceptional performance. Inspired by these natural formations, there is a growing interest in creating and in exploiting artificial bionic porous structures.
The design of these porous structures is heavily influenced by the capabilities of manufacturing technologies. Traditional methods like cutting or milling are inadequate for producing porous structures with complex topologies and intricate internal pores akin to those found in nature. To address this, specialized techniques such as salt leaching, gas foaming, and phase separation followed by freeze-drying have been developed, though they offer limited control over pore shape, size, and connectivity.
Fortunately, **the advent of revolutionary AM** provides new opportunities for fabricating porous structures, significantly reducing the limitations posed by topological complexity. However, designing porous structures with controllable geometries, reliable manufacturing quality, and broad application potential remains still significant challenge. Porous media can be categorized based on the design methods into three types:

1. 2D honeycombs and 3D foams
2. Strut-based materials
3. **TPMS materials**

The first category includes two-dimensional honeycombs and three-dimensional foams, which can often be produced using traditional cutting technologies. Honeycombs, with their two-dimensional geometric properties, are commonly used as cores in sandwich panels. Foams, typically created through salt leaching or gas foaming, offer less control over their porous features and performance. The second category consists of lattice structures, composed of struts and nodes, where geometric properties and performance can be adjusted by altering the strut dimensions and their connections. These intricate lattice structures are usually fabricated through additive manufacturing but may suffer from stress concentration at strut junctions. The third category focuses on porous structures designed using triply periodic minimal surfaces (TPMS), which offer further enhanced performance and are the primary focus of our work.

In this section, we first explore the geometrical properties of porous media, which are discussed in detail in Section 2.1. Next, we examine Darcy's Law in Section 2.2, a fundamental principle that models fluid flow through porous media. Darcy's Law describes the relationship between fluid velocity and pressure gradient as a diffusion equation, under the assumptions of incompressibility, steady-state, and laminar flow conditions. We also cover various extensions of Darcy's Law such as the Brinkman-Forchheimer law. After, we define the Reynolds number for porous media in Section 2.4 and use this definition to categorize the typical flow regimes in porous media as established by existing literature, as discussed in Section 2.5. Finally, all the foundational understanding introduced allows us to introduce the materials of interest, specifically Triply Periodic Minimal Surfaces (TPMS), as outlined in Section 2.6, in order to understand better their properties and potential for future applications.

2.1 Geometrical properties of porous media

Porous media are materials characterized by the presence of void spaces, or pores, within a solid matrix. These pores can vary in size, shape, distribution, and connectivity, resulting in a diverse range of porous structures. The material is termed **homogeneous** if pore geometrical properties are invariant in all directions; otherwise, it is defined as **heterogeneous**. Understanding the geometrical properties of porous media is crucial for their applications in fluid dynamics and combustion.
The primary geometrical properties of porous media include:

1. **Porosity:** Porosity is defined as the ratio of the void volume (or pore volume) to the total volume of the material. It quantifies the fraction of the material's volume that is occupied by voids.

$$\phi = \frac{V_{\text{void}}}{V_{\text{total}}} \tag{1}$$

2. **Permeability:** Permeability measures a porous medium's ability to transmit fluids. For a detailed discussion, refer to Section 2.2.1.

3. **Tortuosity:** Tortuosity quantifies the complexity of fluid flow pathways within a porous medium. It is defined as the ratio of the actual path length traveled by the fluid to the straight-line distance between two points.

$$\tau = \frac{L_{\text{actual}}}{L_{\text{straight}}} \tag{2}$$

   Higher tortuosity increases flow resistance and can impact transport properties such as diffusion and dispersion.

4. **Specific Surface Area (or Surface to Volume ratio):** The specific surface area is the total surface area per unit volume of solid material. This property accounts for the interfacial area available for interactions with fluids or other phases, influencing processes such as adsorption, reaction kinetics, and particle trapping.

5. **Capillary Pressure:** In multi-phase configurations, capillary pressure arises from the curvature of fluid-fluid interfaces within small pores and affects fluid distribution and phase behavior in porous media. It can be expressed locally as:

$$P_c = \frac{2\gamma\cos(\theta)}{r} \tag{3}$$

   where:

   - P_c is the capillary pressure.
   - γ is the interfacial tension between the two fluids.
   - θ is the contact angle between the fluid and the solid surface of the pore.
   - r is the radius of curvature of the fluid-fluid interface.

   Capillary pressure is significant in processes such as capillary rise, imbibition, and drainage.

2.2 Darcy's Law for porous media

Darcy's law describes the flow of a fluid through a porous medium as:

$$\mathbf{u} = -\frac{k}{\mu}\nabla p \tag{4}$$

where:

- $\mathbf{u} = \frac{\mathbf{Q}}{A}$ $[\frac{m^3/s}{m^2}]$ is the Darcy velocity (specific discharge) which represents a volumetric flow rate **Q** divided a the cross-sectional area A.
- k $[m^2]$ is the intrinsic permeability of the porous medium.
- μ $[\frac{kg}{m \cdot s}]$ is the dynamic viscosity of the fluid.
- p $[Pa]$ is the pressure.

Key assumptions of the theory are:

- The flow is incompressible, steady-state and in laminar regime.
- The medium is homogeneous and isotropic.
- The fluid properties are constant.
- Inertial effects are negligible (low Mach number).

2.2.1 Permeability

Intrinsic permeability k $[m^2]$, often simply referred to as permeability, is a fundamental property of a porous medium that characterizes its ability to transmit fluids. It is independent of the type of fluid flowing through the medium and can be easily determined experimentally rearranging Darcy's law 1D:

$$k = \frac{u\mu L}{\Delta p}$$

where $\frac{\Delta p}{L}$ is the homogeneous gradient along the desired direction.
Intrinsic permeability shouldn't be confused with the hydraulic conductivity K, which depends on both the properties of the porous medium and the fluid, intrinsic permeability is a property solely of the porous medium itself. Hydraulic conductivity K $[m/s]$ is related to intrinsic permeability k through the following equation:

$$K = \frac{k\rho g}{\mu} \tag{5}$$

where:

- k is the intrinsic permeability of the porous medium [m^2].
- ρ is the density of the fluid [$\mathrm{kg/m}^3$].
- g is the acceleration due to gravity [$\mathrm{m/s}^2$].
- μ is the dynamic viscosity of the fluid [kg/(ms)].

2.3 Extensions of Darcy's Law

As fluid velocities increase or in more complex flow situations, the assumptions of Darcy's law may no longer hold. This necessitates extensions to account for additional physical effects.

2.3.1 Brinkman Extension

The Brinkman extension modifies Darcy's law to include the effects of viscous shear within the porous medium:

$$\mu\nabla^2\mathbf{u} - \frac{\mu}{k}\mathbf{u} = \nabla p \tag{6}$$

where the term $\mu\nabla^2\mathbf{u}$ accounts for the viscous shear effects within the fluid.

2.3.2 Forchheimer Extension

The Forchheimer extension addresses the inertial effects that become significant at higher flow velocities:

$$\nabla p = \mu\frac{1}{k}\mathbf{u} + \beta\rho|\mathbf{u}|\mathbf{u} \tag{7}$$

where β is the Forchheimer coefficient (a dimensionless parameter). The term $\beta\rho|\mathbf{u}|\mathbf{u}$ represents the inertial resistance to flow.

2.3.3 Combined Brinkman-Forchheimer Equation

The combined Brinkman-Forchheimer equation incorporates both viscous shear effects and inertial effects:

$$\mu\nabla^2\mathbf{u} - \frac{\mu}{k}\mathbf{u} + \beta\rho|\mathbf{u}|\mathbf{u} = \nabla p \tag{8}$$

2.4 Reynolds number for porous media

The Reynolds number (Re) is a dimensionless quantity that helps predict fluid flow patterns (commonly "flow regimes") in different situations by measuring the ratio between inertial and viscous forces. In porous media literature several definition have been adopted. To avoid confusion, we present the main definitions with a few comments:

- **Pore Reynolds number**
  This is the most intuitive definition that adopts the size of the pores within a porous material d_p as the reference physical length scale and for the reference velocity it can adopt either the intrinsic average velocity $\mathbf{u_i} = \frac{\mathbf{u_{Darcy}}}{\phi}$:

$$\mathrm{Re}_p = \frac{\rho \|\mathbf{u_i}\| d_p}{\mu} \tag{9}$$

  or simply the Darcy velocity:

$$\mathrm{Re}_D = \frac{\rho \|\mathbf{u_{Darcy}}\| d_p}{\mu} = \mathrm{Re}_p \phi$$

- **Hydraulic Pore Reynolds number**
  Used especially when the porous media has a complex geometry and the size of a pore is not clear:

$$\mathrm{Re}_H = \frac{\rho \|\mathbf{u_i}\| d_H}{\mu}$$

  where the hydraulic diameter is user-defined as $d_H = \frac{4A}{P}$, where A and P are the area and the perimeter respectively of a representative section of the pore.

- **Permeability Reynolds number**
  Permeability as defined by Darcy has dimensions $[m^2]$ and so a reference length scale can be found in it as follows:

$$\mathrm{Re}_k = \frac{\rho \|\mathbf{u_i}\| \sqrt{k}}{\mu}$$

  Although this definition is not very spread.

Obviously Re_p is based on principles that are closer to the physical measures of the turbulent fluctuations and that's why this definition has been more widely adopted in the modern literature. We will adopt the same convention in this work. In table 1, we present same examples of applications of porous media and of their ranges of pore Reynolds number.

2.5 Flow regimes in porous media

As pointed out by Wood & Al. [194], flow regime prediction in porous media is not evident and historically there have been even doubts about the existence of turbulence in this materials. Nowadays we know that turbulence inside porous media is more common then we thought in the past. The behavior of the flow inside a porous media depends on the Reynolds number but it's highly geometry-dependent so that there is not a systematic rule as in more traditional flows where we define critical values of Re. Even so a qualitative description can be done as follows:

1. **Darcy Regime** ($Re_p < 25$): In this regime, the flow field is well approximated by Stokes flow.
2. **Inertial Regime** ($25 < Re_p < 375$): In this range, inertial effects begin to manifest, with pore spaces dominated by inertial cores; the velocity distribution in the pores differs markedly from that of the Darcy regime. Steady vortical structures have been observed in this regime [193]. For more insights about porous media in inertial regime check the work done by Koch & Hill [79] at the begin of the century and by Lasseaux & Valdes-Parada more recently [92].

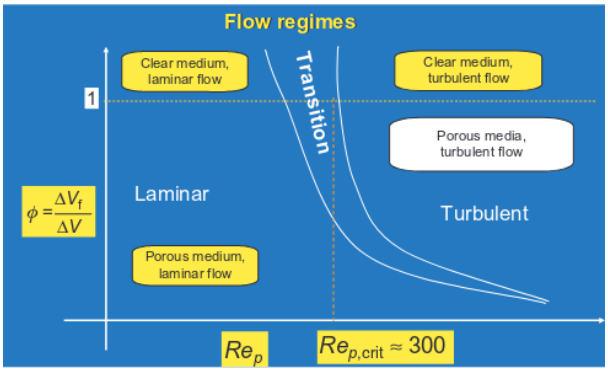

Figure 8: Flow regimes in a porous media as a function of the pore Reynolds number Re_p and the porosity ϕ. Reference:[**lemos_2012**]

, pag.16

3. **Unsteady Laminar (Transitional) Regime** ($375 < Re_p < 750$): In this regime, unsteady, transitional flows are observed. These flows vary from periodic behavior in vortexes to large-scale structures exhibiting intermittency.

4. **Turbulent Regime** ($Re_p > 750$): The structure of the flows within the pore space begins to resemble more conventional turbulent flows.

5. **Asymptotic Regime** ($Re_p >$ 3,400): The value of Re_p is high enough such that the turbulence can be approximated as being locally isotropic over most of the pore space.

In figure 8, if we consider the porosity ϕ as the parameter that represents the geometrical complexity of the porous media, it can be stated that for decreasing porosity, turbulence is delay and is reached at higher Re_p.

2.6 Triple Periodic Minimal Surface (TPMS)

TPMSs are a type of implicit surfaces characterized by zero mean curvature. Compared to other structures, TPMS porous structures offer two notable advantages:

- They can be accurately represented using mathematical functions, allowing for precise control over properties like porosity and surface area by adjusting function parameters.
- TPMSs are smooth, lacking the sharp edges or junctions found in other lattice structures. Additionally, TPMS structures have interconnected, non-tortuous pores, making them particularly suitable for various applications, especially in fluid-dynamics and acoustics.

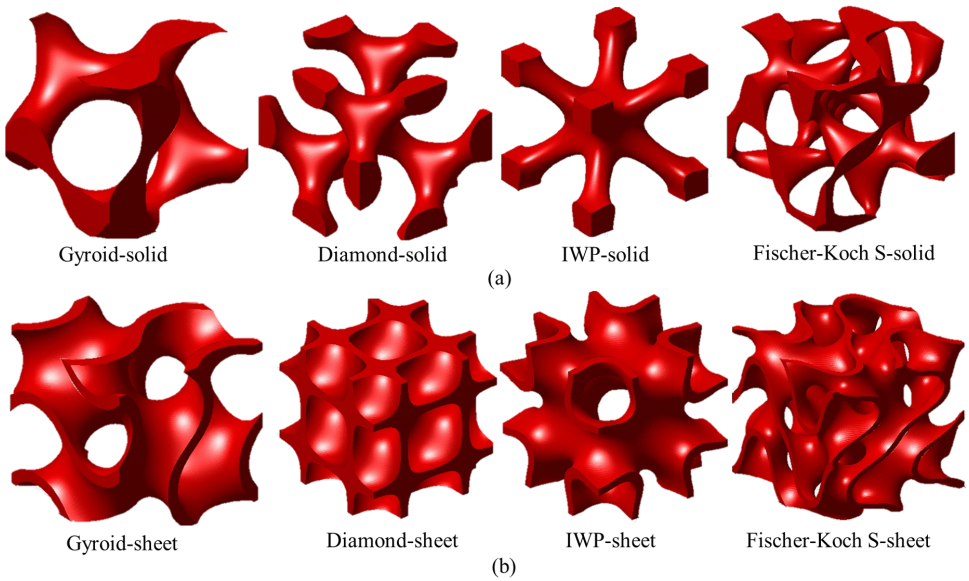

Figure 9: The 4 most known topologies of TPMS lattices: Schoen-G (Gyroid) , Schoen-D (Diamond), Martin-IWP and Fischer-Koch-S. They are represented in both their variations: (a) as a solid or (b) as a sheet.

Due to these benefits, TPMS has attracted significant research interest across multiple disciplines, including computer graphics, manufacturing science, mechanics, thermology, optics, acoustics, chemistry, and biology. The design, manufacturing, and application of TPMS require the use of computer-aided design (CAD) methods to generate 3D models. TPMS's implicit nature allows for easy control of their range, curvature, and periodicity, as well as the execution of complex calculations like Boolean operations, modulation, and convolution.
To meet diverse application needs and mimic natural porous structures, researchers have developed graded, heterogeneous, and multiscale TPMS, as well as new TPMS formulations with complex external shapes. These complex structures can be precisely fabricated using various additive manufacturing technologies. The geometry of TPMS significantly influences its performance in different applications, with most studies focusing on mechanical properties such as Poisson's ratio, anisotropy, elasticity, yield strength, fatigue behavior, vibration, and buckling characteristics. Like other porous structures, TPMS can also function as energy absorbers under compression.
Moreover, TPMS porous structures are widely used in tissue engineering and implant devices due to their smooth internal surfaces and interconnected pores, which provide ample space for cell attachment and growth. Their high surface area also makes them suitable for use as heat sinks, chemical microreactors, and membranes. Additionally, TPMS structures are effective as sound absorbers, electromagnetic microwave absorbers, and photonic crystals, due to their ability to weaken wave energy through multiple internal reflections.
Despite the growing interest in TPMS across various fields, their full potential remains underutilized, with most research focusing on the performance or application of a single discipline. The current research landscape is fragmented and incomplete, highlighting the need for interdisciplinary studies to expand TPMS's applications.

We hope that our work will bring some light over the physics inside the TPMS in turbulent regime to have a better understanding about the fluid-dynamics stability, the flow properties varying the inlet parameters and topology, and finally the potential qualities of reactions inside it for combustion applications in the future.

2.6.1 Properties of TPMS materials

TPMS matrices as repeated lattice structures have attracted much research interest because they have shown better mechanical performance, mass transfer, and thermal conductivity than conventional and strut-based structures, which have been employed in different disciplines. Their main properties are resumed here:

- **Well defined mathematical description:**

  Each TPMS is described by a level-set equation $f(x, y, z) = c$ derived from a sum defined in terms of the Fourier series where minimal surface condition is imposed.
  For example a TPMS of the type gyroid can be obtained with the function:

  $$f(x, y, z) = C_x \sin(k_x x)\cos(k_y y) + C_y \sin(k_y y)\cos(k_z z) + C_z \sin(k_z z)\cos(k_x x) = c \qquad (10)$$

  where:

  - (x, y, z) are the spatial coordinates;
  - C_x, C_y and C_z are the scaling factors along x, y and z respectively;
  - k_x, k_y and k_z are the wavenumbers along x, y and z respectively.
  - c is the offset parameter, also called as the structural factor (abbr: *struct*).

  The iso-surfaces $f(x, y, z) = 0$ divide space into two subdomains of equal volume. There are two primary methods for generating TPMS lattices based on these minimal surfaces. The first approach involves using the volume enclosed by the minimal surface to create a solid-TPMS structure, also known as a skeleton-TPMS structure, as illustrated in Figure 10(a). The second approach generates a sheet-TPMS structure by offsetting the minimal surface along its normal direction to form a double surface, as shown in Figure 10(b).

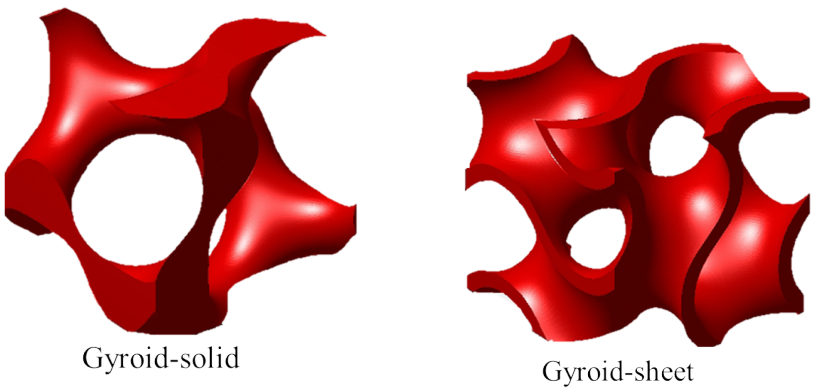

(a) (b)

Figure 10: Two solids can be defined using the TPMS-Gyroid: the Gyroid-solid taking the volume enclosed by the surface, and the Gyroid-sheet by offsetting through a thickness value the surface.

- **Minimal Surface Area:**

  TPMS are characterized by having minimal surface area within their periodic unit cell. This property makes them efficient structures for partitioning space into cells while minimizing interfacial energy.

- **Constant Mean Curvature:**

  TPMS have constant mean curvature, meaning that the average curvature of the surface remains the same throughout. This property is related to the minimal surface condition and is significant in understanding the mechanical stability and physical behavior of TPMS-based structures.

- **Periodicity in three directions**.
- **Symmetry:**

  Many TPMS exhibit symmetrical properties due to the periodicity of their structures. This symmetry can be rotational, reflectional, or translational, depending on the specific TPMS shape. Symmetry simplifies the analysis and understanding of TPMS-based structures and their properties.

- **Geometric Variability:**

  TPMS encompass a wide range of geometric shapes and structures, from simple shapes like the Schwarz P surface to more complex ones like the Gyroid and Diamond surfaces (see figure 9). This variability allows for the design and engineering of porous materials with diverse properties and functionalities.

2.6.2 Classification of TPMS materials

The first example of a triply periodic minimal surface (TPMS) was the Diamond minimal surface, discovered by the German mathematician Schwarz in 1865 [155]. Another early discovery was the Neovius surface, identified by Neovius, a student of Schwarz, in 1883 [129]. Both Schwarz and Neovius contributed to the discovery of several other minimal surfaces, such as the Primitive and Hexagonal surfaces. Almost a century later, in 1970, Schoen introduced numerous minimal surfaces, with the Gyroid becoming one of the most well-known [154].
The classification of TPMS materials is usually done by introducing the concept of **genus**, which intuitively represents the "number of holes" in a unit volume of the surface in space. In Table 3 are represented some of the most famous TPMS materials with their full name, genus degree, mathematical formulation and representation.

2.6.3 Interest for TPMS materials

TPMS materials, as introduced before, are excellent for engineering applications for the following points:

- **ease of parameter analysis**: systematic approach changing topology and porosity.

  For example, for a Gyroid-solid we can simply play on the structural factor to change both pore size and porosity, providing a flexible approach for tuning material properties. In Figures 11 and 12 we show how the structural factor *struct* modifies the pore size and the porosity of the material.

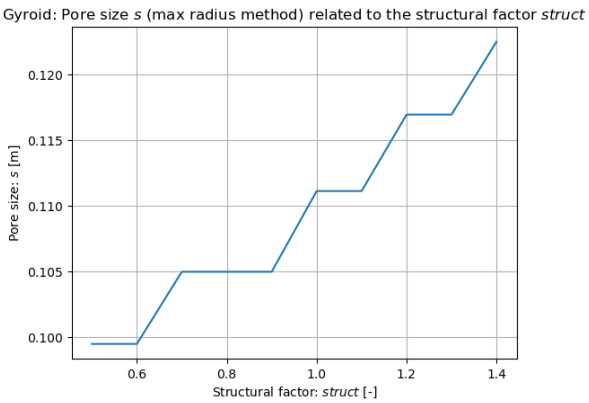

Figure 11: Gyroid with $k_x = k_y = k_z = 2\pi \times 5$: Pore size s (max radius method) related to the structural factor struct

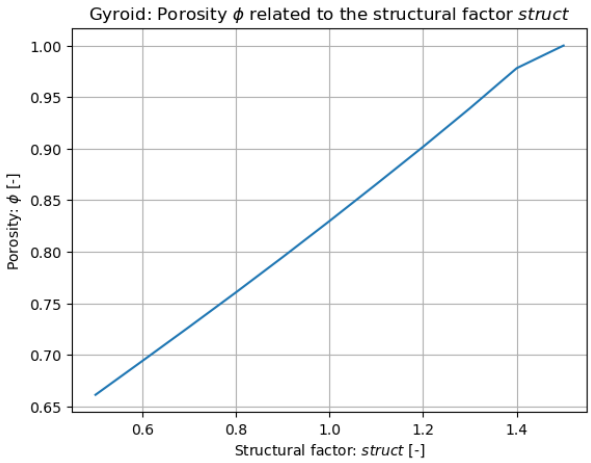

Figure 12: Gyroid with $k_x = k_y = k_z = 2\pi \times 5$: Porosity ϕ related to the structural factor struct

- **relative ease and reliability of production through AM**, through different methods and printing algorithms [45] [200] [77];
- **good mechanical properties**, especially in compression even at medium porosity values [145] [77];
- **thermal conductivity properties**, that led studies oriented to heat-exchangers and channel flows [186] [198], but their are really promising for combustion applications in turbulent regime. In figure 13, we present the thermal conductivity as a function of porosity for various TPMS materials alongside traditional porous media. Generally, the thermal conductivity of most TPMS structures is comparable and significantly higher than that of conventionally manufactured stochastic metal foams and lattice-frame materials. This can be attributed to two main factors: first, TPMS materials inherently have a higher surface area-to-volume ratio compared to other porous media; second, TPMS can be manufactured across a broader range of porosities than conventional materials, thanks to enhanced design control and more consistent mechanical properties. In fact, for TPMS materials larger porosity significantly improve mass transfer and lowered pressure loss [198].

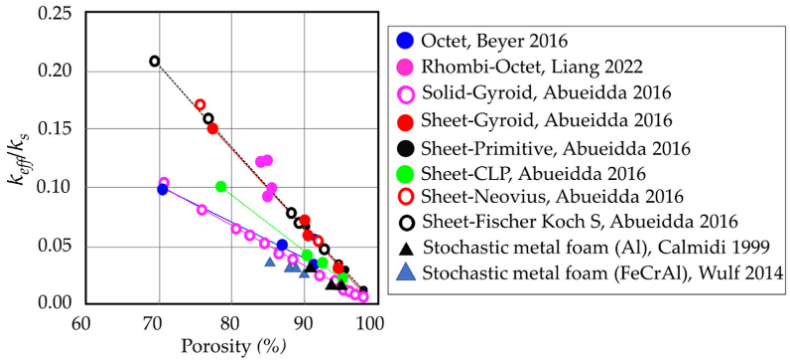

Figure 13: Demonstrations of the normalized thermal conductivity for different unit cell structures plotted against the porosity (k_{eff} is the effective thermal conductivity, and k_s is the thermal conductivity of the solid). Reference: [198])

- **turbulence enhancement properties**, as it has been shown that porous media and especially TPMS solid-lattices creatly increase the TKE locally in the pores, enhancing the exchange of energy from large-scales to low-scales. This point will be treated better in the following sections because it represents also the objective of our work: understanding better the turbulence inside TPMS lattices through a high fidelity approach.

These are the main reasons-why we chose to study turbulent flows in TPMS materials.

Full Name	**Mathematical Expressions:** $f(x,y,z) =$	**3D Models**	**Genus**
Schwarz - P (Primitive)	$\cos(\kappa_x x) + \\ + \cos(\kappa_y y) + \\ + \cos(\kappa_z z) = C$	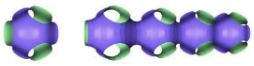	3
Schoen - G (Gyroid)	$\sin(\kappa_x x)\cos(\kappa_y y) + \\ + \sin(\kappa_z z)\cos(\kappa_x x) + \\ + \sin(\kappa_y y)\cos(\kappa_z z) = C$	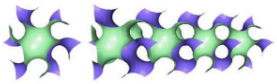	3
Schoen - Diamond (D)	$\cos(\kappa_x x)\cos(\kappa_y y)\cos(\kappa_z z) + \\ - \sin(\kappa_x x)\sin(\kappa_y y)\sin(\kappa_z z) = C$	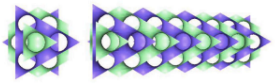	3
Fischer-Koch - S	$\cos(\kappa_x x)\cos(2\kappa_y y)\cos(3\kappa_z z) + \\ + \cos(2\kappa_x x)\cos(3\kappa_y y)\cos(\kappa_z z) + \\ + \cos(3\kappa_x x)\cos(\kappa_y y)\cos(2\kappa_z z) = C$	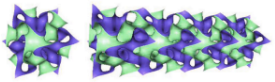	4
Martin - F-RD	$4\cos(\kappa_x x)\cos(\kappa_y y)\cos(\kappa_z z) + \\ - [\cos(2\kappa_x x)\cos(2\kappa_y y) + \\ + \cos(2\kappa_x x)\cos(2\kappa_z z) + \\ + \cos(2\kappa_y y)\cos(2\kappa_z z) \quad = \quad C$	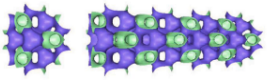	5
Neovius	$3\left[\cos(\kappa_x x) + \cos(\kappa_y y) + \cos(\kappa_z z)\right] + \\ + 4\cos(\kappa_x x)\cos(\kappa_y y)\cos(\kappa_z z) = C$	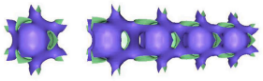	5

Table 3: Mathematical expressions of different TPMS topologies with their genus and 3D representations.

3 Governing equations

Fluid motion can be described by a set of three fundamental equations that govern mass conservation, momentum, and energy. These equations, known as the Navier-Stokes (NS) equations, are remarkable both for their mathematical complexity and for the challenge involved in solving them, which often requires a number of simplifying assumptions. The NS equations reveal the intricate nature of physical processes and highlight the limitations of our knowledge. In particular, the question of whether smooth solutions exist in three dimensions remains unresolved. This is known as the Navier-Stokes existence and smoothness problem. The Clay Mathematics Institute has designated this issue as one of the seven most important open problems in mathematics and has offered a US $1 million prize for a solution or counterexample.
In practical applications, significant advancements have been made in CFD and modeling. While we strive for high-fidelity solutions within the shortest possible time, achieving this often involves trade-offs, and improvements are always on the horizon. Progress in this field relies heavily on a deep understanding of foundational principles and past research efforts. True advancement stems from building on previous knowledge and asking the right questions—questions often posed by those who have dedicated their lives to this pursuit.

In this section, we provide an overview of the essence behind the NS equations, which describe the behavior of Newtonian fluids with constant properties, two key assumptions that allow us to simplify their resolution. For more detailed discussions, refer to the works of Batchelor works [11] [12]. First we introduce the general formulation of a conservation law (Section 3.1). Then, we describe NS equations (Section 3.2), their main assumptions, their transformation properties and their resolution. From NS equations we derive some interesting equations in Section 3.2.7 among which the vorticity equation, detailed in Section3.3, which is key in the study of turbulence.

3.1 Fundamental Conservation Equations

The basic conservation equations describing the flow of a fluid through an infinitesimal volume can be written in a compact form as:

$$\frac{\partial(\rho\varphi)}{\partial t} + \frac{\partial}{\partial x_j}\left(\rho u_j \varphi\right) = \frac{\partial}{\partial x_j}\left(\Gamma_\varphi \frac{\partial \varphi}{\partial x_j}\right) + S_\varphi \tag{11}$$

In this context, φ is a general variable (distinct from the porosity, also denoted by ϕ, which will be introduced later). Here, u_j represents the j-th component of the velocity, ρ denotes the density, and Γ_ϕ and S_ϕ are the diffusion coefficient and source terms, respectively. The specific form of ϕ and its associated parameters (Γ_ϕ and S_ϕ) varies depending on the conserved quantity in question, such as mass, momentum, energy, chemical species, or turbulent kinetic energy. The conservation laws, when rewritten in the form of Eq. 11, are commonly found in many texts focused on the control-volume approach. This representation offers a convenient way to describe all transport phenomena occurring within a given flow, especially useful in turbulence quantity analysis.

3.2 NS equations

3.2.1 Velocity field

Before dwelling in the beautiful world of the fluid dynamics equations, it's important to fix some ideas about the velocity field and its characterization. In fact, the velocity field and especially its perturbations are at the center of the turbulence analysis.
The velocity field is:

$$\mathbf{U} = \{U, V, W\} = U\hat{e_x} + V\hat{e_y} + W\hat{e_z}$$

and its gradient can be expressed as:

$$\nabla\mathbf{U} = \frac{1}{2}(\nabla\mathbf{U} + \nabla\mathbf{U}^T) + \frac{1}{2}(\nabla\mathbf{U} - \nabla\mathbf{U}^T) = \mathbf{S} + \mathbf{R} \tag{12}$$

where:

- $\mathbf{S} = \frac{1}{2}(\nabla\mathbf{U} + \nabla\mathbf{U}^T)$ is the **rate-of-strain tensor** with the following properties:

  - isotropic symmetric-deviatoric tensor;
  - $tr(\mathbf{S}) = \nabla \cdot \mathbf{U}$.
- $\mathbf{R} = \frac{1}{2}(\nabla \mathbf{U} - \nabla \mathbf{U}^T)$ is the **rate-of-rotation tensor** with the following properties:
  - $R_{ii} = 0$, for i=1,2,3 so that $tr(R) = 0$;
  - $\mathbf{R}_{ij} = \frac{1}{2}\omega_k$, for $i, j, k = 1, 2, 3$ with $i \neq j$ and $k \perp (i, j)$, where $\omega \equiv \nabla \times \mathbf{U}$ is the vorticity vector.

3.2.2 Continuum hypothesis

NS equations are valid under the **continuum hypothesis**, meaning that the Knudsen number Kn has to be negligible:

$$Kn = \frac{\lambda}{l} \ll 1 \tag{13}$$

where λ is the the mean free path of the molecular motion and l is the smallest geometric characteristic length scale of the flow. In air under atmospheric conditions, the mean free path λ is 6×10^{-8} m, and the mean time between successive collisions of a molecule is 10^{-10} s.

3.2.3 Compressible NS equations

NS equations are usually presented as a compact set of 3 partial differential equations of balance for mass, momentum and energy, completed by a series of closure equations to allow the resolution of the system. Closure equations depend on the assumptions done during the resolution and the most widely used ones are the Newtonian fluid hypothesis and the Fourier's law.
The NS equations describe the motion of a simple fluid substance (one-phase hypothesis) through three balance equations:

- balance of mass (or **continuity equation**):

$$\frac{\partial \rho}{\partial t} + \nabla \cdot (\rho \mathbf{U}) = 0 \tag{14}$$

  where:

  - ρ $[kg/m^3]$ is the fluid density,
  - $\mathbf{U}$ $[m/s]$ is the velocity field,

  It can be also expressed as:

$$\frac{D\rho}{Dt} = -\rho(\nabla \cdot \mathbf{U}) \tag{15}$$

- balance of momentum (or **momentum equation**):

$$\rho \frac{D\mathbf{U}}{Dt} = -\nabla p + \nabla \cdot \tau + \rho \mathbf{f} \tag{16}$$

  where:

  - $\mathbf{u}$ $[m/s]$ is the velocity field,
  - p $[Pa]$ is the pressure,
  - τ $[N/m^2]$ is the stress tensor,
  - $\mathbf{f}$ $[N/m^3]$ represents external forces (e.g., gravity such that $\mathbf{f}_{gravity} = \mathbf{g} = \nabla \phi_g$).

  Based on Newton's second law, this equation relates the fluid particle acceleration DU/Dt to the surface forces and body forces experienced by the fluid. In general, the surface forces, which are of molecular origin, are described by the stress tensor $\tau(\mathbf{x}, t)$ – which is symmetric and can be expressed by the **Stokes-Newtonian fluids constitutive equation**:

$$\tau = \mu[(\nabla \mathbf{U}) + (\nabla \mathbf{U})^T - \frac{2}{3}(\nabla \cdot \mathbf{U})\mathbf{I}] \tag{17}$$

where μ is the dynamic viscosity [kg/(m·s)] of the media assumed as independent from the velocity field so that $\mu = const(\mathbf{u}, \nabla\mathbf{u})$, and $\mathbf{I}$ is the identity tensor.
The external forces $\mathbf{f}$, if not negligible, are usually connected either to gravity either to electromagnetic fields.

- balance of energy (or **energy equation**):
  Navier-Stokes equations can be extended to include energy balance. The energy equation accounts for the various forms of energy within the fluid, such as internal energy, kinetic energy, and total energy:
  - The **internal energy equation** accounts for the energy associated with the microscopic motions and interactions within the fluid.

$$\rho\frac{De}{Dt} = -p(\nabla\cdot\mathbf{U}) + \rho\mathcal{D} - \nabla\cdot\mathbf{q} + \dot{q_v} \tag{18}$$

    where:
    * e $[J/kg]$ is the specific internal energy,
    * $\mathcal{D} = \frac{1}{\rho}(\tau\cdot\nabla)\cdot\mathbf{U}$ $[W/kg]$ is the viscous dissipation function,
    * $q = -k\nabla T$ $[W/m^2]$ is the surface heat flux that can be expressed with the Fourier's law,
    * k [W/(m·K)] is the thermal conductivity of the media,
    * T $[K]$ is the temperature,
    * $\dot{q_v}$ $[W/m^3]$ are any heat sources or sinks, also called "volumetric heat sources".
  - The **kinetic energy equation** accounts for the energy associated with the macroscopic motion of the fluid.

$$\rho\frac{D(\frac{1}{2}|\mathbf{u}|^2)}{Dt} = -\nabla p\cdot\mathbf{U} + \mathbf{U}\cdot(\nabla\cdot\boldsymbol{\tau}) + \rho\mathbf{f}\cdot\mathbf{U} \tag{19}$$

    where $\frac{1}{2}|\mathbf{u}|^2$ is the specific kinetic energy.
  - The **total energy equation** is the sum of internal energy, kinetic energy, and potential energy (if applicable). It can be expressed in conservative form as:

$$\rho\frac{DE}{Dt} = \nabla\cdot(p\mathbf{U}) + \nabla\cdot(\tau\cdot\mathbf{U}) + \rho\mathbf{f}\cdot\mathbf{U} - \nabla\cdot\mathbf{q} + \dot{q_v} \tag{20}$$

    where $E = e + \frac{1}{2}|\mathbf{u}|^2$ is the specific total energy.

  The energy equation to use depends on the specific case of application. Another common alternative to the energy equations presented are the **specific enthalpy equation**:

$$\rho\frac{Dh}{Dt} = \frac{Dp}{Dt} - \nabla\cdot\mathbf{q} + \dot{q_v} \tag{21}$$

  where $h = e + \frac{p}{\rho}$ is the specific enthalpy.

Note that usually, neglecting the influence of other external fields than the gravitational one, we can approximate $\mathbf{f} \simeq \mathbf{g} = \{0, 0, -g\}$, where g is the gravitational acceleration $g = 9.81[m/s^2]$.

Finally, there are 5 equations (Eq.15, Eq.15, Eq. 20 under the assumptions of Newtonian fluid, Fourier law validity and constant coefficients of viscosity and thermal conductivity) and 10 unknowns (p,ρ,T,$\mathbf{u}$,E). Thus further 2 equations are required to close the problem. Common strategies are to introduce:

- enthalpy definition:

$$\nabla e = \nabla h - p\nabla v = c_p\nabla T - p\nabla(\frac{1}{\rho}) \tag{22}$$

  that allows to express the internal energy in terms of thermodynamic quantities defining the heat capacity (or thermal capacity) at constant pressure c_p $[J/(kg\cdot K)]$.

- **Equation of state for the gas:**

$$f(p, \rho, T) = 0 \tag{23}$$

That can be:

  - ideal gas law:

$$P = \rho \frac{R}{M} T \tag{24}$$

  - real gas law (Van der Waals model):

$$\left(P + \frac{a}{V^2}\right)(V - b) = RT \tag{25}$$

where a $[N \cdot m^4]$ is the cohesion forces coefficient and b $[m^3]$ is the molecular co-volume coefficient b. Usually both are constants.

  - further developments of the previous models.

Note that the coefficients $\mu(T)$ (e.g. Southerland's law), $k(T)$ and $c_p(T)$ are usually functions of the temperature but for slight variations of temperature at low temperatures they can be assumed as constants of T.

3.2.4 NS equations properties

Once added the appropriate closure equations and defined the boundary conditions, the NS equations represent a deterministic set of equations, which stability properties depending mainly by the Reynolds number have been studied by several authors [4] [12].
Moreover they possess the following transformation properties:

- Reynolds number similarity;
- invariance under fixed rotations and reflections of the coordinate axes;
- Galilean invariance;
- lack of invariance under frame rotations.

These transformations are useful to compare observations in different conditions and reference frames or to make additional deductions or simplifications based on symmetries or similitudes ([142] chap.2, [12]).

3.2.5 Incompressible NS equations

Typically, the term "incompressible" refers to a condition where the velocity field is solenoidal or divergence-free. This is mathematically expressed as:

$$\nabla \cdot \mathbf{U} = 0 \tag{26}$$

Under the assumption of incompressible flow, Eq. 29 implies that:

$$\frac{D\rho}{Dt} = 0 \tag{27}$$

This should not be confused with the assumption of homogeneous density, which is expressed as:

$$\nabla \rho = 0 \tag{28}$$

The latter means that the density is uniform in space.
For incompressible flow, and assuming no external forces ($\mathbf{f} = 0$), the Navier-Stokes equations simplify to the following equations, known as the Euler equations:

$$\nabla \cdot \mathbf{U} = 0 \tag{29}$$

$$\frac{D\mathbf{U}}{Dt} = -\frac{1}{\rho}\nabla p + \nu \nabla^2 \mathbf{U} \tag{30}$$

where $\nu = \frac{\mu}{\rho}$ is the kinematic viscosity $[m^2/s]$.

So, when can we consider a flow to be incompressible? Through an order-of-magnitude analysis of the compressible Navier-Stokes equations and thermodynamic principles, we find that a flow can be considered incompressible if the following conditions are met [4]:

$$\begin{cases} M \ll 1 \\ \dfrac{|\Delta T|}{T} \ll 1 \end{cases} \tag{31}$$

where M is the Mach number and $\frac{|\Delta T|}{T}$ represents the relative temperature change. In practice, gases with $M < 0.3$ can be treated as incompressible fluids.
Finally, note the role of pressure in incompressible NS equations: pressure is now an independent variable from the thermodynamics variables (ρ,T) and it has to adapt instantaneously to the velocity field. In fact, if we take $\nabla\cdot$ (Eq. 30):

$$\nabla^2 p = -\rho \nabla \cdot (\nabla \mathbf{U} \cdot \mathbf{U}) \tag{32}$$

called **Poisson's equation**.

3.2.6 Resolution of NS equations

It's evident that NS equations in their general formulation (Eq.15, Eq.16, Eq.20) present an undetermined system cause we have way more variables than equations. That's why we introduced assumptions and constitutive equations.
Analytical solutions to the Navier-Stokes equations are rare due to their nonlinear nature, exeption for some 2D particular flows. In fact, until today one of the major unsolved problems in mathematics is proving whether smooth and globally defined solutions exist for the three-dimensional Navier-Stokes equations with arbitrary initial conditions, or if singularities. This is one of the seven Millennium Prize Problems for which the Clay Mathematics Institute offers a prize of one million dollars. Unfortunately in this work we do not even try to win this price and we solve the complexity of the Navier-Stokes equations in three dimensions and turbulent flow regimes employing numerical solutions. These involve discretizing the equations and solving them using computational methods. Common numerical techniques include:

- Finite Difference Method (FDM): Approximates the derivatives in the equations using differences between function values at discrete grid points.
- Finite Volume Method (FVM): Integrates the equations over control volumes to ensure conservation laws are satisfied.
- Finite Element Method (FEM): Divides the domain into elements and uses variational methods to solve the equations.
- Spectral Methods: Expand the solution in terms of a series of basis functions (e.g., Fourier or Chebyshev polynomials) and solve for the coefficients.

In this work we will use a state-of-the-art numerical spectral method called Spectral Difference Method (SDM). The method is implemented in the Jaguar code, owned by Onera and Cerfacs in Toulouse, France (see Section 6).

3.2.7 Derived equations

From the set of classical NS equations (eqs.15,16 and 20) one can derive other really useful equations such as:

- **Entropy transport equation**, introducing the 1st thermodynamics law:

$$\rho T \frac{Ds}{Dt} = \rho \mathcal{D} - \nabla \cdot \mathbf{q} + q_v \tag{33}$$

  where s is the specific entropy $[J/kg]$

- **Crocco's equation** for specific entropy, derived from the previous one using the definition of directional variation:
$$T\nabla s = \frac{\partial \mathbf{U}}{\partial t} + \nabla H - \mathbf{U} \times \omega - \frac{1}{\rho}\nabla \cdot \tau - \mathbf{f} \tag{34}$$
where $H = h + \frac{1}{2}|\mathbf{u}|^2$ is the specific total enthalpy.

- **Vorticity equation**, derived from $\nabla\times$ (eq. 16):
$$\frac{D\omega}{Dt} = -\omega(\nabla \cdot \mathbf{U}) + \omega \cdot \nabla \mathbf{U} - \nabla(\frac{1}{\rho}) \times \nabla p + \nabla \times (\frac{1}{\rho}\nabla \cdot \tau) + \nabla \times \mathbf{f} \tag{35}$$

Especially the vorticity equation (Eq.35) is interesting to understand the physics behind some turbulent phenomena as discussed in the paragraph

3.3 Vorticity equation

One of the key characteristics of turbulent flows is their rotational nature, characterized by non-zero vorticity. The vorticity, denoted by $\boldsymbol{\omega}(\mathbf{x}, t)$, is defined as the curl of the velocity field $\boldsymbol{\omega} = \nabla \times \mathbf{U}$ and a conservation equation for vorticity can be derived as it has been done in Eq.35. Using the assumptions of incompressible Newtonian fluid with negligeable external forces $\mathbf{f} = 0$, the equation can be simplified as:

$$\frac{D\boldsymbol{\omega}}{Dt} = \nu\nabla^2\boldsymbol{\omega} + \boldsymbol{\omega} \cdot \nabla \mathbf{U}, \tag{36}$$

where:

- $\nu\nabla^2\boldsymbol{\omega}$: diffusion term, representing the dissipation of vorticity due to the viscous effects
- $\boldsymbol{\omega} \cdot \nabla \mathbf{U}$: stretching term, representing the redistribution of vorticity through stretching or compression of the leading to the dampening or amplification respectively of it. This is a feed-back mechanism between the vorticies and this term is absent in 2D leading to not accurate description of turbulence, which is a typically 3D phenomenon. In fact 2D vorticity can only decay, cause there is no stretching term.

.
Moreover, the dynamics of an infinitesimal material line element $\mathbf{s}(t)$ is described by the equation:

$$\frac{d\mathbf{s}}{dt} = \mathbf{s} \cdot \nabla \mathbf{U}, \tag{37}$$

which is analogous to the vorticity equation, excluding the viscous term. Consequently, in inviscid flow, the vorticity vector evolves in a manner similar to that of an infinitesimal material line element, in accordance with Helmholtz's theorem. When the strain rate induced by velocity gradients acts to elongate the material line element aligned with $\boldsymbol{\omega}$, the magnitude of $\boldsymbol{\omega}$ increases. This phenomenon, known as vortex stretching, is a crucial process in turbulent flows, and the term $\boldsymbol{\omega} \cdot \nabla \mathbf{U}$ is referred to as the vortex-stretching term.

4 Turbulence statistics

When studying turbulence it's crucial to acknowledge that it represents a **random process**. This statement means that if we take a turbulent event under the same boundary and initial conditions it won't never have an unique value if we repeat the measurement. But how we can justify the consistency between the random nature of turbulent flows and on the other side the deterministic nature of the NS equations? The answer lies in the fact that high Reynolds numbers flows such as turbulent regimes are highly sensitive to even the smallest perturbations of initial conditions, boundary conditions and material properties. In other words we have to keep in mind that in real-life it is impossible (or almost) to reproduce the same conditions for two different measurements. A consequence of this extreme sensitivity to initial conditions is that after some time, the state of a dynamic system cannot be exactly predicted [105]. That's how NS equations, instantaneously deterministic, have steady solutions at sufficiently low Re, but chaotic, turbulent solutions at high Re [55] [123].

In this section, we will focus on how we can describe turbulence as a random process with the classical tools of statistics. To get there we will first discuss what is a random variable and the probability density function (PDF) with its properties through the statistical moments (Section 4.1). Then we extend the same concepts to join random variables in Section 4.2 and to a random process in Section 4.3.3. Afterwards we characterize the discrete statistics and the evaluation of its incertitude in Section 4.4 because in real-life we cannot never really have infinite samples as it is assumed in the continuous theory. Finally, in Section 4.5 turbulence as a random process is analyzed.

4.1 Characterization of a random variable

A random process such as turbulence has multiple variables that interact between them, such as the velocity components $\mathbf{U} = \{U, V, W\}$, each of which represents a random variable its-self. In the following discussion, we consider as an instance of a random variable the velocity component along x-axis $U(\mathbf{x}, t)$. In a turbulent flow we cannot know its exact value or its evolution in time but we can determine the probability of a certain event connected to it.
If we define an event B such as $B \equiv \{U < V_b\}$, we can define the **probability** p of the event B:

$$p = P(B) = P\{U < V_b\} \tag{38}$$

where p is a real number so that $(0 \leq p \leq 1)$ signifying the likelihood of the occurrence of the event. For an impossible event p=0; for a sure event p=1.

If we want to generalize the idea of probability over all the range of possible values of $V_b \in V$ called the **sample space**, we can introduce the **cumulative distribution function (CDF)**:

$$F(V) = P(U < V) \tag{39}$$

The three basic properties of the CDF are:

- $F(-\infty) = 0$
- $F(\infty) = 1$
- $F(V_b) \geq F(V_a) \quad \text{for} \quad V_b > V_a$

The third point proves that CDF is a non-decreasing function and so:

$$F(V_b) - F(V_a) = P\{V_a \leq U < V_b\} \geq 0$$

What is interesting in probability is to see how sensible is a random variable to a shift in the sample space and so it makes sense to look at the derivative of the CFD, the well-known **probability density function (PDF)**:

$$f(V) = \frac{dF(V)}{dV} \tag{40}$$

The three basic properties of the PDF are:

- $f(+\infty) = f(-\infty) = 0$

- $\int_{-\infty}^{\infty} f(V)\,dV = 1$
- $f(V) \geq 0$

Its meaning can be well understood analyzing its definition related to the probability

$$P\{V \leq U < V + dV\} = F(V + dV) - F(V) = f(V)\,dV$$

so that:

$$P\{V_a \leq U < V_b\} = F(V_b) - F(V_a) = \int_{V_a}^{V_b} f(V)\,dV \tag{41}$$

Thus the PDF f(V) is the probability per unit distance in the sample space and has the dimensions of the inverse of U.
It is emphasized that **the PDF $f(V)$ (or equally the CDF $F(V)$) fully characterizes the random variable**, in this case $U(\mathbf{x}, t)$. Two or more random variables that have the same PDF are said to be **(statistically) identically distributed** (abbreviation: **i.d.**).

4.1.1 PDF properties

The shape of the PDF provides crucial insights into the behavior of a random variable. It is essential to analyze this shape thoroughly using the tools of **descriptive statistics**, particularly focusing on the properties of central tendency and variability. These statistical properties are initially introduced in the context of discrete formulations and later extended to continuous cases. For a detailed comparison between discrete and continuous statistics, refer to Section 4.4. In this discussion, we consider a general PDF $f(x)$, with x represented as $x = U(\mathbf{x}, t)$ to link with the previous analysis.

- **Central tendency properties**:

  These properties are the mean, the mode and the median. A visual example of them is given in Figure 14.

  - Mean:
    Represents the mathematical average value defined as:

    $$\bar{x} \equiv < x >= \frac{\sum_{i=1}^{N} x_i}{N} = \int_{-\infty}^{+\infty} f(x)\,dx \tag{42}$$

    It's definition allows us to extract the fluctuation x' of our variable related to its mean $\bar{x}$:

    $$x' = x - \bar{x}$$

  - Mode:
    Most frequently occurring value in the sample:

    $$x_{mode} \mid f(x_{mode}) \equiv max(f(x)) \tag{43}$$

  - Median:
    The middle value of the sample space for an odd sample size N, or the average of the two middle values for an even N:

    $$x_{median} \equiv (max(x) - min(x))/2. \tag{44}$$

- **Variability properties**:
  They can be resumed in the statistical moment of n-th order defined as:

  $$\mu_{x,n} \equiv \frac{\sum_{i=1}^{N}(x_i - \bar{x_i})^n}{N} =< (x - \bar{x})^n > \tag{45}$$

  - n=2: **variance** $\mu_{x,2} = \sigma_x^2$
    where σ_x is called standard deviation of x.
    It represents the dispersion of data from the mean value as shown in Figure 15).

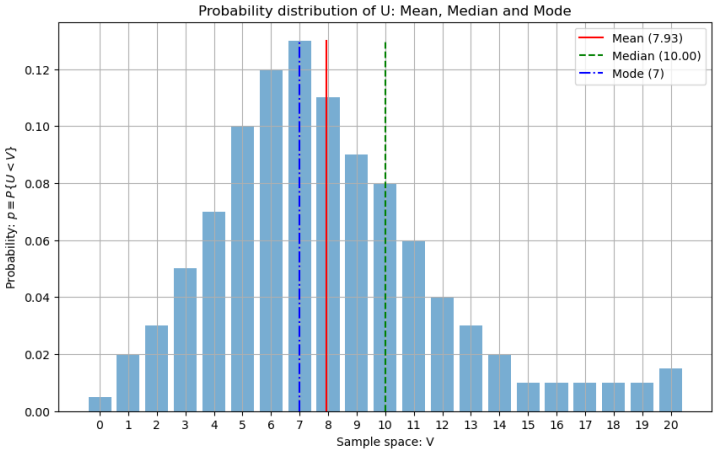

Figure 14: PDF of U in sample space V and its central tendency properties: mean, median and mode.

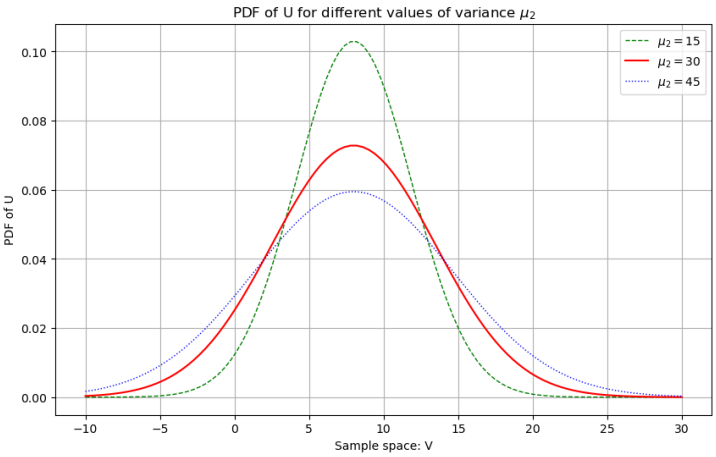

Figure 15: PDF of U in sample space V for different values of variance μ_2.

– n=3: **skewness** $\mu_{x,3}$
  It represents the asimmetry of data from the mean value as shown in Figure 16). In statistical slang we talk also about "small tail position" or just "tail position". Note that the "tails" of a probability distribution refer to the parts of the distribution that are far from its center or peak and the name derives from their shape, if we have enough imagination.
– n=4: **kurtosis** $\mu_{x,4}$
  It represents the sharpness of the data around the mean value or peak as shown in Figure 17. In statistical slang we talk also about "tail-thickness".

Most of the PDF in nature are close to a **normal distribution** also called "Gaussian" distribution. A random variable x with a normal distribution means that $f(x) \equiv \mathcal{N}(x)$, where $\mathcal{N}(x)$ is the normal distribution function defined as:

$$\mathcal{N}(x; \mu_x, \sigma_x) = \frac{1}{\sqrt{2\pi}\sigma_x} exp(\frac{-(x-\mu_x)^2}{2\sigma^2}) \tag{46}$$

where $\mu_x =< x >$ and $\sigma_x = \sqrt{< (x - < x >)^2 >}$ are the mean and variance of x respectively. If the PDF is not Gaussian, taken a certain tolerance, we define it a **skewed distribution** following the statistical terminology. An important theorem in statics is the so-called **Central Limit Theorem** [122] [90] [109]:

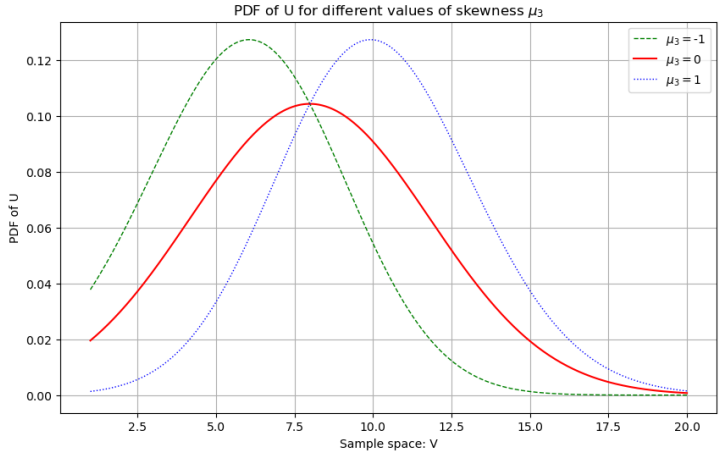

Figure 16: PDF of U in sample space V for different values of skewness μ_3.

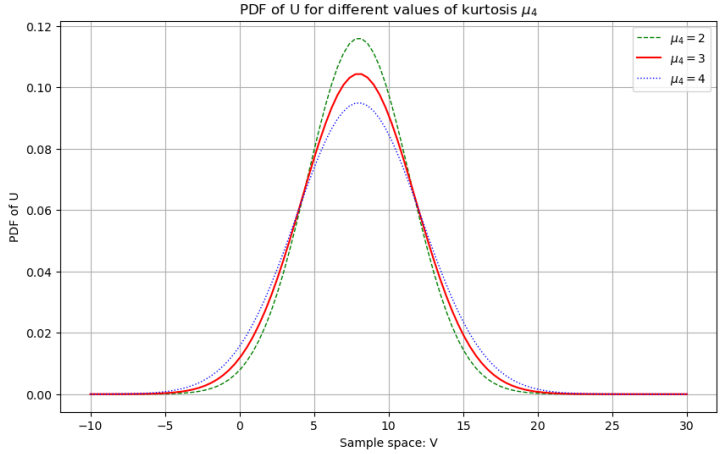

Figure 17: PDF of U in sample space V for different values of kurtosis μ_4.

Central Limit Theorem

The sampling distribution of the sample mean $\bar{x}$ can be approximated by a normal distributed, regardless of the original distribution of the population, provided that the sample size n is large enough and that the population has a finite standard deviation σ_x. Mathematically, if $x_1, x_2, \ldots, x_n$ are i.i.d. random variables with mean $\mu_{x,i}$ and variance $\sigma^2_{x,i}$ for $i = 1, 2, .., n$, then the standardized sample mean:

$$Z = \frac{\bar{x} - \mu}{\sigma/\sqrt{n}} \tag{47}$$

converges in distribution to a standardized normal distribution $\mathcal{N}(0, 1)$ as $n \to \infty$.

4.2 Characterization of a joint random variables

In this section the results obtained for the single random variable U are extended to two or more random variables such as (U_1, U_2) and (U_1, U_2, U_3).
For two random variables (U_1, U_2) we can define:

- **Joint PDF (JPDF)**:

$$f_{12}(V_1, V_2) \equiv \frac{\partial^2}{\partial V_1 \partial V_2} F_{12}(V_1, V_2) \tag{48}$$

The three basic properties of the JPDF are:

- $f_{12}(V_1, V_2) > 0$
- $\int_{-\infty}^{+\infty} f_{12}(V_1, V_2)\, dV_1 = f_2(V_2)$
- $\int_{-\infty}^{+\infty} \int_{-\infty}^{+\infty} f_{12}(V_1, V_2)\, dV_1 dV_2 = 1$

Note that $f_2(V_2)$ is called **marginal PDF** of U_2, and it corresponds to the definition given for the single random variable, independent from any other eventual variable.

- Joint variance or **covariance**:

$$cov(U_1, U_2) \equiv < u_1 u_2 >= \int_{-\infty}^{+\infty} int_{-\infty}^{+\infty}(V_1 - < U_1 >)(V_2 - < U_2 >) f_{12}(V_1, V_2)\, dV_1 dV_2 \tag{49}$$

- Normalized joint variance or **correlation coefficient**:

$$\rho_{12} = \frac{< u_1 u_2 >}{\sqrt{< u_1^2 >< u_2^2 >}} \tag{50}$$

which is basically a normalization of the covariance formulation. For the Cauchy–Schwarz inequality $\rho_{12} \in [-1, 1]$. If the correlation coefficient $\rho_{12} = 0$ (which implies that $< u_1 u_2 >= 0$) then the random variables U_1 and U_2 are **uncorrelated**. In contrast, if $\rho_{12} = 1$, U_1 and U_2 are **perfectly correlated**; and, if $\rho_{12} = -1$, they are perfectly negatively correlated. Saying that two functions or signals are correlated means that the functions are similar in behavior. Thus the perfect correlation happens when the function or signal is correlated with him-self leading to $\rho_{12} = 1$.

- **Conditional PDF**:
The PDF of U_2 conditional on $U_1 = V_1$ is

$$f_{2|1}(V_2|V_1) \equiv f_{12}(V_1, V_2)/f_1(V_1) \tag{51}$$

A word on notation: '$|V_1$' is an abbreviation for '$|U1 = V1$,'and is read 'conditional on $U_1 = V_1$,' or 'given $U_1 = V_1$', or just 'given V_1'.

The **concept of independence** is of paramount importance. If U1 and U2 are independent, then the knowledge of the value of either one of them provides no information about the other. Consequently, 'conditioning' has no effect, and the conditional and marginal PDFs are the same:
$f2|1(V2|V1) = f2(V2)$, for U1 and U2 independent
so that:

$$f_{12}(V_1, V_2) = f_1(V_1) f_2(V_2), \text{ for U1 and U2 independent} \tag{52}$$

Independent random variables are uncorrelated; but, in general, the inverse is not true.
A classical theorem connected to conditional PDFs is the Bayes' one, which represents the basis of the Bayesian statistics described in Section 4.4.1.

Bayes' theorem

It describes the probability of an event based on prior knowledge of conditions that might be related to the event. It is named after Thomas Bayes [15], an 18th-century British mathematician. The theorem can be stated as follows:

$$P(V_1|V_2) = \frac{P(V_2|V_1) \cdot P(V_1)}{P(V_2)} \tag{53}$$

Where:

- $P(V_1 \mid V_2)$ is the conditional probability of event $U < V_1$ occurring given that $U < V_2$ is true;
- $P(V_2 \mid V_1)$ is the conditional probability of event $U < V_2$ occurring given that $U < V_1$ is true;
- $P(V_1)$ and $P(V_2)$ are the probabilities of events $U < V_1$ and $U < V_2$ occurring independently of each other.

4.3 Characterization of a random processes

In general in turbulence we have a velocity field that is time and space dependent $\mathbf{U}(\mathbf{x}, t)$ so that the statistical randomness of its behavior depends on both space and time. The problem can quickly become really complex if statistical assumptions are not introduced. The most common ones in physics are the statistical stationarity and homogeneity. This assumptions depend on the process statistical behaviour in time and space respectively. In the following discussion we will treat individually the statistical approaches in time and space for a random process. Once we have the general notions, we will put them together in our case of interest: statistics in turbulent flows in Section 4.5).

4.3.1 Random processes in time: two points-time correlations

Until now we have considered our case variable U as fixed in space and time under the assumption of repeatable experiment that assures the independence between the N sample observations. In this context The random variable U is completely characterized by its PDF, $f(V)$. On the other side, it seems obvious that what is really interesting to study is the temporal evolution of U in a flow so that it has to be considered as a function of time $U(t)$. Such a time dependent random variable is called a random process as it can be seen as a random variable it-self at each instant in time with a probability distribution called **one-time PDF**:

$$f(V;t) \equiv \frac{\partial F(V,t)}{\partial V} \tag{54}$$

In this context, we define the **N-time joint PDF**:

$$\begin{aligned} f_N(V_1,t_1;V_2,t_2;\ldots;V_N,t_N) &\equiv \frac{\partial}{\partial t_1 \partial t_2 \ldots \partial t_N} F_N(V_1,t_1;V_2,t_2;\ldots;V_N,t_N) \\ &= \frac{\partial}{\partial t_1 \partial t_2 \ldots \partial t_N} P\{U(t_1) < V_1, U(t_2) < V_2, \ldots, U(t_N) < V_N\}, \end{aligned} \tag{55}$$

It becomes clear that the only way to completely characterize the random process is to know its N-time joint PDF for all instants, which is clearly impossible because already trying to evaluate the one-time PDF is really challenging, due to the infinite nature of time.
Considerable simplification occurs if the process is **statistically stationary**: all multi-time statistics are invariant under a shift in time such that

$$f(V_1, t_1 + T; V_2, t_2 + T; ...; V_N, t_N + T) = f(V_1, t_1; V_2, t_2, ..., V_N, t_N), \ \forall T \in \mathbb{R} \tag{56}$$

For a statistically stationary process, the ensemble mean (Eq. 42) can be considered as time independent and so related to the time average of the random variable:

$$< U(t) > \equiv < U(t) >_T \tag{57}$$

where:

- $< U(t) > \equiv \bar{U} = \int_{-\infty}^{+\infty} V f(V;t)\ dV$: ensemble average
- T: time interval
- $< U(t) >_T \equiv \frac{1}{T} \int_t^{t+T} V U(t')\ dt'$: time average

If we defined the velocity time fluctuation as $u(t) \equiv U(t) - \bar{U(t)}$, the simplest multi-time statistical property that can be considered is the **auto-covariance** with lag time τ:

$$R(\tau) \equiv < u(t)u(t+\tau) > \tag{58}$$

and the (**two-points time) auto-correlation function**:

$$\rho(\tau) \equiv \frac{R(\tau)}{R(0)} = \frac{< u(t)u(t+\tau) >}{< u(t)^2 >} \tag{59}$$

Note that: $\rho(0) = 1$, $|\rho| \leq 1$ and $\rho(\tau) = \rho(-\tau)$. For processes where the correlation diminishes as the lag time τ increases, we can define a characteristic integral time-scale of the random process:

$$\bar{\tau} \equiv \int_0^{\infty} \rho(\tau),\ d\tau \tag{60}$$

Usually high-frequency processes have a narrower auto-correlation function (and hence a smaller $\bar{\tau}$). This means that the statistical influence in time vanishes quicker so that the characteristic period of the process is smaller. This is in accordance with his high frequency response.
In this context, it becomes interesting to have information about the frequency components of the auto-correlation function. That's why a Fourier-transform is widely use in pair with the auto-covariance, allowing to define the spectrum $E(\omega)$ in frequency domain ω:

$$E(\omega) \equiv \frac{1}{\pi}\int_{-\infty}^{+\infty} R(\tau)\exp\left(-i\omega s\right),\ d\tau = \frac{1}{\pi}\int_{-\infty}^{+\infty} R(\tau)\cos\omega s,\ d\tau \tag{61}$$

where $\omega = \frac{2\pi}{\tau}$ is the angular frequency in [rad/s]. It is strictly related to the frequency $f = \frac{\omega}{2\pi}$ [Hz]=[1/s]. Clearly $R(s)$ and $E(\omega)$ contain the same information, just in different forms. The spectral representation allows us to know which are the modes (values of the frequency ω) that give the higher contribution to the auto-covariance $R(0)$. In fact, a frequency range $\omega \in [\omega_a, \omega_b]$ contribute to the auto-covariance as:

$$\Delta_{a,b}(< uu >) = \int_{\omega_a}^{\omega_b} E(\omega),\ d\omega \tag{62}$$

so that the variance is given by the integral over the whole spectrum of frequencies:

$$R(0) \equiv < uu >_T = \int_0^{+\infty} E(\omega),\ d\omega \tag{63}$$

So in practice, if we assume statistical stationarity, the frequency spectrum or the auto-correlation functions is the only quantity used to characterize the multi-time properties of a random process. However, it should be appreciated that the one-time PDF provide only a partial characterization of the process. Further simplifications can be obtained if the process is Gaussian, but this is not discussed here.

4.3.2 Random processes in space: two-points-space correlations

In real-life, physical variables such as the velocity component U are also space random variables, meaning that their value is influenced by their position in space. In the same fashion as for the random processes in time, we can think of fully characterizing these variables knowing their multi-space PDF, which is usually a complex task as it can involve at the same time really small microscales and really large macroscales. A consistent simplification is given when we assume **statistical homogeneity**, meaning that the statistical properties are invariant under a translation in space so that we can relate the ensemble mean to the spatial average of U.
If we take a cubic domain of side $\mathscr{L}$, the ensemble average of U can be computed as the spatial average:

$$< U(t) > = < U(t) >_{\mathscr{L}} \tag{64}$$

where:

- $< U(\mathbf{x},t) > \equiv \bar{U} = \int_{-\infty}^{+\infty} V f(V;t)\ dV$: ensemble average
- $< U(\mathbf{x},t) >_{\mathscr{L}} = \frac{1}{\mathscr{L}^3}\int_0^{\mathscr{L}}\int_0^{\mathscr{L}}\int_0^{\mathscr{L}} U(\mathbf{x},t)\ dx\ dy\ dz$: spatial average

A further assumption is the **statistical isotropic** that is a particular case of spatial homogeneity where the statistics are invariant under rotations and reflections of the coordinates system.

$$f_N(U_0(\mathbf{x_0})) = f_N(U_{rot/refl}(\mathbf{x}_{rot/refl})),\ \text{, under isotropic assumption} \tag{65}$$

where $(\mathbf{x}_{rot/refl}, U_{rot/refl})$ denotes the position and the velocity in any coordinates system obtained by rotations or reflections of the coordinates axis starting from $(\mathbf{x}_0, U_0)$.
The concept of isotropy is key in turbulence: hundreds of wind-tunnel experiments have been performed on (approximately) isotropic turbulence, and much of turbulence theory centers on this assumption because of the huge simplifications that are introduced.
Generally speaking, the simplest statistical property containing some information on the spatial structure of the random variable is the **two-points space auto-covariance** and the related **auto-correlation**:

$$R_{11}(\mathbf{r},\mathbf{x},t) \equiv < u(\mathbf{x},t)u(\mathbf{x}+\mathbf{r},t) > \tag{66}$$

$$\rho_{11}(\mathbf{r},\mathbf{x},t) \equiv \frac{R_{11}(\mathbf{r})}{R_{11}(0)} \tag{67}$$

In analogy with how we calculate the time-scale from the two-points time auto-correlation, from the two-points space auto-correlation we can define an integral length-scale such that:

$$L_{11,x} = \int_0^{+\infty} \rho_{11}(r\mathbf{e_x},\mathbf{x},t)\ dr \tag{68}$$

where e_x is the unit vector in the x-axis direction. In this way we can think of defining a length-scale for each direction as proposed by Pope([142], chap.3)

In the context of homogeneous or, even more strict condition of isotropic statistics, it is clear that the auto-covariance as well as the auto-correlations are independent from $\mathbf{x}$ at a fixed time: $\rho_{11}(\mathbf{r},\mathbf{x},t) = \rho_{11}(\mathbf{r},t)$. So it makes sense to re-express the spatial information contained in $R_{11}(\mathbf{r},t)$ in the wave-number spectrum using the Fourier transform:

$$\phi_{11}(\mathbf{k},t) = \frac{1}{(2\pi)^3} \iiint_{-\infty}^{+\infty} R_{11} \exp\left(-i\mathbf{k}\cdot\mathbf{r}\right)\ d\mathbf{r} \tag{69}$$

where ϕ_{11}, called **velocity spectrum function**, represents the contribution of the modes $\mathbf{k} \in [\mathbf{k_a},\mathbf{k_b}]$ to the covariance $< uu >= R_{11}(0,t)$:

$$\Delta_{a,b}(< uu >) = \iiint_{\mathbf{k_a}}^{\mathbf{k_b}} \phi_{11}(\mathbf{k},t)\ d\mathbf{k} \tag{70}$$

where the notation $\Delta_{a,b}(f(r))$ represents the contribution of the modes between $[k_a,k_b]$ to the generic function f(r) in the physical domain.
The two-point correlation and the spectrum contain two different kinds of directional information. The dependencies of $R_{11}(\mathbf{r},t)$ on $\mathbf{r}$, and of $\phi_{11}(\mathbf{k},t)$ on $\mathbf{k}$, give information about the directional dependence of correlation; while the components of R_{11} and ϕ_{11} give information about the directions of the velocities.
In turbulence theory, the **energy spectrum function** $E(\kappa,t)$ is a crucial quantity used to describe how the TKE is distributed among different scales of motion, represented by the wave-number κ. This function encapsulates the energy contained in turbulent eddies of various sizes and is defined by the following integral:

$$E_{11,k}(\kappa_k,\mathbf{x},t) \equiv \frac{1}{\pi}\int_{-\infty}^{+\infty} R_{11,k}(r,\mathbf{x},t)\exp\left(-i\kappa_k r\right)dr = \frac{2}{\pi}\iint_{-\infty}^{+\infty} \phi_{11}(\kappa,\mathbf{x},t)\,dr_h dr_q \tag{71}$$

with $h,q \neq k \vee h \neq q \vee h,k,q = 1,2,3$.
For example if I want to analyse the energy along a line parallel to the x-axis I set $(k,h,q) = (1,2,3)$ so that I get a function $E_{11,1}(\kappa_1,\mathbf{x},t)$.
The formulation is also called **directional energy spectrum** and it can be extended for a generic correlation $R_{ij,k}$ so that we have $E_{ij,k}$:

$$E_{ij,k}(\kappa_k,\mathbf{x},t) \equiv \frac{1}{\pi}\int_{-\infty}^{+\infty} R_{ij,k}(r,\mathbf{x},t)\exp\left(-i\kappa_k r\right)dr = \frac{2}{\pi}\iint_{-\infty}^{+\infty} \phi_{ij}(\kappa,\mathbf{x},t)\,dr_h dr_q \tag{72}$$

In this way we have 18 spectra to analyse given the different proportional properties contained in each. That's why several authors [142, 11] introduce the **isotropic energy spectrum** in order to remove the directional information of the velocity spectrum ϕ_{ij}:

$$E(\kappa) = \oint_S \frac{1}{2} tr(\Phi_{ij}(\mathbf{k},t))\,dS(\kappa) \tag{73}$$

where S is the surface of the sphere of radius $\kappa = ||\mathbf{k}||_2$

In this way we can focus only on the contributions of the different modes to the energy of the flow. In fact, the integral of the isotropic energy spectrum function over all wave-numbers gives the total TKE k:

$$\int_0^\infty E(\kappa,t)d\kappa = \frac{1}{2}R_{ii}(0,t) = \frac{1}{2}\langle u_i u_i\rangle \equiv k, \tag{74}$$

where:

- $R_{ii}(0,t)$ is the trace of the velocity correlation tensor at zero separation, which is equal to the total turbulent kinetic energy.
- $\langle u_i u_i\rangle$ is the mean square velocity, representing the total kinetic energy per unit mass in the turbulent flow.

Thus, $E(\kappa,t)d\kappa$ represents the contribution to the turbulent kinetic energy from all eddies with wave-numbers in the range $\kappa \leq |\kappa| < \kappa + d\kappa$. This provides a detailed look at how energy is distributed across different scales in the turbulent flow.
Velocity spectra in turbulence are further examined in Section 5, where the distribution and dynamics of energy among different scales are analyzed in detail. This involves understanding the cascade of energy between larger scales (lower wave-numbers) and smaller scales (higher wave-numbers), and how this affects the properties of the turbulence.

4.3.3 Random processes in a vector field

The last level of complexity in the statistical analysis of a random process is introduced by the dependence between different variables. For instance if we consider always the velocity as our random variable, in real-life we cannot assume that studying only one of the components of a random vector field is enough. That's why now that we have introduced the main concepts around the statistical analysis in time and space for a single random variable $U(\mathbf{x},t)$, we can finally expand the discussion over the whole random vector field $\mathbf{U}(\mathbf{x},t) = U_i(\mathbf{x},t)$for i=1,2,3. For random fields we can use all the ideas developed for a single random variable but now introducing Joint PDFs and cross-correlations (or simply correlations) two-points time or two-points space:

Time-correlations

Assumption: statistical stationary random process

$$R_{ij}(\mathbf{x}, t, \tau) = R_{ij}(\mathbf{x}, \tau)$$

In time domain t:

- two-points time-covariance:

$$R_{ij}(\tau) \equiv < u_i(t) u_j(t+\tau) > \tag{75}$$

- two-points time-correlation:

$$\rho_{ij}(\tau) \equiv \frac{R_{ij}(\tau)}{R_{ij}(0)} = \frac{< u_i(t) u_j(t+\tau) >}{< u_i(t) u_j(t) >} \tag{76}$$

- integral time-scale:

$$\bar{\tau_{ij}} \equiv \int_0^\infty \rho_{ij}(\tau),\ d\tau \tag{77}$$

In frequency domain $\omega = 2\pi f$:

- energy spectrum:

$$E_{ij}(\omega) \equiv \frac{1}{\pi} \int_{-\infty}^{+\infty} R_{ij}(\tau) \exp(-i\omega s),\ d\tau = \frac{1}{\pi} \int_0^{+\infty} R_{ij}(\tau) \cos \omega s,\ d\tau \tag{78}$$

- energy spectrum meaning:

$$R_{ij}(0) \equiv < u_i(t) u_j(t) >_T = \int_0^{+\infty} E_{ij}(\omega),\ d\omega \tag{79}$$

with $i, j = 1, 2, 3$ such that $\{u_1, u_2, u_3\} = \{u, v, w\} = \mathbf{U} - < \mathbf{U} >$ are the velocity fluctuations.

Space-correlations

In space domain $\mathbf{x}$:

- two-points space-covariance:

$$R_{ij}(\mathbf{r},\mathbf{x},t) \equiv < u_i(\mathbf{r},\mathbf{x},t)u_j(\mathbf{r},\mathbf{x},t) > \tag{80}$$

- two-points space-covariance (along k-axis):

$$R_{ij,k}(r,\mathbf{x},t) \equiv < u_i(re_k,\mathbf{x},t)u_j(re_k,\mathbf{x},t) > \tag{81}$$

- two-points space-correlation:

$$\rho_{ij}(\mathbf{r},\mathbf{x},t) \equiv \frac{R_{ij}(\mathbf{r},\mathbf{x},t)}{R_{ij}(0,\mathbf{x},t)} = \frac{< u_i(\mathbf{r},\mathbf{x},t)u_j(\mathbf{r},\mathbf{x},t) >}{< u_i(\mathbf{r},\mathbf{x},t)u_j(\mathbf{r},\mathbf{x},t) >} \tag{82}$$

- integral length-scale:

$$L_{ij,k} = \int_0^{+\infty} \rho_{ij}(r\mathbf{e_k},\mathbf{x},t)\ dr \tag{83}$$

In wave-number domain κ:

- velocity spectrum:

$$\phi_{ij}(\kappa,\mathbf{x},t) \equiv \frac{1}{(2\pi)^3} \iiint_{-\infty}^{+\infty} R_{ij}(\mathbf{r},\mathbf{x},t) \exp\left(-i\kappa\cdot\mathbf{r}\right)\ d\mathbf{r} \tag{84}$$

- energy spectrum (isotropic definition):

$$E(\kappa) = \oint_S \frac{1}{2} tr(\Phi_{ij}(\mathbf{k},t))\, dS(\kappa) \tag{73}$$

  where S is the surface of the sphere of radius $\kappa = ||\mathbf{k}||_2$

- energy spectrum (along k-axis):

$$E_{ij,k}(\kappa_k,\mathbf{x},t) \equiv \frac{1}{\pi}\int_{-\infty}^{+\infty} R_{ij,k}(r,\mathbf{x},t)\exp\left(-i\kappa_k r\right) dr = \frac{2}{\pi}\iint_{-\infty}^{+\infty} \phi_{ij}(\kappa,\mathbf{x},t)\, dr_h dr_q \tag{72}$$

  with $h,q \neq k \vee h \neq q \vee h,k,q = 1,2,3$

- energy spectrum meaning (isotropic definition):

$$k \equiv \frac{1}{2}\langle u_i u_i\rangle = \frac{1}{2}R_{ii}(0,t) = \int_0^{\infty} E(\kappa,t)\, d\kappa, \tag{85}$$

- energy spectrum meaning (along k-axis):

$$R_{ij,k}(0,\mathbf{x},t) = 2\int_0^{\infty} E_{ij,k}(\kappa,\mathbf{x},t)\, d\kappa \tag{86}$$

with $i,j = 1,2,3$ such that $\{u_1,u_2,u_3\} = \{u,v,w\} = \mathbf{U} - < \mathbf{U} >$ are the velocity fluctuations and $k = x,y,z$ defines e_k as the unit vectors in the direction of the x, y and z-axis respectively. Possible assumption: statistically homogeneous random process

$$R_{ij}(\mathbf{r},\mathbf{x},t) = R_{ij}(\mathbf{r},t)$$

4.4 Discrete description in statistics

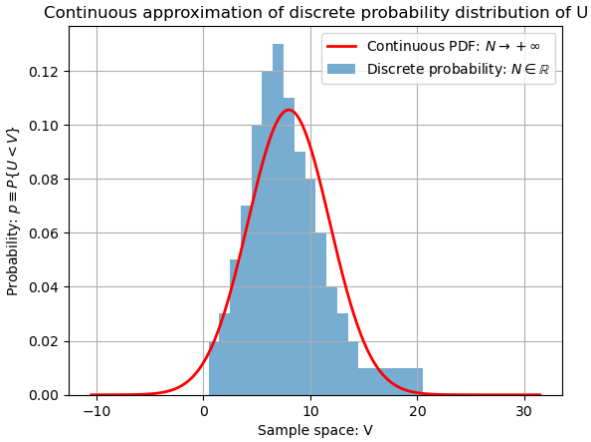

Figure 18: Example of a discrete description (blue blocks) of a PDF compared to its continuous realization (red line).

Until now we talked about probability, CDF and PDF as continuous functions in the ideal case where we have access to infinite quantities of data. But in real-life we have limited data so that our functions are discrete, e.g. in Figure 18. For instance if we perform a series of N observations of our random variable U for a fixed position, we will have a "sample" of data to analyze such as $\{U_1, U_2, ..., U_N\}$. So we don't know exactly the value of U and we are not even sure if the N observations that we performed are enough to characterize the discrete PDF of the random variable U. Ideally we wish we could take $N \to \infty$, so that the sample approaches the entire "population" of the variable, which can fully represent its statistics. In this context the distinction between sample and population becomes imperative:

- **sample**: given discrete $N \in \mathbb{R}$ number of observations,

$$U_{sample} = \{U_1, U_2, ..., U_N\} \in U$$

  and a numerical characteristic calculated from a sample of data is called **statistic**;

- **population**: given the ideal case $N \to \infty$,

$$U \equiv U_{population} = \{U_1, U_2, ..., U_N\}, \text{for } N \to \infty$$

  and a numerical characteristic calculated from population data is called **parameter**.

This makes evident that in practice we have always a limited number of data and so a sampling error is inevitable because we cannot get to the exact behavior of the population. At this point the main questions are two:

1. how great should we take N so that we can fairly approximate the behavior of our random variable?
2. how can we quantify the sampling error committed related to the population?

The branch of statistics that gives as answers is the **inferential statistics**. Its objective is to make inferences or predictions about a population based on sample data. Its main tools are:

- **Estimations** involve using sample data to estimate unknown population parameters, such as means or proportions. Point estimates give single values (like sample means) as estimates, while confidence intervals provide ranges of values likely to contain the true population parameter with a specified level of confidence (e.g. 95% confidence). They help manage uncertainty by quantifying the precision of our estimates and they are crucial for making informed decisions based on sample data about larger populations. Some of the main methods to compute confidence intervals are:
  - **Normal Distribution Method**: Suitable for large samples ($N \geq 30$), uses the standard normal distribution and sample standard deviation.

  - **T-Distribution Method**: Used for small samples ($N < 30$) or when population standard deviation is unknown, utilizes the t-distribution.
  - **Wald Method (Approximate Method)**: Common for proportions, assumes approximate normality of the sampling distribution.
  - **Jack-knife Method**: Resamples data to create empirical sampling distributions, useful when distributional assumptions are unclear.
  - **Bootstrap Method**: Generalization of the previous Jackknife Method
  - **Bayesian Methods**: Provides credible intervals based on Bayesian inference, representing the range of parameter values with a specified degree of belief.

  These methods vary in complexity and assumptions, based on sample size, data characteristics and statistical philosophy (Frequentist vs. Bayesian, see Section 4.4.1).

- **Test statistics** are numerical measures used in hypothesis testing to assess the strength of evidence against a null hypothesis based on sample data. As a reminder, hypothesis testing involves making a decision or drawing a conclusion about relationships or comparisons between populations based on sample data. We say that a null hypothesis (H_0) is the assumption that is in contrast with the one that we want to prove while the alternative hypothesis (H_i, $i > 0$) is the claim that we consider as a possible alternative to the null hypothesis. It represents what we are trying to establish or prove but we reach it usually by proving that the null hypothesis is not true, so we use a reverse approach. In fact test statistics are calculated from sample data and compared to critical values from known distributions. This comparison helps determine whether to reject the null hypothesis in favor of an alternative hypothesis, providing a rigorous method to make statistical decisions based on observed data.

4.4.1 Statistics philosophy: Frequentist vs. Bayesian approaches

In statistics, the Frequentist and Bayesian approaches represent two distinct philosophies of inference:

- **Frequentist approach**:
  Frequentist statistics views probability as the long-run frequency of events occurring in repeated experiments. It treats parameters as fixed, unknown constants that are estimated using sample data. Inference involves using sample statistics to make decisions about population parameters, such as constructing confidence intervals and performing hypothesis tests based on p-values. The emphasis is on the properties of estimators and the frequentist interpretation of probability.

- **Bayesian approach**:
  Bayesian statistics, on the other hand, uses probability to represent degrees of belief or uncertainty about events or parameters. It treats parameters as random variables with probability distributions that incorporate prior beliefs and are updated with observed data using Bayes' theorem. Bayesian inference integrates prior knowledge or beliefs with data to provide posterior distributions for parameters. This approach allows for a more flexible and intuitive handling of uncertainty, as probabilities are interpreted as measures of subjective belief.

To sum up, The fundamental difference between the two approaches lies in how probability is interpreted and how parameters are treated. Frequentists interpret probability as long-run frequencies and treat parameters as fixed while Bayesians interpret probability as a measure of belief and treat parameters as random variables with distributions that can be updated with new information.

4.5 Characterization of the turbulence as a random process

In turbulence, the main physical values in play are the components of the velocity field and so we can use the analysis tools introduced for random processes in time and space introduced in the Section 4.3.3. The historical and theoretical development of these tools in the field of turbulence it's discussed in Section 5. In general, a turbulent flow, statistically speaking, has the following properties:

1. **Non-Gaussian distribution** with high Reynolds number dependance;

2. **Intermittency** or highly irregular activity: this leads to regions of intense activity interspersed with relatively calm areas.

3. **Statistically stationary**, after an initial transient period where the flow has to develop.
4. **Energy cascade** with local microscale isotropy: free fully-developed turbulence involves the transfer of energy from large scales (injection scales) to small scales (dissipation scales) through a process known as the energy cascade, often described statistically by the Kolmogorov theory [82].
5. **Anisotropy and Inhomogeneity**: while small-scale turbulence tends to be isotropic and homogeneous, large-scale turbulent structures are often anisotropic and inhomogeneous due to boundary conditions, mean flow gradients, or external forces.
6. **Coherent Structures**: despite the chaotic nature of turbulence, coherent structures such as vortices and eddies are statistically significant features. These structures contribute to the transport of momentum, heat, and other quantities, and their statistical properties are key to understanding turbulence dynamics.

Points 1. and 2. imply that turbulence has to be described through higher order higher-order moments of the velocity fluctuations. Points 4., 5. and 6. need to be treated in a more physical view, as done in Section 5.
In point 3. the assumption of statistical stationary allows as to use as ensemble mean the time mean under the condition that our data sample is fairly well resolved in time to properly capt the low and high frequencies, and so to correctly describe the physics of the problem. A good choice should capture at least 90% of the energy spectrum. So the time-step choice is crucial for a correct mean as well as the time-span considered. In this context it is imperative to estimate the sampling error, topic that we already touched, even if just in surface, in paragraph 4.4. In the specific case of turbulence statistics the confidence interval estimation has been treated by different authors [19] [32] [80].

4.5.1 Evaluation of the interval of confidence

In this work we evaluation the confidence interval of higher order statistics as proposed by Benedict and Gould [19]. This method does not make any assumption about the normality of the random variable distribution and it is based on the resampling algorithm of the type jack-knife. Given a generic dataset $U = \{U_1, U_2, ..., U_N\}$ and a statistical estimator $\hat{\theta}$ calculate from U, that can be a correlation or a higher order statistics such skewness or kurtosis, we define the jackknife estimate of variance for $\hat{\theta}$ as:

$$var(\hat{\theta}) = \frac{N-1}{N} \sum_{i=1}^{N} (\hat{\theta} - < \hat{\theta}_{jack,i} >)^2 \tag{87}$$

where:

- $< \hat{\theta}_{jack,i} >= \frac{1}{N} \sum_{i=1}^{N} \hat{\theta}_{jack,i}$: jack-knife samples ensemble mean
- $\hat{\theta}_{jack,i}$: statistical estimator calculated on $U_{jack,i}$
- $U_{jack,i} = \{U_1, U_2, ..., U_{i-1}, U_{i+1}, ..., U_N\}$: jack-knife sample

So that the confidence interval for the estimator $\hat{\theta}$ ca be approximated with:

$$\Delta_{\hat{\theta}} = \hat{\theta} \pm \sqrt{var(\hat{\theta})} \tag{88}$$

It should be remarked that in this work we take into account only the uncertainty associated with the sampling of a random process such as turbulence. Additional uncertainties due to the particular character of each measuring instrument or those related to the experimental facility as a whole must also be accounted if we are doing experimental measurements. We neglected this aspect in our case because we are following a purely numerical approach. In the next paragraph an example of statistical study used to determine the best sub-sampling factor as a compromise between accuracy and data storage.

4.5.2 Evaluation of the interval of confidence: example for Gyroid struct=1.20 simulation

We conducted a simulation of a Gyroid structure with a structural factor struct = 0.75 at Re = 2500, spanning a time period of $T = 8.2$s, using a simulation time step $\Delta t = 8.7 \times 10^{-5}$s, constrained by a constant CFL = 0.25. Ideally, we would extract data from every time step, but the storage requirements are prohibitive. Thus, we explored two approaches: first, reducing the data extracted per time step by focusing on sections of the computational domain or extracting point-wise data, as detailed in Section 7.1; second, extracting data at fewer time steps using a down-sampling factor, which is the focus of this analysis. Moreover, keep in mind that our simulations have way higher frequency resolution than the physical phenomena that take part in it, due to the CFL requirements for stability. This gives us a supplementary confidence in introducing a sub-sampling factor without compromising too much the physics of the problem. Of course, ideally we should use a cut-off frequency in the post-treatment data but it can be hard and not practical to define exactly the Kolmogorov's frequency (computed from the time-scale) for each point or a global one. Hopefully the high frequency numerical noise does not have almost any influence on the global results as it has really small energetic contribution: from 4 orders of magnitude up. In fact, in Figure 22 we plot a frequency spectrum E_11 with an estimated Kolmogorov's frequency around $f_k = 20 - 25Hz$, and we can underline how big is the difference between the physical frequency resolution and the simulated one due to the numerical stability limitations.
Coming back to us, the aim here is to select the down-sampling factor N_{ds}, i.e., the frequency of time-step extraction for post-processing, while preserving accuracy. This was done by evaluating different values of N_{ds} and analyzing the confidence intervals for statistical moments of the velocity field. The focus is on the x-component of velocity U, as it corresponds to the streamwise direction, where fluctuations are expected to be more relevant than in the crosswise components.
The analysis was conducted by computing confidence intervals (using the jackknife estimation method as described in Section 4.5.1) for various statistical measures, including variance (Figure 19), skewness (Figure 20), and kurtosis (Figure 21) of the velocity components, as well as the energy spectra of the flow (Figure 22). For each N_{ds}, the confidence intervals of higher-order statistical measures were calculated to quantify the uncertainty introduced by temporal down-sampling.
As expected, lower N_{ds} values resulted in narrower confidence intervals, reflecting more accurate statistics due to the higher number of samples. However, the relationship between the uncertainty interval and the down-sampling factor N_{ds} is not linear. It is immediately apparent that the uncertainty over the variance is minimal, ranging from 0.005% to 0.035%, which is satisfactory. However, turbulence analysis often focuses on second-order statistics like correlations and their derivatives, making it important to limit the skewness uncertainty (a third-order statistical moment) to below 20%, while accepting kurtosis uncertainty (a fourth-order statistical moment) below 80-90% [19].
Down-sampling also affects the frequency spectrum, as shown in Figure 22. Another way to assess the accuracy of the data is to compare the energy captured, $\langle uu \rangle$ (the integral of the correlation spectrum), for different N_{ds} values, with the reference case being $N_{ds} = 1$ (no down-sampling). While most of the energy is concentrated at low frequencies, down-sampling can affect the shape of the spectrum due to the Fast Fourier Transform (FFT) operation combined with Blackman windowing.
The down-sampling analysis is summarized in Table 4. Based on the previously defined criteria, we select $N_{ds} = 50$ (meaning the extraction of data each 50 time steps) as a compromise between accuracy and data storage. The energy captured remains nearly constant for N_{ds} values between 2 and 175, and the uncertainties in skewness and kurtosis are limited to below 19% and 83%, respectively. For $N_{ds} > 50$, the skewness uncertainty increases exponentially, which could degrade the reliability of our statistical post-processing.

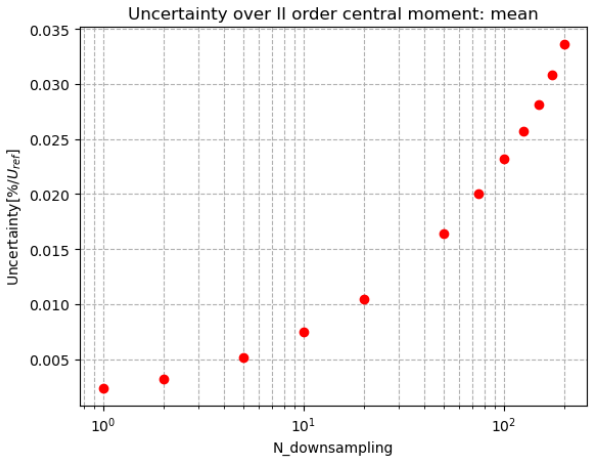

Figure 19: Variance uncertainty analysis for different N_{ds}.

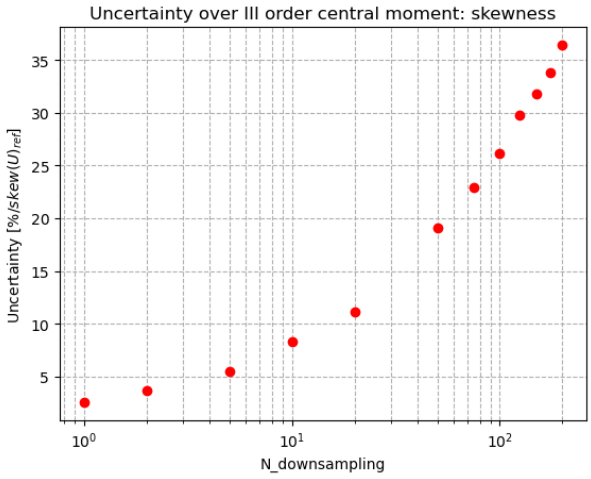

Figure 20: Skewness uncertainty analysis for different N_{ds}.

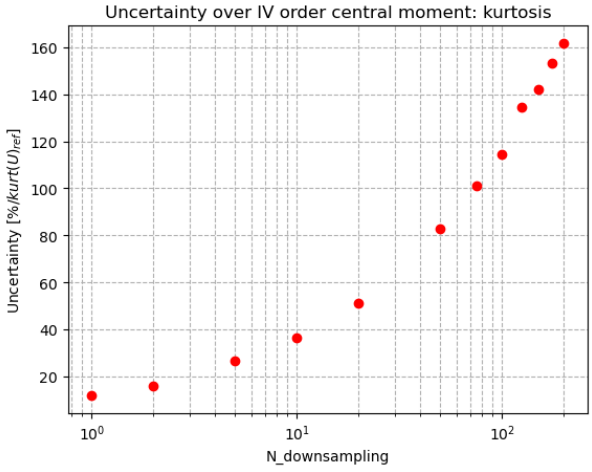

Figure 21: Kurtosis uncertainty analysis for different N_{ds}.

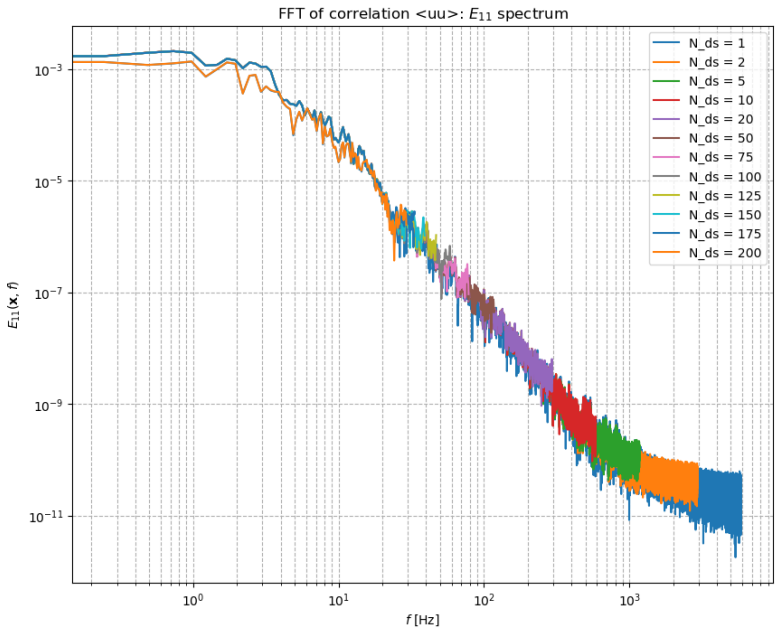

Figure 22: Energy spectra analysis for different N_{ds}.

Table 4: Confidence interval and statistical data fidelity analysis for a Gyroid struct=0.75 at Re=2500.

N downsampling	**dt [$e-05$ s]**	**Nb data [$\times 10^3$]**	$\frac{<uu>}{<uu>_{\text{ref}}}$ [%]	ΔVar[%]	ΔSkew[%]	ΔKurt[%]
1	8.7	96.3	100.0	0.0	2.5	11.8
2	17.4	48.1	139.4	0.0	3.6	16.1
5	43.5	19.3	138.1	0.01	5.5	26.5
10	87.0	9.6	137.5	0.01	8.3	36.5
20	174.0	4.8	136.9	0.01	11.2	51.2
50	435.0	1.9	134.8	0.02	19.1	82.7
75	652.5	1.3	133.3	0.02	22.9	100.9
100	870.0	0.96	131.8	0.02	26.1	114.6
125	1087.5	0.77	130.1	0.03	29.7	134.7
150	1305.0	0.64	128.5	0.03	31.8	142.2
175	1522.5	0.55	127.3	0.03	33.8	153.3
200	1740.0	0.48	87.2	0.03	36.4	161.7

5 Turbulence physics

Turbulence it's a 3D, unsteady and random (in jargon we say "chaotic") state of a fluid flow that we observe in nature and that arises as a solution of the NS equations. The challenge it's always been to understand the physics behind this phenomenon so that we could predict it and eventually mitigate it or exploit it in our applications. Some of the main points in turbulence theory are about its nature, its conditions to happen (usually connected to high values of the Reynolds number) and its scale of motions. In fact lots of studies focused on distinguishing between small-scale turbulence and large-scale motions in turbulent flows at high Reynolds numbers. The large-scale motions are significantly influenced by the geometry of the flow, i.e., by the boundary conditions, and they dominate the processes of transport and mixing. In contrast, the behavior of small-scale motions is largely governed by the rate at which they receive energy from the large scales and by viscosity. Consequently, these small-scale motions exhibit a universal character that is largely independent of the flow geometry. This raises important questions: What are the characteristics of small-scale motions? Can they be predicted? How?
This is the heart of **turbulence theory** [11] [142] and it is key to understand turbulence and model its behavior for numerical applications in CFD.

In this section, we begin by introducing the governing equations for the mean flow, specifically the Reynolds-Averaged Navier-Stokes (RANS) equations, derived from the incompressible Navier-Stokes (NS) equations (Section 5.1). A key feature that distinguishes these equations from the traditional NS formulation is the appearance of the Reynolds Stress Tensor (RST), which we explore in detail. We then proceed to derive transport equations for the components of the RST, as well as for the turbulent kinetic energy (TKE) k and the dissipation rate ϵ, both of which are fundamental to understanding turbulence. Following this mathematical framework, in Section 5.2, we delve into the nature of turbulent motion, examining its origins in vorticity and multi-scale behavior, including a discussion of Kolmogorov's theory and the theory of turbulence correlations (Section 5.3). In Section 5.4, we analyze the turbulence energy spectrum, its significance, and the approaches for its modeling. Finally, we conclude by presenting the main turbulence analysis tools available today, alongside some methods developed in-house (Section 5.5).

5.1 RANS equations

In section 4.5, various statistical quantities (means, PDFs, two-point correlations, etc.) were introduced to describe a random variable such as the turbulent velocity field. It is possible to derive equations for the evolution of all of these quantities, starting from the NS equations that govern the underlying field $\mathbf{U}(\mathbf{x}, t)$.
The most basic of these equations, first derived by Reynolds in 1894, are the RANS equations that govern the mean velocity field $\langle \mathbf{U}(\mathbf{x}, t) \rangle$.
The velocity can be decomposed in:

$$\mathbf{U}(\mathbf{x}, t) = \langle \mathbf{U}(\mathbf{x}, t) \rangle + u'(\mathbf{x}, t) \tag{89}$$

where $\langle \mathbf{U} \rangle$ is the mean velocity and u is the fluctuating component. So that RANS equations for an incompressible flow using Einstein's notation are:

$$\frac{\partial \langle U_j \rangle}{\partial x_j} = 0, \text{ for j=1,2,3} \tag{90}$$

$$\frac{\partial \langle U_j \rangle}{\partial t} + U_i \frac{\partial \langle U_j \rangle}{\partial x_i} = \nu \nabla^2 \langle U_j \rangle - \frac{\partial \langle u_i u_j \rangle}{\partial x_i} - \frac{1}{\rho} \frac{\partial \langle p \rangle}{\partial x_j}, \text{ for i, j= 1, 2, 3} \tag{91}$$

This equations are formally the same as the incompressible NS equations with exception for the non linear term $\langle u_i u_j \rangle$, called **Reynolds stress tensor (RST)**. In fact if we recast Eq. 91, this term behaves as a "turbulent shear stress" tensor:

$$\frac{\partial \langle U_j \rangle}{\partial t} + U_i \frac{\partial \langle U_j \rangle}{\partial x_i} = \frac{\partial}{\partial x_j} (\tau_{ij} - \langle u_i u_j \rangle) - \frac{1}{\rho} \frac{\partial \langle p \rangle}{\partial x_j} \tag{92}$$

where:

- $\tau_{ij} = 2\nu \langle S_{ij} \rangle$ is the viscous shear stress tensor;

- $S_{ij} = \frac{1}{2}(\frac{\partial U_i}{\partial x_j} + \frac{\partial U_j}{\partial x_i})$ is the rate-of-strain tensor;

By averaging the equations over time, RANS reduces the complexity compared to solving the full Navier-Stokes equations for turbulent flows but the non-linear RST term has to be modeled properly. In fact this term involves an average of a product of fluctuations, with is in general a hard computational task so that the literature around the modeling of it, is wide and different approaches exist (see Pope chap.8-chap.13 [142]). But before modeling its crucial to understand the physics behind this tensor.

5.1.1 Reynolds Stress Tensor (RST) properties

The RST has some important features:

- **II order tensor**;
- **symmetric**: $\langle u_i u_j \rangle = \langle u_j u_i \rangle$;
- $\langle u_i u_i \rangle$, for i= 1, 2, 3 are called **normal RST components**;
- $\langle u_i u_j \rangle$, for i, j= 1, 2, 3 and $i \neq j$ are called **shear RST components**.

The distinction between shear stresses and normal stresses is dependent on the choice of cooordinates system. An intrinsic distinction can be made between isotropic and anisotropic stresses. The deviatoric anisotropic part is defined base on the isotropic stress such that:

$$a_{ij} \equiv \langle u_i u_j \rangle - \frac{2}{3} k \delta_{ij} \tag{93}$$

where:

- $k = \frac{1}{2}\langle u_i u_i \rangle$, for i= 1, 2, 3 is the TKE;
- δ_{ij} is the Kronecker's delta function;

The anisotropy tensor a_{ij} in eq. 93 can be normalized as follows:

$$b_{ij} \equiv \frac{a_{ij}}{2k} = \frac{\langle u_i u_j \rangle}{u_l u_l} - \frac{1}{3}\delta_{ij}, \text{ for l= 1, 2, 3} \tag{94}$$

In this context it's important to remark that the anisotropic component of a_{ij} is the only that is effective in transporting momentum, which is deeply connected with the irrotational nature of turbulence. That's why several turbulence analysis focus is given to understanding the behavior of a_{ij} in turbulent flows. An important tool in this context is the Lumley triangle, that we describe in Section 5.5.6.

5.1.2 Trasport equations for Reynolds Stress Tensor (RST)

A transport equation for the RST components can be derived combining RANS equations and incompressible NS equations:

$$\frac{\partial \overline{u_i' u_j'}}{\partial t} + \overline{u_k}\frac{\partial \overline{u_i' u_j'}}{\partial x_k} = P_{ij} + \underbrace{(D_{ij}^v + D_{ij}^p + D_{ij}^\nu)}_{D_{ij}} + \phi_{ij} - \epsilon_{ij} \tag{95}$$

where:

- $\frac{\partial \overline{u_i' u_j'}}{\partial t}$: **Time derivative term**
  - Represents the rate of change of the Reynolds stress components with respect to time.
- $\overline{u_k}\frac{\partial \overline{u_i' u_j'}}{\partial x_k}$: **Advection/convection term**
  - Represents the transport of Reynolds stresses by the mean flow.
- $P_{ij} = -\overline{u_i' u_k'}\frac{\partial \overline{u_j}}{\partial x_k} - \overline{u_j' u_k'}\frac{\partial \overline{u_i}}{\partial x_k}$: **Production term**
  - Represents the production of Reynolds stresses due to the mean velocity gradients.
  - The term is typically positive in regions with significant velocity gradients, indicating energy transfer from the mean flow to the turbulent fluctuations.
- $D_{ij}^v = -\frac{\partial \overline{u_i' u_j' u_k'}}{\partial x_k}$: **Velocity fluctuations diffusion term or (Turbulent Diffusion Term)**
  - Represents the diffusion by velocity fluctuations, significant in high Reynolds number flows.
  - A triple correlation term that describes how interactions between different components of the fluctuating velocities contribute to the redistribution of turbulence.
- $D_{ij}^p = -\frac{1}{\rho}\left(\overline{\frac{\partial (p' u_i')}{\partial x_j}} + \overline{\frac{\partial (p' u_j')}{\partial x_i}}\right)$: **Pressure fluctuations diffusion term**
  - Represents the diffusion due to pressure fluctuations.
  - Captures how pressure fluctuations correlate with velocity fluctuations, leading to a net flux of turbulent stresses.
- $D_{ij}^\nu = +\nu\frac{\partial^2 \overline{u_i' u_j'}}{\partial x_k \partial x_k}$: **Viscous diffusion term or (Molecular diffusion term)**
  - Represents the diffusion due to molecular viscosity
  - Significant in low Reynolds number flows but typically small in high Reynolds number flows compared to turbulent diffusion.
- $\phi_{ij} = +\frac{1}{\rho}\left(\overline{p_i'(\frac{\partial u_i'}{\partial x_j} + \frac{\partial u_j'}{\partial x_i})}\right)$: **Pressure-strain term**
  - Redistributes turbulent kinetic energy among different components of the Reynolds stress tensor.
  - Can transfer energy between different components of the stress tensor or act to isotropize the turbulence.
- $\epsilon_{ij} = -2\nu\overline{\frac{\partial u_i'}{\partial x_k}\frac{\partial u_j'}{\partial x_k}}$: **Dissipation term**
  - Represents the rate at which turbulent kinetic energy is converted into thermal energy by viscous effects.
  - Always positive and acts to reduce the turbulent kinetic energy.
  - Directly related to the smallest scales of turbulence where viscosity dominates.

Note that:

- for homogeneous turbulence: $\frac{\partial \overline{u_i' u_j'}}{\partial t} = P_{ij} + \phi_{ij} - \epsilon_{ij}$
- for isotropic turbulence: $\frac{\partial \overline{u_i' u_j'}}{\partial t} = -\epsilon_{ij}$ and $\overline{u_i' u_i'} = \frac{2}{3}k$ while $\overline{u_i' u_j'} = 0$

5.1.3 Transport equation for Turbulent Kinetic Energy (TKE)

The TKE is defined as half of the trace of the RST:

$$k \equiv \frac{1}{2} < u_i u_i >= \frac{1}{2}(< u^2 > + < v^2 > + < w^3 >) \tag{96}$$

Using eq.95 and the previous definition:

$$\frac{\partial k}{\partial t} + \overline{u_k}\frac{\partial k}{\partial x_k} = P_k + \underbrace{D_k^v + D_k^p + D_k^\nu}_{D_k} - \epsilon \tag{97}$$

where:

- $\frac{\partial k}{\partial t}$: Time derivative term
- $\overline{u_k}\frac{\partial k}{\partial x_k}$: Advection/convection term
- $P_k = -\overline{u_i' u_k'}\frac{\partial \overline{u_i}}{\partial x_k}$: Production term
  - The production term describes the rate at which turbulent kinetic energy is generated by the mean velocity gradients.
  - It is usually given as $P_k = R_{ij}\frac{U_i}{x_j}$, where $R_{ij} =< u_i u_j >$ is the RST.
- $D_k^v = -\frac{\partial \overline{u_i' u_i' u_k'}}{\partial x_k}$: Velocity fluctuation diffusion term (or Turbulent diffusion term)
- $D_k^p = -\frac{1}{\rho}\overline{u_i'\frac{\partial p'}{\partial x_i}}$: Pressure fluctuation diffusion term
- $D_k^\nu = +\nu\frac{\partial^2 k}{\partial x_k \partial x_k}$: Viscous diffusion term
- $\epsilon = -\nu\overline{\frac{\partial u_i'}{\partial x_k}\frac{\partial u_i'}{\partial x_k}}$: Dissipation term
  - This term represents the rate at which turbulent kinetic energy is converted into thermal energy through viscous dissipation.
  - It is typically modeled as a function of kk and other turbulent quantities.

Note that:

- for the TKE the pressure-strain term vanishes as $tr(\phi_{ij}) = 0$;
- for homogeneous turbulence: $\frac{\partial k}{\partial t} = P_k - \epsilon$
- for isotropic turbulence: $\frac{\partial k}{\partial t} = -\epsilon$

For modeling reasons such for the $k-\epsilon$ model [142] [192], constants, dependencies and **turbulent viscosity assumption** are introduced to simplify the equation:

$$\frac{\partial k}{\partial t} + \overline{u_k}\frac{\partial k}{\partial x_k} = P_k + \underbrace{\frac{\partial}{\partial x_j}\left[\left(\nu + \frac{\nu_t}{\sigma_k}\right)\frac{\partial k}{\partial x_j}\right]}_{D_k^\nu + D_k^v} - \epsilon \tag{98}$$

Note that $P_k = \overline{u_i' u_j'}\frac{\partial \overline{u_i}}{\partial x_j}$ can become a function of the turbulent viscosity ν_t introducing the **Boussinesq hypothesis** [12] [142], that assumes the proportionality between the RST and the rate-of-strain tensor S_{ij}:

$$\overline{u_i' u_j'} = 2\nu_t S_{ij} - \frac{2}{3}k\delta_{ij} \tag{99}$$

5.1.4 Transport equation for Dissipation ϵ

Using the definition of dissipation rate given before in eq.128:

$$\epsilon = -\nu \overline{\frac{\partial u_i'}{\partial x_k} \frac{\partial u_i'}{\partial x_k}} \tag{100}$$

We can derive a transport equation for ϵ using the trasport equation for a single fluctuation as proposed by [84]:

$$\frac{D\epsilon}{Dt} = \frac{\partial \epsilon}{\partial t} + \overline{u_k} \frac{\partial \epsilon}{\partial x_k} = \underbrace{P_\epsilon^{(1)} + P_\epsilon^{(2)} + P_\epsilon^{(3)} + P_\epsilon^{(4)}}_{P_\epsilon} + T_\epsilon + V_\epsilon + \pi_\epsilon - \Upsilon_\epsilon, \quad (3) \tag{101}$$

where:

- $\frac{\partial \epsilon}{\partial t}$: **Time derivative term**
- $\overline{u_k} \frac{\partial \epsilon}{\partial x_k}$: **Advection/convection term**
- $P_\epsilon^{(1)} = nu \overline{\frac{\partial u_i'}{\partial x_m} \frac{\partial u_k'}{\partial x_m}} \left(\frac{\partial \overline{u_i}}{\partial x_k} + \frac{\partial \overline{u_k}}{\partial x_i} \right)$: **Mixed Production**
- $P_\epsilon^{(2)} = \nu \overline{\frac{\partial u_i'}{\partial x_m} \frac{\partial u_i'}{\partial x_k}} \left(\frac{\partial \overline{u_k}}{\partial x_m} + \frac{\partial \overline{u_m}}{\partial x_k} \right)$: **Production by mean velocity gradient**
- $P_\epsilon^{(3)} = \nu \overline{u_k' \frac{\partial u_i'}{\partial x_m}} \frac{\partial^2 \overline{u_i}}{\partial x_m \partial x_k}$: **Gradient production**
- $P_\epsilon^{(4)} = 2\nu \overline{\frac{\partial u_i'}{\partial x_m} \frac{\partial u_k'}{\partial x_m} \frac{\partial u_i'}{\partial x_k}}$: **Turbulent production**
- $T_\epsilon = \frac{\partial}{\partial x_k} \left(\nu \overline{u_k' \frac{\partial u_i'}{\partial x_m} \frac{\partial u_i'}{\partial x_m}} \right)$: **Turbulent diffusion**
- $V_\epsilon = \nu \frac{\partial^2}{\partial x_k^2} \left(\nu \overline{\frac{\partial u_i'}{\partial x_m} \frac{\partial u_i'}{\partial x_m}} \right)$: **Viscous diffusion**
- $\pi_\epsilon = -\frac{2}{\rho} \frac{\partial}{\partial x_k} \left(\overline{\frac{\partial u_k'}{\partial x_m} \frac{\partial p'}{\partial x_m}} \right)$: **Pressure diffusion**
- $\Upsilon_\epsilon = 2 \left(\overline{\nu \frac{\partial^2 u_i'}{\partial x_m \partial x_k}} \right)^2$: **Dissipation**

A few comments about these terms:

- Dissipation can be produced through 4 different mechanisms:
  - Mixed production term $P_\epsilon^{(1)}$ due to the correlation of fluctuating velocity gradients;
  - Production by mean velocity gradient $P_\epsilon^{(2)}$, contributing to the generation of turbulent kinetic energy;
  - Gradient production term $P_\epsilon^{(3)}$, involving the interaction between fluctuating velocity gradients and mean velocity gradients;
  - Turbulent production term $P_\epsilon^{(4)}$, related to the interaction between three fluctuating velocity gradients.
- Diffusion terms are always due to velocity fluctuations, pressure fluctuations and molecular viscosity;
- The dissipation term Υ_ϵ also called "Destruction term" represents the rate at which turbulence kinetic energy is converted into heat through viscous effects.

For modeling purposes such for the $k-\epsilon$ model [142] [192], constants (C_1, C_2) and dependencies from (k,ϵ) are introduced to simplify the equation:

$$\frac{\partial \epsilon}{\partial t} + \overline{u_k} \frac{\partial \epsilon}{\partial x_k} = \underbrace{C_1 \frac{\epsilon}{k} P_k}_{P_\epsilon} \underbrace{- C_2 \frac{\epsilon^2}{k}}_{\Upsilon_\epsilon} \underbrace{+ \nu \frac{\partial^2 \epsilon}{\partial x_k \partial x_k}}_{V_\epsilon} \underbrace{+ C_1 \frac{\epsilon}{k} \left(\frac{\partial^2 k}{\partial x_k \partial x_k} - \frac{1}{\rho} \overline{\frac{\partial p'}{\partial x_k}} \right)}_{T_\epsilon + \pi_\epsilon} \tag{102}$$

5.2 Scales of turbulent motion

Its common sense to think about turbulence as a complex and chaotic motion. Its inherent intricacies posed and continue to pose significant challenges for theoretical, experimental, and computational fluid dynamics. Understanding turbulence requires dissecting its multifaceted nature, primarily characterized by vortical structures and energy cascades spanning a wide range of scales.
In this discussion, we delve into the so-called "Scales of Turbulent Motion", where we explore the vortical essence of turbulence and the pivotal theories and equations that frame our comprehension of this chaotic phenomenon. We begin by examining the vorticity dynamics that underscore the rotational aspect of turbulent flows. Vorticity, a vector field representing the local spinning motion of the fluid, is a cornerstone in understanding the spatial and temporal evolution of turbulence.
Central is the Kolmogorov theory, which provides a statistical framework for describing turbulence. Andrey Kolmogorov's groundbreaking work [82] elucidates the energy cascade process, where kinetic energy transfers from large eddies to progressively smaller ones until dissipated by viscosity at the smallest scales. This theory introduces the concept of inertial subrange and lays the foundation for predicting turbulent behavior based on universal scaling laws.
Further, we explore the two-point correlation theory developed by Theodore von Kármán and Leslie Howarth. This theory extends our understanding by quantifying the spatial correlations of velocity fluctuations within the turbulent flow. The Kármán-Howarth equation, a cornerstone of turbulence theory, describes how these correlations evolve, providing insights into the distribution and dissipation of turbulent energy.
We then proceed to the Lin equation, which encapsulates the dynamical behavior of turbulence. This equation, derived from the Navier-Stokes equations, highlights the interplay between non-linear interactions and dissipative effects, offering a comprehensive view of turbulence dynamics.
Finally, the significance of the velocity spectra is emphasized. These functions provide a detailed representation of the energy distribution across different scales of motion, serving as a critical tool for both theoretical analysis and practical applications. By examining the spectral characteristics, we can infer the efficiency of energy transfer and the underlying mechanisms driving turbulence.
Together, these foundational concepts and theories offer a cohesive framework for understanding the scales of turbulent motion. By dissecting the vortical structures, energy cascades, and statistical correlations, we aim to unravel the complexity of turbulence and pave the way for our advanced research in porous media.

5.2.1 Vortical origin of turbulence

Already in the late 15th century, Leonardo Da Vinci started observing the chaotic behaviour of the water in a fontane (Figure 23). His series of drawings "Studies of Turbulence" meticulously depicts the swirling, spiraling motion of water as it flows and interacts with various obstacles. His sketches capture the complexity of turbulent flows, showcasing vortex formations, eddies, and the interplay of forces within fluids. For sure Leonardo was asking him-self: why the flow breaks in this structures? Why are they chaotic? Are their size and behavior somehow predictable?

Figure 23: Studies of Turbulence, Leonardo da Vinci, c.1517-1518), pen and ink on paper, located in the Royal Collection (Windsor Castle, UK).

As pointed out by Jimenez [69], the origin of turbulence can be strictly related to an excess of inertial energy than cannot stand the flow to be laminar. In fact the main parameter that characterizes flow regime is the Reynolds number Re. If we increase slowly Re, taking also into account the particular boundary conditions, we can say that under a certain critical value Re_{cr} the forcing over the flow is weak and it can be dissipated by the system while retaining its smoothness. But if Re increases beyond the point in which this ceases to be possible, instabilities appear and the system responds by fractalizing. In this way singular mechanisms are created to accomodate the higher energy input making the flow "turbulent". So basically fractalization allows to handle strong inertial sollecitation. **Vortical fractalization** refers to the process where larger vortices break down into smaller and smaller vortices in a self-similar manner. This fractal nature of turbulence means that similar structures can be observed at different scales. The fractalization process contributes to the transfer of energy from larger scales (large eddies) to smaller scales (small eddies) in turbulent flows, and leading finally to the molecular dissipation. Note that vorticity interacts with the flow its-self with a feedback loop leading to an extra complexity.
For a detailed discussion about vortical motion we recommend the already mentioned work by Jimenez [69]. Here we mention just the main concepts about vortex dynamics:

- A random vorticity distribution organizes itself after a while into a **system of roughly circular independent cores** and it can happen with different processes such as the self-circularization process or the break-up of a non uniform vortex layer.
- Vortices interact between them if close to each other in phenomena called vortex merging or vortex cascading.
- **Vortices interact with the flow** beeing influenced by the strain field **S** around, that can be generated also by a strong but far in space vortical motion.
- **A vorticity equation** can be derived from the curl of the NS momentum equation (Eq. 35 and Eq. 36):

$$\frac{D\boldsymbol{\omega}}{Dt} = \nu\nabla^2\boldsymbol{\omega} + \boldsymbol{\omega}\cdot\nabla\mathbf{U} \tag{36}$$

  3D vorticity can be amplified/damped through two main phenomena:

  - vortex stretching: represented by the term $\mathbf{S}\cdot\omega$ in Eq. 35 so that if the strain field **S** stretches/compresses the vortex, its vorticity is damped/amplified;
  - viscosity effect: represented by the term $\nu\nabla^2\omega$ in Eq. 35 so that a vortex line in a viscous fluid tends to get broader and weaker.

  That's why 2D vorticity cannot be amplified and it decays inevitably, making any two dimensional representations of turbulence a low fidelity strategy.
- **Vorticity represents the density of angular momentum** so pressure has no influence over its behavior.

5.2.2 Kolmogorov theory

As explained in Section 5.2.1, fractalization in a vaste range of vortical structures called "energy cascade" is the natural way for a flow to adapt to strong inertial sollecitations. The idea of the energy cascade (introduced by Richardson in 1922 [151]) is that kinetic energy enters the turbulence (through the production mechanism) at the largest scales of motion. This energy is then transferred (by inviscid processes) to smaller and smaller scales until, at the smallest scales, the energy is dissipated by viscous action. Kolmogorov [82] added to and quantified this picture. In particular he identified the smallest scales of turbulence through a dimensional analysis and nowadays these scales bear his name.
Let's consider a fully developed turbulent flow at high Reynolds number with characteristic velocity $\mathcal{U}$ and lengthscale $\mathcal{L}$ so that its Reynolds number $Re = \mathcal{U}\mathcal{L}/\nu$ is really large. If we consider that the range of fractalized vortices called eddies is wide so that for a generic one of size l its speed is u(l) and its timescale $\tau(l) \equiv l/u(l)$. An 'eddy' eludes precise definition, but it is conceived to be a turbulent motion, localized within a region of size l, that is at least moderately coherent over this region. The region occupied by a large eddy can also contain smaller eddies.

The eddies in the largest size range are characterized by the lengthscale l_0 which is comparable to the flow scale $\mathcal{L}$, and their characteristic velocity $u_0 \equiv u(\lambda_0)$ is on the order of the r.m.s. turbulence intensity $u' \equiv u_{rms} = (2/3k)^{1/2}$ which is comparable to $\mathcal{U}$. The Reynolds number of these eddies $Re_0 = u_0 l_0/\nu$ is therefore large (i.e., comparable to Re), so the direct effects of viscosity are negligibly small.
Richardson's notion is that the large eddies are unstable and break up, transferring their energy to somewhat smaller eddies. These smaller eddies undergo a similar break-up process and transfer their energy to yet smaller eddies. This energy cascade, in which energy is transferred to successively smaller and smaller eddies, continues until the Reynolds number $Re(l)$ defined as $Re(l) \equiv u(l)l/\nu$ is sufficiently small that the eddy motion is stable, and molecular viscosity is effective in dissipating the kinetic energy.
One reason that this picture is of importance is that it places dissipation at the end of a sequence of processes. The rate of dissipation ϵ is determined, therefore, by the first process in the sequence, which is the transfer of energy from the largest eddies. These eddies have energy of order u_0^2 and timescale $\tau_0 = l_0/u_0$, so the rate of transfer of energy can be supposed to scale as $u_0^2/\tau_0 = u_0^3/l_0$. Consequently, consistent with the experimental observations in free shear flows, this picture of the cascade indicates that ϵ scales as a u_0^3/l_0 (i.e. the kinetic energy $k_0 \propto u_0^2$ times the velocity u_0 for the energy containing eddies), independent of ν (at the high Reynolds numbers being considered):

$$\epsilon \propto \frac{k_0}{\tau_0} = \frac{u_0^3}{l_0} \tag{103}$$

The **key assumptions of Kolmogorov's theory** are:

- **Kolmogorov's hypothesis of local isotropy:**

  At sufficiently high Reynolds number, the small-scale turbulent motions ($l << l_0$) are statistically isotropic so that we can define l_{EI} as the demarcation between the anisotropic large eddies ($l > l_{EI}$) and the isotropic small eddies ($l < l_{EI}$).

- **Kolmogorov's first similarity hypothesis:** In every turbulent flow at sufficiently high Reynolds number, the statistics of the small-scale motions ($l < l_{EI}$) have a universal form that is uniquely determined by ν and ϵ so that there are (to within multiplicative constants) unique length, velocity, and time scales that can be formed:

$$\eta \equiv \left(\frac{\nu^3}{\varepsilon}\right)^{1/4}, \tag{6.1}$$

$$u_\eta \equiv (\varepsilon\nu)^{1/4}, \tag{6.2}$$

$$\tau_\eta \equiv \left(\frac{\nu}{\varepsilon}\right)^{1/2}. \tag{6.3}$$

  where η is the Kolmogorov scale that defines the very smallest, dissipative eddies defined such that the Reynolds number based on the Kolmogorov scales is unity, i.e., $\eta u_\eta/\nu = 1$

- **Kolmogorov's second similarity hypothesis:**

  In every turbulent flow at sufficiently high Reynolds number, the statistics of the motions of scale l in the range $l_0 >> l >> \eta$ have a universal form that is uniquely determined by ϵ, independent of η.

To sum up, the Kolmogorov cascade is divide in three groups of scales based on their behavior as shown in Figure 24:

1. **Large-Scale Energy Input**: Energy is injected into the fluid at large scales (large eddies) due to some external force or instability.

2. **Energy Transfer Through Scales**: The large eddies break up into smaller eddies, transferring energy to progressively smaller scales. This process continues through the inertial range.

3. **Dissipation at Small Scales**: Eventually, the energy reaches a scale where viscous forces become significant, and the energy is dissipated as heat.

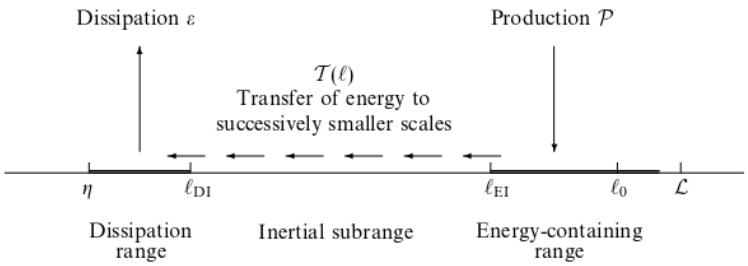

Figure 24: A schematic diagram of the energy cascade at very high Reynolds number. Reference: [142], chap.6

Note that:

$$\frac{\eta}{l_0} \simeq Re^{-3/4} \tag{104}$$

Kolmogorov proposed that within the inertial range, the rate of energy transfer per unit mass $\mathcal{T}$ is constant and denoted by ϵ (the energy dissipation rate):

$$\mathcal{T}_{EI} = \mathcal{T}_{DI} = \epsilon$$

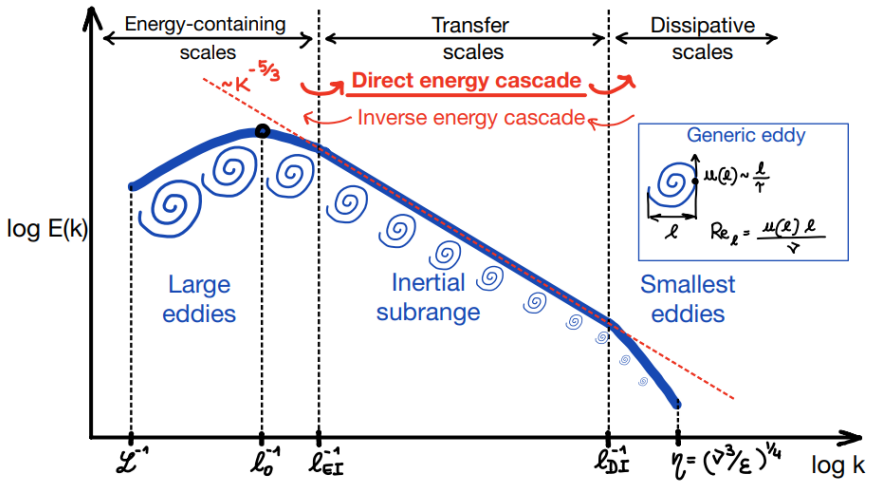

Figure 25: Schematic representation of an energy spectrum E(k) following the Kolmogorov power law $k^{-\frac{5}{3}}$, where $k = l^{-1}$ is the wavenumber $[m^1]$ and l the size of an eddy.

In his studies, Kolmogorov derived a relationship for the energy spectrum $E(k)$, which describes how the energy is distributed across different wave-numbers k (where $k \sim 1/l$ [1/m] and l [m] is the length scale). Kolmogorov's power law for the energy spectrum is given by:

$$E(k) = C\epsilon^{2/3}k^{-5/3} \tag{105}$$

where:

- $E(k)$ is the energy density at wave-number k,
- ϵ is the rate of energy dissipation per unit mass,
- k is the wave-number,
- C is a universal constant (Kolmogorov constant).

This $k^{-5/3}$ scaling is a signature of the inertial range in turbulence and is a cornerstone of turbulence theory, confirming that energy cascades from larger to smaller eddies in a predictable manner until

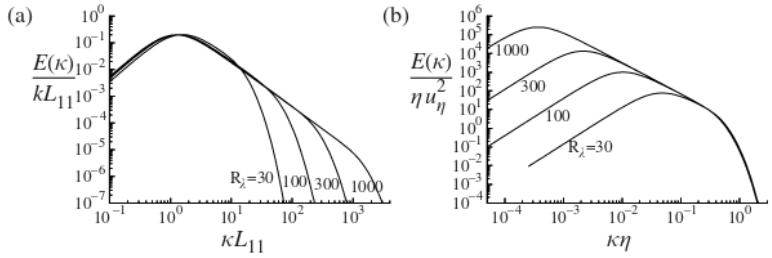

Figure 26: The model spectrum for various Reynolds numbers, scaled by (a) macroscopic scales such that $L_{11} \equiv l_0$ and $k \equiv k_0 = u_{rms}^2$, and (b) Kolmogorov scales η and u_η^2. Reference:[142], chap.6

it is eventually dissipated by viscous forces. An example of an energy spectrum under Kolmogorov assumptions is shown in Figure 25
Note that the universality at high Reynolds means that under adimensionalisation the inertial scales behave in the same manner, independent from Re as we can see in Figure 26.

5.2.3 Kolmogorov theory limitations

Kolmogorov theory represents for sure a milestone in the turbulence studies but it shouldn't never be forget that it is valid under strong assumptions, i.e. fully developed and not-bounded turbulence at sufficiently high Reynolds number.
From these assumptions we can remark the main limitations of this model:

- The magnitude of the Reynolds number for the validity of the theory is not defined and ideally it should tend to infinity. In real-life Reynolds number is finite and the existence of the inertial sub-range depends on the specific case, so that we can be confident about it only through accurate DNS or experimental measurements. In fact many laboratory and practical flows exhibit relatively high Reynolds numbers (e.g., $Re \approx 10,000$), yet even at the dissipative scales, the motions remain anisotropic [51].

- Close scrutiny of the inertial range spectra shows that the Kolmogorov $-5/3$ spectrum is approached slowly as the Reynolds number increases. From experiments on grid turbulence at quite high Reynolds number ($Re_\lambda \approx 50, 500$), Mydlarski and Warhaft (1998) [127] conclude that the inertial-range spectrum is indeed a power law, $E(\kappa) \sim \kappa^{-p}$, but that the exponent p depends on Re_λ. As the curve in Fig. 27 illustrates, it is quite plausible that p approaches 5/3 at very large Re_λ, but, at $Re_\lambda \approx 200$ (which is typical of many laboratory flows), p is around 1.5.

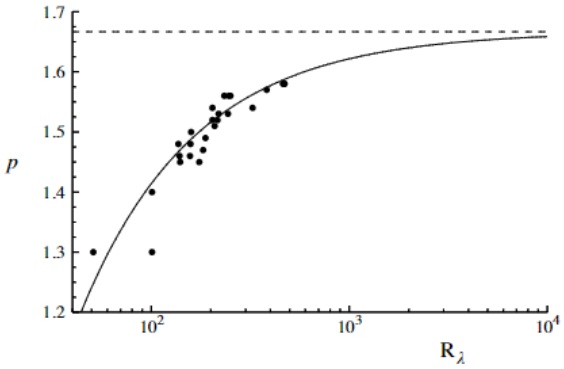

Figure 27: The spectrum power-law exponent p ($E(\kappa) \sim \kappa^{-p}$) as a function of the Reynolds number in grid turbulence: symbols represent the experimental data of Mydlarski and Warhaft (1998) [127]; the dashed line indicates $p = 5/3$; and the solid line represents the empirical curve $p = 5/3 - 8Re_\lambda^{-3/4}$.

- Kolmogorov assumes a **one-directional energy cascade** while it has been proved through experiments and DNS that the energy transfer is both to smaller (direct energy cascade) and to larger

scales (inverse energy cascade), with the net transfer being toward smaller scales. In wavenumber space, the energy transfer is accomplished by triad interactions, that is, interactions among three modes with wavenumbers $\mathbf{k}_a$ $\mathbf{k}_b$ and $\mathbf{k}_c$ such that $\mathbf{k}_a + \mathbf{k}_b + \mathbf{k}_c = 0$ (it can be proved from Eq. 117). The DNS results suggest that the transfer is predominantly local (e.g., between modes a and b with $\mathbf{k}_a \approx \mathbf{k}_b$), but that it is effected by interactions with a third mode of significantly smaller wavenumber (i.e., $\mathbf{k}_c \ll \mathbf{k}_a$). Further studies have been performed by Domaradzki [43] [42] and Zhou [203].

- **Turbulence internal intermittency** is not taken into account in the theory leading to discrepancies between the Kolmogorov predictions and the experimental values of the higher-order moments, especially for velocity derivative (see Pope, chap.6 [142]). This phenomenon is largely accounted for in the **refined similarity hypotheses** proposed by Obukhov (1962) [133], who defined the power law exponent as:

$$p = \frac{5}{3} + \frac{1}{9}\mu \tag{106}$$

  where μ is a positive value called **intermittency exponent** that is determined based on the mean-square dissipation fluctuations. See Section 5.3.4 for more details.

- Kolmogorov's theory is a **mean field theory** since it assumes that the relevant dynamical parameter is the mean energy dissipation rate. In fluid turbulence, the energy dissipation rate fluctuates in space and time, so it is possible to think of the micro-scales as quantities that also vary in space and time. However, standard practice is to use mean field values since they represent the typical values of the smallest scales in a given flow. In 1961, Kolmogorov published a refined version of the similarity hypotheses that accounts for the log-normal distribution of the dissipation rate [81].

5.3 Correlation theory

Kolmogorov assumptions, and deductions drawn from them, have no direct connection to the NS equations. It is natural, therefore, to try to extract from the NS equations useful information about the energy cascade. The earliest attempts are those of Taylor (1935) [168] and Howarth (1938) [64] which are based on the two-point correlation.

5.3.1 Correlation functions in HIT

If we consider homogeneous isotropic turbulence (HIT), the two-point correlation (Eq. 82) is only a function of the distance and time: $R_{ij}(\mathbf{r}, t)$. A consequence of the isotropy is that R_{ij} can be expressed in terms of two non-dimensional scalar functions ([142], chap.6):

$$R_{ij}(\mathbf{r}, t) \equiv u_{rms}^2 \left(g(r,t)\delta_{ij} + [f(r,t) - g(r,t)] \frac{r_i r_j}{r^2} \right) \tag{107}$$

where

- $u_{rms} \equiv \sqrt{\overline{u^2} + \overline{v^2} + \overline{w^2}}$: r.m.s. velocity perturbation that in the particular case of HIT is $u_{rms} = \overline{u^2} = \overline{v^2} = \overline{w^2} = \frac{2}{3}k$
- $f(r,t)$: longitudinal correlation function
- $g(r,t)$: transversal correlation function

$u_{rms} \equiv \sqrt{\overline{u^2} + \overline{v^2} + \overline{w^2}}$
Continuity equation eq.15 implies that $\partial R_{ij}/\partial r_j = 0$. In this way we find a relation between $f(x,t)$ and $g(x,t)$ and we can say that $R_{ij}(\mathbf{r}, t) = fun(f(r,t))$.

Why this is interesting? In the first stages of turbulence studies the determination of these two scalar functions became crucial to characterize the turbulent behavior of in HIT. That's why there are several length-scales that are derived from them:

- longitudinal integral scale:

$$L_{11}(t) \equiv \int_0^{+\infty} f(r,t)\ dr \tag{108}$$

- transversal integral scale:

$$L_{22}(t) \equiv \int_0^{+\infty} g(r,t)\, dr = L_{11}/2 \tag{109}$$

- longitudinal Taylor microscale $\lambda_f(t)$:

$$\lambda_f(t) \equiv \left[-\frac{1}{2} f''(0,t)\right]^{-1/2} \tag{110}$$

- transverse Taylor microscale $\lambda_g(t)$:

$$\lambda_g(t) \equiv \left[-\frac{1}{2} g''(0,t)\right]^{-1/2} = \lambda_f(t)/\sqrt{2} \tag{111}$$

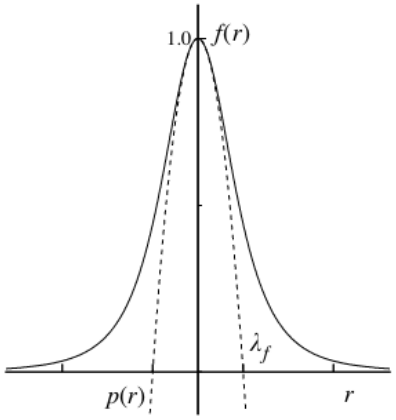

Figure 28: A sketch of the longitudinal velocity correlation function $f(r,t)$ showing the definition of the Taylor microscale $\lambda_f(r,t)$, with $p(r)$ the parabola osculating $f(r)$ at $r = 0$.

The Taylor length scale λ_g is an intermediate between the macroscales and the Kolmogorov microscales and does not have a clear physical interpretation. However, it is an easy quantity to compute and well-defined mathematically so that is often used in theoretical descriptions. Really common is the use of the Reynolds number based on λ_g so that:

$$Re_\lambda \equiv \frac{u_{rms}\lambda_g}{\nu} = \left(\frac{20}{3} Re_L\right)^{1/2} \tag{112}$$

where $Re_L = L_1 1 u_{rms}/\nu$ is the Reynolds number based on the integral length scale. The relationships between the Taylor and Kolmogorov length-scales is:

$$\lambda_g = \sqrt{10}\eta^{2/3} L^{1/3} \tag{113}$$

Note that the ratio:

$$\frac{\lambda_g}{u_{rms}} = \sqrt{15}\tau_\eta \tag{114}$$

correctly characterizes the timescale of the small eddies (Kolmogorov time-scale) [47].

5.3.2 Kármán-Howarth equation

The Kármán-Howarth equation describes the evolution of the longitudinal correlation function f(r,t). It can be obtained from the NS equations using the two-points correlation theory. For more about its derivation see the following reference [63]. The equation writes:

$$\frac{\partial}{\partial t}(u_{rms}^2 f) - \frac{u_{rms}^3}{r^4}\frac{\partial}{\partial r}(r^4 \overline{k}) = \frac{2\nu u_{rms}^2}{r^4}\frac{\partial}{\partial r}\left(r^4 \frac{\partial f}{\partial r}\right) \tag{115}$$

where:

- $\overline{k} = \overline{S_{111}}(r\mathbf{e_x}, t)/u_{rms}^3$
- $\overline{S_{ijk}}(\mathbf{r}, t) = \overline{u(\mathbf{x}, t)u(\mathbf{x}, t)u(\mathbf{x}+\mathbf{r}, t)}$

The principal observations that follow are:

- There is a closure problem. This single equation involves two unknown functions, $f(r,t)$ and $\overline{k}(r,t)$.
- The terms in $\overline{k}$ and ν represent inertial and viscous processes respectively.
- The term in $\overline{k}$ vanishes for r=0 meaning that the trasport of energy from larger to smaller scales is an inertial process (at lest for $r >> \eta$).
- There is a connection among the skewness of the velocity derivative ($\alpha\overline{k'''}$), vortex stretching, and the transfer of energy between different scales.
- If $\mathbf{u}(\mathbf{x}, t)$ were a Gaussian field then $\overline{k}(r,t) = 0$. Hence the energy cascade depends on non-Gaussian aspects of the velocity field.
- If we consider the limit $R \to +\infty$ and assume that f and $\overline{k}$ decrease sufficiently fast with r we find the so called **Loitsyanskii integral** B_2:

$$B_2 \equiv \int_0^{+\infty} u_{rms}^2 r^4 f(r,t) dr \tag{116}$$

that converges so that it is also called **Loitsyanskii invariant** because it does not change with time. The meaning of this relation is that statistically if the lengthsclaes are decreased so the velocity u_{rms} increases and viceversa. However, the assumptions made are incorrect. Depending on how the isotropic turbulence is created, the Loitsyanskii integral can be finite or it can diverge. But still the Loitsyanskii invariant presents a cornerstone in turbulence studies that makes as conscious of the difference between statistical results and local results: if we decrease the eddy size, its velocity decreases locally but statistically the number of indivual eddies increase so that the statistical behaviour says that the u_{rms} increases.

5.3.3 Lin equation: energy spectrum balance

For isotropic turbulence, the Kármán-Howarth equation (Eq.115), which stems from the Navier–Stokes equations, fully describes the dynamics of the two-point velocity correlation. It does not, however, provide a very clear picture of the processes involved in the energy cascade. Some further insights can be gained by examining the Navier–Stokes equations in wavenumber space thorough Fourier transform. This approach leading to the so-called Lin's equation that represents an evolution equation for $\hat{E}$ as derived by Pope ([142], chap.6):

$$\frac{d}{dt}\hat{E}(\kappa, t) = \hat{T}(\kappa, t) - 2\nu\kappa^2\hat{E}(\kappa, t) \tag{117}$$

where:

- $\hat{E}(\kappa, t) = \frac{1}{2}\hat{R_{ii}}(\kappa, t)$: contribution to TKE for wavenumber κ;
- $\hat{T}(\kappa, t)$: contribution to transfer of energy for wavenumber κ;
- $2\nu\kappa^2\hat{E}(\kappa, t)$: contribution to dissipation for wavenumber κ;
- $\hat{R_{ii}}(\kappa, t) =< \hat{u_i}^*(\kappa, t)\hat{u_i}(\kappa, t) >$ are the coefficients of the discrete Fourier transform of R_{ii} so that $R_{ii}(\mathbf{x}, t) = \sum_k \hat{R_{ii}} \exp(i\kappa \cdot \mathbf{r})$;
- $\mathbf{u}(\mathbf{x}, t) = \sum_k \exp(i\kappa \cdot \mathbf{x})\hat{\mathbf{u}}(\kappa, t)$ is the discrete Fourier series of a generic velocity perturbation with $\hat{u}$ the Fourier coefficients.

Note that:

- $k(t) = \sum_\kappa \hat{E}(\kappa, \mathbf{t})$: TKE;
- $\epsilon(t) = \sum_\kappa 2\nu\kappa^2\hat{E}(\kappa, \mathbf{t})$: dissipation;

- $\sum_\kappa \hat{T}(\kappa, \mathbf{t}) = 0$ thus $\hat{T}(\kappa, \mathbf{t})$ represents a transfer of energy between modes and the Lin's equation summed over all wave-numbers comes back to HIT transport equation for k such that $dk/dt = -\epsilon$
- There is a direct correspondence between Lin's equation (Eq. 117) and the Karman-Howarth equation (Eq. 115). They contain essentially the same information but are expressed differently. An advantage of the formulation in terms of Fourier modes is that it provides a clear quantification of the energy at different scales of motion, and an explicit expression for the energy-transfer rate $\hat{T}$, which plays a central role in the energy cascade, is obtained.

5.3.4 Higher order statistics and intermittency analysis

Until now we have considered only second-order velocity statistics (i.e., velocity space/time correlations R). These are the most important quantities since they determine the kinetic energy and the Reynolds stresses. But for the study of dissipation, which is a second-order statistics of the velocity derivative it makes sense to take into account higher-order statistics such as the normalized velocity-derivative moments M_n:

$$M_n = \frac{\langle \left(\frac{\partial u_1}{\partial x_1}\right)^n \rangle}{\langle \left(\frac{\partial u_1}{\partial x_1}\right)^2 \rangle^{n/2}} \tag{118}$$

For n = 3 and n = 4 these are the velocity-derivative skewness S and kurtosis K. (Recall that, for a Gaussian random variable, S is zero and K is 3.) According to the Kolmogorov hypotheses, for each n, M_n is a universal constant. However, it is found that S and K are not constant, but increase with Reynolds number as we show in Figure 29.

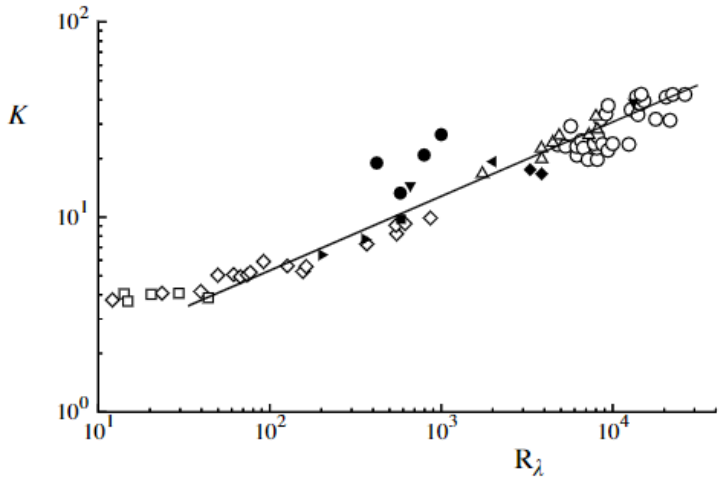

Figure 29: Measurements (symbols) compiled by Van Atta and Antonia (1980) [177] of the velocity-derivative kurtosis as a function of Reynolds number. The solid line is $K \propto R_\lambda^{3/8}$.

The velocity-derivative moments M_n (e.g., the skewness S and the kurtosis K) pertain to the dissipative range. The simplest higher-order statistics pertaining to the inertial subrange are the longitudinal velocity structure functions:

$$D_n(r) \equiv \langle (\Delta_r u)^n \rangle = \langle (U_1(x + e_1 r, t) - U_1(x, t))^n \rangle \tag{119}$$

According to Kolmogorov's second hypothesis, for inertial-range separations ($L \ll r \ll$) $D_n(r)$ depends only on ϵ and r, and hence dimensional analysis yields

$$D_n(r) = C_n(\epsilon r)_n^\chi \tag{120}$$

where $\epsilon \leq \frac{n}{3}$ and $\epsilon \to \frac{n}{3}$ for $r \to 0$ as predicted by Kolmogorov theory.
It is instructive to examine the PDFs that underlie these higher-order moments. The standardized PDF of the normalized velocity derivative $\partial u_1/\partial x_1$ is defined as:

$$Z = \frac{\partial u_1/\partial x_1}{\langle(\partial u_1/\partial x_1)^2\rangle^{1/2}} \tag{121}$$

and in Figure 30 we show the results of Van Atta & Al. [178] atmospheric boundary layer at high Re. Its exponential decay at the tails is of course much slower than that of the standardized Gaussian. Tails are rare events, however they can make vast contributions to higher moments.

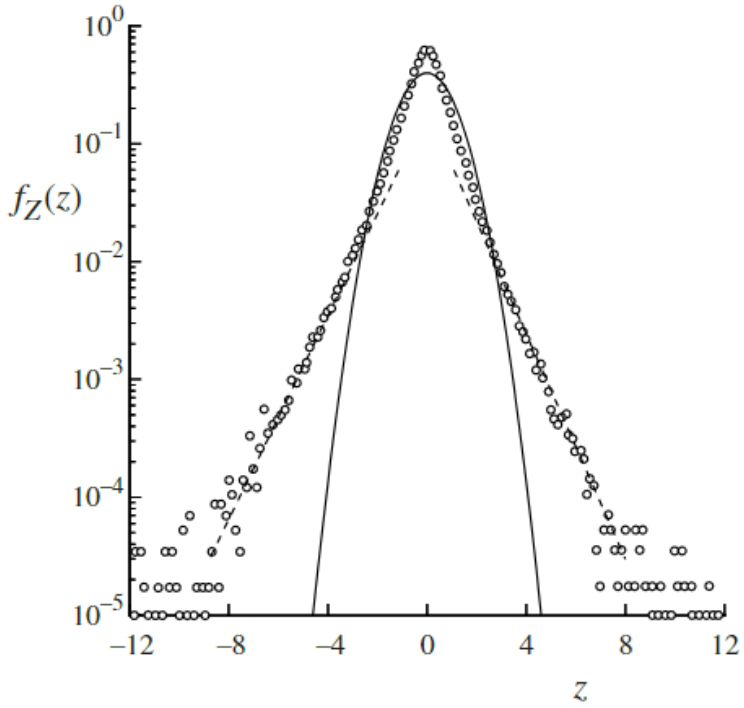

Figure 30: The PDF $f_Z(z)$ of the normalized velocity derivative Z measured by Van Atta and Chen [178] in the atmospheric boundary layer (high Re). The solid line is a Gaussian; the dashed lines correspond to exponential tails with equations $f_Z(z) = 0.2exp(1.1|z|)$, for z $>$ 4 and $f_Z(z) = 0.2exp(1.0|z|)$, for z $<$ 4.

The discrepancies between the Kolmogorov predictions and the experimental values of the higher-order moments M_n and $D_n(r)$ at high Re are attributed to the phenomenon of internal intermittency, and are largely accounted for in the refined similarity hypotheses proposed by Obukhov [133].
The instantaneous dissipation $\epsilon_0(x,t)$ is defined as:

$$\epsilon_0 = 2\nu s_{ij} s_{ij}, \tag{122}$$

where ν denotes the kinematic viscosity, and s_{ij} represents the strain-rate tensor components. For a given distance r, the average of ϵ_0 over a sphere $V(r)$ of radius r is expressed by:

$$\epsilon_r(x,t) = \frac{3}{4\pi r^3} \int\int\int_{V(r)} \epsilon_0(x+r,t)\, dr \tag{123}$$

However, direct measurement of ϵ_0 and ϵ_r is often impractical. Therefore, one-dimensional surrogates are typically employed. These surrogates are defined as:

$$\hat{\epsilon}_0 = 15\nu \left(\frac{\partial u_1}{\partial x_1}\right)^2 \tag{124}$$

$$\hat{\epsilon}_r(x,t) \equiv \frac{1}{r} \int_0^r \hat{\epsilon}_0(x+e_1 r,t)\, dr \tag{125}$$

In the context of locally isotropic turbulence, each of these quantities is assumed to have a mean value of ϵ. Although the statistics of ϵ_0 and $\hat{\epsilon}_0$ are generally believed to be qualitatively similar, significant quantitative differences are known to exist. Historical experiments revealed that the instantaneous

dissipation $\hat{\epsilon}_0$ can intermittently reach extremely large values. Moreover, the peak value of $\hat{\epsilon}_0/\epsilon$ is observed to increase with the Reynolds number. For instance, Meneveau and Al. (1991) [116] reported a peak value of $\hat{\epsilon}_0/\epsilon \approx 15$ in laboratory experiments with moderate R_λ, while a corresponding value of 50 was observed in the atmospheric surface layer with higher R_λ.
Kolmogorov hypothesized that the mean-square dissipation fluctuations scale as:

$$\frac{\langle \epsilon_0^2 \rangle}{\epsilon^2} \sim \left(\frac{L}{\eta}\right)^\mu \tag{126}$$

Similarly,

$$\frac{\langle \epsilon_r^2 \rangle}{\epsilon^2} \sim \left(\frac{L}{r}\right)^\mu, \quad \text{for } \eta < r \ll L \tag{127}$$

where μ is a positive constant known as the intermittency exponent. Experiments have confirmed the validity of Eq. 127 for the surrogate $\hat{\epsilon}_r$, and have determined $\mu = 0.25 \pm 0.05$ [162].
Note that $\frac{\langle \hat{\epsilon}_0^2 \rangle}{\epsilon^2}$ is equivalent to the velocity-derivative kurtosis K.

5.4 Energy spectrum theory

The velocity-spectrum tensor is defined for homogeneous turbulence as the Fourier transform of the two-point correlation tensor $R_{ij}(r,t)$ as describe in Section 4.5:

$$\phi_{ij}(\kappa,\mathbf{x},t) \equiv \frac{1}{(2\pi)^3}\iiint_{-\infty}^{+\infty} R_{ij}(\mathbf{r},\mathbf{x},t)\exp\left(-i\kappa\cdot\mathbf{r}\right)\,d\mathbf{r} \tag{84}$$

where $\kappa = (\kappa_x,\kappa_y,\kappa_z)$ is the wavenumber vector. This tensor is of great significance as it represents the Reynolds-stress density in spectral space.
Although the tensor Φ_{ij} contains a wealth of information as it is a matrix of a vector field, it can be challenging to manipulate, particularly for qualitative discussions on turbulence. To simplify analysis, a more accessible variable, the energy spectrum function $E(\kappa)$, is often employed as already mentioned in Eq 73. This function represents the kinetic energy density per wavenumber, with units of $\left[\mathrm{m}^3\cdot\mathrm{s}^{-2}\right] = \left[\mathrm{m}^2\cdot\mathrm{s}^{-2}\cdot\mathrm{m}^{-1}\right]$. It is derived from Φ_{ij} by eliminating directional information—taking half the trace of Φ_{ij} and integrating over the surface of a sphere S of radius $\kappa = ||\kappa||_2$ [142]:

$$E(\kappa) = \int_S \frac{1}{2}\Phi_{ii}(\kappa)\,dS(\kappa) \tag{73}$$

where $\Phi_{ii} = \Phi_{11} + \Phi_{22} + \Phi_{33}$ is the trace of Φ_{ij}. As illustrated in Equation 73, the energy spectrum function is significantly simpler than Φ_{ij} since it is a scalar function of a scalar. The primary advantage of using $E(\kappa)$ lies in its ability to encapsulate all the information characterizing turbulent structures in a homogeneous isotropic turbulence (HIT) field. In fact, knowing the energy spectrum function determines the type of HIT field generated. Under HIT assumptions, it can be shown that:

$$k = \int_0^\infty E(\kappa)\,d\kappa \tag{128}$$

$$\epsilon = 2\nu\int_0^\infty \kappa^2 E(\kappa)\,d\kappa \tag{129}$$

$$L_0 = \frac{\pi}{2u_{\mathrm{rms}}^2}\int_0^\infty \frac{E(\kappa)}{\kappa}\,d\kappa \tag{130}$$

where ϵ and L_0 are the dissipation rate of turbulence and the longitudinal integral length scale of the HIT field, respectively. From the quantities defined in Equations (128), (129), and (130), two additional significant quantities can be derived:

$$\tau_\varepsilon = \frac{L_0}{u_{\mathrm{rms}}} \tag{131}$$

$$Re_t = \frac{u_{\mathrm{rms}}L_0}{\nu} \tag{132}$$

where τ_ε and Re_t are the large eddies turnover time and the turbulent Reynolds number, respectively.
The following sections are dedicated to two specific examples of energy spectrum functions under the assumption of HIT (where $Re_t \to \infty$ so that $k = \frac{3}{2}u_{rms}^2$): the Passot-Pouquet spectrum [138] and the von Karman-Pao spectrum [136].

5.4.1 Passot-Pouquet Energy Spectrum Function

The Passot-Pouquet (PP) energy spectrum function is used to characterize turbulent flows based on a given turbulent intensity u_{rms} and a characteristic length scale L_e. It is defined by:

$$E(\kappa) = A\left(\frac{\kappa}{\kappa_{e,PP}}\right)^4 \exp\left(-2\left(\frac{\kappa}{\kappa_{e,PP}}\right)^2\right) \tag{133}$$

where $\kappa_{e,PP} = \frac{2\pi}{L_e}$ and A is a constant determined by ensuring that the spectrum satisfies the normalization condition (HIT assumption):

$$\int_0^\infty E(\kappa)\,d\kappa = \frac{3}{2}u_{rms}^2 \tag{134}$$

Solving for A, we obtain:

$$A = \frac{16u_{rms}^2}{\kappa_{e,PP}\sqrt{2\pi}} \tag{135}$$

In the PP spectrum, $\kappa_{e,PP}$ represents the wavenumber at which $E(\kappa)$ reaches its maximum. This indicates that L_e corresponds to the size of the most energetic structures within the PP spectrum. Using the provided equations, the dissipation rate ϵ_{PP} and the integral length scale $L_{0,PP}$ for the PP spectrum are given by:

$$\epsilon_{PP} = \frac{15}{4}\nu u_{rms}^2 \kappa_{e,PP}^2 \tag{136}$$

$$L_{0,PP} = \sqrt{2\pi}\frac{1}{\kappa_{e,PP}} \tag{137}$$

The PP spectrum accurately describes the large eddies (low κ values) in turbulence, but it does not account for the smaller eddies (high κ values). Therefore, it is most suitable for use in cases where the Reynolds number is relatively low, although not low enough to be laminar, and in comparison to highly turbulent flows.

5.4.2 von Karman-Pao Energy Spectrum Function

As with the PP spectrum, the von Karman-Pao (VKP) energy spectrum is defined in terms of turbulent intensity u_{rms} and a characteristic length denoted L_e. The VKP energy spectrum is given by:

$$E(\kappa) = \alpha\frac{u_{\text{rms}}^2}{\kappa_{e,\text{VKP}}}\left(\frac{\kappa}{\kappa_{e,\text{VKP}}}\right)^4\left(1+\left(\frac{\kappa}{\kappa_{e,\text{VKP}}}\right)^2\right)^{-17/6}\exp\left[-2\left(\frac{\kappa}{\kappa_{\text{Kol}}}\right)^2\right] \quad (6.62) \tag{138}$$

where α, $\kappa_{e,\text{VKP}}$, and κ_{Kol} are constants that can be determined in two ways:

- under the assumption of $Re \to \infty$ that leads to $\left(\frac{\kappa_{\text{Kol}}}{\kappa_{e,\text{VKP}}}\right)^2 \to \infty$ [113]:

  This is the classical approach followed also by Pao him self[136]. The constant α is obtained by enforcing that the integral of the spectrum equals the TKE in HIT conditions, and is that

  $$\int_0^\infty E(\kappa)d\kappa = \frac{3}{2}u_{\text{rms}}^2 \quad \Longleftrightarrow \quad \alpha = \frac{55\Gamma(5/6)}{9\sqrt{\pi}\Gamma(1/3)} \approx 1.453 \tag{139}$$

  where Γ is the gamma function [49] $\Gamma(z) = \int_0^\infty t^{z-1}e^{-t}\,\mathrm{d}t, \quad \Re(z) > 0$. This value of α

  The characteristic wavenumber $\kappa_{e,\text{VKP}}$ satisfies the expression:

  $$L_e = \frac{\pi}{2u_{\text{rms}}^2}\int_0^\infty \frac{E(\kappa)}{\kappa}d\kappa \tag{140}$$

  yielding, under the usual assumption $\left(\frac{\kappa_{\text{Kol}}}{\kappa_{e,\text{VKP}}}\right)^2 \to \infty$:

  $$\kappa_{e,\text{VKP}} = \frac{9\pi\alpha}{55L_e} \tag{141}$$

  Thus, for the VKP spectrum, the input characteristic length L_e is the longitudinal integral length scale L_f.

  Finally, κ_{Kol} is obtained by solving the following system for κ_{Kol} and ϵ:

  $$\kappa_{\text{Kol}} = \left(\frac{\epsilon}{\nu^3}\right)^{1/4} \tag{142}$$

  $$\epsilon = 2\nu\int_0^\infty \kappa^2 E(\kappa)d\kappa \tag{143}$$

Combining Eqs.142 and 143 in the limit $\left(\frac{\kappa_{\mathrm{Kol}}}{\kappa_{e,\mathrm{VKP}}}\right)^2 \to \infty$ gives an expression for ϵ_{VKP}:

$$\epsilon_{\mathrm{VKP}} = [\alpha\Gamma(2/3)]^{3/2}\,\kappa_{e,\mathrm{VKP}}^2 u_{\mathrm{rms}}^3 \quad (6.67) \tag{144}$$

and κ_{Kol} is deduced from Eq. 142.

It is often noted that ϵ_{VKP} is simply computed by:

$$\epsilon_{\mathrm{VKP}} = \frac{u_{\mathrm{rms}}^3}{L_e} \quad (6.68) \tag{145}$$

Additionally, it should be noted that the maximum energy occurs at the wavenumber $\sqrt{\frac{12}{5}}\kappa_{e,\mathrm{VKP}}$ and not at κ_e as for the PP spectrum:

$$L_{e_{max},VKP} = \sqrt{\frac{5}{12}} L_{e,VKP} \tag{146}$$

- fixing Re, still large but finite:

  This is the approach that we use to set our simulation. We fix the values of $L_{e_{max},VKP}$ through Eq. 146 wherethe defined size of the energy containing eddies $L_{e_{max},VKP}$ is given and we fix also the u_rms defining a desired turbulence rate at the inlet $Tu = u_{rms}/|U_{in}|$. In this way the only free parameters in our simulation are $\kappa_{e,VKP}/\kappa_{Kol}$ and α and we can set an optimization problem such that:

$$E_{VTK}(\kappa_{e,VKP}/\kappa_{Kol}, \alpha) \quad \text{so that} \quad min(\epsilon_L + \epsilon_k) \tag{147}$$

  where the VTK energy spectrum function is optimized so that the relative errors on the injection scale length ϵ_L and on the TKE ϵ_k are minimized:

  - $\epsilon_L = |L_{e_{max},VKP} - \pi/(2u_{rms}^2) \int E_{VKP}(\kappa)/\kappa d\kappa|/L_{e_{max},VKP}$
  - $\epsilon_k = |\int E_{VKP}(\kappa)d\kappa - 3/2 * u_{rms}^2|/u_{rms}^2$

  In this way we can get closer to the ideal theory based on the HIT assumption.

  Note that the value of $\alpha = \alpha_{True}$ computed in this way is not the value that we should put defining the VKP spectrum where the value of this parameter $\alpha = \alpha_{JAG} \neq \alpha_{True}$ is fixed by the relation in Eq. 139. Instead we should consider that the "true" values calculated through the minimization process proposed are related to the values that we set in JAGUAR as follows:

$$u_{rms,JAG} = \sqrt{\frac{\alpha_{True}}{\alpha_{JAG}}} u_{rms,True} \tag{148}$$

Finally, the VKP spectrum can represent both the large and small turbulent structures. From a numerical perspective, it is a more realistic spectrum than the one from Passot and Pouquet, but it requires better mesh resolution to capture the small scales.

5.5 Turbulence analysis tools

There are different ways to analyze the properties of turbulence. Here we list the most used ones and in the following paragraphs we detail from a practical standpoint some of these tools:

- **2 points space-correlation theory**: length-scales, PSD analysis in spatial frequency (or wave-number) domain
- **2 points time-correlation theory**: time-scales, PSD analysis in temporal frequency domain
- **Integral scales analysis**: relationship between length-scales and time-scales
- **PSD (Power Spectral Density) analysis**, derived from space and time correlations
- **Higher order statistics and intermittency analysis**: velocity derivative moments and velocity structure functions
- **Coherent structures analysis** (vorticity, Q-criterion, Δ-criterion, λ_2-criterion)
- **Anisotropy analysis**: Lumley triangle
- **Quadrant/Octant analysis**
- **Multiscale homogeneization analysis**
- **Cyclostationarity analysis**

5.5.1 2 points-space correlation theory

As already discussed in section 4.5, space correlations are the best way to have directional information about turbulence as they help in understanding the spatial distribution and organization of flow structures within the flow. Analyzing spatial correlations can reveal the relationships and interactions between these structures, providing insights into the fundamental nature of turbulence. We remind those tools in Table 5.5.3.

5.5.2 2 points time-correlation theory

As already discussed in section 4.5, time correlations are the best way to have frequency information about turbulence because they help in understanding the temporal dynamics of the turbulent flow and so how the turbulent flow evolves over time, revealing patterns and structures that are otherwise hidden in instantaneous snapshots. We remind those tools in Table 5.5.3.

5.5.3 PSD analysis

Based on the space and time correlations, it becomes really useful to analyze the same functions in the wavelength and frequency spectrum, to have more information about the scales involved and their contributions to the total energy balance. Usually we look at the isotropic energy spectrum in wave-number domain Eq. 73 and at the energy spectrum in time-frequency domain Eq. 78. If the anisotropy is strong it makes sense to analyze the directional energy spectra in wave-number domain Eq. 72 for each auto- and cross-correlation.
Note that it can be interesting also to look at:

- The pre-multiplied energy spectrum $\kappa E(\kappa)$, which provides a clearer picture of how the energy is distributed among different scales, especially for the peak identification (dominant scale or range of scales that contain the most energy).
- The dissipation spectrum $D(\kappa) = 2\nu\kappa^2 E(\kappa)$, which provides insight into how the kinetic energy of the flow is converted into thermal energy by viscous forces at different scales. The peak indicates the scales where most of the dissipation occurs.

In figures 32 and 31 we give a concrete example of how this spectra look like for a probe inside the porous media in our simulations. In this work, we compute the frequency spectrum using the Fast Fourier Transform (FFT) in combination with Welch's method to minimize noise, utilizing Blackman windowing for tapering the signal. This approach provides an accurate representation of the energy distribution across frequencies, ensuring a smooth and reliable spectrum analysis.

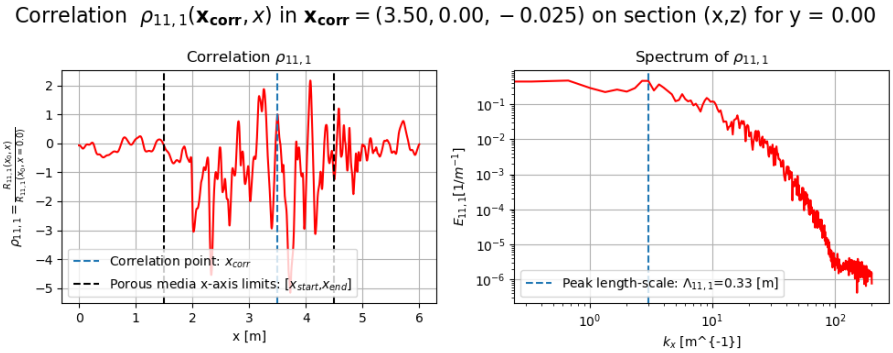

Figure 31: Example of energy spectrum $E_{11,1}$ for a probe inside the porous media. Simulation: Gyroid struct=1.20 at Re=2500 in Section 7.3.

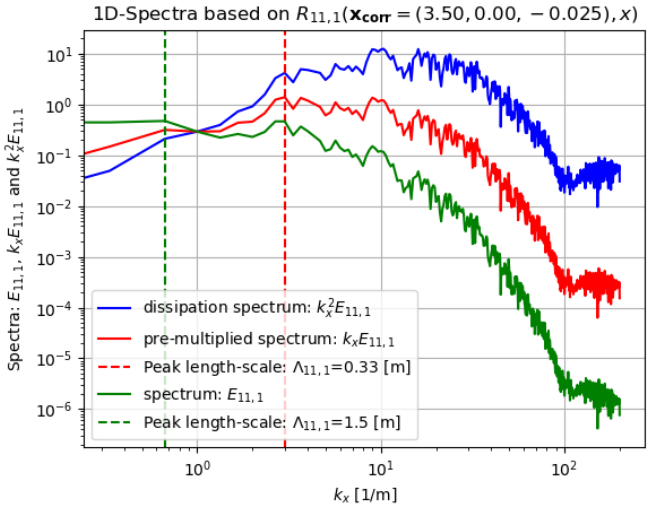

Figure 32: Example of energy spectrum $E_{11,1}$, pre-multiplied energy spectrum $k_x E_{11,1}$ and dissipation spectrum $k_x^2 E_{11,1}$ for a probe inside the porous media. Simulation: Gyroid struct=1.20 at Re=2500 in Section 7.3.

Space-correlations

In space domain $\mathbf{x}$:

- two-points space-covariance:

$$R_{ij}(\mathbf{r},\mathbf{x},t) \equiv < u_i(\mathbf{r},\mathbf{x},t)u_j(\mathbf{r},\mathbf{x},t) > \tag{81}$$

- two-points space-covariance (along k-axis):

$$R_{ij,k}(r,\mathbf{x},t) \equiv < u_i(r\hat{e_k},\mathbf{x},t)u_j(r\hat{e_k},\mathbf{x},t) > \tag{81}$$

- two-points space-correlation:

$$\rho_{ij}(\mathbf{r},\mathbf{x},t) \equiv \frac{R_{ij}(\mathbf{r},\mathbf{x},t)}{R_{ij}(0,\mathbf{x},t)} = \frac{< u_i(\mathbf{r},\mathbf{x},t)u_j(\mathbf{r},\mathbf{x},t) >}{< u_i(\mathbf{r},\mathbf{x},t)u_j(\mathbf{r},\mathbf{x},t) >} \tag{82}$$

- integral length-scale:

$$L_{ij,k} = \int_0^{+\infty} \rho_{ij}(r\hat{e_k},\mathbf{x},t)\ dr \tag{83}$$

In wave-number domain κ:

- velocity spectrum:

$$\phi_{ij}(\kappa,\mathbf{x},t) \equiv \frac{1}{(2\pi)^3} \iiint_{-\infty}^{+\infty} R_{ij}(\mathbf{r},\mathbf{x},t) \exp\left(-i\kappa\cdot\mathbf{r}\right)\ d\mathbf{r} \tag{84}$$

- energy spectrum (isotropic definition) [142]:

$$E(\kappa) = \oint_S \frac{1}{2} tr(\Phi_{ij}(\mathbf{k},t))\, dS(\kappa) \tag{73}$$

  where S is the surface of the sphere of radius $\kappa = ||\mathbf{k}||_2$

- energy spectrum (along k-axis):

$$E_{ij,k}(\kappa_k,\mathbf{x},t) \equiv \frac{1}{\pi}\int_{-\infty}^{+\infty} R_{ij,k}(r,\mathbf{x},t)\exp\left(-i\kappa_k r\right) dr = \frac{2}{\pi}\iint_{-\infty}^{+\infty} \phi_{ij}(\kappa,\mathbf{x},t)\, dr_h dr_q \tag{72}$$

  with $h,q \neq k \vee h \neq q \vee h,k,q = 1,2,3$

- energy spectrum meaning (isotropic definition):

$$k \equiv \frac{1}{2}\langle u_i u_i\rangle = \frac{1}{2}R_{ii}(0,t) = \int_0^{\infty} E(\kappa,t)\, d\kappa, \tag{85}$$

- energy spectrum meaning (along k-axis):

$$R_{ij,k}(0,\mathbf{x},t) = 2\int_0^{\infty} E_{ij,k}(\kappa_k,\mathbf{x},t)\, d\kappa \tag{86}$$

with $i,j = 1,2,3$ such that $\{u_1,u_2,u_3\} = \{u,v,w\} = \mathbf{U} - < \mathbf{U} >$ are the velocity fluctuations and $k = 1,2,3$ so that $\mathbf{e} = e_1,e_2,e_3$ as the unit vectors in the x-axis, y-axis and z-axis direction respectively.
If statistically homogeneous random process: $R_{ij}(\mathbf{r},\mathbf{x},t) = R_{ij}(\mathbf{r},t)$

Time-correlations

For a statistical stationary random process: $R_{ij}(\mathbf{x}, t, \tau) = R_{ij}(\mathbf{x}, \tau)$.
In time domain t:

- two-points time-covariance:

$$R_{ij}(\tau) \equiv < u_i(t) u_j(t+\tau) > \tag{75}$$

- two-points time-correlation:

$$\rho_{ij}(\tau) \equiv \frac{R_{ij}(\tau)}{R_{ij}(0)} = \frac{< u_i(t) u_j(t+\tau) >}{< u_i(t) u_j(t) >} \tag{76}$$

- integral time-scale:

$$\bar{\tau_{ij}} \equiv \int_0^\infty \rho_{ij}(\tau),\ d\tau \tag{77}$$

In frequency domain $\omega = 2\pi f$:

- energy spectrum:

$$E_{ij}(\omega) \equiv \frac{1}{\pi} \int_{-\infty}^{+\infty} R_{ij}(\tau) \exp(-i\omega s),\ d\tau = \frac{1}{\pi} \int_0^{+\infty} R_{ij}(\tau) \cos \omega s,\ d\tau \tag{78}$$

- energy spectrum meaning:

$$R_{ij}(0) \equiv < u_i(t) u_j(t) >_T = \int_0^{+\infty} E_{ij}(\omega),\ d\omega \tag{79}$$

with $i, j = 1, 2, 3$ such that $\{u_1, u_2, u_3\} = \{u, v, w\} = \mathbf{U} - < \mathbf{U} >$ are the velocity fluctuations.

5.5.4 Integral scales

In the turbulent work-frame, integral scales defined from auto- or cross- correlations in space $L_{ij,k}$ and time $\hat{\tau}_{ij}$ are considered to be characteristic of the largest motions of a turbulent flow, and as such, they represent an input parameter in modern and classical approaches of turbulence theory and numerical simulations. We remind that for the classical theory [142]:

$$\text{integral length-scale: } L_{ij,k}(\mathbf{x}) = \int_0^{+\infty} \rho_{ij,k}(r\hat{e_k}, \mathbf{x}, t)\ dr \tag{83}$$

$$\text{integral time-scale: } \hat{\tau}_{ij}(\mathbf{x}) = \int_0^{+\infty} \rho(\tau, \mathbf{x})\ d\tau \tag{77}$$

Being integral values depending on statistical functions (auto- or cross- correlations) the integral scales values need to be carefully computed, especially when the configuration of the problem is not the classical HIT in a large domain. Different works focus most on the determination of a meaningful integral length-scale rather than on the integral time-scale, because the latter represents the integration of a time signal which has been widely treated in the literature.
The main points to underline about the computation of the integral length-scale $L_{ij,k}$ are:

- In practice the integration domain is never infinite, so it is better to define the integral length-scale $L_{ij,k}$ between [0,r], where r is the max distance available in our experimental or numerical measurements:

$$\text{integral length-scale: } L_{ij,k}(\mathbf{x}) = \int_0^{r} \rho_{ij,k}(r\hat{e_k}, \mathbf{x}, t)\ dr \tag{149}$$

What is the influence of r over the computation of $L_{ij,k}$?
It has been shown by O'Neill et al. [132] that the integral length-scales have an asymptotic behavior for a domain size r bigger than 6 times the integral-scale its-self. So an estimation of the latter should be made a priori. Moreover the same authors proved that higher Reynolds numbers (based on the Taylor length-scale) reduce the domain requirements but a systematic law hasn't been found. This observation opened the doors to further studies over the relationship between the Reynolds number and the integral length-scale, especially in anisotropic flows [20] [29].

- In an anisotropic flow, it makes sense to define directional integral length-scales as pointed out by Carlotti & Drobinski [29], especially in wall-bounded flows at high Reynolds numbers. For example, they define an inward ($z-$) and an outward($z+$) integral length-scales as follows, considering the correlation in the normal wall direction $\hat{e_3}$ with r the normal distance from the wall:

$$L_{ij}^{z-} = \int_0^z \rho_{ij,3}(\mathbf{x}, r\hat{e_3})dr L_{ij}^{z+} = \int_z^{+\infty} \rho_{ij,3}(\mathbf{x}, r\hat{e_3})dr \tag{150}$$

- In practice, auto- and cross- correlation functions can have complex shapes due to anisotropy, inhomogeneity, experimental/numerical measurements, domain limitations, etc. so that their shape is far from the ideal gaussian shape expected. That's why the computation of the lenght-scale is not unique and it can get ambiguous sometimes. In fact, the computed discrete correlation functions usually have negative values and strong oscillations on the tails of their distribution. Several ways of computing in a more systematic way this length have been proposed. We can mainly see three big families of methods:

  – correlation integral methods [172]:
  These include: integrating up to the first zero crossing; integrating up to a minimum value of the correlation function; integrating up to the value where the correlation falls below 1/e or via standard Kolmogorov scalings. Puga & LaRue [144] have recommended estimating the integral length scale as:

$$L = \int_0^{r_0} \rho(r)\, dr \tag{151}$$

  with $r_0 = U\tau_0 = U\tau\,(\rho(\tau) = \delta)$. The parameter δ quantifies the dispersion on the estimation of $\rho(r)$. It is usually found by averaging different segments extracted from the velocity time signal. Therefore, when $\int_0^{r_0} \rho(r)\, dr$ is estimated by this method, δ plays an important role in the value of L obtained. Nevertheless, the choice of δ is ambiguous as it strongly depends on the averaging chosen for the computation of $\rho(r)$.

  – velocity fluctuation methods [124]:
  To overcome the unusual shape of the correlation function especially when not crossing zero, some methods have been developed arounbd the zero crossing of the primitive function of the correlation consider, inn other words the velocity fluctuation itself.

  – power spectral methods [172]:
  Spectral techniques define the integral turbulence length scale as the vortex size corresponding to the maximum spectral energy. In order to determine the length scale, the time scale corresponding to the frequency with the maximum energy in the spectrum (i.e. peak frequency) is used. The peak frequency is obtained from the fitting of spectral turbulence models to the measured turbulence spectrum.

In our work, we utilize a refined correlation integral method known as the **Zero-crossing Peak Integration Method (Z-PIM)** to enhance the accuracy of turbulence correlation functions before integration. As illustrated in Figure 33, this method involves two essential steps to modify the raw correlation data. First, we apply:

1. **gradient change peak extraction**,

   which identifies points of significant gradient changes, allowing us to capture critical peaks in the correlation function that are most indicative of the turbulent flow behavior.

2. Second, we use **zero-crossing removal**,

   a technique that eliminates the less informative parts of the function around zero-crossings, which could otherwise introduce noise or distortions into the integration process.

These steps together ensure that the integral focuses on the most relevant parts of the correlation function, providing a cleaner and more accurate representation of the turbulence dynamics, that allows especially to avoid strong correlations between pores if the simulations is not fully converged at low frequencies, which are the slowest ones (and so the most computationally demanding).

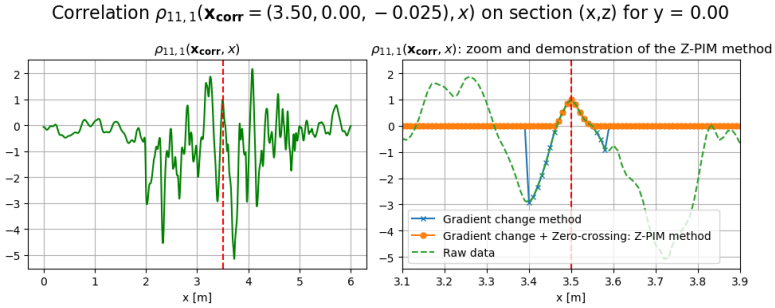

Figure 33: Demonstration of the Z-PIM method showing the gradient change peak extraction and zero-crossing removal on a turbulence correlation function.

5.5.5 Coherent Structures in Turbulence

In turbulence, a coherent structure is defined as a connected volume with a physical property α that satisfies a certain threshold criterion τ:

$$\alpha(\mathbf{x}) \geq \tau \tag{152}$$

where α usually is a vorticity or strain derived quantity of the type $\frac{\omega'}{|\omega|}$ or $\frac{S'}{|S|}$.
In most of the cases the attention is focus on vortex clusters that are identified as coherent structures where the physical property can be chosen between:

- **Q-criterion**:

  It identifies vortices based on the balance between the rates of rotation and strain. It is defined as:

  $$Q = \frac{1}{2}\left(\|\mathbf{\Omega}\|^2 - \|\mathbf{S}\|^2\right) \tag{153}$$

  A vortex is considered to exist where $Q > 0$, meaning the rotational effects dominate over the strain effects.

- **Δ-criterion**:

  It identifies vortices based on the discriminant of the characteristic polynomial of the velocity gradient tensor $\nabla\mathbf{u}$. It is defined by solving for the eigenvalues λ of the tensor and determining the discriminant Δ:

  $$\Delta = \left(\frac{p}{3}\right)^3 + \left(\frac{q}{2}\right)^2 \tag{154}$$

  where p and q are coefficients of the characteristic polynomial:

  $$\lambda^3 + p\lambda + q = 0$$

  For a vortex to exist needs $\Delta > 0$ that indicates complex conjugate eigenvalues, implying rotational motion or vortices.

- λ_2**-criterion**:

  The λ_2-criterion identifies vortices by examining the second-largest eigenvalue (λ_2) of the tensor $\mathbf{S}^2 + \mathbf{\Omega}^2$. The criterion defines a vortex as a region where $\lambda_2 < 0$:

$$\mathbf{T} = \mathbf{S}^2 + \mathbf{\Omega}^2 \tag{155}$$

  where λ_2 is the second eigenvalue of $\mathbf{T}$. For a vortex to exist needs $\lambda_2 < 0$, meaning that the pressure is locally lower in the vortex core, indicating the presence of a vortex.

A brief comparison between the proposed physical properties to use for vortex clusters identification:

- Q-criterion: Simple and widely used due to its straightforward physical interpretation. It balances rotation and strain, making it suitable for identifying regions where rotational effects dominate.
- Δ-criterion: More mathematically complex, considering the discriminant of the characteristic polynomial, useful for identifying regions with complex eigenvalues, indicative of swirling motion.
- λ_2-criterion: Physically intuitive as it directly relates to the pressure minimum in vortices. It is effective in isolating vortex cores by focusing on the second-largest eigenvalue of the combined rate of strain and vorticity tensor.

Coherent strctures have been the focus of recent works by Aztori & Vinuesa [8] [7]. They described two different cases: HIT turbulence and wall-bounded turbulence.

- **HIT turbulence**:

  We can find two main types of clusters with inertial size:

  - vorticity structures, energy containing with dimension ratios between $1:2:8$ and $1:1:10$
  - strain structures, dissipation containing with dimension ratios between $1:5:8$ and $1:2:8$

- **Wall-bounded turbulence**:

  Turbulence close to wall is more complex as the wall segregation creates a strong in-homogeneity in the wall-normal direction (y^+), leading to a turbulent Reynolds number that becomes lower as far as we get closer to the wall. So basically we can see the turbulence as main of different layers parallel to the wall. In reality the coherent structures are more complex then that because the wall-segregation creates also strong diffusive phenomena. The main structures that have been recognized until today are well described in [8] and [142]:

  - **streaks** ($y^+ < 15$): low speed stream-wise moving flow with a characteristic behavior, known as bursting. With increasing downstream distance, a streak migrates slowly away from the wall; but then, at some point (typically around $y^+ \simeq 10$), it turns and moves away from the wall more rapidly, a process referred to as "streak lifting",or **ejection**. As it is lifted, the streak exhibits a rapid oscillation followed by a breakdown into finer-scale motions. With fluid moving away from the wall in ejections, continuity demands a flow toward the wall in some other regions. These regions of high-speed fluid moving toward the wall in events called **sweeps**.
  - **rolls** ($y^+ < 100$): counter-rotating stream-wise vortices.
  - **hairpin vortices** ($y^+ > 100$): large scale vortical structures.
  - **viscous superlayer** ($y^+ > 100$): the delimitation structures between the hairpins and the non-turbulent flow.

5.5.6 Anisotropy analysis: barycentric and anisotropy-invariant maps

There are two main tools to analyse and visualize the anisotropy of a turbulent flow:

- **anisotropy-invariant map** (or simply Lumley triangle): mapping of the anisotropy tensor invariants
- **barycentric map**: mapping of the anisotropy tensor eigenvalues

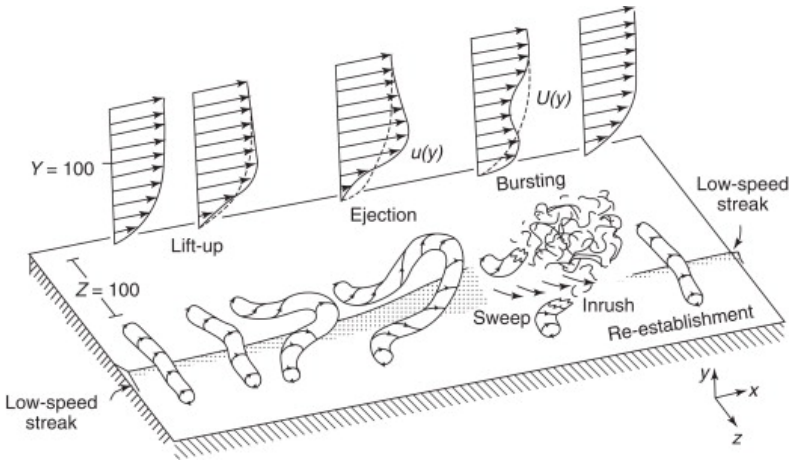

Figure 34: Caption

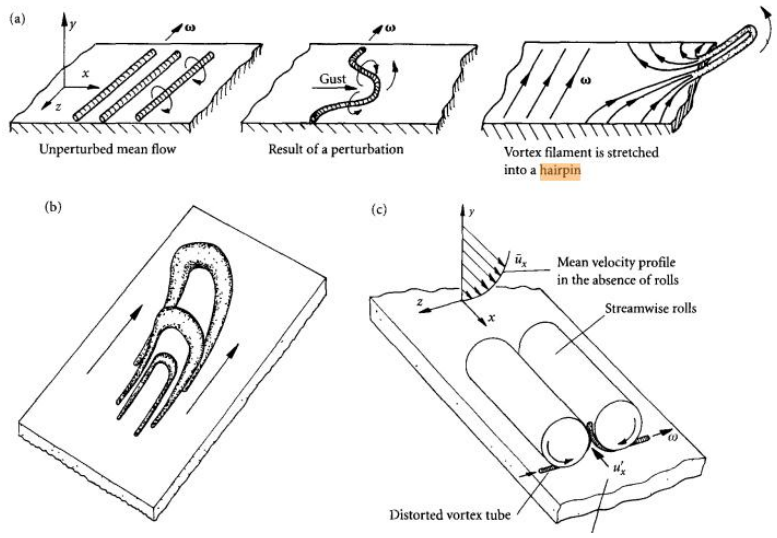

Figure 35: Hairpin formation explained connected to the rolls generation.

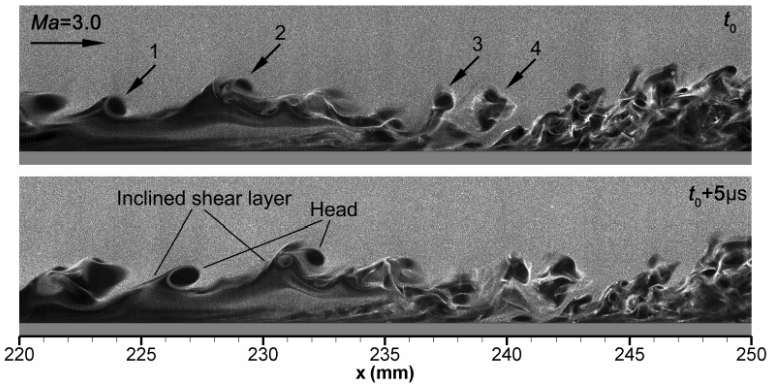

Figure 36: Amazing flow visualization of haipins in a turbulent boundary layer over a plane plate by He & Al. [59].

The Lumley triangle is a graphical representation used in turbulence anisotropy analysis to characterize the state of turbulence in a fluid flow [108] [107]. It maps the invariants of the Reynolds stress anisotropy tensor, specifically the second (II) and third (III) invariants, into a two-dimensional map:

$$II = -\frac{1}{2}a_{ij}a_{ji} \tag{156}$$

$$III = \frac{1}{3}a_{ij}a_{jk}a_{ki} \tag{157}$$

The position on the plane (II, III) has to be inside a specific region, studied by Lumley itself and called after him. The shape of the Lumley triangle is determined by the physically realizable states of turbulence, bounded by specific lines corresponding to different types of turbulence states:

- **One-component turbulence (1C)**: Represents flows dominated by one component of velocity fluctuation.
- **Two-component turbulence (2C)**: Represents flows where two velocity components are significant.
- **Three-component (isotropic) turbulence (3C)**: Represents fully isotropic turbulence where all three components are equal.

By plotting the states (II, III) for a given flow on this triangle, one can visualize the degree and nature of turbulence anisotropy. The position within the triangle provides insights into whether the turbulence is closer to isotropic or anisotropic states, and if it is anisotropic, the specific nature of that anisotropy.

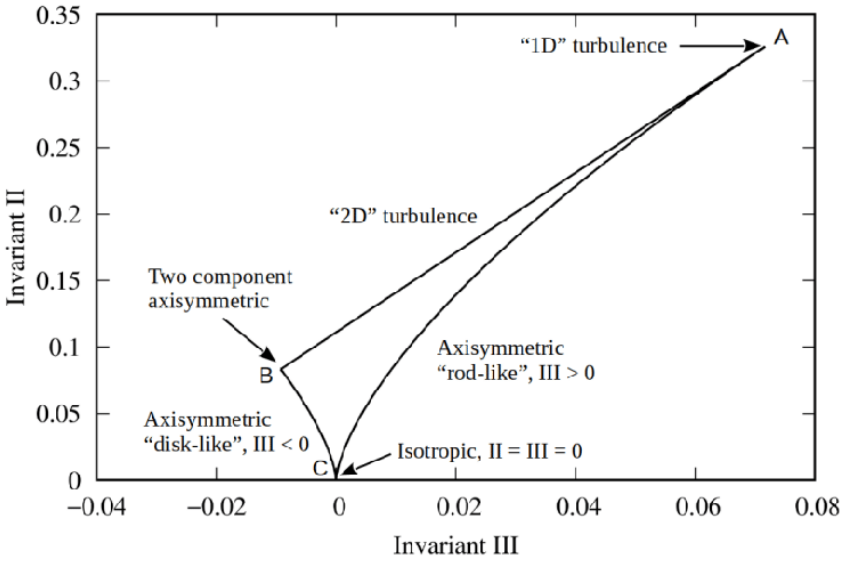

Figure 37: Lumley triangle. Reference: [52]

Limitations of the anisotropy-invariant map introduced by Lumley are discussed by Banerjee & Al. [10] and Jofre & Al. [74]: invariants are nonlinear functions of stresses so that the representation over the plane (II,III) can be distorted. That's why Banerjee & Al. in their work propose an alternative approach by using an equivalent linear representation of anisotropy invariants based on eigenvalues, introducing a barycentric map (x_{bar}, y_{bar}). This map employs a convex combination of scalar metrics that depend on eigenvalues, enabling an undistorted view of the normalized Reynolds stress and any anisotropic stress tensor. The most important aspect is that the barycentric map allows for the quantification of the weighting of any point within it, relative to the limiting states of one-component, two-component, and three-component anisotropy. In Figure 38 we show that there is a bijection between the barycentric map (x_{bar}, y_{bar}) and the invariant map (II, III). In the following discussion we present briefly what are the barycentric coordinates (x_{bar}, y_{bar}) as proposed by Banerjee & Al. [10].
It can be seen that for any physically realizable Reynolds stress tensor, it is possible to construct exactly one corresponding anisotropy tensor in its canonical form as:

$$\hat{a}_{ij} = \begin{pmatrix} \lambda_1 & 0 & 0 \\ 0 & \lambda_2 & 0 \\ 0 & 0 & \lambda_3 \end{pmatrix} \tag{158}$$

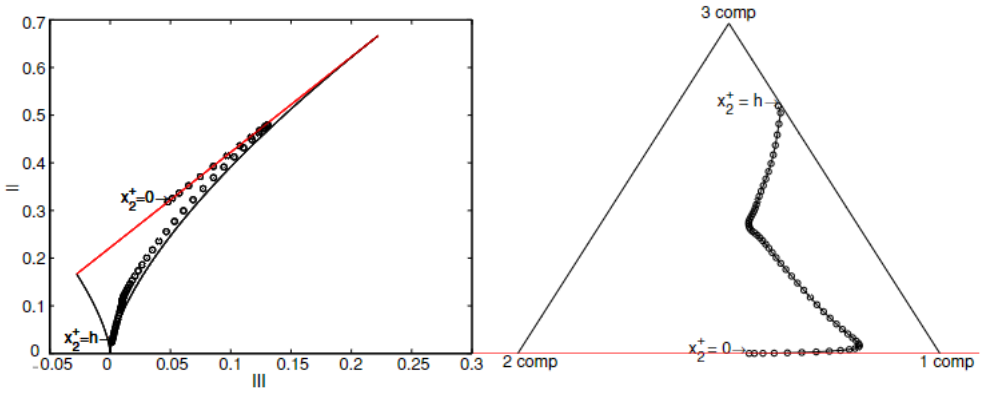

Figure 38: Invariant characteristics of the anisotropy tensors for the Reynolds stress $[\circ] - u_i u_j$ are shown on the anisotropy invariant map (III, II) (left) and on the barycentric map (right), which uses scalar metrics (C_{1c}, C_{2c}) based on the eigenvalues of the anisotropy tensor for the Reynolds stress. Data were extracted from a direct numerical simulation of fully developed turbulent channel flow for $Re_\tau = 180$ by Kim et al. [78].

The anisotropy tensor $\hat{a}_{ij}$ can be expressed as a convex combination of the limiting states (one-component, two-component, three-component):

$$\hat{a}_{ij} = C_{1c}\hat{a}_{1c} + C_{2c}\hat{a}_{2c} + C_{3c}\hat{a}_{3c} \tag{159}$$

where:

- $\{C_{1c}, C_{2c}, C_{3c}\}$ scalar metrics or weighting factors of the limiting states 1C, 2C and 3C respectively:

$$C_{1c} = \lambda_1 - \lambda_2, \quad C_{2c} = 2(\lambda_2 - \lambda_3), \quad C_{3c} = 3\lambda_3 + 1.$$

- $C_{1c} + C_{2c} + C_{3c} = 1$: normalization chosen by the authors to ensure that all metrics C_{1c}, C_{2c}, C_{3c} lie in the range $[0, 1]$.

- $\{\hat{a}_{1c}, \hat{a}_{2c}, \hat{a}_{3c}\}$ tensor basis of the limiting states such that:

$$\hat{a}_{1c} = \begin{pmatrix} \frac{2}{3} & 0 & 0 \\ 0 & -\frac{1}{3} & 0 \\ 0 & 0 & -\frac{1}{3} \end{pmatrix}, \quad \hat{a}_{2c} = \begin{pmatrix} \frac{1}{6} & 0 & 0 \\ 0 & \frac{1}{6} & 0 \\ 0 & 0 & -\frac{1}{3} \end{pmatrix}, \quad \hat{a}_{3c} = \begin{pmatrix} 0 & 0 & 0 \\ 0 & 0 & 0 \\ 0 & 0 & 0 \end{pmatrix}$$

So that the barycentric map (x_{bar}, y_{bar}) can be constructed as:

$$x_{\text{bar}} = C_{1c}x_{1c} + C_{2c}x_{2c} + C_{3c}x_{3c} \tag{160}$$
$$y_{\text{bar}} = C_{1c}y_{1c} + C_{2c}y_{2c} + C_{3c}y_{3c} \tag{161}$$

where (x_{1c}, y_{1c}), (x_{2c}, y_{2c}), and (x_{3c}, y_{3c}) are three arbitrary basis points, chosen usually to make an equilateral triangle as shown in Figure39.

5.5.7 Quadrant/octant analysis

Quadrant analysis, as conceived by Wallace et Al. (1972) [184], is a direct conditional averaging of quadrant sorted data so that we can define conditional covariance over a quadrant q: $\langle u_i u_j \rangle_q$. The quadrants Q1,Q2,Q3,Q4 are defined through a combination of positive/negative combinations of two variables such as the velocity fluctuations (u_i, u_j).
It was first used to study the wall-bounded turbulence which is characterized by sweeps and ejections, so that it was interesting to analyze the quadrant contributions of the velocity fluctuations in a plane normal to the wall: (u,v) and the covariance $\langle uv \rangle_q$. In Figure 41 the PDF of the velocity fluctuations u and v. Moreover, it was remarked that Q2 and Q4 have the largest contributions over the Reynolds

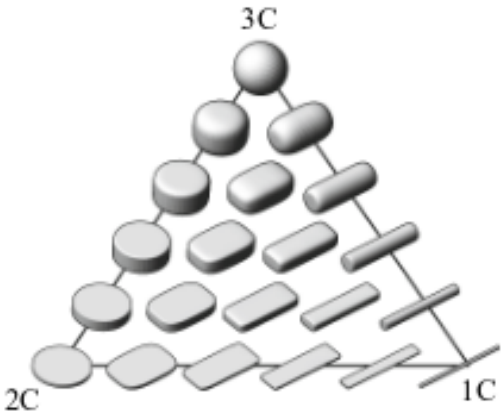

Figure 39: Schematic representation of a "barycentric triangle" proposed by Banerjee & Al. [10] and Jofre & Al. [74].

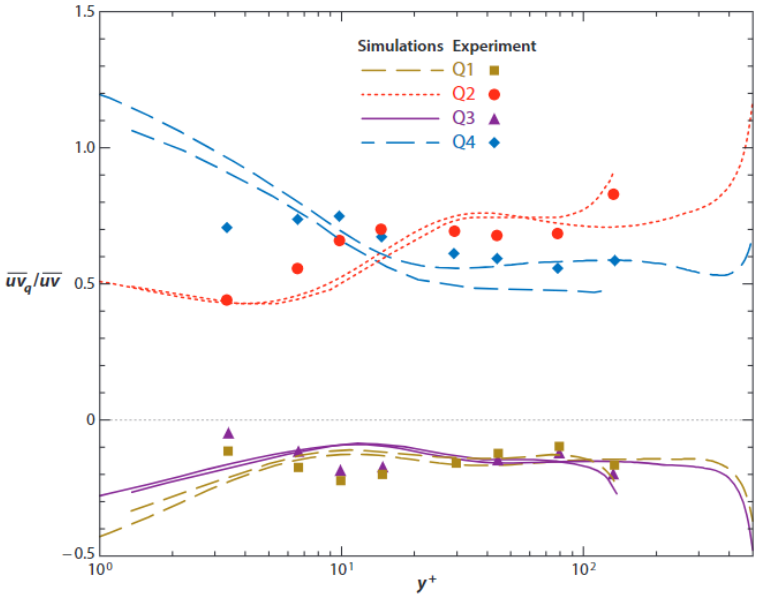

Figure 40: Quadrant contributions to the Reynolds shear stress in turbulent channel flow. Symbols represent the experiment at $Re_\tau = 187$ by Wallace & al. (1972) [184], and lines represent direct numerical simulations at $Re_\tau = 180$ by Kim & al. (1987) [78] and at $Re_\tau = 590$ by Moser & al. (1999) [125]. Reference: [184]

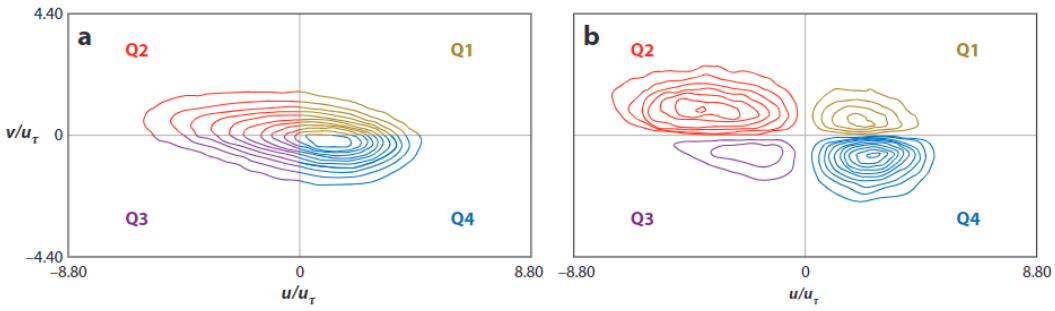

Figure 41: (a) Joint probability distribution function, P(u, v), and (b) covariance integrand, $uv\ P(u, v)$, at $y^+ = 45$ in a turbulent channel flow with $Re_\tau = 194$. Reference: [183]

shear stress component $\langle u_i u_j \rangle$. As shown in Figure 40 in particular Q4 dominates for $y^+ < 15$ and Q2 for $y^+ > 15$. This was an important proof to the existence of the sweep/ejection mechanism and their location in wall normal distance.
The concept has been further extended to octant analysis (taking into account three parameters, and also parameters that are not only the velocity fluctuations), quadrant trajectory analysis, etc. See the review done by Wallace & Al. (2016) [185] for further insights.

6 Numerical approach

Numerics in porous media turbulence research faces several formidable challenges, stemming from the intricate and multi-scale nature of the phenomena involved so that the complex interactions between fluid flow and solid structures demand precise computational techniques to capture their dynamics accurately. The physics of turbulence inside these materials it's still unknown that's why turbulence modeling-based approaches such as RANS or LES have to be avoid in favor of high fidelity simulations such as DNS. This is the only way to dig in the real physics before starting developing some ad-hoc models in the future.
One of the primary challenges is the requirement for fine mesh resolution. To resolve the smallest turbulent eddies, the Kolmogorov scales, a highly refined mesh is essential, which significantly increases computational costs and resources. Moreover, accurately modeling the solid surfaces within porous media adds another layer of complexity. These surfaces exhibit intricate geometries that necessitate a proper spatial discretization to ensure accurate representation and interaction with the fluid flow. The risk when trying to mesh complex geometries is to have skewed or degenerated cells while using classical methods such as the Finite Volume Method (FVM). Balancing the computational expense while maintaining accuracy in capturing both the minute turbulent structures and the detailed solid surfaces forms the crux of the challenges in numerics for porous media turbulence research.
Another challenge is that turbulence is an unsteady phenomenon and so the simulation complexity gets even higher given that the time step has to be quite small, proportional to the mesh size through a CFL number for stability reasons. Moreover it is required also a significant simulated time span, so that also the big scale motions are captured properly. The objective is to be well resolved both at high frequencies (small time step) and at low frequencies (sufficiently large time span).
To sum up, numerical simulations of turbulence in porous media bring with them the following challenges:

- unknown physics:
  models such as RANS and LES cannot be used for now and the only solution is to use DNS;
- wide range of turbulence scales:
  small mesh size to capture Kolmogorov scales, combined small time step and relatively large time span to correctly capture high and low time frequencies respectively;
- geometrical complexity:
  fine mesh size with careful management of cells or nodes placement to correctly describe solid walls and its interactions with the fluid, avoiding degenerated or highly skewed cells.

For the given reasons, the recent development of new CFD codes and powerful calculators allows the ongoing research in this still unexplored world of pores. In our work we opt for DNS simulations run through a high-order CFD code called JAGUAR, owned by CERFACS and ONERA in Toulouse (France). In particular, this code implements the Spectral Difference Method (SDM) for the spatial discretization.

In this section, we go through a review of our numerical setup explaining what is a high-order CFD code (Section 6.1) so that we can introduce the JAGUAR code (Section 6.2), with its motivation and features. Among these features, we detail the spatial discretization method which makes JAGUAR so special, the SDM (Section 6.3), and the extensions around it to optimize the performance of the code: the Immersed Boundary Conditions (IBC) in Section 6.4, the Temporal Discretization in Section 6.5, the Pressure Gradient Scaling (PGS) in Section 6.6, and the Synthetic Turbulence Injection (STI) in Section 6.7. We close this section describing the numerical approach used in this work and its specific parameters (Section 6.8).

6.1 High-order CFD simulations

6.1.1 What is a high-order CFD simulation?

Mathematically speaking, a numerical method is said to be of order k if the solution error e is proportional to the mesh size h to the power of k ($e \propto h^k$). Many production codes used in aerospace community are first or second-order accurate (e.g. StarCCM+, ANSYS Fluent) that's why usually we refer to a high-order method when $k > 2$.

6.1.2 Why doing high-order CFD?

In the last three decades, high-order CFD methods have received considerable attention for their potential higher accuracy with lower cost than low-order methods [2, 191]. Of course these codes are mainly dedicated to high-fidelity research where their high resolution and reduced numerical dissipation and dispersion allow to study complex flows such as those vortex-dominated, like in our case of turbulence inside porous media. On the other hand, it is clear that higher-order simulations bring with them complexity, high-memory requirements, higher CPU time if not managed correctly and possible numerical instabilities if adapted stabilization techniques are not introduced. All these aspects are key to be adressed for a future in which industrial simulations could achieve higher-orders.

6.1.3 High-order CFD techniques

When we think about high-order CFD techniques, we connect immediately the high space discretization to an increase of the stencil. This was true for the first methods but in-use high-order techniques avoid the use of large stencils defining a compact stencil for each cell. The idea is to increase the number of DoF inside each mesh element (structured or unstructured) through a high-order interpolation procedure but keeping always the same stencil structure for each mesh element. At cell boundaries, the reconstructed data are not equal and a Riemann solver is used to take into account these discontinuities. So the main difference with the classical FVM is that the DoF are not the number of cell elements.

Most of the methods proposed in the literature based on those ideas can be classified into three main groups:

- The Discontinuous Galerkin (DG) technique:
  it is based on the Finite Element (FE) framework. The principle is to look for a polynomial representation of the solution that satisfies a variational form of the governing system within each element. Even if the technique is quite old (Reed & Hill (1973) [150]), its extension to the full NS equations is recent and many papers have been published recently.
- The Spectral Volume (SV) technique:
  it is based on the Finite Volume (FV) framework and it follows the pioneering work of Wang & al. (2002) [189]. It consists in defining element subdivisions on which a classical FV technique is considered. The mean quantity over each volume is necessary to build the high-order representation of data inside the element.
- The Spectral Difference (SD) technique:
  it follows the Finite Difference (FD) approach. This technique has been first developed by Kopriva & Kolias (1996) [83] and then published in a more general presentation by Liu, Vinokur & Wang (2006) [104]. The idea is to define high-order approximation of the quantities but to solve the strong form of the equations, as in FD, inside each mesh cell.

As mentioned above, the interest of all these methods comes from the possibility to manage both the space refinement parameter h and the degree of the polynomial p.

6.1.4 High-order methods used in Europe/US

High-order methods are quite recent compared to low-order ones and scientists from Europe and the United States (US) have started to create groups to promote and develop these methods. In Europe we have to mention the Adaptive High-order Variational Methods for Aerodynamic Applications in Industry (ADIGMA) project [2], supported by a consortium consisting of 22 organizations including main European aircraft manufacturers, major European research establishments and several universities, all

with well-proven expertise in CFD. In 2007, several authors of ADIGMA became members of the CFD Algorithm Discussion Group (CFDADG) in the American Institute of Aeronautics and Astronautics Fluid Dynamics Technical Committee (AIAA FDTC). In the first meeting of the CFDADG they tried to find some ways to overcome the difficulties mentioned in paragraph 6.1.2. They decided to focus on the mathematical explanations of high-order methods, error estimates and efficient time marching methods. Wang's book, "Adaptive high-order methods for CFD" [190], co-written by a lot of ADIGMA and CFDADG members in 2011, gives the basis of high-order discretizations. The review paper of the 1st Workshop on High-Order CFD Methods [191], is also an excellent reference where comparisons between several high-order methods are done on many test cases.
Some of the main existing high-order codes are presented in Table 5.

Country	**City**	**Main Developers**	**Code Name**	**Numerical Method**	**Order of Precision**
France	Toulouse	CERFACS	JAGUAR	SDM	User-defined
USA	Austin	University of Texas	SPECFEM3D	SEM	Up to 12th-order
USA	Argonne	Argonne National Laboratory	Nek5000	SEM (with SDM)	TUp to 10th-order
Germany	Stuttgart	University of Stuttgart	DUNE	Spectral Methods, DG	User-defined
World-wide			OpenFOAM	FVM (High-order extensions)	Up to 4th-order
USA	Stanford	Stanford University	SU2	FVM (High-order extensions)	User-defined
UK	London	Imperial College London	Nektar++	SEM, DG	Up to 10th-order
USA	Princeton	Princeton University	CUBISM	SDM	User-defined
Czech Republic	Liberec	Technical University of Liberec	Flow123d	Spectral Methods, DG	User-defined

Table 5: High-order CFD codes in the world and their details. (SEM: Spectral Element Method, SDM: Spectral Difference Method, FVM: Finite Volume Method, DG: Discontinuous Galerkin.)

In the next section we will discuss the code adopted in our work: JAGUAR.

6.2 JAGUAR (proJect of an Aerodynamic solver using General Unstructured grids And high ordeR schemes)

JAGUAR is a high-order CFD code implementing the SDM developped starting from 2012 in Toulouse (France) between ONERA (the french National Office for Aerospace Studies and Research) and CERFACS (European Centre for Research and Advanced Formation in Scientific Computation).

6.2.1 Why the SDM?

The choice of this approach was motivated by several reasons: initially the SD technique has been built in order to correct some drawbacks of DG and SV. Firstly, SD seems more efficient in term of CPU usage and less difficult to understand "physically" than the DG technique. Secondly, the SV method suffers from a high sensitivity (in term of stability of the method) with respect to element decomposition which is less present with SD method. Finally, the SD approach is very recent compared to DG then the potential of research was obviously greater and still it is.

6.2.2 Main features of JAGUAR

The main features of the JAGUAR code, for our application, are:

- Space discretization:
  - high-order (HO) discontinuous method: Spectral Difference Method (SDM)
  - diffusion model: classical method [83] (default), SDLIFT method with different correction schemes [67] (Bassi and Rebay 1 scheme, Bassi and Rebay 2 scheme, I-continuous scheme) or Sun's method [166]
  - Riemann solver for interface solutions: Roe, HLLC, Godunov, etc.
  - p-adaptation (p: polynomial degree) available: Mortar element method
  - h-refinement (h: mesh size) available
  - flux divergence computation: classical divergence scheme [83] (default) or entropy stable schemes [112]
  - Immersed Boundary Conditions (IBC) [38] available: Brinkmann Penalization Method (BPM) with already implemented TPMS boundary conditions

  - Pressure Gradient Scaling (PGS) available
  - Synthethic Turbulence Injection (STI) [111] available

- Time discretization: explicit/implicit Runge-Kutta
- High Processing Computing (HPC): classical "domain decomposition" approach

Especially the recent developments done on the code through the implementation of the IBC and PGS increased exponentially the performance of the code in our configuration, that made possible this and further works over the turbulence in porous media.

6.3 Spectral Difference Method (SDM)

This section focuses on the spatial discretization of the governing equations using the Spectral Difference Method (SDM). It begins with a one-dimensional formulation to establish the fundamental concepts of the method. Following this, we extend the method to the 2D and 3D cases on hexahedral elements. Due to the discontinuous nature of the method across elements, we detail briefly also the Riemann solvers for convective fluxes and diffusion schemes for diffusive fluxes at interfaces, along with gradient computation within the SD framework. Then we discuss the temporal integration of the equations.

6.3.1 General principle for 1D equation: Isoparametric transformation

This section aims to describe the SD discretization process for one-dimensional configurations such as pure convection or diffusion equations and to introduce notations that will be useful in subsequent chapters.
To introduce the basics of the SDM, consider a hyperbolic (or convective) 1D-equation in divergent form:

$$\frac{\partial U}{\partial t} + \frac{\partial E}{\partial x} = 0, \quad \text{for } (x,t) \in \Omega \times [t_0, t_f] \tag{162}$$

Here, $U = U(x,t)$ represents the vector of conservative variables (also known as the solution vector), $E = E(U)$ is the flux vector of U, t denotes time, t_0 and t_f are the initial and final time of the computation, Ω is the physical domain, and x is the 1D spatial coordinate within Ω. Equation 162 generally represents 1D conservation laws with N_{eq} equations, such as:

- The 1D scalar advection equation ($N_{\text{eq}} = 1$) where $U = u$ and $E = cu$, with c as the advection speed.
- The 1D Euler equations ($N_{\text{eq}} = 3$) where $U = (\rho, \rho u, \rho E)^T$ and $E = (\rho u, P + \rho u^2, u(P + \rho E))^T$. These are a simplification of the NS equations discussed in 3 for a mono-species gas in a 1D inviscid and non-reacting flow.

To numerically solve Eq. 162, Ω is divided into N_e non-overlapping and possibly non-uniform elements Ω_e:

$$\Omega = \bigcup_{e=1}^{N_e} \Omega_e \tag{163}$$

where $\Omega_e = \{x \in \Omega \mid x \in [a,b]\}$ with $h_e = b - a$ as its length, as shown in Figures 42a and 42b. The principle of the SD technique is to work not with element Ω_e, but with a standard line $L = \{\xi, 0 \leq \xi \leq 1\}$ into which each Ω_e is transformed. Thus, there is no index e for L, as it is the same standard line for all Ω_e. This transformation is typically expressed from the **isoparametric** or standard domain L **to the physical domain** Ω for each element Ω_e:

$$x(\xi) = \sum_{i=1}^{N_v} M_i(\xi) x_i^e \tag{164}$$

where $\xi \in [0,1]$ is the 1D spatial coordinate in L (or isoparametric coordinate), x_i^e is the physical coordinate of vertex i of Ω_e, N_v is the number of vertices of Ω_e, and M_i are the shape functions.
For example, in the case of 1D linear elements composing Ω, each element Ω_e is defined by $N_v = 2$ vertices with the following shape functions [180]:

$$M_1(\xi) = 1 - \xi \quad \text{and} \quad M_2(\xi) = \xi \tag{165}$$

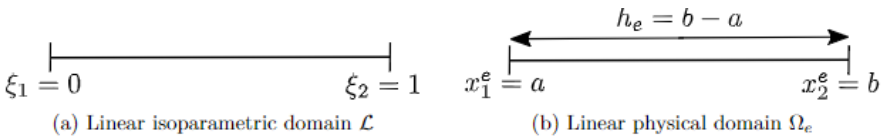

(a) Linear isoparametric domain $\mathcal{L}$ (b) Linear physical domain Ω_e

Figure 42: Linear isoparametric ($N_v = 2$) and physical domains in 1D. Figure from [95].

These shape functions are used to transition from the linear isoparametric domain shown in Figure 42a to the linear physical domain illustrated in Figure 42b. For the 1D linear isoparametric element, shape functions M_1 and M_2 are respectively the 1D Lagrange polynomials constructed at ξ_1 and ξ_2 since:

$$M_1(\xi) = \frac{\xi - \xi_2}{\xi_1 - \xi_2} = \frac{\xi - 1}{0 - 1} = 1 - \xi \equiv l_1^{VT}(\xi) \tag{166}$$

and

$$M_2(\xi) = \frac{\xi - \xi_1}{\xi_2 - \xi_1} = \frac{\xi - 0}{1 - 0} = \xi \equiv l_2^{VT}(\xi) \tag{167}$$

where l_i^{VT} (VT: VerTices) is the i-th **1D Lagrange polynomial** built at vertex i using the coordinates of the remaining vertices $s \neq i$ in the isoparametric domain such that for definition:

$$l_i(\xi) = \prod_{\substack{s=1 \\ s \neq i}}^{N_v} \frac{\xi - \xi_s}{\xi_i - \xi_s}, \quad \text{for } i \in \{1, \ldots, N_v\} \tag{168}$$

We use the specification exponent VT to avoid confusion with other steps of the SDM where we use the Lagrange polynomial l_i but for different purposes.
The same reasoning done over a linear element can be applied for quadratic elements (and higher-order types of elements) which are defined with $N_v = 3$ vertices as represented in Figures 43a and 43b respectively in the isoparametric and physical domains.

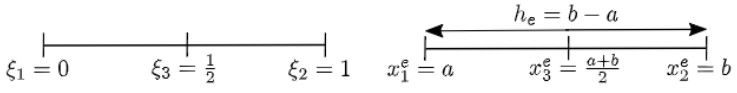

(a) Quadratic isoparametric domain $\mathcal{L}$ (b) Quadratic physical domain Ω_e

Figure 43: Quadratic isoparametric ($N_v = 3$) and physical domains in 1D. Figure from [95].

In that case, there are three shape functions [180]:

$$M_1(\xi) = 1 - 3\xi + 2\xi^2, \quad M_2(\xi) = 2\xi^2 - \xi, \quad \text{and} \quad M_3(\xi) = 4(\xi - \xi^2). \tag{169}$$

The isoparametric transformation is characterized by a non-singular Jacobian matrix J, which is a scalar in 1D, given by:

$$J = \frac{\partial x}{\partial \xi} \equiv x_\xi = \sum_{i=1}^{N_v} \frac{\partial M_i}{\partial \xi} x_i^e \tag{170}$$

The inverse transformation from the physical domain to the isoparametric domain is then related to the inverse of J defined as:

$$J^{-1} = \frac{\partial \xi}{\partial x} \equiv \xi_x \tag{171}$$

Consequently, Eq. 162 is solved in the isoparametric domain using the derivation chain rule for $\partial E/\partial x$ and multiplying by the determinant of J noted $|J|$:

$$\frac{\partial U}{\partial t} + J^{-1}\frac{\partial E}{\partial \xi} = 0 \implies \frac{\partial(|J|U)}{\partial t} + \frac{\partial(|J|J^{-1}E)}{\partial \xi} = 0 \tag{172}$$

because $|J|J^{-1} = 1$ in 1D. Variables defined in the standard domain are introduced so that Eq. 172 becomes:

$$\frac{\partial \hat{U}}{\partial t} + \frac{\partial \hat{E}}{\partial \xi} = 0, \quad \text{for } (\xi, t) \in L \times [t_0, t_f] \tag{173}$$

where:

$$\hat{U} = |J|U \tag{174}$$

$$\hat{E} = |J|J^{-1}E \tag{175}$$

$\hat{U}$ and $\hat{E}$ are respectively the solution vector and the flux vector in the isoparametric domain. The main objective of the SDM discretization is the computation of the term $\partial\hat{E}/\partial\xi$ corresponding to the divergence of the flux in the isoparametric domain. The formulation shown in Eq. 173
allows for treating each element Ω_e with exactly the same methodology to compute this flux divergence. It is worth mentioning that in Eq. 172, $|J|$ is assumed to be independent of time. It implies that the mesh cannot change during the computation, which was the case during this work but we are not going to discuss this more complex situation. For further insights check the following references [111, 180].

6.3.2 Solution points (SP) and Flux points (FP): definition

To achieve a $(p+1)$-th order accuracy within each element Ω_e when solving Eq. 173, the SDM assumes that the vector $\hat{U}$ varies as a polynomial of degree p inside the reference element L. This implies that $\hat{U}$ must be known at $p+1$ points in L, referred to as solution points (SP). Furthermore, the flux divergence should also be a polynomial of degree p, necessitating that $\hat{E}$ be a polynomial of degree $p+1$. Consequently, $p+2$ points, termed flux points (FP), are required within L to construct a polynomial of degree $p+1$ for $\hat{E}$.
Evaluating fluxes at the FP requires the solution values at these points. It has been demonstrated that interpolating U from SP to FP, rather than interpolating $\hat{U}$, is more robust, particularly for curved elements [199]. Therefore, it is a common practice within the SD community to construct the solution polynomial using the values of U at the SP.
The SP within L are typically chosen as the **Gauss-Chebyshev quadrature points** of the first kind over $[0, 1]$, defined by:

$$\xi_j = \frac{1}{2}\left[1 - \cos\left(\frac{2j-1}{2N_{\text{SP}}^{1d}}\pi\right)\right], \quad \text{for } j \in \{1, 2, \ldots, N_{\text{SP}}^{1d}\} \tag{176}$$

with $N_{\text{SP}}^{1d} = p+1$ being the number of SP in 1D within a standard element of degree p. Figures 44 and 45 illustrate the positions of the SP within L for $p = 2$ and $p = 3$, represented by red triangles. Since any element Ω_e is transformed into L, the SP coordinates introduced in Eq. 176 are the same for all elements, assuming they share the same p value. If p-adapted simulations are considered, p can vary between elements, resulting in different SP coordinates for each element within L.
Another set of SP, used by some authors, is the $p+1$ **Gauss-Legendre** quadrature points. Using Gauss-Legendre quadrature points for SP should minimize aliasing errors.
The total number of SP within the physical domain Ω is referred to as the DoF of the solution. More generally, for any numerical method, DoF are the points where the numerical solution is stored and advanced in time. For example, in a classical Finite Volume (FV) method, DoF corresponds to cell centers. For a fair comparison between two numerical methods in terms of accuracy and computational time, the same DoF value should be used for both methods.
The FP within L are usually located at the Gauss-Legendre quadrature points for the p interior FP, with the remaining two FP positioned at the boundaries of L, specifically at $\xi = 0$ and $\xi = 1$. Figures 44 and 45 display the distribution of the $N_{\text{FP}}^{1d} = p+2$ FP for $p = 2$ and $p = 3$, represented by blue squares. It is important to note that the stability of the SD method depends on the FP locations, while the SP locations do not influence stability. Research indicates that using Gauss-Legendre quadrature points for the p interior FP is stable for any p value. Similar to SP, when p is uniform across all elements, FP coordinates remain consistent in the reference element L; however, they differ in p-adapted simulations. Thus, the two sets of points utilized in the SD method are established. For a given polynomial order p, the SP and FP locations in 1D will consistently be:

- Gauss-Chebyshev quadrature points of the first kind over $[0, 1]$ as defined by Eq. 176 for SP.

- Gauss-Legendre quadrature points for the p interior FP, with the two end points of L serving as FP.

The interpolation and extrapolation processes between these sets of points will now be explained.

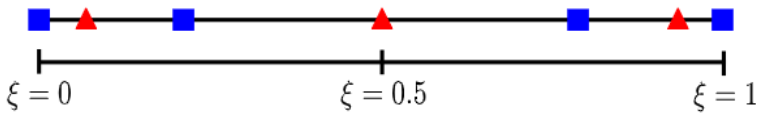

Figure 44: Locations of SP (▲) and FP (■ for p = 2 in isoparametric domain L. Figure from [95].

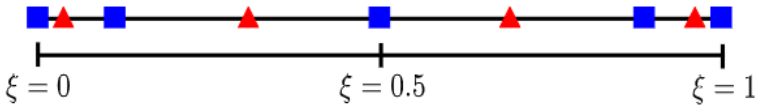

Figure 45: Locations of SP (▲) and FP (■) for p = 3 in isoparametric domain L. Figure from [95].

6.3.3 Solution points (SP) and Flux points (FP): interpolation

Within the SD framework, the interpolation process employs the Lagrange interpolation principle. To approximate $\hat{U}$ as a polynomial of degree p inside L, the Lagrange polynomial basis of degree p constructed at the SP is given by:

$$l_j^{\mathrm{SP}}(\xi) = \prod_{\substack{s=1 \\ s \neq j}}^{N_{\mathrm{SP}}^{1d}} \frac{\xi - \xi_s}{\xi_j - \xi_s}, \quad \text{for } j \in \{1, 2, \ldots, N_{\mathrm{SP}}^{1d}\} \tag{177}$$

Here, l_j^{SP} is the j-th one-dimensional Lagrange polynomial constructed at the SP ξ_j using all other SP ξ_s with $s \neq j$.
Similarly, using the values of $\hat{E}$ at N_{FP}^{1d} FP, a $(p+1)$-degree polynomial can be constructed using the following Lagrange polynomial basis of degree $p+1$:

$$l_k^{\mathrm{FP}}(\xi) = \prod_{\substack{s=1 \\ s \neq k}}^{N_{\mathrm{FP}}^{1d}} \frac{\xi - \xi_s}{\xi_k - \xi_s}, \quad \text{for } k \in \{1, 2, \ldots, N_{\mathrm{FP}}^{1d}\} \tag{178}$$

Here, l_k^{FP} is the k-th one-dimensional Lagrange polynomial constructed at the FP ξ_k using all other FP ξ_s with $s \neq k$.
In the SD process, the derivative of Eq. 178 is used when $\hat{E}$ is differentiated at the SP along the ξ direction. Hence, the analytical formula for the derivative is recalled:

$$\frac{\partial l_k^{\mathrm{FP}}}{\partial \xi}(\xi) = \sum_{\substack{s=1 \\ s \neq k}}^{N_{\mathrm{FP}}^{1d}} \left[\prod_{\substack{m=1 \\ m \neq s}}^{N_{\mathrm{FP}}^{1d}} \frac{\xi - \xi_m}{\xi_k - \xi_s} \right], \quad \text{for } k \in \{1, 2, \ldots, N_{\mathrm{FP}}^{1d}\} \tag{179}$$

Since l_j^{SP}, l_k^{FP}, and $\frac{\partial l_k^{\mathrm{FP}}}{\partial \xi}$ are constructed from the SP and FP locations, their values are independent of the mesh element in the constant p case but are element-dependent for p-adapted simulations.

6.3.4 General algorithm for a 1D equation

Since the equations are solved in the reference domain, the SD discretization process can be explained within the standard element L without loss of generality. At a given time instant, the solution vector $\hat{U}$ contains the conservative variables in the isoparametric domain stored at each SP ξ_j within L, denoted $\hat{U}_j$. These values at the SP are used to construct a polynomial representation of degree p for the continuous solution U_h across L, using the Lagrange polynomial basis:

$$U_h(\xi) = \sum_{j=1}^{N_{\mathrm{SP}}^{1d}} \hat{U}_j \left|J\right|_j l_j^{\mathrm{SP}}(\xi), \quad \text{for } \xi \in [0,1] \tag{180}$$

Using this equation, the conservative variables are interpolated at internal FP ($2 \leq k \leq N_{\mathrm{FP}}^{1d} - 1$) and extrapolated at interface FP ($k = 1$ and $k = N_{\mathrm{FP}}^{1d}$). The conservative variables at a FP k in the physical domain are denoted by U_k. At an internal FP, E_k is directly obtained from U_k, and the flux in the isoparametric domain $\hat{E}_k$ is derived from Eq. 179. However, at an interface FP, U_k is not uniquely defined since interface FP are shared by two elements. To ensure a continuous flux across the entire domain and maintain conservativity, a Riemann solver is employed at interface FP to compute an interface flux, denoted $\hat{E}_{I_k}$ (where I stands for interface). It should be noted that $\hat{E}_{I_k}$ is referred to as a numerical flux because it is computed based on a numerical treatment (the Riemann solver) rather than a direct link between E and U.
Once $\hat{E}_k$ at internal FP and $\hat{E}_{I_k}$ at interface FP have been computed, a $(p+1)$-degree polynomial representation of a continuous flux $\hat{E}_h(\xi)$ across L can be constructed from the flux values at FP:

$$\hat{E}_h(\xi) = \sum_{k=1}^{N_{\mathrm{FP}}^{1d}} \hat{E}_k l_k^{\mathrm{FP}}(\xi), \quad \text{for } \xi \in [0,1] \tag{181}$$

where $\hat{E}_1 = \hat{E}_{I_1}$ and $\hat{E}_{N_{\mathrm{FP}}^{1d}} = \hat{E}_{I_{N_{\mathrm{FP}}^{1d}}}$. The flux polynomial $\hat{E}_h(\xi)$ defined is differentiated along the ξ direction and evaluated at each SP ξ_j to obtain:

$$\frac{\partial \hat{E}_h}{\partial \xi}(\xi_j) = \sum_{k=1}^{N_{\mathrm{FP}}^{1d}} \hat{E}_k \frac{\partial l_k^{\mathrm{FP}}}{\partial \xi}(\xi_j), \quad \text{for } j \in \{1, 2, \ldots, N_{\mathrm{SP}}^{1d}\} \tag{182}$$

Finally, Eq. 173 can be advanced in time using any explicit temporal scheme at each SP inside L:

$$\frac{d\hat{U}}{dt}(\xi_j) = -\frac{\partial \hat{E}_h}{\partial \xi}(\xi_j) = -\sum_{k=1}^{N_{\mathrm{FP}}^{1d}} \hat{E}_k \frac{\partial l_k^{\mathrm{FP}}}{\partial \xi}(\xi_j), \quad \text{for } j \in \{1, 2, \ldots, N_{\mathrm{SP}}^{1d}\} \tag{183}$$

The SD discretization process described for a hyperbolic 1D equation (1D pure convection equation) is summarized in six distinct steps, as shown in Figures 46a through 48b for the $p = 2$ case. This example illustrates the procedure for a given element Ω_e and its left (respectively right) neighbor Ω_{e-1} (respectively Ω_{e+1}), which have been transformed into the standard element L for applying the SD discretization process.

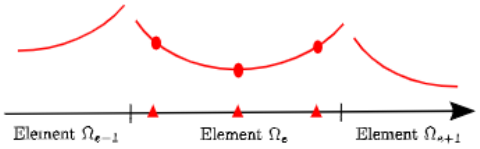

(a) **Step 1:** build a continuous polynomial of degree $p = 2$ for $\mathbf{U}$ based on the 3 values of $\mathbf{U}$ (●) at the 3 SP (▲).

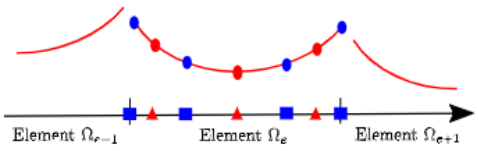

(b) **Step 2:** evaluation of $\mathbf{U}$ (●) at the 4 FP (■).

Figure 46: 1st and 2nd steps of the SD process in 1D for a pure convection equation. Figures from [95].

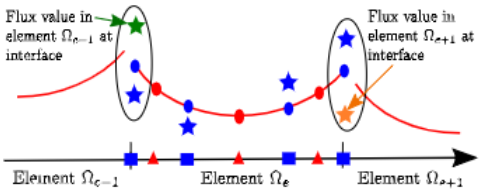

(a) **Step 3:** evaluation of $\widehat{\mathbf{E}}$ (★) at the 4 FP (■). There are 2 flux values at interfaces between elements...

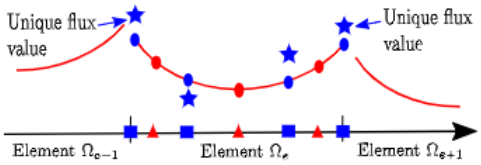

(b) **Step 4:** use a Riemann solver to have a unique flux value (★) at element interfaces.

Figure 47: 3rd and 4th steps of the SD process in 1D for a pure convection equation. Figures from [95].

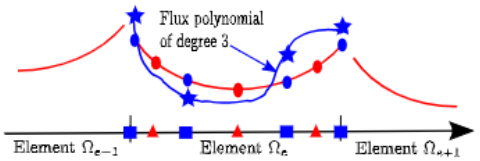

(a) **Step 5:** build flux polynomial of degree $p+1 = 3$ based on values of $\widehat{\mathbf{E}}$ (★) at the 4 FP (■).

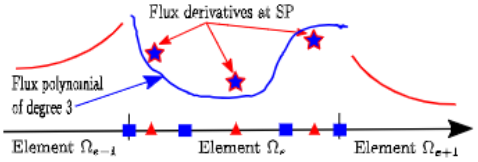

(b) **Step 6:** derivation of flux polynomial at the 3 SP (▲) to get $\left(\partial\widehat{\mathbf{E}}_h/\partial\xi\right)_j$ for $j \in [\![1,3]\!]$.

Figure 48: 5th and 6th steps of the SD process in 1D for a pure convection equation. Figures from [95].

6.3.5 Riemann solvers for a 1D equation

In this section, we consider the Riemann problem in the context of a 1D hyperbolic equation, where the convective flux $E = E_c$:

$$U(x,0) = \begin{cases} U^L, & \text{if } x < 0 \\ U^R, & \text{if } x > 0 \end{cases} \tag{184}$$

This situation, where $U^L \neq U^R$, is depicted in Figure 49 and is typical at each interface FP when using the SD method. The solution approach for a Riemann problem depends on the specific system of equations considered, particularly whether U is a scalar or vector and whether E_c is a linear or nonlinear function of U. In our case the focus is on systems of equations derived from conservation laws where U is a vector and E_c is nonlinear. Lax [93] reviewed the general Riemann problem for conservation laws. However, solving a Riemann problem efficiently for conservation laws is highly dependent on the specific system from which Eq. 162 originates [171]. As this work focuses on CFD simulations, the Riemann solvers are introduced within the context of the unsteady Euler equations, for which the 1D case was discussed in Section 6.3.1.

Exact and Approximate Solutions to the Riemann Problem

Godunov [56] was the first to propose a method for solving the Riemann problem for the unsteady 1D Euler equations in a calorically perfect gas, providing an exact solution, albeit at a high computational cost. Consequently, the development of less computationally expensive Riemann solvers, with properties close to Godunov's exact solver, became popular. These are known as approximate Riemann solvers.

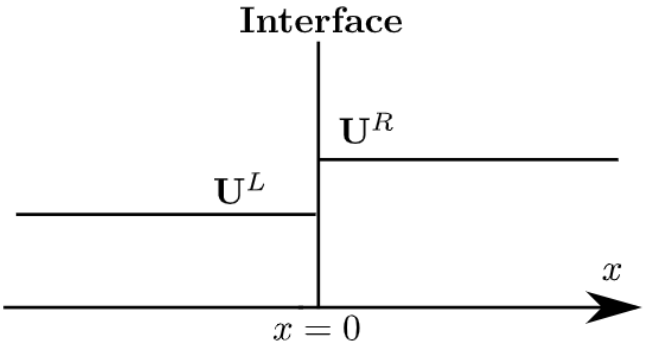

Figure 49: Illustration of the Riemann problem in a 1D general case.

On JAGUAR, we employ the Harten, Lax, and van Leer Contact (HLLC) [13] Riemann solver, which is discussed here, but also other solvers are available such as Roe and Godunov. For a comprehensive review of approximate Riemann solvers, refer to Toro's book [171].

The HLLC Riemann Solver

The HLLC Riemann solver is typically presented using the three-dimensional Euler equations for the 3D flux projected onto an interface with a unit normal $\mathbf{n^u} = [n_x^u, n_y^u, n_z^u]^T$, separating two states U_L and U_R, as shown in Figure 49. The state vector U and the normal flux $\mathbf{F}_c \cdot \mathbf{n^u} \equiv \mathbf{F}_{c,n}$ are defined as:

$$\mathbf{U} = \begin{pmatrix} \rho \\ \rho u \\ \rho v \\ \rho w \\ \rho E \end{pmatrix}, \quad \mathbf{F}_c(\mathbf{U}) \cdot \mathbf{n}^u \equiv \mathbf{F_{c,n}}(\mathbf{U}) = \begin{pmatrix} \rho u_n \\ \rho u u_n + P n_x \\ \rho v u_n + P n_y \\ \rho w u_n + P n_z \\ u_n(P + \rho E) \end{pmatrix} \tag{185}$$

where $u_n = u n_x^u + v n_y^u + w n_z^u$ is the velocity component in the $\mathbf{n^u}$ direction. This scheme assumes a three-wave model for the Riemann problem solution, as illustrated in Figure 50 for $\mathbf{n^u} = [1, 0, 0]^T$. The waves include two acoustic waves with speeds S_L and S_R, and a contact wave with speed S_*, which lies between S_L and S_R.

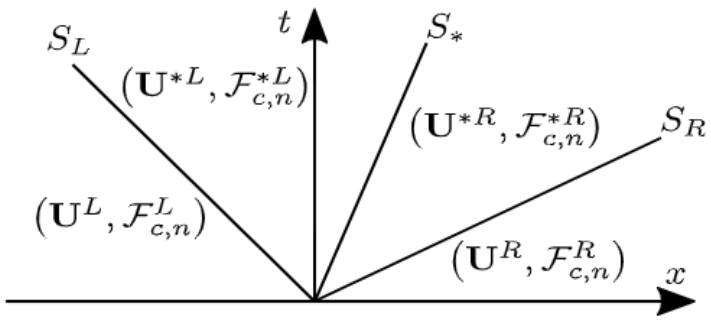

Figure 50: Consider the situation of the Riemann problem solved with the HLLC (Harten-Lax-van Leer-Contact) solver, where the velocity vector is given by $\mathbf{n^u} = \begin{bmatrix} 1 \\ 0 \\ 0 \end{bmatrix}$. In this scenario, the star region consists of two constant states separated by a contact wave with speed S_*.

The HLLC solver computes the interface numerical flux based on the signs of S_L, S^*, and S_R [171]:

$$\mathbf{F}_{I,c,n} = \begin{cases} \mathbf{F}_{c,n}^L, & \text{if } S_L > 0 \\ \mathbf{F}_{c,n}^{*L}, & \text{if } S_L \leq 0 < S_* \\ \mathbf{F}_{c,n}^{*R}, & \text{if } S_* \leq 0 \leq S_R \\ \mathbf{F}_{c,n}^R, & \text{if } S_R < 0 \end{cases} \tag{186}$$

where $\mathbf{F}^L_{c,n} = \mathbf{F}_{c,n}(U_L)$ and $\mathbf{F}^R_{c,n} = \mathbf{F}_{c,n}(U_R)$. The intermediate fluxes $\mathbf{F}^{*L}_{c,n}$ and $\mathbf{F}^{*R}_{c,n}$ in the star region are determined using the Rankine-Hugoniot conditions across each wave:

$$\mathbf{F}^{*L}_{c,n} = \mathbf{F}^L_{c,n} + S_L(U^{*L} - U^L) \tag{187}$$

$$\mathbf{F}^{*R}_{c,n} = \mathbf{F}^{*L}_{c,n} + S_*(U^{*R} - U^{*L}) \tag{188}$$

$$\mathbf{F}^{*R}_{c,n} = \mathbf{F}^R_{c,n} + S_R(U^{*R} - U_R) \tag{189}$$

Here, U^{*L} and U^{*R} are the left and right states in the star region, and they are unknowns. Therefore, there are four unknowns $\mathbf{F}^{*L}_{c,n}$, $\mathbf{F}^{*R}_{c,n}$, U^{*L}, and U^{*R}, but only three equations (Eqs.187-189), leaving the problem underdetermined. An additional condition, typically based on the exact solution of the Riemann problem, is required. It is common to assume [171]:

$$P^{*L} = P^{*R} \equiv P^* \quad \text{(Continuity of pressure in the star region)} \tag{190}$$

$$u^{*L} = u^{*R} \equiv S_* \quad \text{(Continuity of normal velocity in the star region)} \tag{191}$$

The goal is to find expressions for the variables in the star region. Assuming S_L and S_R are known, the first components of Eqs. yield the densities in the star region:

$$\rho^{*L} = \rho_L \frac{S_L - u^L_n}{S_L - S_*}, \quad \rho^{*R} = \rho_R \frac{S_R - u^R_n}{S_R - S_*} \tag{192}$$

By multiplying the second, third, and fourth components of Eqs.187 and 189 by n^u_x, n^u_y, and n^u_z respectively and then summing, we obtain:

$$P^{*L} = P_L + \rho^{*L}(S_L - S_*)S_* - \rho^L u^L_n(S_L - u^L_n) \quad \text{and} \quad P^{*R} = P_R + \rho^{*R}(S_R - S_*)S_* - \rho^R u^R_n(S_R - u^R_n) \tag{193}$$

From the continuity in the star region and using the previous expressions, the contact wave speed S^* can be computed as:

$$S_* = \frac{P_R - P_L - \rho^L u^L_n(u^L_n - S_L) + \rho^R u^R_n(u^R_n - S_R)}{\rho^R(u^R_n - S_R) - \rho^L(u^L_n - S_L)}. \tag{194}$$

Once the densities $\rho^{*L/R}$, pressure $P^{*L/R} = P^*$, and normal velocity S^* are determined, they can be used to calculate the remaining components of U^*_L and U^*_R using the following equations:

$$(\rho u)^{*L/R} = \frac{(P^* - P^{L/R})\, n^u_x + \rho^{L/R} u^{L/R}(S_{L/R} - u^{L/R}_n)}{S_{L/R} - S_*}. \tag{195}$$

$$(\rho v)^{*L/R} = \frac{(P^* - P^{L/R})\, n^u_y + \rho^{L/R} v^{L/R}(S_{L/R} - u^{L/R}_n)}{S_{L/R} - S_*}. \tag{196}$$

$$(\rho w)^{*L/R} = \frac{(P^* - P^{L/R})\, n^u_z + \rho^{L/R} w^{L/R}(S_{L/R} - u^{L/R}_n)}{S_{L/R} - S_*}. \tag{197}$$

$$(\rho E)^{*L/R} = \frac{P^* S^* - P^{L/R} u^{L/R}_n + (\rho E)^{L/R}(S_{L/R} - u^{L/R}_n)}{S_{L/R} - S_*}. \tag{198}$$

The numerical fluxes $F^{*L}_{c,n}$ and $F^{*R}_{c,n}$ can then be computed, and the final interface numerical flux is determined using Eq. 186. It is important to note that $U^{*L/R}$ is not used to compute $F^{*L/R}_{c,n}$ directly through $F^{*L/R}_{c,n} = F_c(U^{*L/R})$, unlike in approximate-state Riemann solvers. The methodology presented here is applicable for any equation of state (EOS), provided S_L and S_R are known. The EOS affects only the values of S_L and S_R, as the expression for the sound speed differs with each EOS.

Wave Speed Estimates in the HLLC Riemann Solver

The previous computations assumed that the values of S_L and S_R were known. In practice, several choices for these values are available in the literature. The choice employed in this work is given by:

$$S_L = \min\left(u_n^L - c^L, \tilde{u}_n - \tilde{c}, u_n^R - c^R\right), \tag{199}$$

$$S_R = \max\left(u_n^L + c^L, \tilde{u}_n + \tilde{c}, u_n^R + c^R\right), \tag{200}$$

where c^L and c^R are the sound speeds in the left and right states, respectively. For ideal multi-species gases, these sound speeds are computed as:

$$c^{L/R} = \sqrt{\frac{\gamma^{L/R} P^{L/R}}{\rho^{L/R}}}, \tag{201}$$

where γ^L and γ^R are the heat capacity ratios in the left and right states. The variables with a tilde ($\tilde{\cdot}$) are Roe's averages [152] and are recalled here for completeness:

$$\tilde{r} = \sqrt{\frac{\rho^R}{\rho^L}}, \tag{202}$$

$$\tilde{u}_n = \frac{\tilde{r} u_n^R + u_n^L}{1 + \tilde{r}}, \tag{203}$$

$$\tilde{H} = \frac{\tilde{r} H^R + H^L}{1 + \tilde{r}}, \tag{204}$$

$$\tilde{\gamma} = \frac{\tilde{r}\gamma_R + \gamma_L}{1 + \tilde{r}}, \tag{205}$$

$$\tilde{c}^2 = (\tilde{\gamma} - 1)\left(\tilde{H} - \frac{\tilde{u}_n^2}{2}\right). \tag{206}$$

where $H = E + \frac{p}{\rho}$ stands for the total enthalpy. It should be mentioned that technically, Eq. 206 is valid only for a calorically mono-species gas ($\tilde{\gamma} = \gamma$ is constant) as presented by Roe in its original paper [152].

6.3.6 Extension to diffusion equation: gradient computation in 1D

There are three available gradient computation algorithms for the SDM: original formulation [83] and SDLIFT formulation [67] [111] and Sun's formulation [165, 166]. The latter is not going to be discussed.

- **Original formulation** by Kopriva [83]:

  The discretization process described in the previous discussion is sufficient if the equation being solved is hyperbolic, i.e., when E is only a function of U. However, if the equation is not hyperbolic but parabolic, E depends on either or both U and ∇U. Such equations are often associated with diffusion processes, hence the term diffusion equation. The NS equations introduced in Section 3.2 also have a parabolic part due to their viscous terms $\nabla \cdot (\mu \nabla \mathbf{U})$, which is why the discretization of parabolic equations using the SD method is described here.

  Thus, if E depends on $\frac{\partial U}{\partial x}$, then $\frac{\partial U}{\partial x}$ is needed at flux points (FP) to compute E at these points. The situation considered is represented in Figure 51 where, for clarity, an element Ω_e is shown with its two interfaces between Ω_{e-1} on its left and Ω_{e+1} on its right.

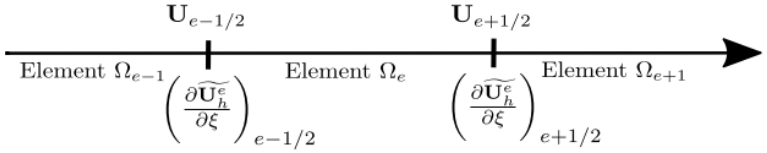

Figure 51: Interfaces for an element Ω_e.

First, as with the hyperbolic 1D equation, Eq. 181 is employed to evaluate U at FP. At element interfaces $\xi = 0$ and $\xi = 1$, U is discontinuous across elements, requiring the definition of interface (or common) values at these points. These are usually taken as the arithmetic average (original formulation) between the two states available at each interface:

$$U^{e-\frac{1}{2}} = \frac{U_h^{e-1}(1) + U_h^e(0)}{2} \quad \text{and} \quad U^{e+\frac{1}{2}} = \frac{U_h^e(1) + U_h^{e+1}(0)}{2} \tag{207}$$

where superscripts $e-1$, e, and $e+1$ are added for clarity. Once common values have been computed at interface FP, U is continuous across all elements, and its values at FP are denoted by U_k^C for $k \in \{1, \dots, N_{FP}^{1d}\}$. Consequently, as with the flux polynomial defined by Eq. 182, a $(p+1)$-degree polynomial representation of a continuous solution vector can be constructed. This polynomial is differentiated along the ξ direction and evaluated at solution points (SP) to obtain:

$$\frac{\partial U_h^e}{\partial \xi}(\xi_j) = \sum_{k=1}^{N_{FP}^{1d}} U_k^C \frac{\partial l_k^{FP}}{\partial \xi}(\xi_j), \quad \text{for } j \in \{1, \dots, N_{SP}^{1d}\} \tag{208}$$

which is the gradient of U along ξ evaluated at SP.

The same process is repeated for these gradients at SP:

1. A p-degree polynomial representation of the gradient is built from the values defined in Eq. (208) and evaluated at FP:

$$\frac{\partial \widetilde{U_h^e}}{\partial \xi}(\xi_k) = \sum_{j=1}^{N_{SP}^{1d}} \left(\frac{\partial U_h^e}{\partial \xi}\right)_j l_j^{SP}(\xi_k), \quad \text{for } k \in \{1, \dots, N_{FP}^{1d}\} \tag{209}$$

2. Values of $\left(\frac{\partial \widetilde{U_h^e}}{\partial \xi}\right)(\xi_k)$ are discontinuous at element interfaces. In the SD community, the usual approach is to take the arithmetic average, as in Eq. 207 for states, to define common gradient values at element interfaces:

$$\left(\frac{\partial \widetilde{U_h^e}}{\partial \xi}\right)_{e-\frac{1}{2}} = \frac{1}{2}\left[\frac{\partial \widetilde{U_h^{e-1}}}{\partial \xi}(1) + \frac{\partial \widetilde{U_h^e}}{\partial \xi}(0)\right] \tag{210}$$

$$\left(\frac{\partial \widetilde{U_h^e}}{\partial \xi}\right)_{e+\frac{1}{2}} = \frac{1}{2}\left[\frac{\partial \widetilde{U_h^e}}{\partial \xi}(1) + \frac{\partial \widetilde{U_h^{e+1}}}{\partial \xi}(0)\right] \tag{211}$$

3. Once common gradients have been computed, a $(p+1)$-degree polynomial for the gradient of U along the ξ direction, continuous across all elements, is obtained, denoted by $\left(\frac{\partial \widetilde{\widetilde{U_h^e}}}{\partial \xi}\right)_k$.

4. Values of $\left(\frac{\partial \widetilde{\widetilde{U_h^e}}}{\partial \xi}\right)_k$ are scaled by ξ_x to get the gradient of U along the x direction:

$$\left(\frac{\partial U}{\partial x}\right)_k = \xi_x \left(\frac{\partial \widetilde{\widetilde{U_h^e}}}{\partial \xi}\right)_k, \quad \text{for } k \in \{1, \dots, N_{FP}^{1d}\} \tag{212}$$

Finally, the values of $\left(\frac{\partial U}{\partial x}\right)_k$ are used to compute E_k, and Eq. 175 ends the process to obtain $\bar{E}_k$ at each FP $k \in \{1, \dots, N_{FP}^{1d}\}$.

The methodology introduced in this section to compute the gradient at FP is the original one proposed by Kopriva [83], later used by Sun [165, 166]. It is referred to as the *average approach* due to the averaging of both states (with Eq. (207)) and gradients (with Eq. (210) and Eq. (211)) at element interfaces.

- **SDLIFT formulation** by Huynh[67, 111]:

  The average approach discussed before lacks the flexibility required for computing common state and gradient values at element interfaces. This method has also shown significant instability when applied to coarse meshes, particularly in scenarios involving multi-species reacting gases. An alternative methodology can be explored by adopting the Flux Reconstruction (FR) principles

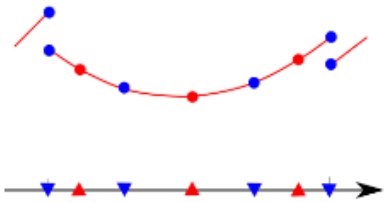

(a) Step 1 : Extrapolation of solution (●) at the flux points (▼)

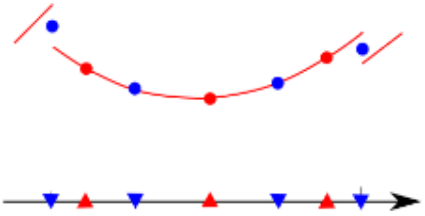

(b) Step 2 : Computation of solution (●) at interfaces by mean average

Figure 52: 1st and 2nd steps of the gradient computation in the SD original formulation by Kopriva in 1D for a diffusion equation. Figures from [95].

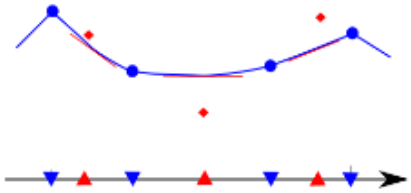

(a) Step 3 : Building the continuous polynomial (blue) at flux points and computing the derivative (◆) at solution points

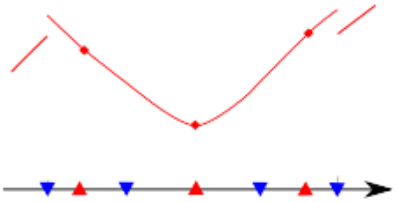

(b) Step 4 : Defining the derivative (red) at solution points

Figure 53: 3rd and 4th steps of the gradient computation in the SD original formulation by Kopriva in 1D for a diffusion equation. Figures from [95].

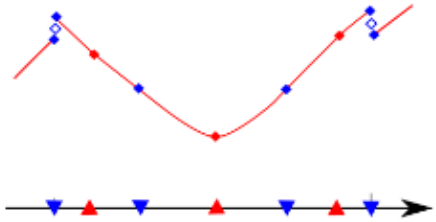

Figure 54: Step 5 : Extrapolation of the derivative (◆) at the flux points.
5th step of the gradient computation in the SD original formulation by Kopriva in 1D for a diffusion equation. Figure from [95].

introduced by Huynh [67] for solving the diffusion equation using an FR scheme. The situation under consideration remains as depicted in Figure 51, where a diffusion equation must be solved using a Spectral Difference (SD) discretization.

Starting from Equation 174, a $(p-1)$-degree polynomial can be constructed for the gradient of U along the ξ direction:

$$\frac{\partial U_h^e}{\partial \xi}(\xi) = \sum_{j=1}^{N_{1d}^{SP}} \frac{U_j^{b,e}}{|J|_j^e} \frac{\partial l_j^{SP}}{\partial \xi}(\xi), \quad \text{for } \xi \in [0,1] \tag{213}$$

If $U_{e-1/2}$ and $U_{e+1/2}$ are the common state values (computed, for example, using Equation (207)), the gradient $\frac{\partial U_h^e}{\partial \xi}$ can be corrected into a p-degree polynomial following the FR approach:

$$\frac{\partial \tilde{U}_h^e}{\partial \xi}(\xi) = \frac{\partial U_h^e}{\partial \xi}(\xi) + \left(U_{e-1/2} - U_h^e(0)\right) \frac{\partial g_R^e}{\partial \xi}(\xi) + \left(U_{e+1/2} - U_h^e(1)\right) \frac{\partial g_L^e}{\partial \xi}(\xi) \tag{214}$$

Here, g_L^e and g_R^e are the left and right correction functions at the right and left interfaces of Ω^e, respectively. It is important to note that the superscripts L and R refer to the sides of the interface, not the element side, as originally done in Huynh's papers [67, 66]. For example, g_L^e has the superscript L because it is used on the left side of the interface $e+1/2$, while g_R^e is defined analogously for the right side of the interface at $e-1/2$. These correction functions are polynomials of degree $p+1$ that approximate zero in a specific manner [67] and satisfy the following conditions:

$$g_L^e(1) = 1 \quad \text{and} \quad g_L^e(0) = 0 \tag{215}$$

$$g_R^e(1) = 0 \quad \text{and} \quad g_R^e(0) = 1 \tag{216}$$

With these correction functions, $\frac{\partial \tilde{U}_h^e}{\partial \xi}$ is a polynomial of degree p, though it remains discontinuous across elements. To address this, a further correction step introduces common gradient values at the element interfaces (computed, for instance, using Eq: 210 and Eq: 211):

$$\frac{\partial \tilde{\tilde{U}}_h^e}{\partial \xi}(\xi) = \frac{\partial \tilde{U}_h^e}{\partial \xi}(\xi) + \left[\frac{\partial \tilde{U}_h^e}{\partial \xi}\Big|_{e-1/2} - \frac{\partial \tilde{U}_h^e}{\partial \xi}(0)\right] g_R^e(\xi) + \left[\frac{\partial \tilde{U}_h^e}{\partial \xi}\Big|_{e+1/2} - \frac{\partial \tilde{U}_h^e}{\partial \xi}(1)\right] g_L^e(\xi) \tag{217}$$

Equation (217) defines a $(p+1)$-degree polynomial for the gradient of U along the ξ direction, ensuring continuity across the computational domain. This gradient is then evaluated at all flux points to obtain $\left(\frac{\partial U}{\partial \xi}\right)_{C_k}$ for $k \in \{1, \ldots, N_{1d}^{FP}\}$. Finally, using these values of $\left(\frac{\partial U}{\partial \xi}\right)_{C_k}$, Equation (212) is applied to compute the gradient along the x direction used for flux calculations at flux points.

This methodology is termed the "SDLIFT" approach, as it combines the SD method with lifting/correction functions in the FR framework. It allows for different choices in computing common states and gradients at element interfaces, each corresponding to a numerical diffusion scheme. Different diffusion schemes (or correction schemese) are available: Bassi and Rebay 1 scheme, Bassi and Rebay 2 scheme, I-continuous scheme. For further insights, see the work done by Marchal [111].

6.3.7 Extension to 2D and 3D

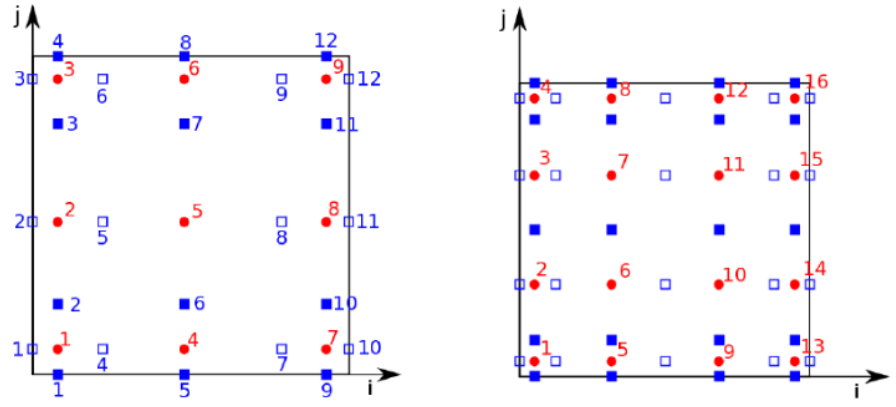

(a) Solution points and flux points in 2D inside one cell for $p = 2$ case.

(b) Solution points and flux points in 2D inside one cell for $p = 3$ case.

Figure 55: Positions of solution points (●) and flux points (□) for i-direction and (■) for j-direction in 2D inside one cell for p = 2 in (a) and p = 3 in (b). Figures from [95].

For 2D and 3D cases, the solution and flux points are arranged direction by direction, repeating the 1D process described in the previous paragraph. Consequently, the solution points remain the Gauss points,

positioned in each direction, while the flux points can be either Legendre or Gauss-Lobatto points, also placed in each direction. Thus, if d represents the spatial dimension, the number of solution and flux points per cell are given by:

$$N_{SP} = (p+1)^d \tag{218}$$

$$N_{FP} = d \times (p+2)\frac{(p+1)^{d-1}}{(p+1)^d - 1} \tag{219}$$

A 2D example of the positions of solution and flux points for $p = 2$ and $p = 3$ is illustrated in Figure 55. For 2D and 3D meshes, cells may have varying shapes and volumes. Unlike 1D cells, which are always segments and thus allow for uniform placement of points, 2D and 3D cells require an isoparametric transformation to map all mesh cells from the physical domain (x, y, z) to a standard cubic element $(\xi, \eta, \zeta) \in [0, 1]^3$. This transformation is typically expressed as:

$$\begin{pmatrix} x \\ y \\ z \end{pmatrix} = K \sum_{i=1}^{K} M_i(\xi, \eta, \zeta) \begin{pmatrix} x_i \\ y_i \\ z_i \end{pmatrix} \tag{220}$$

where K is the number of points defining the physical element (e.g., $K = 4$ for a tetrahedral element or $K = 8$ for a hexahedral element), (x_i, y_i, z_i) are the Cartesian coordinates of these points, and $M_i(\xi, \eta, \zeta)$ are the shape functions. An example of shape function computation in 2D is provided in [95].
For the transformation given above, the Jacobian matrix is:

$$J_{\text{iso}} = \frac{\partial(x, y, z)}{\partial(\xi, \eta, \zeta)} = \begin{pmatrix} \frac{\partial x}{\partial \xi} & \frac{\partial x}{\partial \eta} & \frac{\partial x}{\partial \zeta} \\ \frac{\partial y}{\partial \xi} & \frac{\partial y}{\partial \eta} & \frac{\partial y}{\partial \zeta} \\ \frac{\partial z}{\partial \xi} & \frac{\partial z}{\partial \eta} & \frac{\partial z}{\partial \zeta} \end{pmatrix} \tag{221}$$

If the transformation is non-singular ($|J_{\text{iso}}| \neq 0$), its inverse transformation (from physical space to isoparametric space) exists and is given by:

$$J_{\text{iso}}^{-1} = \frac{\partial(\xi, \eta, \zeta)}{\partial(x, y, z)} = \begin{pmatrix} \frac{\partial \xi}{\partial x} & \frac{\partial \xi}{\partial y} & \frac{\partial \xi}{\partial z} \\ \frac{\partial \eta}{\partial x} & \frac{\partial \eta}{\partial y} & \frac{\partial \eta}{\partial z} \\ \frac{\partial \zeta}{\partial x} & \frac{\partial \zeta}{\partial y} & \frac{\partial \zeta}{\partial z} \end{pmatrix} \tag{222}$$

Consider unsteady 3D equations written in conservative form (such as the unsteady compressible 3D Navier-Stokes equations):

$$\frac{\partial \mathbf{U}}{\partial t} + \frac{\partial \mathbf{F}}{\partial x} + \frac{\partial \mathbf{G}}{\partial y} + \frac{\partial \mathbf{H}}{\partial z} = 0 \tag{223}$$

where $\mathbf{U}$ is the vector of conserved variables, and $\mathbf{F}$, $\mathbf{G}$, and $\mathbf{H}$ represent the total fluxes in the x, y, and z directions, respectively. In the isoparametric domain, this equation transforms to:

$$\frac{\partial \tilde{\mathbf{U}}}{\partial t} + \frac{\partial \tilde{\mathbf{F}}}{\partial x} + \frac{\partial \tilde{\mathbf{G}}}{\partial y} + \frac{\partial \tilde{\mathbf{H}}}{\partial z} = 0 \tag{224}$$

with

$$\tilde{\mathbf{U}} = |J_{\text{iso}}|\mathbf{U} \tag{225}$$

$$\begin{pmatrix} \tilde{\mathbf{F}} \\ \tilde{\mathbf{G}} \\ \tilde{\mathbf{H}} \end{pmatrix} = |J_{\text{iso}}| J_{\text{iso}}^{-1} \begin{pmatrix} \mathbf{F} \\ \mathbf{G} \\ \mathbf{H} \end{pmatrix} \tag{226}$$

At each time step, space discretization is performed in the isoparametric space, and then the updated solution in the physical space is computed using the above transformations. For more details on the spatial discretization of the unsteady compressible 3D Navier-Stokes equations check the work of Sun et al. (2006) [166].

6.4 Immersed Boundary Conditions (IBC)

The immersed boundary condition (IBC) method is a technique used in CFD to simulate fluid flow around complex geometries without requiring a body-fitted mesh that follows the boundaries of these geometries exactly. This avoids cells of low quality for complex surfaces such as the pores of a TPMS. The main idea around this method is that instead of modifying the mesh to conform to the geometry, we keep the computational grid fixed and allow the boundary to pass through it, using a combination of interpolation and/or forcing terms to apply boundary conditions at grid points close to the immersed boundary.
Since Peskin's pioneering work [140], various IBC methods have been developed, mostly for incompressible flows.

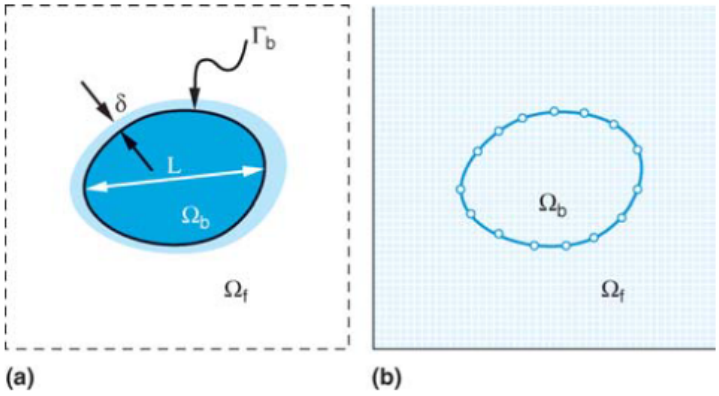

Figure 56: (a) Schematic showing a generic body past which flow is to be simulated. The body occupies the volume Ω_b with boundary Γ_b. The body has a characteristic length scale L, and a boundary layer of thickness δ develops over the body. (b) Schematic of body immersed in a Cartesian grid on which the governing equations are discretized.

If we consider a body volume Ω_b, with surface Γ_b, embedded in a fluid volume Ω_f as shown in Figure56the NS equations can be simplified in the form:

$$\begin{cases} \mathcal{N}(\mathbf{q}) = \mathbf{0}, \text{ in } \Omega_f \\ \text{with } \mathbf{q} = \mathbf{q}_\Gamma \text{ on } \Gamma_b \end{cases} \tag{227}$$

where $\mathcal{N}$ is the NS operator and $\mathbf{q} = \{\mathbf{U}, p, ...\}$ are the variables of the NS equations. Using Eq.227, we explain the two main categories of IB methods:

1. **Continuous Forcing Methods**:

   introduction of a fictitious forcing term $\mathbf{f}_b$ in the governing equations continuously over the entire fluid domain:

   $$\begin{cases} \mathcal{N}(\mathbf{q}) = \mathbf{f}_b, \text{ in } \Omega \\ \text{with } \mathbf{q} = \mathbf{q}_\Gamma \text{ on } \Gamma_b \end{cases} \tag{228}$$

   So that after the spatial discretization, the system of discrete equations to solve is:

   $$[\mathcal{N}]\{\mathbf{q}\} = \{\mathbf{f}_b\} \tag{229}$$

   In this category we have IBC models such as the classical one introduced by Peskin [140], where the boundaries are seen as elastic media that exert localized elastic forces on the fluid:

   $$\mathbf{f}_b(\mathbf{x}, t) = \sum_k \mathbf{F}_\mathbf{k}(t) d(|\mathbf{x} - \mathbf{X}_\mathbf{k}|) \tag{230}$$

   where:

- $\mathbf{F_k}(t)$ is the forcing term, that should be an elastic constitutive law such as Hooke's law;
- $\mathbf{x}$ is a grid point coordinate;
- $\mathbf{X_k}$ is the boundary coordinate k;
- $d(x)$ is a distribution function, that describes the way the forcing term is spread based on the distance $x = |\mathbf{x} - \mathbf{X_k}|$ from the boundary coordinate.

It becomes immediately evident that what differentiates the IBMs is the choice of $\mathbf{F_k}(t)$ and $d(x)$.

The idea of Peskin for elastic bodies has been extended for rigid ones by Goldstein et al.[37] and Saiki, Biringen et al. [153]), with the generic forcing term defined as:

$$\mathbf{F_k}(t) = \alpha \int_0^t \mathbf{U}(\tau) d\tau + \beta \mathbf{U}(t) \tag{231}$$

so that the solid can be seen as a damped oscillator defined by the parameters α and β.

The most promising method of this category is the volume penalization technique also called Brinkman Penalization Method (BPM), proposed by Arquis and Caltagirone [6], which models the solid body as a porous medium with very small permeability while the liquid has infinite permeability, so that:

$$\alpha = 0,\ \beta = \frac{\mu}{K}$$

where μ is the viscosity of the fluid and K is the fictitious permeability to be defined.

2. **Discrete Forcing Methods**:

application of forcing terms at discrete points or cells close to the boundaries (called "ghost" points or cells), often using interpolation schemes to map the forces from the structure to the fluid grid and vice versa. This means that the IBC is defined after the spatial discretization modifying the discretized NS operator $\mathcal{N}'$ and adding a discretized forcing term $\mathbf{r}$ to the boundary and ghost cells. Thus we solve a system of discrete equations of the form:

$$[\mathcal{N}]\{\mathbf{q}\} = \{\mathbf{f'}_b\} \tag{232}$$

where $\{\mathbf{f'}_b\} = [\mathcal{N}]\{\mathbf{q}\} - [\mathcal{N}']\{\mathbf{q}\}\{\mathbf{r}\}$.

In this category the most promising method is the Direct Forcing Method (DFM) proposed initially by Mohd-Yusof [121]. It uses a Cartesian grid which contains both fluid and solid cells. The latter are then split into ghost and pure solid cells. The number of ghost cell depends on the scheme used for the space discretization and the direct forcing is applied only on the ghost cells or points through multi-dimensional interpolations.

A general review of immersed boundary methods can be found in Mittal & Iaccarino [119]. The main difference between the two approaches is that the Continous Forcing Approach is independent from the spatial discretization schema allowing for more flexibility and easier implementation, while the discrete approach depending on the discretization schema, is has a more complex implementation that can be case dependent but can allow an increased control over the method, especially in terms of accuracy and stability. To have a more clear comparison between the two approaches we recommend the article of Piquet, Roussel et al. [141] the differences between the most promising methods for both categories: BPM vs DFM. The numerical comparison shows that, with sufficient mesh resolution, the BPM and the DFM methods yield qualitatively similar results. In all considered cases, the BPM is found to be a suitable and a possibly competitive method for IBM in terms of predictive performance, accuracy and computational cost. However, despite its simplicity, the BPM method suffers slightly from a lack of regularity in the very near-wall pressure fluctuations, especially for the turbulent case. This is attributed to the fact that the method requires no specific pressure condition at the fluid/solid interface. On the other hand, the more regular DFM uses ghost-cells to reconstruct the values inside the solid boundaries by projection of the image points from the interface leading to a comparatively hard implementation in 3D cases.
In the following discussion we focus on the continuous forcing approach called Brinkmann Penalization Method (BPM), that is the one implemented on the JAGUAR code.

6.4.1 Brinkmann Penalization Method

JAGUAR code implements a BPM which has been adapted to the SDM by H. D'Ayer [38], which work is still on-going at the present date.
As we have already mentioned, the BPM see the solid as a porous media with really low porosity so that the forcing term can be defined using Eq.231 with the assumptions defined by Arquis et al. [6] that $\alpha = 0$, $\beta = \frac{\mu}{K}$ as:

$$\mathbf{f}_b(\mathbf{x}, t) = \sum_k \frac{\mu}{K} \mathbf{U}(t) d(|\mathbf{x} - \mathbf{X_k}|) \tag{233}$$

and can be even simplified with the following notation [6] [102]:

$$\mathbf{f}_b(\mathbf{x}, t) = \frac{1}{\eta} \chi(\mathbf{x}, t) \mathbf{U}(t) \tag{234}$$

where:

- $\eta = \alpha\phi$: penalization coefficient in the form of a normalized viscous permeability with $0 < \eta \ll 1$, α a coefficient and *phi* the porosity, both depending on the implementation;
- $\chi(\mathbf{x}, t) = d(|\mathbf{x} - \mathbf{X_k}|)$: (characteristic) mask function so that $\chi \in [0, 1]$ so that if solid $\chi = 1$, if fluid $\chi = 0$ and if on boundary points $\chi \in (0, 1)$ based on the definition of the mask function.

The BPM method was successfully adapted to the incompressible NS equations by Arquis et al. [6], and later extended to the compressible regime by Liu et al. [102]. Both studies demonstrated the accuracy and stability of the method through direct numerical simulations, validated against analytical solutions of one- and two-dimensional benchmark cases. Subsequent research has provided further validation and analysis, with additional improvements proposed by other authors [117, 181, 26]. Despite these advancements, BPM encounters challenges at high Reynolds numbers, particularly due to the need for finer grids. This requirement can lead to a significant increase in the number of solution points and necessitates the redefinition of the mask function in relation to mesh size. To mitigate these issues, IBM-compliant wall models and strategies for local or adaptive grid refinement have been developed.

6.5 Temporal Discretization

In the preceding sections of this chapter, the spatial discretization of Eq. 42 using the Spectral Difference (SD) method was discussed, culminating in Eq. 226, which can be expressed in the following generic form:

$$\frac{d\hat{U}}{dt} + \nabla_\xi \cdot \hat{F} = \hat{S} \quad \Leftrightarrow \quad \frac{d\hat{U}}{dt} = \hat{S} - \nabla_\xi \cdot \hat{F} \equiv R \tag{235}$$

where $R = \hat{S} - \nabla_\xi \cdot \hat{F}$ is known as the Residual, representing the discretization of the source terms and flux divergence. To advance $\hat{U}$ in time from t to $t + \Delta t$, with $\Delta t(t)$ being the timestep computed at time t, the simplest method is to use an explicit Euler integration:

$$\hat{U}(t + \Delta t(t)) = \hat{U}(t) + \Delta t(t)\, R(t) \quad \text{or equivalently} \quad \hat{U}^{n+1} = \hat{U}^n + (\Delta t)_n\, R_n \tag{236}$$

where n denotes the current time iteration. However, explicit Euler integration is only first-order accurate in time. To achieve higher order accuracy in time, more complex time integration methods have been developed. One commonly used approach is the Runge-Kutta (RK) scheme, which was employed in this work.

6.5.1 Runge-Kutta Schemes

Characteristics of a Runge-Kutta Scheme
A Runge-Kutta (RK) scheme is characterized by four main properties:

1. The number of stages, denoted Q.
2. The order of accuracy, denoted S.

3. Stability: either A-stable or L-stable. L-stability is a special case of A-stability that is more effective for solving nonlinear stiff equations.

4. The type of integration: explicit or implicit.

RK methods are denoted as *nameRK(Q,S)*, providing information on the order of accuracy and the number of stages.

General Formula of a Runge-Kutta Scheme

The RK integration process involves two main tasks:

Task 1: Compute the Q stage values $\hat{U}_q$ using the stage equation:

$$\hat{U}_q = \hat{U}^n + (\Delta t)_n \sum_{j=1}^{Q} a_{qj} R_j \quad \text{for } 1 \leq q \leq Q \tag{237}$$

with $R_1 = R_n$.

Task 2: Compute the solution at the next time instant $n+1$ using the update equation:

$$\hat{U}^{n+1} = \hat{U}^n + (\Delta t)_n \sum_{q=1}^{Q} b_q R_q \tag{238}$$

where $R_j = R(\hat{U}_j)$, $\mathbf{A} = [a_{qj}]_{1 \leq q,j \leq Q}$ is the stage coefficient matrix, and $\mathbf{b} = [b_q]^T_{1 \leq q \leq Q}$ is the weight vector, both specified by the RK method. These coefficients are typically organized in a Butcher tableau [28] as shown in Table 6 for the general case.

$\mathbf{c}$	$\mathbf{A}$
	$\mathbf{b}^T$

Table 6: General form of a Butcher tableau.

These coefficients are determined by solving a system of equations based on the desired order of accuracy and specific dissipation and dispersion properties [28]. Note that since R does not depend on time in this work, the vector $\mathbf{c}$ in the RK method is not used in Eqs. (237) and (238). However, $\mathbf{c}$ is employed to determine the current time at a given RK stage (see Eq. (268)). Only explicit RK schemes are considered in this work, as implicit schemes are not discussed in the following sections.

6.5.2 Explicit Runge-Kutta Schemes

For explicit RK schemes, $a_{qj} = 0$ for $j \geq q$, meaning that the matrix $\mathbf{A}$ is strictly lower triangular. Consequently, each stage $\hat{U}_q$ is "explicitly" known based on the values of the previous stages, and Eq. (237) can be reformulated as:

$$\hat{U}_q = \hat{U}^n + (\Delta t)_n \sum_{j=1}^{q-1} a_{qj} R_j \quad \text{for } 1 \leq q \leq Q \tag{239}$$

Explicit RK schemes are typically denoted as ERK(Q,S). Examples of Butcher's tableau for forward Euler, ERK(2,2), and ERK(4,4) methods can be found in [28].

Although explicit RK schemes are effective for integrating various equations, more advanced schemes have been developed for specific applications. For instance, to reduce the memory cost of RK methods, low-storage RK schemes have been developed, where $\hat{U}_q$ can be computed using only the values of R_{q-1}:

$$\hat{U}_q = \hat{U}^n + (\Delta t)_n \gamma_q R_{q-1} \quad \text{for } 1 \leq q \leq Q \tag{240}$$

with $R_0 = R_n$ and $\boldsymbol{\gamma} = [\gamma_q]^T_{1 \leq q \leq Q}$ being the input RK coefficients for the low-storage RK scheme. Consequently, for low-storage RK schemes, the solution at time iteration $n+1$ is:

$$\hat{U}^{n+1} \equiv \hat{U}_Q = \hat{U}^n + (\Delta t)_n \gamma_Q R_{Q-1} \tag{241}$$

A popular low-storage RK scheme is the explicit RK of second-order with six stages and low-dissipation and low-dispersion, designed by Bogey and Bailly for aeroacoustic applications [23], denoted ERK(6,2)LDLD. More recently, Vanharen et al. [179] developed a fourth-order, six-stage low-storage RK scheme designed for SD methods with higher stability than the ERK(6,2)LDLD, where the last two coefficients, γ_5 and γ_6, depend on the polynomial degree p. Further details on low-storage RK schemes can be found in [30], particularly on how Butcher's coefficients can be manipulated to obtain a single coefficient γ_q to update the solution at each stage.
However, it is important to note that not all RK schemes can be recast into low-storage RK processes. Another class of Explicit Runge-Kutta (ERK) schemes has been developed specifically for shock applications, where strong discontinuities may appear in the computational domain. These were originally named Total Variation Diminishing (TVD) RK schemes because they were designed to ensure that the total variation (TV) of each component $\hat{U}_i^n$ of the numerical solution vector $\hat{U}^n$ [58]:

$$\mathrm{TV}(\hat{U}^n) = \sum_{i=1}^{\mathrm{DOF}} |\hat{U}_i^n - \hat{U}_{i-1}^n| \tag{242}$$

does not increase over time, meaning that [57]:

$$\mathrm{TV}(\hat{U}^{n+1}) \leq \mathrm{TV}(\hat{U}^n) \tag{243}$$

The solution at each stage of these schemes is often presented in the form of Eq. (244), introduced by Shu and Osher [159]:

$$\hat{U}_q = \sum_{j=0}^{q-1} \left(\alpha_{qj} \hat{U}_j + (\Delta t)_n \beta_{qj} R_j \right) \quad \text{for } 1 \leq q \leq Q \tag{244}$$

with $\hat{U}_0 = \hat{U}^n$ and $\hat{U}_Q = \hat{U}^{n+1}$, where the coefficients α_{qj} and β_{qj} are specified by the TVD-RK scheme. For consistency, these coefficients satisfy:

$$\sum_{j=0}^{q-1} \alpha_{qj} = 1 \quad \text{for } q \in \{1, \ldots, Q\} \tag{245}$$

The formulation in Eq. (244) is preferred for constructing TVD-RK schemes because it is easier to use compared to the Butcher tableau formulation shown in Eqs. (237) and (238). However, any RK scheme written in the Shu-Osher representation has an equivalent Butcher tableau, and vice versa. The relationship between the coefficients α_{qj}, β_{qj}, and the Butcher matrices can be found in [46].
In this work, the five-stage fourth-order Strong Stability Preserving (SSP) RK scheme by Spiteri and Ruuth [161].

6.5.3 Stability Conditions

Explicit time integration methods are subject to stability criteria that limit the timestep to a maximum value. These stability criteria are based on the Courant-Friedrichs-Lewy (CFL) and Fourier (Fo) conditions, which are related to the spatial discretization of the convective and diffusive fluxes, respectively.
First, the convective timestep at each solution point (SP) is determined using the CFL number:

$$\mathrm{CFL} = \frac{(||\mathbf{u}||_2 + c)\Delta t_{\mathrm{conv}}}{\Delta_{\mathrm{SP}}} \quad \Leftrightarrow \quad \Delta t_{\mathrm{conv}} = \frac{\mathrm{CFL} \times \Delta_{\mathrm{SP}}}{||\mathbf{u}||_2 + c} \tag{246}$$

where $||\mathbf{u}||_2 + c$ and Δ_{SP} are the maximum eigenvalue of the convective flux Jacobian matrix and the characteristic size evaluated at the given SP, respectively, given by:

$$\Delta_{\mathrm{SP}} = |J|_{\mathrm{SP}}^{1/d} \times \frac{1}{p+1} \tag{247}$$

Note that Eq. (247) assumes that SPs are equally spaced, which is not true for any value of p if Eq. (176) is used for their location in the isoparametric domain.
Secondly, a diffusive timestep involving viscosity, thermal, and species diffusion effects is computed using the Fo number:

$$\mathrm{Fo} = \frac{\Delta t_{\mathrm{diff}}}{\Delta_{\mathrm{SP}}^2 \max(\nu, \frac{\nu}{\mathrm{Pr}}, \frac{\nu}{\mathrm{Sc}_k})} \quad \Leftrightarrow \quad \Delta t_{\mathrm{diff}} = \mathrm{Fo} \times \frac{\Delta_{\mathrm{SP}}^2}{\max(\nu, \frac{\nu}{\mathrm{Pr}}, \frac{\nu}{\mathrm{Sc}_k})} \tag{248}$$

The timestep at a given SP is then taken as the minimum of the convective and diffusive timesteps:

$$\Delta t = \min(\Delta t_{\mathrm{conv}}, \Delta t_{\mathrm{diff}}) \tag{249}$$

The CFL and Fo numbers are input parameters that depend on the temporal scheme used and the polynomial degree p. Generally, for a given time integration scheme, the values of CFL and Fo need to be decreased as p increases.

6.6 Pressure Gradient Scaling (PGS) method

The PGS method is used to enhance the computational efficiency of numerical simulations involving compressible fluid flow at low Mach numbers, particularly when the pressure field exhibits near-uniformity in space. This characteristic is typically observed at low Mach numbers but it is not a necessary condition. The study demonstrates that in such scenarios, the pressure gradient within the momentum equation can be scaled by a factor $\frac{1}{\alpha^2}$ (where $\alpha > 1$) without significant impact, assuming α is not excessively large and spatial variations in pressure are negligible. This scaling adjustment effectively reduces the acoustic speed by α, consequently increasing the effective Mach number by the same factor. This alignment mitigates the disparity between acoustic and convective time scales, thereby enhancing the computational efficiency of various numerical schemes tailored for compressible flows. Especially we remind that explicit numerical schemes are computationally efficient but they have a severe stability condition on the time step known as CFL condition:

$$\text{CFL condition: } \Delta t = \frac{\Delta x}{c} \cdot CFL \propto Ma \cdot \Delta x \cdot CFL \tag{250}$$

where usually CFL has to be small such that $0 < CFL < 1$.
We present briefly the main ideas around the PGS method as introduced by O'Rourke et al. [146].
We define the pressure fluctuations p' based on the volume averaged pressure $\bar{p}(t) = \frac{\iiint_V p(\mathbf{x},t)d\mathbf{x}}{V}$ such that:

$$p'(t) = p(\mathbf{x}, t) - \bar{p}(t) \tag{251}$$

Under the following assumptions:

- low pressure inhomogeneities: $\frac{p'(\mathbf{x},t)}{\bar{p}(t)} << 1$
- PGS coefficient α such that: $\frac{\alpha(t)p'(\mathbf{x},t)}{\bar{p}(t)} << 1$

compressible NS equations with the addition of a closure state equation can be modified in the following form:

$$\begin{cases} \frac{D\rho}{Dt} = \rho\nabla \cdot \mathbf{u} + R \\ \rho\frac{D\mathbf{u}}{Dt} = -\frac{1}{\alpha^2}\nabla\hat{p} + \mathbf{S} \\ \rho\frac{De}{Dt} = -\hat{p}\nabla \cdot \mathbf{u} + Q \\ \hat{p} = f(\rho, e) \end{cases} \tag{252}$$

where R,S and Q are generic source terms and $\hat{p}(\mathbf{x}, t) = \bar{p}(t) + \alpha^2(t)p'(\mathbf{x}, t)$ is a modified volume averaged pressure. This equations are formally equal to the starting ones but they see a different sound speed, reduced of a factor α so that the Mach number is increased of the same factor and the time step as well. Typical values of alp$\hat{\text{h}}$a can be around $100 - 150$ but in general it depends on the specific case.
At this point it becomes evident the power and simplicity of this method in allowing to increase the time steps of important factors for both explicit and implicit schemes, even if we gain the most over the first ones. Usually the PGS coefficient is dynamic so that $\alpha = \alpha(t)$ is adapted to the highest pressure inhomogeneity in the flow at the previous time step. One example of how this coefficient can be time dependent is proposed:

$$\alpha^2(t^{n+1}) = \alpha^2(t^n) \cdot \frac{\bar{p}}{|\max(\hat{p} - \bar{p})|} \tag{253}$$

where *tol* is a user-defined tolerance value. A common value is $tol = 0.01$. Really sophisticated variants of the PGS method use also relaxation models to smooth the dynamic variations of the coefficient α.

In conclusion, the PGS method provides a robust approach to enhance the performance in terms of CPU time of computational fluid dynamics simulations under conditions of nearly uniform pressure gradients, or simply low Mach number. By introducing the scaling factor α, derived from physical considerations, the method mitigates numerical inaccuracies while preserving the physical integrity of the flow equations as it has been proved by different authors in the context of FVM-based solvers, also coupled with turbulence models ([48]).

6.7 Synthetic Turbulence Injection

The objective of this section is to outline the methodology employed in this work for generating turbulence at the inlet of a CFD simulation with JAGUAR code.
In general, the injection of a turbulent velocity field at an inlet, noted $\mathbf{u_{in}^{turb}}$, is mostly done by injecting a time-average velocity profile $\mathbf{\bar{u}_{in}}$ superimposed by a turbulent fluctuation velocity $\mathbf{u'_{in}}$ in coming from the Reynolds decomposition:

$$\mathbf{u_{in}^{turb}} = \mathbf{\bar{u}_{in}} + \mathbf{u'_{in}} \tag{254}$$

The time-average velocity $\mathbf{\bar{u}_{in}}$ can be imposed based on the velocity profile that we want. If there are no walls in the proximity, as in our configuration, we can simply impose a constant value. While if we are simulating a turbulent channel or a turbulent pipe, we have to use a mean velocity model for that particular case, given either from an analytical analysis either from experimental or numerical datasets. On the other hand, the turbulent velocity fluctuation $\mathbf{u'_{in}}$ injection at the inlet presents a more delicate discussion because it is a vast topic of research and plenty of approaches exist in the literature. The one implemented on JAGUAR is a Synthetic Random Fourier Method (SRFM) [111] where turbulent fluctuations are injected by assimilating them to a sum of random Fourier modes.

6.7.1 The Synthetic Random Fourier Method

Originally introduced by Kraichnan [85] for the diffusion of particles in random velocity fields, the synthetic random Fourier method generates a divergence-free homogeneous isotropic turbulence (HIT) field by summing N Fourier modes, each characterized by a wavenumber vector κ_n for $n \in \{1, \dots, N\}$. In Kraichnan's approach, the components of κ_n are chosen stochastically to satisfy a given energy spectrum. For instance, to achieve a power-law (PP) spectrum as described in Eq. 133, each component of κ_n should be drawn from a Gaussian distribution with a standard deviation of $\kappa_e/2$. However, this stochastic method becomes impractical if a different energy spectrum is required, as it necessitates deriving a new stochastic distribution for κ_n.
To address this, a more practical approach is to determine the components of κ_n deterministically using an explicit mathematical formula derived from the desired energy spectrum. Following the works of Karweit et al. [75] and Bechara et al. [16], a turbulent velocity vector at a given point x can be computed using:

$$u'_{in}(x) = 2\sum_{n=1}^{N} u_{tn}\cos(\kappa_n \cdot x + \psi_n)\sigma_n \tag{255}$$

where u_{tn}, ψ_n, and σ_n represent the amplitude, phase, and direction (unit vector) of the n-th Fourier mode associated with the wavenumber vector κ_n.

- **Determination of u_{tn}**

  The amplitude u_{tn} is determined from the turbulent kinetic energy spectrum E, chosen by the user, using:

  $$u_{tn} = \sqrt{E(\kappa_n)\Delta\kappa_n} \tag{256}$$

  where $\kappa_n = \|\kappa_n\|_2$ and $\Delta\kappa_n$ represents the interval between consecutive modes. This interval can be either linear or logarithmic:

  - Linear Spacing:

    $$\Delta\kappa_n = \frac{\kappa_N - \kappa_1}{N-1} \tag{257}$$

    with $\kappa_n = \kappa_1 + (n-1)\Delta\kappa_{lin}$
  - Logarithmic Spacing:

    $$\Delta\kappa_n = \kappa_{n+1} - \kappa_n \tag{258}$$

    with $\kappa_n = \exp(\ln(\kappa_1) + (n-1)\Delta\kappa_{log})$ and

    $$\Delta\kappa_{log} = \frac{\ln(\kappa_N) - \ln(\kappa_1)}{N-1} \tag{259}$$

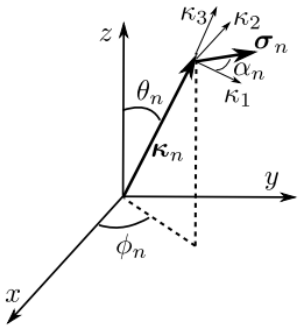

Figure 57: Geometry of the n-th Fourier mode.

The logarithmic distribution provides a better resolution of the spectrum in the lower wavenumber range, which is associated with the larger, energy-containing eddies. A useful property to verify that the generated field aligns with the expected HIT characteristics is:

$$\sum_{n=1}^{N} u_{tn}^2 = \text{TKE} = \frac{3}{2} u_{rms}^2 \tag{260}$$

where TKE denotes the turbulent kinetic energy and u_{rms} is the root mean square velocity.

- **Determination of κ_n Components, ψ_n, and σ_n:**

  To ensure the turbulent velocity field satisfies the incompressibility condition ($\nabla \cdot u'_{in} = 0$), each Fourier mode must adhere to the condition:

$$\kappa_n \cdot \sigma_n = 0 \tag{261}$$

  This implies that the wavenumber vector κ_n and the unit vector σ_n are orthogonal. The wavenumber vector κ_n is described using its spherical coordinates $(\kappa_n, \phi_n, \theta_n)$, while σ_n is determined by its polar angle α_n in the (κ_1, κ_2) plane, as illustrated in Figure 57.

  To generate the homogeneous isotropic turbulence (HIT) field, appropriate probability density functions are used for the four random angles ϕ_n, θ_n, ψ_n, and α_n. These distributions are:

  – Uniform Distributions:

$$P(\phi_n) = P(\alpha_n) = P(\psi_n) = \frac{1}{2\pi} \tag{262}$$

  – Sine Distribution:

$$P(\theta_n) = \sin(\theta_n) \tag{263}$$

  To generate these angles, free software such as that provided by Nishimura & Matsumoto [110] can be used. This software generates random numbers in the range $[0, 1]$ with a uniform distribution. To obtain ϕ_n, α_n, and ψ_n, the generated number is multiplied by 2π.

  For θ_n, which requires a sine probability density function, the inverse transform method can be applied. Using this method, θ_n is computed as:

$$\theta_n = \cos^{-1}(2a - 1) \tag{264}$$

  where a is a random number uniformly distributed in $[0, 1]$, also generated by the software mentioned above.

  Once ϕ_n and θ_n are determined, the Cartesian components of κ_n are calculated as:

$$\kappa_n = \kappa_n \begin{pmatrix} \cos(\phi_n)\sin(\theta_n) \\ \sin(\phi_n)\sin(\theta_n) \\ \cos(\theta_n) \end{pmatrix} \tag{265}$$

where κ_n itself is computed using either Eq. 257 or Eq. 258.

For the unit vector σ_n, instead of directly computing α_n, an intermediate unit vector ζ_n is generated with random Cartesian components uniformly distributed in $[-1, 1]$. σ_n is then determined by:

$$\sigma_n = \frac{\zeta_n \times \kappa_n}{\|\zeta_n \times \kappa_n\|_2} \tag{266}$$

In practice, ζ_n can be generated using spherical coordinates, similar to the method for κ_n components. This approach ensures that σ_n satisfies the orthogonality condition ($\kappa_n \cdot \sigma_n = 0$), and the random polar angle α_n will be implicitly determined.

The steps to generate the turbulent velocity field u'_{in} at a given point x using this methodology are described carefully by Marchal [111].

- **Time-dependent synthetic HIT field**

  For turbulent injection through a boundary, it is necessary to introduce a time dependence in Eq. 255. This approach was implemented by Bailly and Juvé [9] by using a constant velocity vector $\vec{u}_c$, uniform in both time and space, which convects the turbulent field from an imaginary box outside the computational domain. Consequently, Eq. 255 becomes:

$$\vec{u}'_{\text{in}}(\vec{x}, t) = \frac{2}{N} \sum_{n=1}^{N} \vec{u}_{t_n} \cos\left(\vec{\kappa}_n \cdot (\vec{x} - t\vec{u}_c) + \psi_n\right) \sigma_n \tag{267}$$

  where t represents time. The formulation in Eq. (267) corresponds to Eq. (7) in Bailly and Juvé [9], with ω_n set to zero, and it is the formula utilized in this work. In practice, $\|\vec{u}_c\|^2 = U_b$ and is aligned with the axis of the channel or pipe.

  Since Explicit Runge-Kutta (ERK) methods are used for time integration, Eq. (267) is evaluated at each RK stage. Thus, the time t at each RK stage q, denoted as t_q, is required. This time is computed using the Butcher tableau of the RK method:

$$t_q = t_n + c_q(\Delta t)_n \tag{268}$$

  where t_n and $(\Delta t)_n$ are the time and timestep at the n-th time instant, respectively.

6.8 Numerical setup

After a deep dive into the ocean of numerical theory—no one can say we didn't do our bibliographical homework—it's finally time to get to the real action: the numerical setup we used to run DNS with the JAGUAR code.
We start presenting the state of the art simulation up to today presented by Jin et al. (2017) [70] that studied a simple configuration of porous media with DNS. Next we introduce our configuration intended to study TPMS porous media always through DNS. With this comparison we want to remark our effort compared to the actual state of the art, so that others can get inspired in not being afraid of jumping in the unknown.

6.8.1 State of the art

Y. Jin, M.-F. Uth, and H. Herwig from the Hamburg University of Technology (Germany) with A. V. Kuznetsov from the North Carolina State University (US) in 2017 proved through DNS simulations [70] that macroscopic turbulence does not exist in porous media, as the pore size restricts the size of turbulent structures. The underlying assumption is that there is no fundamental qualitatively different flow behaviour when the porous matrix is changed from two-dimensional regular to three-dimensional irregular geometry. Two-point correlations, integral length scales and energy spectra were used in order to answer the question of whether or not macroscopic turbulence can be found in porous media.
Their work represents our latest record of a numerical investigation through DNS in the field of porous media turbulence research, and thus we take their setup as inspiration for the validation of our approach. In particular they study a 2D geometry made by uniformly disposed bars as shown in Figure 58.
Jin et al. [72] use two different DNS solvers, i.e. FVM and LBM. Both methods have been tested against each other in Jin, Uth & Herwig (2015) [71] for the problem of a turbulent flow along a rough wall.

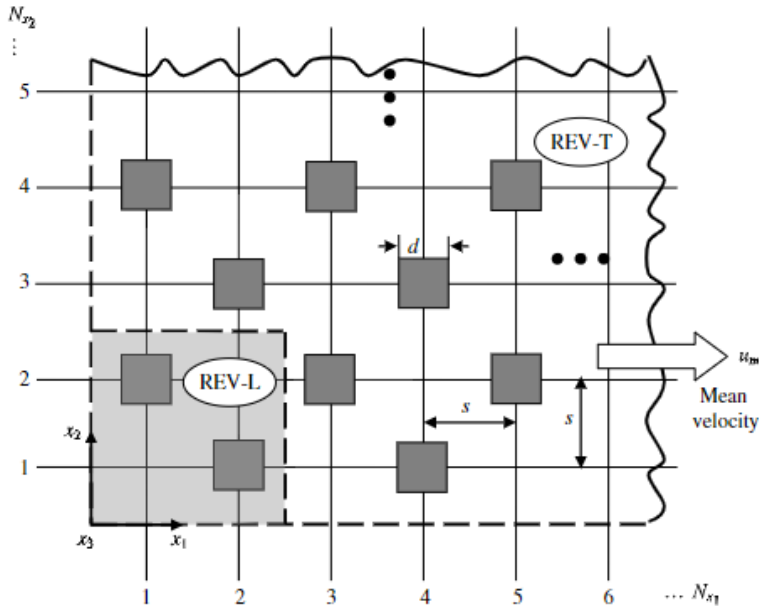

Figure 58: The Gradient Porous Material analysed by Jin et al. [72] made of 2D-disposed bars with rectangular section d so that the pore size is s. A generic representative elementary volume (REV) is represented here. It is the smallest subvolume of a porous matrix that shows the same flow behavior and its dimensions have been analyzed in the study in both the laminar and turbulent case: REV-L and REV-T respectively. Here, u_m is the mean flow velocity, N_{x1} is the size of the REV in the x_1 direction (in pore sizes), and N_{x2} is the size of the REV in the x_2 direction.

In this case, wall roughness was simulated by positioning two-dimensional bars on an otherwise smooth wall, creating a geometry that is similar to a porous medium. That's why they reproposed the same numerical setup of the previous work.
In particular, the DNS solvers are setup as follows:

- **FVM solver setup:**

  Incompressible NS equations are solved imposing a pressure gradient g_i in the momentum equation which ensures a particular flow rate. The time integration of the equations is done with a second-order implicit backward Euler method. To compute the derivatives of the velocity, the variables at the interfaces of the grid cells were obtained with linear interpolation. A second-order central difference scheme was used for spatial discretization. The pressure at the new time level was determined by the Poisson equation. The velocity was corrected by the pressure-implicit scheme with splitting of operators (PISO) pressure–velocity coupling. In this case the mesh is body-fitted with higher concentration in the near-wall region so that 36–123 million grid points where taken as DoF.

- **LBM solver setup:**

  The lattice Boltzmann equation is solved with a D3Q19 grid model for discrete velocities and the collision operator is approximated through the by BGK (Bhatnagar, Gross and Kook) method which models collisions as a relaxation to an equilibrium distribution function. In this case the mesh is a uniformly distributed Cartesian grid: 100–384 million grid points were used.

Periodicity is imposed on all the boundaries (inlet-outlet, left-right walls and buttom-up walls).
As regards the mesh resolution and domain size, they tested different configurations varying also the value of the porosity $\phi = 0.78 - 0.94$ and of the Reynolds number around $Re = 500 - 1000$ defined as: $Re = u_m d/\nu$, where u_m is the mean axial velocity and d is side of a bar transversal section (see Figure 58). The dimensions of the REV-T has been also studied and they concluded that a domain size of 6s x 4s x 4d is satisfactory, even if taking a larger one allows a more conservative approach.
The simulations were initialized so that the statistical values, such as the turbulent two-point correlations (e.g. in Figure 59), did not change with time any more. This process usually needs the computation of 250 wash-out cycles in one REV-L element, which is 1000 time units for the less resolved test case.

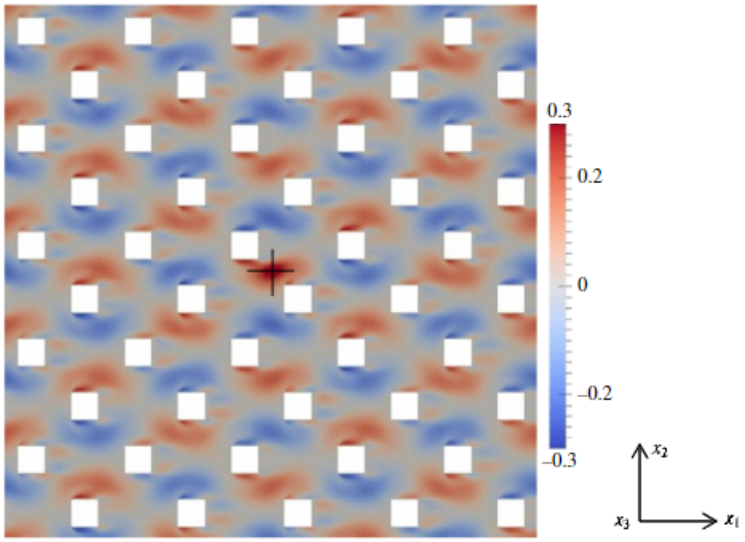

Figure 59: Contour line of the two-point (space) correlation $\frac{R_{11}}{u_m^2}$ in the computational domain for low resolved test case [72]. The correlation point x_0 is marked by the cross in the middle.

The CPU time (processor number × computing time) for one test case varied between 25 000 and 58 000 h.
As final note, Jin et al. tested two kinds of initial conditions: the first one is the uniform velocity field plus a sinusoidal perturbation while the second type of initial condition is an interpolation of the initial field from another fully developed turbulent flow. However they proved that in their configuration the statistical results of the fully developed flow field are not influenced by the initial field.

6.8.2 Our numerical configuration

We use the JAGUAR code and all its potential to have high-fidelity results while preserving reasonable CPU time.
We solve the compressible NS equations implementing a SDM for the spatial discretization with a polynomial degree of 4-5, using its original formulation approach for the gradients computation and an HLLC Riemann solver with Harten velocity correction. The location of the SP is taken using the Gauss-Chebychev quadrature points while the FP using the Gauss-Legendre quadrature points. The 3D Lagrange polynomials are used for the polynomial representation of degree p inside the cells. A PGS method is also implemented with a static PGS factor of 0.05 .
For the time discretization an explicit 4th-order and five steps SSP Runge-Kutta method as proposwd by Ruuth & Spiteri [161] is adopted. A CFL=0.2 is taken with a variable time step (initially defined small as 1e-09) depending on the local velocity at the simulation time.
In Table 7 we present more details about the parameters used to setup our SD solver.

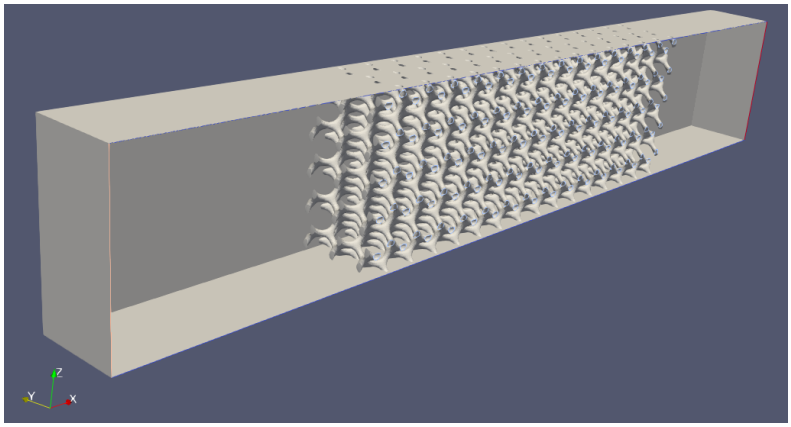

Figure 60: Computation domain of our simulation: case Gyroid struct=1.20 at Re=2500. Results in Section 7.3

.

Category	**Details**
SPLITTER	
Splitter	metis
Number of partitions	7
NUMERICAL SCHEMES	
Time integration scheme	rk54ruuspi
CFL number	0.2
Constant time step	no
Time step	1e-09
Last physical time	1000.0
Riemann solver	HLLC
Harten correction	comp velo
Harten coefficient	0.01
Interpolated field	primitive_p
p refinement	no
Polynomial order	4
Solution point location	gauss_cheby_1st
Flux point location	gauss_legendre
Polynomial representation	Lagrange
GAS CHEMISTRY	
Gamma	1.4
Cv	7.2×10^2
Prandtl number	0.7
Kind of viscosity law	Constant
Reference viscosity	1.7×10^{-4}
Use PGS	yes
PGS factor	0.5×10^{-3}
INFLOW DATA	
Mach	2.9×10^{-3}
α (XoZ)	0.0
β (XoY)	0.0
Pressure	1.0×10^5
Temperature	3.0×10^2

Table 7: Table of the main parameters (partitioning, numerical schemes, gas chemistry, and inflow data) of our SD solver run on JAGUAR code.

As regard the mesh, we use a hexahedric cells distributed uniformly (Cartesian mesh) in a box of size (L_x, L_y, L_z) so that the transversal section is a normalized square so that $L_y = L_z = D = 1m$. We tested different domain sizes with $L_x = 6m - 9m$ and different number of cells per D=1 m over a direction.

We take 60-100 cells per direction per D, values estimated taking into account the value of the injected kolmogorov scale with a downsizing safety factor equal to the number of pores per 1 m, that we call simply N_{pores}. This means that we compute the value of η with the Synthetic Random Fourier Modes method and then we take as smalles length-scale requirement of our simulation the value $(\Delta x)_{min} = \eta/N_{pores}$ and based on it we decide the number of cells per 1 m as $(\Delta x)_{min}$ with some tolerance. Moreover, each cell has a number of DoF equal to the number of SP inside it, i.e. $(p+1)^3$. So we have a mesh resolution of 6M-9M of cells meaning that the number of DoF is around 750M-1000M. Which is a lot. Then, the minimal length size resolved is around 3.33e-03 m and 1.67e-03 m. A representation of our setup is given in Figure 60.
In table 8 we present all the boundary conditions defined.

BOUNDARY CONDITIONS DATA	**Details**
ibc BC	
ibc activated	Yes
ibc penalization parameter	Auto
ibc geometry type	tpms
ibc tpms type	tpms topology
ibc tpms kx	$2\pi \times$ Nb_pores
ibc tpms ky	$2\pi \times$ Nb_pores
ibc tpms kz	$2\pi \times$ Nb_pores
ibc tpms struct	0.75
INLET BC	
Type	Inlet with Synthetic Injection
Injection type	Synthetic Random Fourier Modes
Velocity type	constant
U, V, W [m/s]	1.0, 0.0, 0.0
T [K]	300.00
Spectrum type	VKP spectrum
Nb Fourier modes	300
κ distrib.	Logarithmic
u_{rms} [m/s]	9.11e-02
$L_{e,VKP}$ [m]	2.28-01
L_{ref} [m]	1.00
$\kappa_{\text{kol}} = 1/\eta$ [1/m]	158.00
OUTLET BC	
Type	Pressure outlet
Relaxation	Yes
Pressure [Pa]	1.00e+05
BOTTOM-UP FACES BC	
Type	Periodic
LEFT-RIGHT FACES BC	
Type	Periodic
SPONGE ZONE	
Sponge zone activated	Yes

Table 8: Table of the Boundary conditions and sponge zone parameters of our SD solver run on JAGUAR code.

We use an IBM with an automatic determination of the penalization factor. In this way we define the geometry of the TPMS or porous media. Note that the IBM on JAGUAR has been already adapted for the TPMS geometry so that we have just to define the values (`tpms_name`, k_x, k_y, k_z) and the location in the domain of the media.
At the inlet we inject a synthetic turbulence so that the mean axial velocity is $U_{in} = 1m/s$, the Reynolds number is $Re = DU_{in}/\nu = 1/\nu$, the rate of turbulence Tu is around $Tu = 10\%$ and the energy containing scales are around the size of 2 pores. The method used for the injection is the Synthetic Random Fourier Modes Turbulence Injection Method (see Section 6.7) with a VKP spectrum, which parameters can be computed as done in Section 5.4.2 fixing the value of the energy containing length-scale $L_{e,max}$, the value of the viscosity and the rate of turbulence Tu. In our case, we take $L_{e,max} = 2s$, $\nu = Re^{-1}$ and

$Tu = 10\%$.
As regards the other BCs, we fix an output pressure and we impose the periodicity condition between the bottom-up and left-right faces.
Moreover, we add a sponge zone at the of the domain to avoid the reflection on the outlet face of numerical perturbations, that could make unstable the simulation or false the results.
Finally, what maybe interests more the reader, we discuss the effective CPU- time consumption of our numerical approach. We launched our simulations at GENCI, the French high-performance computing centres organization, using around 5000 CPUs. The average time to run a complete simulation of a porous media takes around 2M CPU hours, including an initialisation part of around 460k iterations where we play with the PGS factor and the degree of the SDM in order to boost the convergence. An example of routine used to initialize our simulations is presented in Table 9.

Init Step	**Nb Iterations**	**PGS Factor**	**p for SD**
1	100k	0.2	2
2	200k	0.1	2
3	100k	0.05	2
4	20k	0.2	4
5	20k	0.1	4
6	20k	0.05	4

Table 9: Table of the main steps to initialize a typical porous media simulation in our configuration with JAGUAR code.

Afterwards we can run the real simulation with the finest parameters specified in Table 7. At this stage we are interested in simulating a good physical time span to have good data also at low frequencies. Knowing that the time step is of the order of 2.0e-5 we can simulated each 25k iterations around half of physical second with a real time of 24h with 5000 CPUs. If we want to simulate at least a few seconds, let's say 3s, we need 3 days. Note that 24h for 25k iterations are required if we take 100 cells per 1 m, while it becomes 24h for 125k iterations if we take 60 cells per 1 m.

7 Results

The geometric and physical complexity of our problem fundamentally resides in selecting an appropriate numerical approach, which must carefully balance performance, stability, and precision, while also considering the available storage capacity. As highlighted in the introduction (Section 1), our objective is to advance the current understanding of turbulent flows in porous media. Achieving this ambitious goal required a comprehensive literature review and an extensive examination of the properties of PM, turbulence theory grounded in statistical approaches, and HO numerical methods, as detailed in Sections 2, 3, 4, 5, and 6. With a deeper understanding of PM and turbulence properties, coupled with insights into CFD and numerical methods, we defined our own numerical approach in Section 6.8. This framework allowed us to set clear research objectives, initiating a systematic analysis of turbulence in TPMS porous media. The analysis encompasses two key steps: first, validating our numerical setup, and second, investigating the influence of topology, inflow parameters, and other critical factors within porous media simulations.
We now present our contribution to this intricate and fascinating field of fluid dynamics, focusing on turbulence in porous media using the results obtained from our simulations with the SDM solver code JAGUAR, where the IBC and PGS methods were employed to enhance stability and efficiency.
Nevertheless, the essence of research extends beyond the results—it thrives in the process itself, a continuous cycle of exploration, adjustment, and discovery. The challenges faced along the way only serve to reinforce perseverance and inspire curiosity about the unknown. At times, adaptation, revision, or even acceleration of plans becomes necessary, especially when deadlines demand that the work be concluded and documented in its current form.
Ultimately, the beauty of research lies in reflecting on the effort invested, with deadlines and presentations marking milestones that offer opportunities to share progress and look towards future endeavors. Constructive feedback and suggestions are always welcome. Research flourishes through collaboration, and there are no true failures when the process remains the focal point of the journey.

In this section, we present the results of our DNS conducted using the JAGUAR code, whose setup was detailed in the previous section (Section 6). We begin by outlining the post-processing strategies and codes employed to extract the necessary data, as described in Section 7.1. The validation of the PGS method, using a simplified single-pore configuration, is discussed in Section 7.2. Finally, the core focus of this work — the analysis of turbulence in TPMS porous media — is presented through the complete turbulence analysis on a Gyroid with struct=1.20 (high porosity) in Section 7.3 and a turbulence analysis comparison based on different structural coefficients (different porosity) in Section 7.4, always for a Gyroid TPMS topology.

7.1 Post-treatment

JAGUAR code, in its current state of development, does not provide any built-in post-processing functionalities. This means that, for any selected iteration in time, we can extract only certain fields, but for all solution points across the computational domain. Fortunately, there is an option to reduce the polynomial degree of the SDM for the output via linear interpolation, allowing us to lower the output solution point (SP) resolution. However, reducing the SP resolution too much would compromise accuracy, particularly for computing spatial correlations. As a result, the solutions per time-step from JAGUAR are typically large and not easy to manage. Table 10 outlines the storage capacity requirements for various simulation setups.
In the following discussion, we assume that for each SP (see Section 6.3 for details), the variables $\{x, y, z, u, v, w\}$ are extracted in double-precision floating-point format (64 bits). For instance, consider a polynomial order of $p = 4$ for the SDM and a domain size of $(N_{x,\text{cells}} \times N_{y,\text{cells}} \times N_{z,\text{cells}}) = (800 \times 100 \times 100)$. Storing six variables $\{x, y, z, u, v, w\}$ as 64-bit floats for a single time step requires 48 GB of storage. If we consider 1000 iterations, which is still insufficient for achieving satisfactory time-data sampling for time-averaged quantities, the storage requirement escalates to 48 PB, an impractical amount. For this reason, our strategy involves performing post-treatment on selected time steps (sub-sampling strategy detailed in Section 4.5.2) directly on the super-calculators at GENCI, that run the JAGUAR code, before transferring the data for further analysis.

p	Domain ($N_{x,cells} \times N_{x,cells} \times N_{x,cells}$)	DoF	Storage per iteration	Storage per 1k iterations
3	$600 \times 100 \times 100$	384 M	18,4 Gb	18,4 Pb
3	$800 \times 100 \times 100$	512 M	24,6 Gb	24,6 Pb
4	$600 \times 100 \times 100$	750 M	36,0 Gb	36,0 Pb
4	$800 \times 100 \times 100$	1000 M	48,0 Gb	48,0 Pb
5	$600 \times 100 \times 100$	1296 M	62,2 Gb	62,2 Pb
5	$800 \times 100 \times 100$	1728 M	82,9 Gb	82,9 Pb

Table 10: Storage requirement examples based on our simulations, considering the extraction of 6 variables such as {x,y,z,u,v,w} (64-bit floats).

So, our plan for the post-treatment was structured as follows:

- **Temporal Analysis (Time-Correlations)**: Take $N_{x,\text{probes}} \times N_{y,\text{probes}} \times N_{z,\text{probes}} = N_{probes}$ probes (each one named probe **p<i>**, with i=1,...,N_{probes} at location $(x_{p<i>}, y_{p<i>}, z_{p<i>})$, with low spatial resolution but high temporal resolution ($N_{\text{subsampling,time}} = 1 - 2$).
- **Spatial Analysis (Space-Correlations)**: Extract only representative planes and a pore volume, such as longitudinal planes defined as $(x, z)_{y=y_0}$ or $(x, y)_{z=z_0}$, transversal planes $(y, z)_{x=x_0}$, and a reduced pore volume chosen at a pore location in the middle-end of the PM given by $(x, y, z) \in ([x_0 - s/2, x_0 + s/2], [y_0 - s/2, y_0 + s/2], [z_0 - s/2, z_0 + s/2])$, with s is the pore size. Once the locations of these planes and volumes are selected, i.e. the filtered SP are selected, data are extracted from the global domain every $N_{\text{subsampling,space}}$ iterations, where obviously $N_{\text{subsampling,space}} \gg N_{\text{subsampling,time}}$. Note that the choice of an adequate value for $N_{\text{subsampling,space}}$ has been discussed in Section 4.5.2 using confidence interval evaluations over the statistical moments of the velocity field, extracted from the probes. This approach provides high spatial resolution over the selected data but low temporal resolution, which can be then carefully compared to the probes data, to be sure about a coherent choice of $N_{\text{subsampling,space}}$. The extraction of sub-volumes is achieved using a Python code that implements the Antares and mpi4py libraries.

The advantages of the post-treatment are summarized in Table 11. For instance, if we consider a simulation run with $p = 4$ and extract data with $p = 3$ through linear interpolation (output option in JAGUAR), we reduce our initial data by a factor of $(4/5)^3 = 0.512$ (-51.2%). On this reduced dataset, we can apply post-treatment to extract, for example, 25 planes (x, z) (61.44 MB per plane), 15 planes (y, z) (7.68 MB per plane), and 1 pore volume of size $20 \times 20 \times 20$ cells (24.576 MB per volume). Consequently, instead of 24.6 GB, we will extract only 1.7 GB of data, resulting in a storage reduction of -93.18% compared to the $p = 3$ output and -99.99% compared to the initial $p = 4$ simulation data.

p	Domain ($N_{x,\text{cells}} \times N_{y,\text{cells}} \times N_{z,\text{cells}}$)	DoF	Storage without PT (per iteration)	Storage with PT (per iteration)
3	$800 \times 100 \times 100$	512 M	24.6 GB	1.7 GB (-93.2%)
4	$800 \times 100 \times 100$	1000 M	48.0 GB	2.6 GB (-94.6%)

Table 11: Advantages of the post-treatment in terms of storage savings based on our simulations. As an example, we consider extracting 25 longitudinal planes, 15 transversal planes, and 1 pore volume of size $20 \times 20 \times 20$ cells. For each simulation point, we extract 6 variables: $\{x, y, z, u, v, w\}$ (64-bit floats).

This is why having an efficient and reliable code for post-treating data from a time step solution is crucial, and it is detailed in the following discussion (Section 7.1.3). Before presenting the code architecture, we introduce two Python libraries used to build our code: Antares (Section 7.1.1) and mpi4py (Section 7.1.2).

7.1.1 Data Treatment with Antares Library

Antares is a Python library developed by CERFACS-ONERA [33] (© Copyright 2012-2024) in Toulouse, France. It extends the functionality of the widely-used VTK library (open source) providing versatile tools and features for manipulating data from CFD simulations, not only in vtk or similar formats. It can be easily integrated into Python workflows during pre-processing, post-processing, or even co-processing. The key features of the Antares library include:

- **API (Application Programming Interface)**:

  Antares organizes data through a four-level hierarchical structure (see Figure 61) composed of **Base**, **Zone** and **Instant** objects, which are essential to its data model:

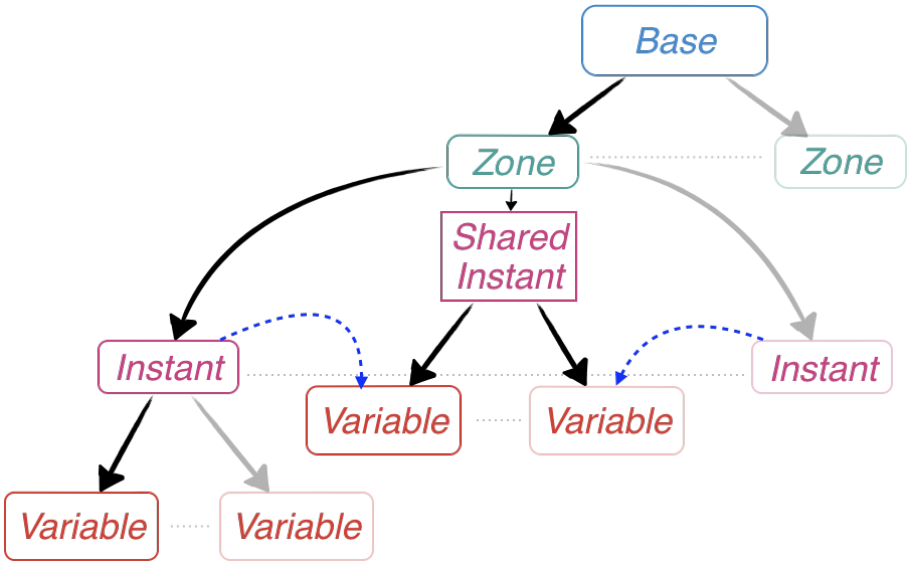

Figure 61: Hierarchical structure of Antares data model. (ref: [33])

- **Base**: The root of the structure, acting as a container for zones.
- **Zone**: Represents a section of the domain, such as a block in a multi-block mesh or a partition in an unstructured mesh. It can be also the whole domain its self.
- **Instant**: Contains variables (usually `numpy` arrays) representing snapshots of the data at specific times or other sampled configurations.
- **Variable**: `numpy` array that represents a certain field or quantity. It is also possible to define a **shared instant** where we can put some **shared variables** between all the instants, avoiding thus redundancy. This is useful especially when dealing with fixed geometry (and so variables such as the coordinates x, y and z) for unsteady data.

The **Base**, **Zone**, and **Instant** classes provide flexible handling of data using a dictionary-like structure. Each zone and instant can be accessed by string keys, and the variables stored in an instant are managed as arrays (e.g., `numpy` arrays).

Below is an example of creating and manipulating these objects:

```
import antares as ant
import numpy as np

# Create the base container
base = ant.Base()

# Add a zone to the base
zone = ant.Zone()
base['zone1'] = zone

# Create an instant and add some variables
instant = ant.Instant()
instant['temperature'] = np.random.random(100)
# Random temperature data at nodes
instant[('velocity', 'cell')] = np.random.random(50)
# Random velocity data at cells
zone['t1'] = instant

# Inspect the base
print(base)
print(base['zone1']['t1'])
```

```
print(base['zone1']['t1'].keys())
# Shows variable names stored in the instant
```

- **Readers**:

  Antares can extract a Base object from various file formats, including Tecplot, HDF, VTK, Matlab, Fieldview, elsA, Fluent, Gmsh, and more.

- **Writers**:

  Once a Base object is created, it can be converted into a file (Tecplot, csv, HDF, VTK, Matlab, Fieldview, Polygon, elsA, Gmsh, etc.), which is essentially the inverse operation of the Reader.

- **Treatments**:

  To perform operations such as data duplication, transformation, or filtering, Antares provides **treatment classes**. These classes implement high-level algorithms for processing the data and they can perform specific tasks, such as duplicating mesh data or more complex operations like extracting a plane or an iso-surface. For example, the following code demonstrates how to use some treatments that we exploited in our code for post-treatment:

  – **Cut** treatment: Cut a grid (structured or unstructured) using a given geometrical shape. It can use either the VTK library ('cut') either an in-built specific function ('acut').

  ```
  import antares

  % The following example shows a cutting with a plane defined
  % with the point (0., 0., 0.) and the normal vector (1., 0., 0.).
  myt = antares.Treatment('cut')
  myt['base'] = base
  myt['type'] = 'plane'
  myt['origin'] = [0., 0., 0.]
  myt['normal'] = [1., 0., 0.]
  cutbase = myt.execute()
  ```

  – **Threshold**: Keep grid points or cells that respect the given threshold values.

  ```
  % The following example shows have to take only the data
  % that respect the condition 50<x<70 V ro<0.9
  myt = antares.Treatment('threshold')
  myt['base'] = base
  myt['variables'] = ['x', 'ro']
  myt['threshold'] = [(50., 70.), (None, 0.9)]
  thres = myt.execute()
  ```

  – **Merge**: Merge zones of a given input Base.

  ```
  myt = antares.Treatment('merge')
  myt['base'] = base
  myt['duplicates_detection'] = True
  myt['tolerance_decimals'] = 13
  merged = myt.execute()
  ```

  In addition to basic operations, Antares supports advanced data analysis and signal processing treatments. For instance, the **Discrete Fourier Transform (DFT)** or **Proper Orthogonal Decomposition (POD)** can be applied to the data to extract useful information from large datasets.

```
# Apply a DFT treatment to the data
dft_treatment = antares.Treatment('fft')
dft_treatment['base'] = base
dft_result = dft_treatment.execute()
```

Antares provides a powerful, Python-based API for organizing, manipulating, and processing simulation data. Its hierarchical structure, based around the Base, Zone, and Instant classes, allows for efficient handling of CFD and other types of scientific data. Combined with its treatments for complex tasks like signal processing or mesh manipulation, Antares is a versatile tool for researchers and engineers seeking to enhance their computational workflows. It has also some optimized treatments especially designed for JAGUAR code's SDM.

7.1.2 Multiprocessing with mpi4py

The **Message Passing Interface (MPI**) is a standardized and portable communication protocol designed to enable parallel computing across distributed memory systems. It provides a set of library routines that allow processes running on different nodes to communicate by sending and receiving messages. MPI is widely used in scientific and engineering applications that require high-performance computing (HPC), as it allows tasks to be split and executed efficiently across multiple processors.
MPI is highly scalable, supporting small- to large-scale clusters, and is essential for solving computationally intensive problems that cannot be handled by a single processor. MPI primarily supports two types of communication:

- **Point-to-Point Communication**: Communication between two specific processes (e.g., using `send` and `recv` operations).
- **Collective Communication**: Involves communication among multiple processes, such as broadcasting data from one process to all others or gathering data from all processes into one.

The `mpi4py` library is a Python package that provides bindings to the MPI standard, allowing Python applications to leverage parallelism using MPI. It offers an object-oriented approach to working with MPI, making it accessible to Python programmers while retaining the performance benefits of the underlying MPI implementation.
The `mpi4py` package enables communication between Python processes across multiple nodes, making it useful for parallel computing in scientific, engineering, and data analysis domains. The key components of `mpi4py` are:

- **Initialization**:

  In any MPI program, it is essential to initialize and finalize the MPI environment to ensure that all processes are set up for communication before any data exchange occurs. While standard MPI programs use `MPI_Init()` and `MPI_Finalize()`, `mpi4py` initializes the MPI environment automatically upon import.

  ```
  from mpi4py import MPI

  # Initialize the communicator
  comm = MPI.COMM_WORLD

  # Get the rank and size of the current process
  rank = comm.Get_rank()  # Process ID (rank)
  size = comm.Get_size()  # Total number of processes
  ```

  Here, `MPI.COMM_WORLD` is the default communicator that includes all processes in the parallel environment. The `rank` provides the unique ID of each process, while `size` gives the total number of processes.

- **Process Communication**:

  Point-to-point communication is the simplest form of data exchange in MPI, where one process sends data to another. In `mpi4py`, this is achieved using the `send` and `recv` methods. Below is a basic example of how two processes can exchange messages:

```
if rank == 0:
    data = "Hello from rank 0"
    comm.send(data, dest=1)
    print("Process 0 sent data:", data)
elif rank == 1:
    received_data = comm.recv(source=0)
    print("Process 1 received data:", received_data)
```

  In this example, process 0 sends the message `"Hello from rank 0"` to process 1, which receives it using the `recv` function.

- **Common Collective Operations**:

  MPI provides collective communication operations to simplify data exchange among multiple processes. These operations include broadcasting, scattering, gathering, and reductions. The `mpi4py` library provides high-level abstractions for these operations.

  Broadcasting allows one process (usually the root) to send data to all other processes. For example, in the following code snippet, process 0 broadcasts a number to all other processes:

```
data = None
if rank == 0:
    data = 42  # Process 0 sets the data to broadcast
data = comm.bcast(data, root=0)
print(f"Process {rank} received data: {data}")
```

  Here, all processes receive the number 42, which is broadcast by process 0.

  Gathering allows all processes to send data to a single process. In the following example, each process sends its rank to the root process (process 0), which gathers all the ranks into a list:

```
data = rank  # Each process contributes its rank
gathered_data = comm.gather(data, root=0)

if rank == 0:
    print("Data gathered at process 0:", gathered_data)
```

  In this case, process 0 will print a list of ranks from all processes.

  In addition to broadcasting and gathering (Figure 62), `mpi4py` also supports scattering data from one process to all other processes and reducing results from all processes into a single result (e.g., summing values across processes). Below is an example of using the `reduce` operation to compute the sum of all ranks:

```
data = rank
sum_of_ranks = comm.reduce(data, op=MPI.SUM, root=0)

if rank == 0:
    print("Sum of all ranks:", sum_of_ranks)
```

While `mpi4py` provides the ease of Python, it is important to note that Python can have performance limitations due to its interpreted nature. However, since `mpi4py` directly binds to native MPI libraries written in C/C++, it inherits the efficiency of these libraries. Therefore, `mpi4py` remains a highly efficient solution for parallel computing tasks, particularly in scenarios where Python is well-suited for data handling and preprocessing but relies on MPI for high-performance parallel execution.

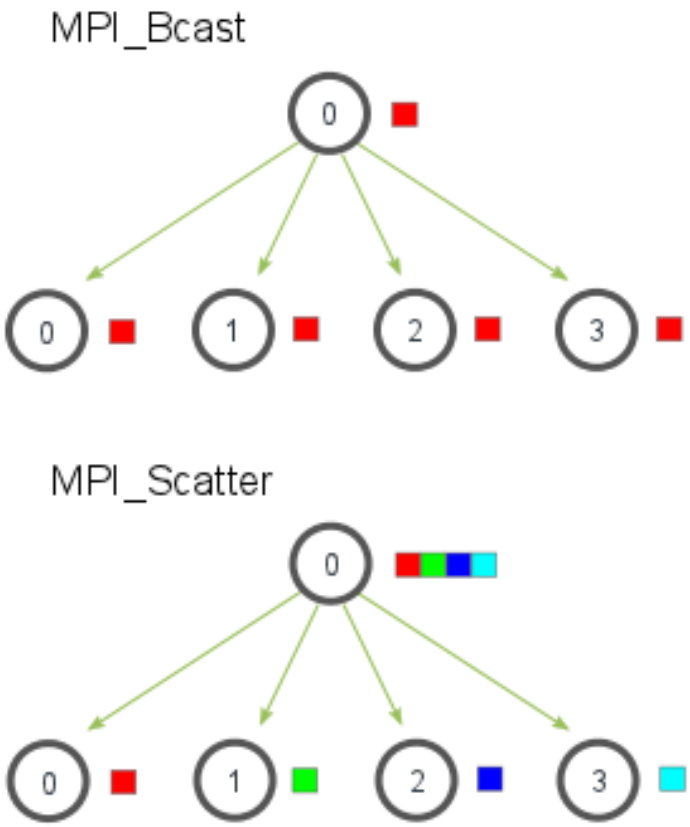

Figure 62: Schema of common collective operations in MPI: gathering and broadcasting from process `rank=0` (also called "conductor" or "director") to the other processes (also called "workers" or "followers"). (ref: [173])

7.1.3 Sub-volumes extraction from JAGUAR solutions using Antares and mpi4py

In this section we present how we designed a code to extract sub-volumes such as planes (a plane can be seen as a volume where in one direction we have just one layer of data) and/or pore volumes from computational domain solution at a given time step. JAGUAR gives solutions organized in the following way: SOLUT/sol_<iteration>/sol_<iteration>_<zone>.vtu. So for each iteration we have a folder (sol_<iteration>) that contains solutions for all the zones composing the domain, in our case in vtu format (sol_<iteration>_<zone>.vtu). To have an an order of magnitude, we have usually around 6000 zones for a simulation in our configuration. Evidently the domain partitioning choice depends a lot on the HPC strategy set on JAGUAR code and on the selected CPU power, as well as on the supercomputing center architecture.
The code used to extract sub-volumes data from JAGUAR code solutions can be divided in three main steps:

1. **Data distribution**

   (a) **MPI communication initialization:**

```
from mpi4py import MPI

# Initialize MPI communication
comm = MPI.COMM_WORLD
rank = comm.Get_rank()  # Get the rank (ID) of the current process
size = comm.Get_size()  # Get the total number of processes
```

   (b) **Data and zones definitions:**

The processor ranked 0 extracts the indices (<zone>) of the zones existing in the solution folder (sol_<iteration>_<zone>.vtu) and it reads also as input the list of data (sub-volumes) to extract (plane (x,z), plane (x,y), plane (y,z) or a pore volume):

- **Zones List (`zones_list`)**: This is a list of zones denoted as `zone_i` where i ranges from 1 to `N_zones`. Each zone represents a spatial region or segment of the domain under consideration.
- **Data Names List (`data_names_list`)**: This list comprises data names `data_name_j` where j ranges from 1 to `N_planes` + `N_volumes` = `N_subvolumes`. The data can be categorized into planes and volumes, indicating the types of spatial data collected or processed.

```
if rank == 0:
    # Define the list of zones
    # Each zone represents a spatial region or segment of the domain.
    zones_list = [zone_1, zone_2, ..., zone_Nzones]

    # Define the list of data names
    # The list includes data related to planes and volumes
    # within the domain.
    data_names_list = [data_name_1, data_name_2, ...,\
    data_name_Nsubvolumes]
```

(c) **Data distribution through broadcasting and scattering**:
The `zones_list` and `data_names_list` need to be distributed among the various computational processes (ranks) for parallel processing:

- **Zones Intervals**: The list of zones is divided into intervals $(\texttt{zone\_a}, \texttt{zone\_b})_k$ for each rank k. This partitioning allows each process to handle a subset of zones. This is used in step 2 of the algorithm.
- **Data Names Chunks**: Similarly, `data_names_list` is divided into chunks $[\texttt{data\_name\_a}, \ldots, \texttt{data\_name\_b}]_k$ for each rank k. This ensures that each rank processes a subset of the data types. This is used only in step 3 of the algorithm.

```
if rank == 0:
    # Split the zones list into chunks and distribute among processes
    zones_intervals = array_split(zones_list, size)
    # Divide zones into equal parts for each process

    # Split the data list into chunks and distribute among processes
    data_name_chunks = list_split(data_names_list, size)
    # Divide data names into equal parts for each process

# Broadcast the data to all processes
zones_list = comm.bcast(zones_list, root=0)
zones_intervals = comm.bcast(zones_intervals, root=0)
data_names_list = comm.bcast(data_names_list, root=0)
data_names_chunk = comm.bcast(data_names_chunk, root=0)

# Scatter the chunks to all processes
zones_interval = comm.scatter(zones_intervals, root=0)
# Distribute zone intervals
data_names_chunk = comm.scatter(data_names_chunks, root=0)
# Distribute data name chunks
```

2. **Data Extraction**

(a) **Data Extraction for each zone in the assigned zones_interval**

The processor extracts data from each zone in its given zones_interval. Based on the data_name string format we can deduce if the considered data is a plane or a volume and its definition. In this way an appropriate appropriate `antares.Treatment` method to extract data can be used on each individual zone:

i. **Cut Treatment** (`antares.Treatment('cut')`): This involves defining a plane with an origin and normal vector to slice through the data.
ii. **Threshold Treatment** (`antares.Treatment('threshold')`): This method applies spatial limits to extract data within specified coordinate ranges.

```
def extract_data_from_zone(data_name, zone):
    # Determine the type of data and apply the appropriate treatment
    if data_name in plane_data_names:
        origin, normal = get_specs_plane(data_name)
        # Apply cut treatment for plane data
        treatment = antares.Treatment('cut')
        treatment.inputs = (origin, normal)
        # Define the cut plane with origin and normal vector
        data = treatment.execute()
        # Extract data from the zone using cut treatment
    elif data_name in volume_data_names:
        (xa, xb), (ya, yb), (za, zb) = get_specs_volume(data_name)
        # Apply threshold treatment for volume data
        treatment = antares.Treatment('threshold')
        treatment.inputs = [(xa, xb), (ya, yb), (za, zb)]
        # Define the threshold limits for each coordinate
        data = treatment.execute()
        # Extract data from the zone using threshold treatment
    return data

# Process each data name and zone
extracted_data = []
for data_name in data_names:
    for zone in zones_interval:
        extracted_data_zone = extract_data_from_zone(data_name, zone)

        if extract_data_zone:
        # take only data that exist
        # reminder: not all sub-volumes are in all zones,
        # meaning that some of them after the treatment
        # can get an empty antares.Base

        extracted_data.append(extract_data_zone)
```

(b) **Merge the data extracted for the zones_interval**
Data extracted for each zone before are put together for the zones_interval considered by the same processor. To do so a merging treatment is adopted (`antares.Treatment('merge')`) creating multiple Zones in the same Base object.

```
# Merge the collected data chunks
merged_data = merge_data_for_zones_interval_and_save(extracted_data)
```

The `merged_data` for the `zones_interval` considered are saved independently, with a clear name of the type `sol_<iteration>_<data_name>_<zones_interval>`. Note that we are working on the same solution in this discussion, meaning that `<iteration>` is defined at the beginning of the loop.

3. **Final data merge**
The data extracted and processed from the zone intervals by each processor are further aggregated. The merge treatment of Antares is used also in this case. Each process aggregates intervals

only for the assigned data_names_chunk assigned in step 1 using the data extracted for each `zones_interval` in step 2.

This choice has a huge impact on the performance of the code because the parallelization of this step of the code avoids the simple merge done by an individual processor.

```
for data_name in data_names_chunk:
    # Collect the merged data, saved in step 2
    all_interval_data = extract_zones_intervals_data(data_name, zones_intervals)
    # Perform the final merge for the data_name selected and save
    final_data = merge_zones_intervals_data_and_save(all_interval_data)
```

At this stage we will have all the selected data for a given solution time. Iterating the 3 steps on multiple time-steps will give as the same data elements but in other simulated times. These files will have the same filename but with the iteration number specified so that we can afterwards easily post-process them.
Additional considerations to be done:

- **Influence of Treatments**: It is important to note that certain zones or data types may be excluded due to the application of cut and threshold treatments. This means that the impact of some zones on specific data types might be nullified if they fall outside the treatment boundaries.
- **Efficiency and Scalability**: The steps outlined involve significant data distribution and merging operations. Careful consideration should be given to optimizing these processes to handle large datasets efficiently and to ensure scalability across multiple ranks.

The three steps described above are summarized in Figure 63 with also some visual help for a clear understanding.

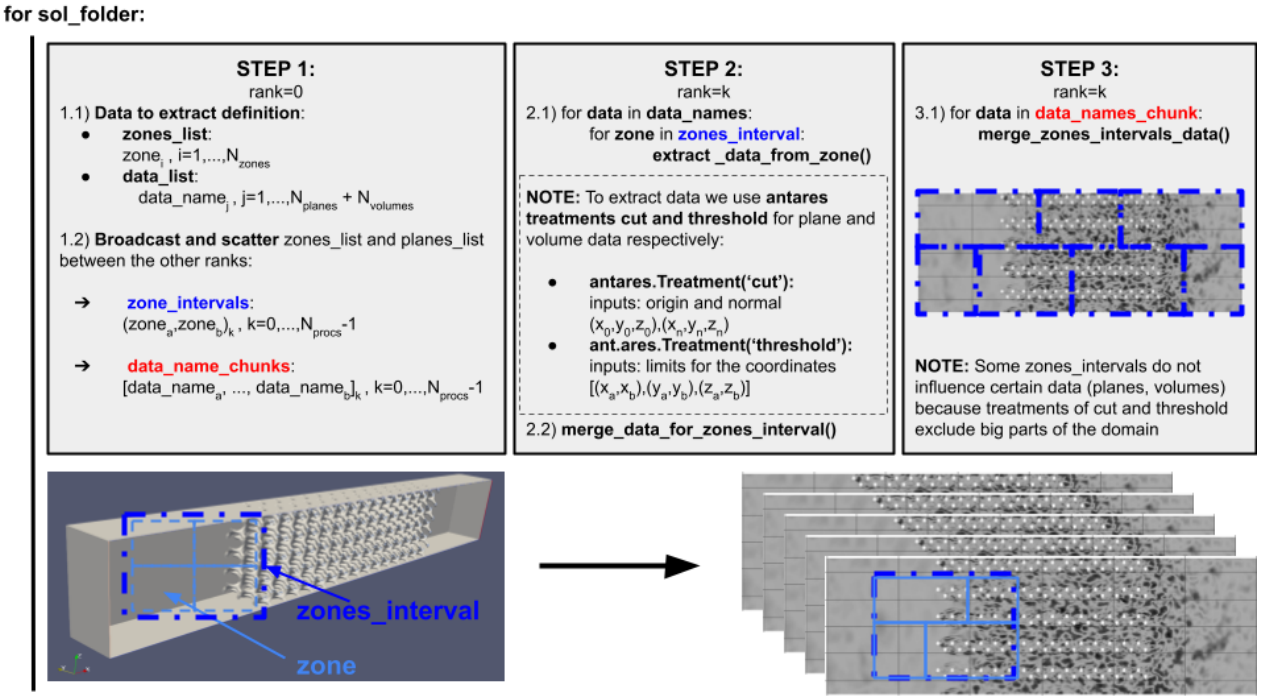

Figure 63: A schematic view of the 3 main steps of the sub-volumes extraction code used in this work.

7.2 Validation of the numerical setup

The initial step in our study involves validating the PGS numerical approach within the context of complex porous media geometries. While PGS has been introduced in Section 6.6 and its efficacy has

been demonstrated by various authors ([146], [48]), it has yet to be thoroughly evaluated within the specific framework of an SDM solver incorporating IBM for the treatment of complex geometries. Therefore the objective of this validation is to compare simulations using both PGS and no-PGS approaches (each employing IBC), independently of the physical accuracy of the computational setup. To achieve this, a simplified configuration was selected (called by the authors "minigyroid"), consisting of a single transverse pore replicated four times in the longitudinal direction, as depicted in Figure 64. A coarse mesh resolution of $(n_x, n_y, n_z) = (16, 16, 120)$ cells was employed for the entire domain, with an SDM polynomial order of $p = 3$, resulting in approximately 2 million DoF. This choice significantly reduces the computational cost of the simulations. The CFL number and the PGS factor α^{-2} were held constant throughout the simulations and equal to 0.25 and 0.15 respectively. The TPMS geometry utilized was a gyroid with $k_x = k_y = k_z = 2\pi$ and a structural factor of $struct = 0.75$. A representative time span of more than 10 approximated large scales time cycles at the inlet ($\tau_0 = \frac{l_0}{u_0} \simeq 3.0s$, where $u_0 = u_{rms}$) was selected for comparison, with a sufficiently large dataset to enable a robust statistical analysis. In Table 12, we present a summary of the compared configurations in terms of time signals (Figure 66) and CPU usage. It is important to note that the time step in our simulations is constrained by the combination of the CFL condition and the high spatial resolution required for accurately modeling complex geometries, rather than the physical timescales of turbulence. Specifically, the Kolmogorov time scales within the pores for the minigyroid configuration are on the order of centiseconds (1.0×10^{-2}), whereas the time steps used in the simulations are on the order of 1.0×10^{-5}. This results in the extraction of very high frequencies that are not only unnecessary for our analysis but also computationally expensive. This highlights the relevance of validating the PGS method for this case study.

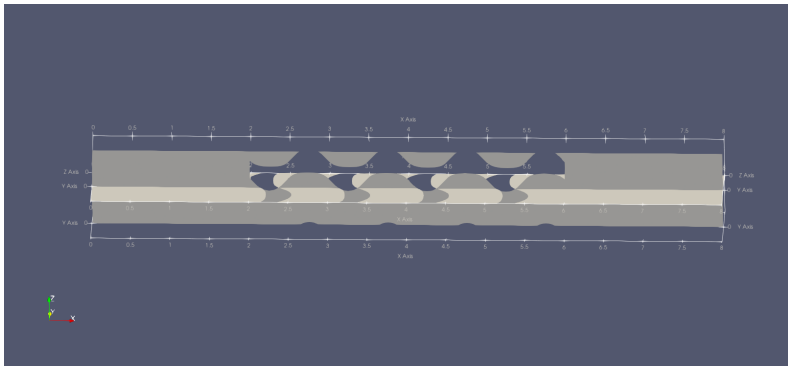

Figure 64: Configuration called by the authors "minigyroid" used for the PGS validation. In figure we display the fluid regions on two plane sections extracted from the computational domain: section (x,z) for y=0.0 and section (x,y) for z=0.0 .

The comparison focuses on the following points:

1. **Validation of the PGS method assumption of low pressure inhomogeneities**:

   Figure 65 shows the magnitude of the pressure gradient along the two center-crossing longitudinal axes in the no-PGS case. It is evident that the PGS assumptions are largely satisfied, as the gradient values remain low, with some localized regions near IBC boundary cells exhibiting higher gradients. At first glance, these phenomena can be considered negligible.

2. **First-order velocity field statistics:**

   Table 15 presents the errors (mean absolute, maximum absolute, and mean (specific) relative errors) observed between PGS and no-PGS simulations. The data are extracted from a longitudinal (x, z) section, though we confirmed that similar trends are observed when averaging over multiple longitudinal planes of the same type (e.g., averaging over discrete i planes (x, z), fixed $y = y_i$ for $i = 0, 1, \ldots, N_{sections}$). To provide a more detailed distribution of the errors and differences between the simulations, we analyzed all the velocity components and the velocity magnitude on a longitudinal section, as shown in Figures 85, 86, 87, and 88.

   The error statistics show that first-order statistics (i.e., mean velocities) exhibit low overall mean errors. Given that the reference velocity at the inlet is $U_{in} = 1\,\mathrm{m/s}$, the absolute errors can be interpreted as global relative errors, all of which are 1% or below. These results are encouraging, as they demonstrate the effectiveness of the PGS method, which alters the mean velocity field by

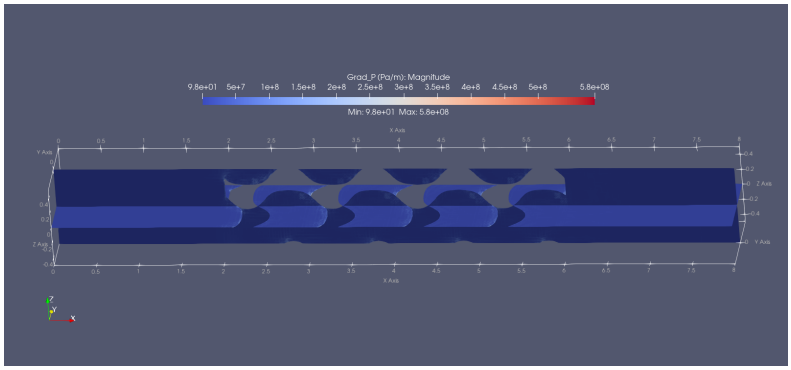

Figure 65: Pressure gradient magnitude in [Pa/m] in the one transversal pore simulation in the no-PGS case.

no more than 1%. A more rigorous evaluation involves the specific relative errors (computed using local quantities from the no-PGS configuration rather than the reference velocity U_{in}). In this case, some discrepancies are observed, particularly in the transverse velocity components. Notably, the relative error in $\langle V \rangle$ exceeds 50%, which is likely attributed to higher-order effects, such as internal intermittency or low-frequency motions that are not well resolved between the two simulations. Furthermore, normalizing by individual components may not provide meaningful insight. A more relevant specific relative error is found in the velocity magnitude, where the mean relative error is limited to approximately 3.5%.

The higher-order moments for the velocity components on a probe inside the porous media are presented and compared in Table 13. The significant differences in the kurtosis indicate that the HO statistics are not completely converged in our simulation. It could underline also the high sensitivity of these quantities to signal post-processing (such as sub-sampling treatments) and maybe also a slight influence of the PGS coefficient over the HO statistical properties. However, this should not raise major concerns, as the variance and skewness remain consistent.

From this analysis, we can validate the PGS method coupled with IBC for first-order velocity statistics.

3. **Second-order velocity field statistics**

   The errors associated with RST components are illustrated in Figures 89, 90, 91, 92, 93, and 94, and summarized in Table 15. Errors are generally quite limited, with mean absolute errors below 1%, particularly for the normal components. Some discrepancies are observed in the cross-correlation terms, specifically $\langle uv \rangle$ and $\langle vw \rangle$, when examining (specific) relative errors. These discrepancies highlight localized error amplification near IBC cells, where the solid boundary is modeled by modifying the source terms in the NS equations (Section 6.4). However, this remains a highly localized phenomenon, likely also influenced by the incomplete convergence of some higher-order statistical quantities. For a more meaningful analysis, we focus on the turbulent kinetic energy (TKE) which mean absolute error is limited to 0.2%, while the mean (specific) relative error is around 5%. Figure 95 shows the error distribution of the TKE, which is localized near the wall. This error is likely due to a combination of factors, including IBC interaction with a low-resolution mesh, slight pressure modifications induced by the PGS method, and data extraction via linear interpolation from solution points. This analysis demonstrates that PGS is suitable for studying second-order statistics (e.g., turbulence analysis), particularly considering that future simulations will use higher spatial resolution to better capture the IBC.

4. **Frequency spectra of second-order statistics**

   As the final point of our validation, we compare two velocity fluctuation signals at the same spatial point, $(x_0, y_0, z_0) = (3.75, 0, 0)$ (details in Table 12). For clarity, the shapes of the $u(\mathbf{u}, t)$ signals over time are shown in Figure 66, with the corresponding statistical moments and captured energy presented in Table 13. The variance and skewness are consistent between PGS and no-PGS cases, though significant divergence is observed in the kurtosis, likely due to a lack of HO statistical convergence and differences in frequency resolution, time span, as well as IBC effects on high-order velocity perturbations. However, for a better understanding of turbulence, it is crucial to

correctly predict the spectra in both time and space. Figure 67 shows the pre-multiplied spectra of $\langle uu \rangle$, $\langle vv \rangle$, and $\langle ww \rangle$, which exhibit strong coherence, especially in terms of the captured energy. In Table 14, we demonstrate that the time scales, derived from the inverse of the pre-multiplied spectra peaks, are of the same order, confirming the method's quality. The larger time step and so time span simulated in the PGS case lead to a slight overestimation of time scales and spectra, which is expected, as more time evolution can be captured with the same number of iterations and the fact that we proved that the simulations are not completely converged for HO statistics.

The final validation of the PGS method comes from the very small differences in captured energy (less than 1.5%).

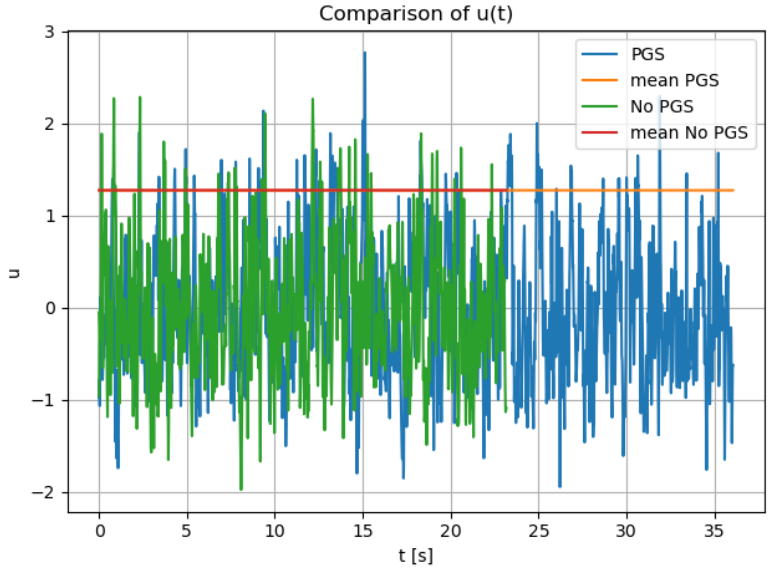

Figure 66: PGS vs No-PGS: Fluctuating component along x of the velocity ($u(\mathbf{x}, t)$).

Configuration	N_{sample} **[e+06]**	**T [s]**	$dt_{extraction}$ **[e-05 s]**	$dt_{simulation}$ **[e-05 s]**	T_{CPU} **[h]**
PGS	1.2	36.1	2.9	2.9	49.3
no-PGS	0.5	23.2	1.2	0.5	20.0

Table 12: PGS vs No-PGS: Comparison of CPU time and sample data for the minigyroid. A CPU power of 150k iterations each 24h is considered.

HO statistical moments	**u [m/s]**	**v [m/s]**	**w [m/s]**
μ_2 (No PGS)	4.7×10^{-1}	3.6×10^{-1}	5.5×10^{-1}
μ_3 (No PGS)	3.8×10^{-1}	4.0×10^{-1}	-2.5×10^{-1}
μ_4 (No PGS)	4.6×10^{-2}	3.5×10^{-1}	-2.6×10^{-1}
μ_2 (PGS)	5.2×10^{-1} (**8.7%**)	3.7×10^{-1} (**2.8%**)	5.2×10^{-1} (**-4.6%**)
μ_3 (PGS)	3.0×10^{-1} (-21.1%)	3.4×10^{-1} (-15.6%)	-2.9×10^{-2} (-88.7%)
μ_4 (PGS)	-3.1×10^{-1} (-771.7%)	9.6×10^{-2} (-72.7%)	-5.2×10^{-1} (104.4%)

Table 13: PGS vs No-PGS: Comparison of variance μ_2, skewness μ_3, and kurtosis μ_4 for the velocity components. In parenthesis the relative errors computed as $\epsilon_{rel} = \frac{\mu_{PGS} - \mu_{No-PGS}}{\mu_{No-PGS}}$.

In summary, from Table 15, it can be stated that the PGS method offers a substantial boost in computational efficiency while preserving the fidelity of the first- and second-order velocity field statistical properties. However, caution should always be exercised, as the method can be sensitive to mesh quality and the IBM approach. In this case, the simulation used to validate the PGS+IBM approach was simple, employed a coarse mesh, and was not fully developed at low frequencies. Nevertheless, the limited observed errors, particularly in second-order statistics, give us confidence in the method's applicability. However, the localized near-wall errors highlight potential limitations in capturing finer turbulence details, which may affect predictions of mixing, transport, and energy dissipation in highly anisotropic and

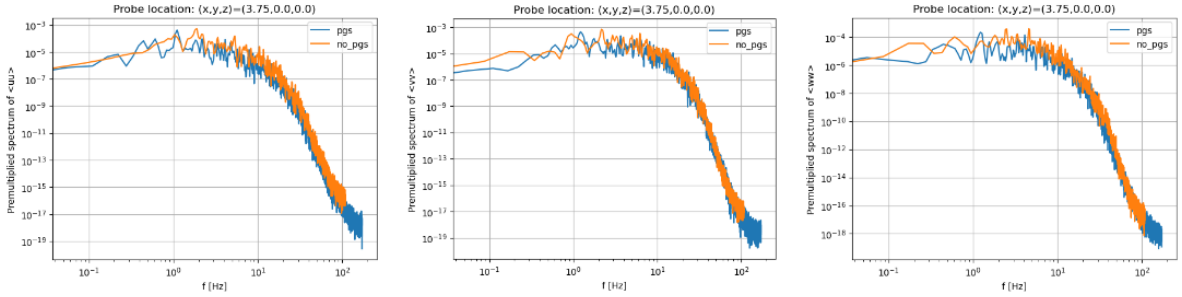

Figure 67: PGS vs No-PGS: Comparison of the spectra $E_{ii}(f = \frac{\omega}{2\pi})$ in frequency domain at the probe location $(x_0, y_0, z0) = (3.75, 0.0, 0.0)$, in the middle of the porous media.

Data	τ_{PGS} **[s]**	τ_{noPGS} **[s]**	$\Delta\langle u_i u_i\rangle$ **[%]**
$\langle uu\rangle$	9.0×10^{-1}	5.3×10^{-1}	-0.9
$\langle vv\rangle$	8.2×10^{-1}	4.6×10^{-1}	-0.8
$\langle ww\rangle$	8.2×10^{-1}	2.2×10^{-1}	-1.4

Table 14: PGS vs No-PGS: Comparison of time scales and the energy captured for the normal RST components. The captured energy $\Delta\langle u_i u_i\rangle$ is computed as the integral of the energy spectrum over its frequency domain.

Quantity: Q	**Mean Absolute Error:** **mean**$(Q_{PGS} - Q_{noPGS})$	**Max Absolute Error:** **max**$(Q_{PGS} - Q_{noPGS})$	**Mean Relative Error:** $(Q_{PGS} - Q_{noPGS})/Q_{PGS}$ [%]
$\langle U\rangle$	-1.2×10^{-2}	4.6×10^{-1}	-0.51%
$\langle V\rangle$	-3.3×10^{-4}	3.8×10^{-1}	-50.38%
$\langle W\rangle$	-1.2×10^{-4}	4.4×10^{-1}	25.45%
$\langle\lvert\mathbf{V}\rvert\rangle$	-9.2×10^{-3}	4.7×10^{-1}	3.58%
$\langle uu\rangle$	-3.9×10^{-3}	2.4×10^{-1}	3.39%
$\langle vv\rangle$	5.2×10^{-5}	3.4×10^{-1}	6.75%
$\langle ww\rangle$	5.3×10^{-4}	1.6×10^{-1}	8.00%
$\langle uv\rangle$	2.8×10^{-4}	2.1×10^{-1}	12.33%
$\langle uw\rangle$	-1.2×10^{-4}	1.1×10^{-1}	-415.62%
$\langle vw\rangle$	3.2×10^{-4}	1.1×10^{-1}	-687.90%
TKE	-1.7×10^{-3}	-1.7×10^{-3}	5.28%

Table 15: PGS vs No-PGS: errors summary on the section (x,z) for y=0.0 (minigyroid configuration).

heterogeneous flows. Thus, a deeper understanding of the interaction between higher-order statistics and IBM is necessary and has to be developed better in the future works.
For the purpose of validating the PGS+IBM numerical setup, however, we are satisfied.

7.3 Turbulence analysis for a gyroid with struct=1.20

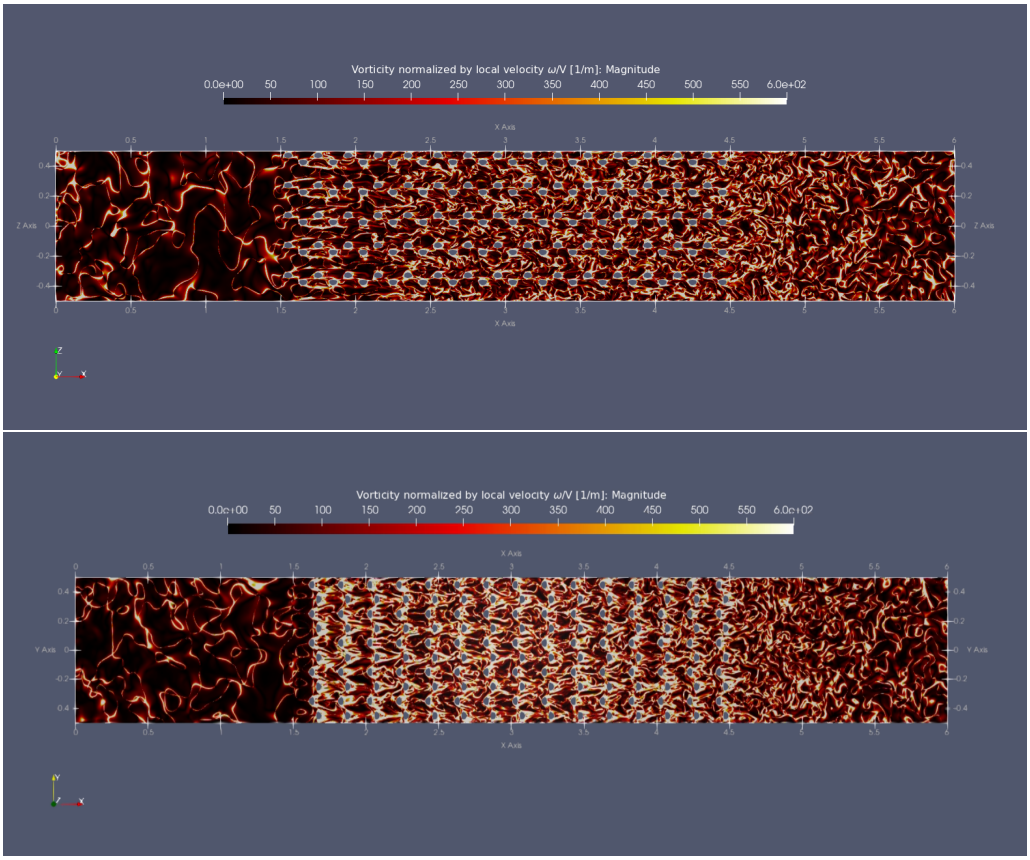

Figure 68: Gyroid with struct=1.20: Vorticity magnitude normalized by the local velocity magnitude on two plane sections: (x,z) for $y = 0.0$ and (x,y) for $z = 0.0$.

In this section, we analyze the turbulence characteristics in a TPMS material of gyroid topology, characterized by a structural coefficient of $struct = 1.20$. This high structural coefficient corresponds to a porosity value of approximately $\phi \approx 0.9$, indicating that the fluid occupies a significant portion of the domain, with the solid matrix contributing minimally to the overall volume. The computational geometry, as shown in Figure 69, consists of a gyroid structure with a pore arrangement of $15 \times 5 \times 5$ along the x, y, and z directions, respectively. This configuration is governed by the wavenumbers $k_x = k_y = k_z = 2\pi \times 5$, which define the spatial periodicity and the orientation of the gyroid surface (refer to Section 2.6 for more details on the geometry). The numerical setup is detailed in Section 6.8.
Figure 69 provides a visualization of some sections extracted from the computational domain for the post-treatment. It also gives a first idea of the 3D flow field across the porous media, revealing the development of complex flow structures within the pores. These structures are shaped by the interplay between the solid walls of the gyroid and the fluid flow, leading to a rich turbulence field. The iso-surfaces of the Q-criterion in a pore volume, as depicted in Figure 71 (a), highlight regions of high vorticity, identifying the characteristic coherent vortex structures. These regions represent areas where the flow experiences high rotational energy, contributing to the overall turbulent energy within the system. Such vortex formations are further emphasized by the von Karman vortex shedding visible in Figure 71 (b), a classic turbulence feature indicative of unsteady flows. These vortices shed downstream of the pore edges, inducing a complex wake structure that enhances mixing and energy dissipation. To have a better understanding of the physics inside a single pore of the simulations, animations are available for the Q-criterion iso-surface https://youtu.be/ZIIItg-7djw and the velocity streamlines on an x-normal https://youtu.be/Kq$_d$*anDtwBo* and z-normal planes https://youtu.be/BPGmvmxTHEg. In Figure 68 we plot the vorticity magnitude normalized by the local velocity magnitude in order to have a visualization of the eddies size evolution before, inside and after the porous media. It's also comforting to see that size of the injected eddies matches the injected length-scale $L_{0,inj} \approx 0.25$

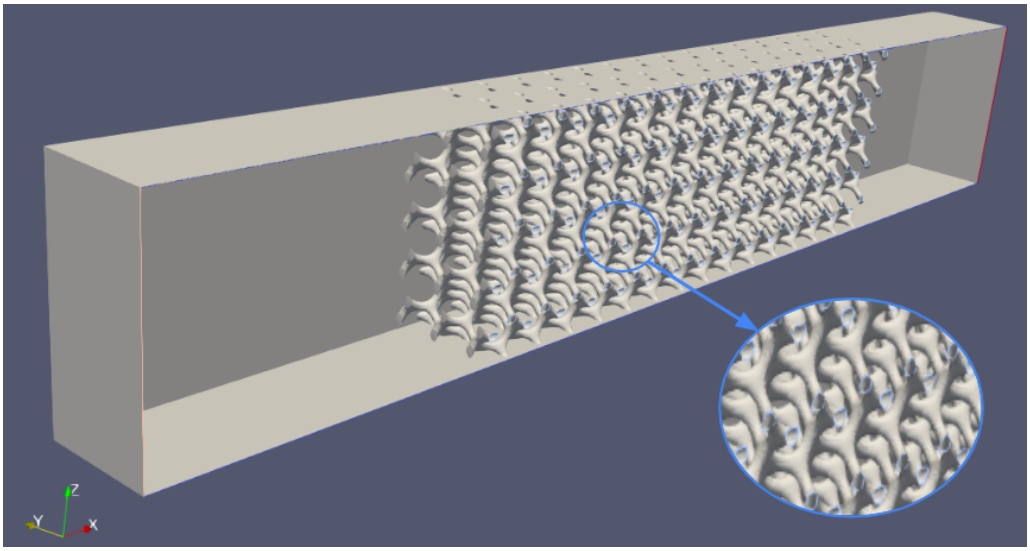

Figure 69: Gyroid with struct = 1.20: 3D domain visualization with zoom on the porous media geometry.

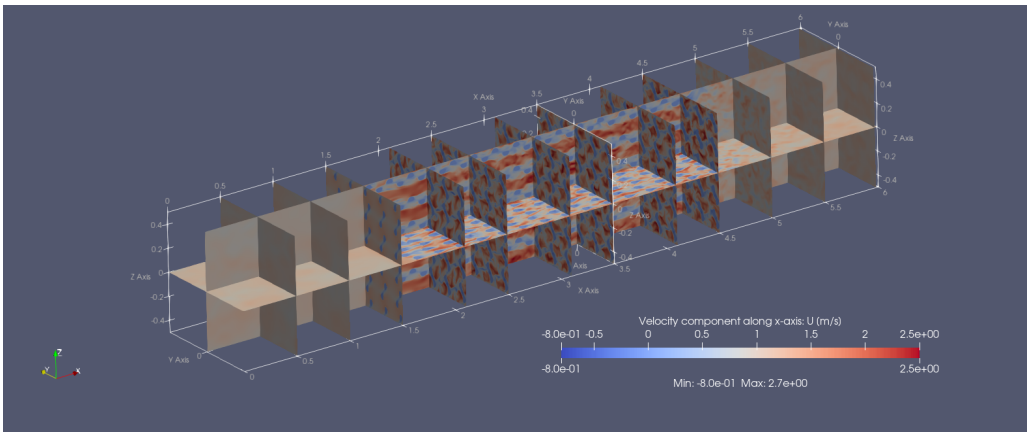

Figure 70: Gyroid with struct = 1.20: 3D visualization of some post-treatment sections extracted from the overall computational domain.

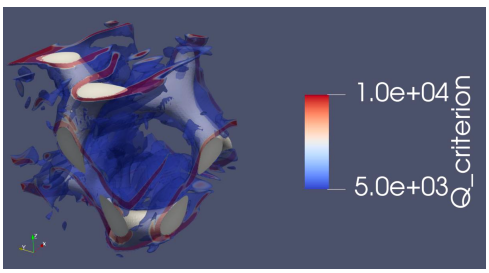

(a)

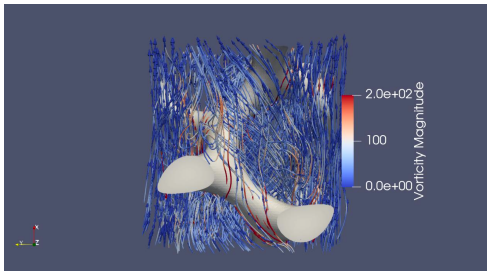

(b)

Figure 71: Gyroid with struct = 1.20: Vorticity visualization in a pore volume. (a): Q-criterion [-] iso-surfaces with values between 5.0e+03 and 1.0e+04. (b): Velocity streamlines colored with the vorticity magnitude [1/s] with values between 0.0e+00 and 2.0e+02 .

7.3.1 Mean flow

The mean flow behavior is critical to understanding the underlying turbulence dynamics. Figure 96 presents the mean velocity component $\langle U \rangle$ along the x-axis on the two main longitudinal sections of the gyroid (xz-plane at $y = 0$ and xy-plane at $z = 0$). The plot reveals a pronounced jet-like flow at the center of the pores, where the flow accelerates as it navigates through the gyroid structure. This central

region experiences the highest fluid velocities, peaking at approximately 2.1 m/s (more than the twice of the unitary inlet velocity), while the velocities diminish near the pore walls, where boundary layer effects slow down the fluid. Interesting also the stagnation areas created at the exit of the media, connected with a Von Karman vortex shedding behavior.
In contrast, the mean velocity components $\langle V \rangle$ (Figure 97) and $\langle W \rangle$ (Figure 98) provide insight into the transversal flow patterns. Both components exhibit significant cross-flows in regions near the pore edges, where recirculating zones are observed. The $\langle V \rangle$ component demonstrates the presence of a counter-rotating flow structure near the pore exits, indicating strong lateral mixing and swirl effects. Similarly, the $\langle W \rangle$ profile captures longitudinal fluctuations that enhance longitudinal mixing, particularly in regions where the pore constrictions lead to flow separation, so mostly in the first 2-3 longitudinal pores in this case. So it is evident that in the cross-directions the TPMS material has some preferential directions, and there is no symmetry but only periodicity.
The velocity magnitude (Figure 99), defined as $V_{\text{mag}} = \sqrt{\langle U^2 \rangle + \langle V^2 \rangle + \langle W^2 \rangle}$, highlights regions where the total velocity is maximized. In these areas, high-speed jets dominate, particularly in the pore centers, whereas lower velocities are concentrated near the pore walls. The velocity magnitude distribution shows clear asymmetries due to the interaction between the complex gyroid geometry and the flow, resulting in regions of both flow acceleration and stagnation. For a better understanding, also a line is extracted from the plane (Figure 72) to visualize how evolve the mean velocity components inside the material.
The turbulent kinetic energy (TKE), shown in Figure 106, quantifies the intensity of turbulence across the gyroid structure. TKE is computed as $TKE = \frac{1}{2}(\langle u^2 \rangle + \langle v^2 \rangle + \langle w^2 \rangle)$. The plot indicates that the highest TKE values are located near the pore walls, particularly in regions adjacent to the vortex cores identified in the Q-criterion analysis. These areas of high turbulence intensity are indicative of energy dissipation and mixing, driven by strong velocity gradients and vortex interactions. A line evolution of the TKE and its components is given in Figure 73 and it shows how TKE increases along the stream-wise direction inside the porous media with a rate of approximately 3.6% per pore. It is stressed that this increase happens even for a highly porous material as in this case. What really seems to matter in fact, is the size of the turbulence injected compared to the pore size. In fact for the PSPH, the pore size s should limit the macroscopic turbulence (if bigger than s) creating smaller scales as the local Reynolds number changes from outside to inside the material. This phenomenon evidently enhances the TKE, and we expect it to be more relevant in less porous TPMS, i.e. with a smaller *struct*.
Furthermore, the spatial distribution of TKE reveals an asymmetric pattern, with elevated turbulence levels near the pore exits where vortex shedding occurs. This suggests that the porous structure not only influences the mean flow but also amplifies the turbulence intensity, particularly in regions where flow separation and reattachment are frequent.
To have a better understanding of the distribution of the RST components, all correlations ($\langle uu \rangle$, $\langle vv \rangle$, $\langle ww \rangle$, $\langle uv \rangle$, $\langle uw \rangle$, $\langle vw \rangle$) are shown on two longitudinal sections in Figures 100, 101, 102, 103, 104 and 105 respectively. What we underline is especially their periodic pattern, as they increase inside each pore and decrease between two pores while the RST intensity (absolute value) usually seems to slightly increase from the first pores to the last ones, following the stream-wise direction especially for the normal components of the tensor. This observations will be further developped in order to study the TKE budget in my PhD thesis.
The analysis of the mean flow and turbulence intensity within the gyroid structure provides crucial insights into the behavior of turbulent flows in porous media with high porosity. The interaction between the intricate geometry and the fluid results in complex flow patterns, characterized by strong vortices, recirculation zones, and areas of enhanced turbulence, which are vital to understanding transport and mixing mechanisms in such systems.

7.3.2 Temporal analysis

In this section, we explore the temporal characteristics of the turbulent flow within the gyroid structure. The PSD analysis was conducted to identify the dominant frequency components of the flow as well as its spectral distribution. Figure 74 presents the temporal spectra $E_{ii}(\mathbf{x}, f = \frac{\omega}{2\pi})$ across different positions in the domain: before, in the middle and after the porous media. The energy distribution across the frequency domain shows that low-frequency components dominate the flow dynamics, which is characteristic of large-scale turbulent structures. Higher frequencies, associated with smaller eddies, display lower energy, indicating dissipation of turbulent kinetic energy at smaller scales. This is the expected behaviour through the cascade theory (Section 5.2.2). Moreover, the Kolmogorov's $-5/3$ spectral power law is found just for a short range of frequencies, showing as that first we are not in a perfectly developed

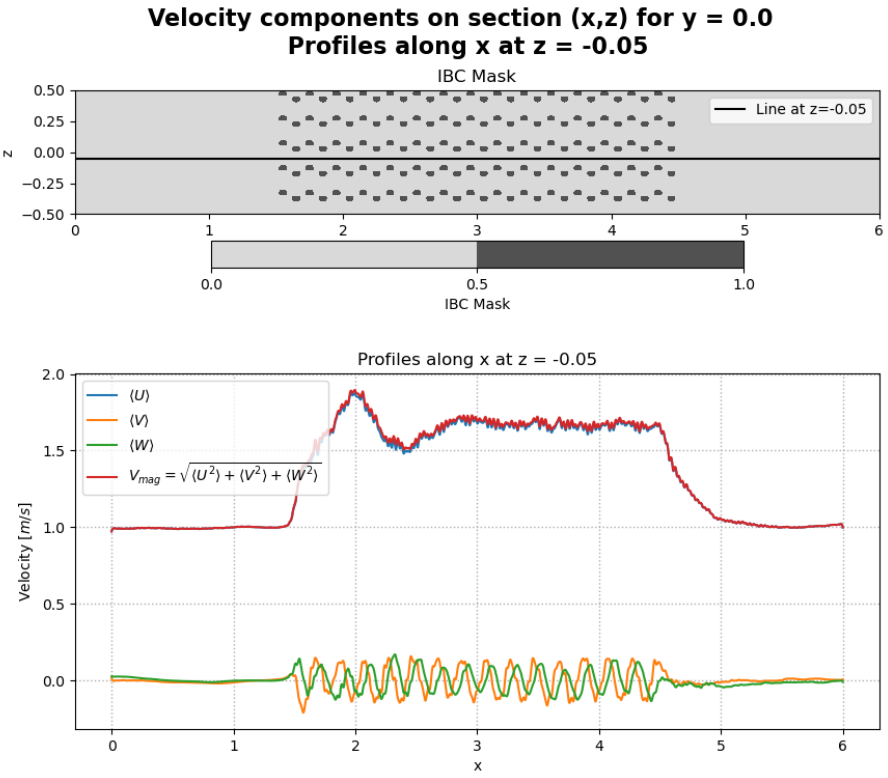

Figure 72: Gyroid with struct = 1.20: Velocity components and magnitude visualization on a line in x-direction on the plane section (x,z) at y=0.0 .

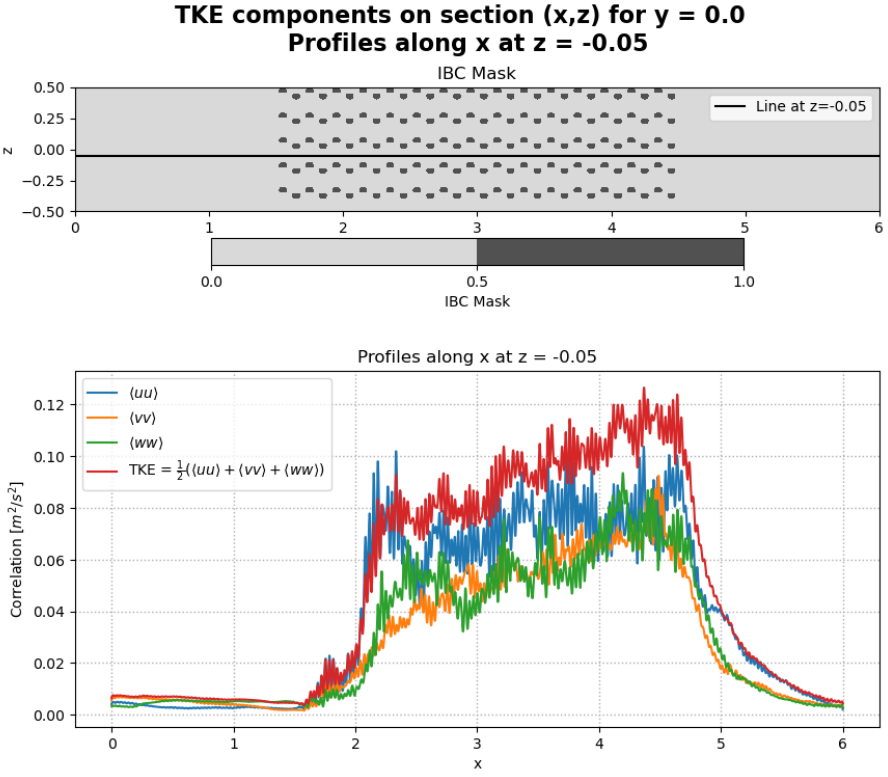

Figure 73: Gyroid with struct = 1.20: Velocity components and magnitude visualization on a line in x-direction on the plane section (x,z) at y=0.0 .

isotropic flow, except for the inlet, and second that the time resolution adopted goes way more further then required by the physical problem. In fact, before the porous media we expect the law to be coherent with the simulation because we inject an isotropic turbulence at the inlet. The large eddies time-scale is of the order of $\tau_0 = \frac{l_0}{u_0} = \frac{L_0}{u_{rms}} = \frac{0.258}{0.088} = 2.93s$ ($f_0 = 0.34Hz$) meaning an approximated Kolmogorov time-scale of $\tau_\eta \propto \tau_0 Re_0^{-\frac{1}{2}} = 0.39$ ($f_\eta = 2.57Hz$) where $Re_0 = \frac{u_0 L_0}{\nu} = \frac{0.088 \cdot 0.258}{2500^{-1}} = 56.8$.
Furthermore, Figure 75 illustrates the integral timescales ($\bar{\tau}_{11}$, $\bar{\tau}_{22}$, and $\bar{\tau}_{33}$), computed using the classical method (integration of the time auto-correlation function over the time-shifting domain) and averaged along the x-axis. These time-scales provide insight into the temporal scales of the energy containing eddies of the turbulent flow in different directions. The plot reveals that $\bar{\tau}_{11}$, corresponding to the stream-wise velocity component, exhibits the highest values, especially near the pore centers, where large-scale coherent structures persist for longer periods. Conversely, $\bar{\tau}_{22}$ and $\bar{\tau}_{33}$, associated with the cross-flow components, respectively, display a bit lower timescales, especially close to the inlet where they should be equal by definition. This is probably a sign of a not perfect convergence in large-scales motions. On the other side, the overall trend shows that temporal scales decrease along the x-axis as the flow transitions through different pore regions, with the lowest values observed near pore exits, where small regions of flow separation, vortex shedding and flow mixing occur. After the porous media the scales increase, meaning that some eddies merge, increase in size and so they become slower and persist for longer periods. This behaviour is well depicted in the already mentioned Figure 68 through the normalized vorticity magnitude.

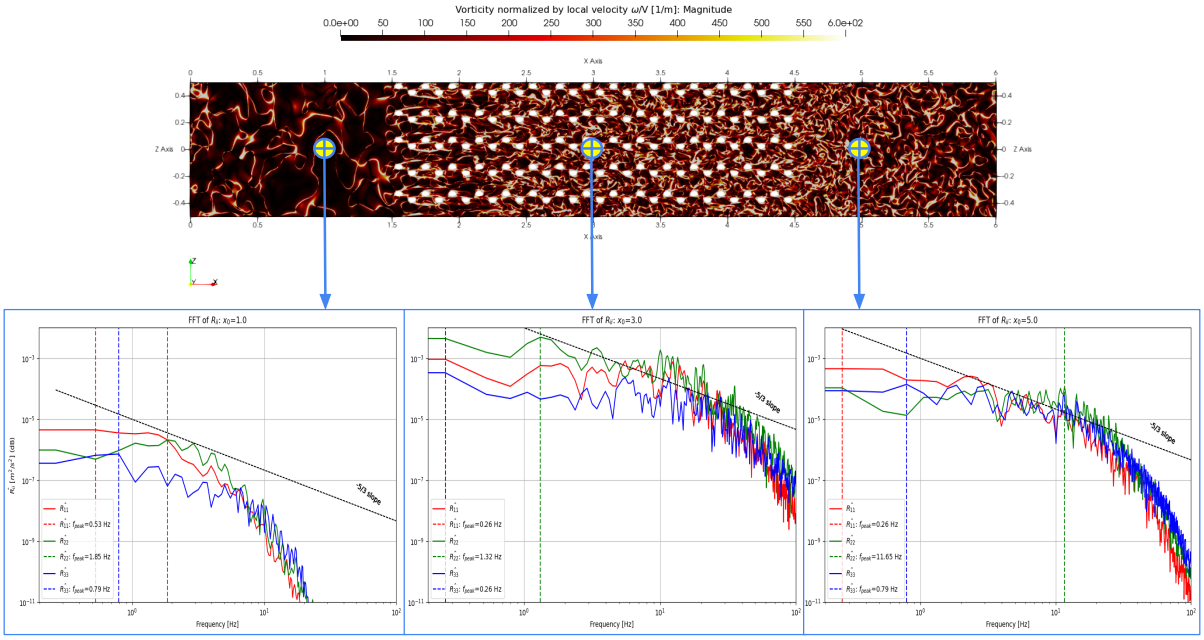

Figure 74: Gyroid struct = 1.20: Spectra E_{ii} across different positions in the domain along the line (y,z)=(0.0, 0.0): just before the PM in $x = 1.0$, in the middle of the PM in $x = 3.0$ and after the PM in $x = 5.0$.

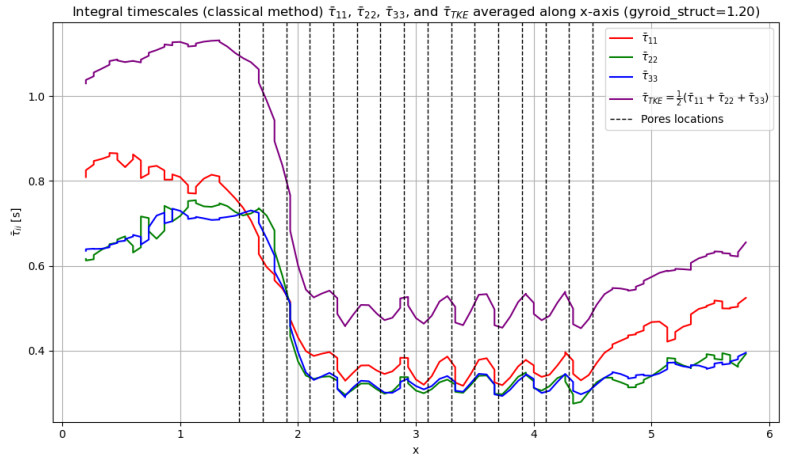

Figure 75: Gyroid with struct = 1.20: 1D integral time-scales ($\bar{\tau}_{11}$, $\bar{\tau}_{22}$, $\bar{\tau}_{33}$) and their half-trace $\tau_{TKE} = \frac{1}{2}(\bar{\tau}_{11}+\bar{\tau}_{22}+\bar{\tau}_{33}) \simeq \tau_0$ averaged along the longitudinal axis x. The computation of the integral time-scales is done using the traditional method where the integration of the time auto-correlation functions over the time-shifting domain is performed.

7.3.3 Spatial analysis

We now turn to the spatial analysis of the flow through the gyroid structure.
In figure 76 we shown on two longitudinal plane-sections the 2 points space-correlation function (not normalized) based on a correlation point located inside the porous media. The function is complex, even if it is possible to find some common patterns, connected with the periodicity of the structure and its anti-symmetrical matrix. Probably the chaotic behavior is due to a lack of resolution at low frequencies, that are the most influencing the mean flow but also the slowest to converge. This aspect should be analyzed more in detail in the future. However the apparent complexity of the space-correlations, some important informations can be deduced in order to derive important porperties of turbulence in this material.
The spatial spectra for different axes and velocity components are shown in Figures 78 and 77. These spectra reveal the distribution of energy across spatial wave-numbers, allowing us to examine how energy is distributed at various spatial scales. The spatial spectra for the x-, y-, and z-axis exhibit characteristic peaks corresponding to the periodicity of the gyroid geometry, with energy concentrating at wave-numbers related to the pore size, once we enter the PM. The velocity components display distinct energy distributions, with the stream-wise velocity autocorrelation ($\langle uu \rangle$) showing the most significant energy at large scales, while the transverse ($\langle vv \rangle$, $\langle ww \rangle$) components display more energy at smaller spatial scales, indicating enhanced mixing and turbulence in these directions but only once the porous media has been entered. Moreover we can observe that the PM tends to isotropize the flow as the spectra between the case at the beginning of the PM and after it are way closer in the latter, underlying their similitude in the 3 directions. This is a combined effect of the enhanced dissipation induced by the reduction of eddy scales and its diffusion properties, that energize also the other components of velocity V and W, given that at the inlet $V = W = 0m/s$.
To further quantify the spatial characteristics, we computed the integral length-scales (L_{11}, L_{22}, L_{33}) in Figures 79, 80, and 81 using the zero-crossing peak integration method (Z-PIM), explained in Section 5.5.4. The Z-PIM method allows us to overcome the complexity of the space-correlation while interacting with other pores, with the IBC and the not completely converged simulation data. These length scales provide a measure of the spatial extent over which velocity fluctuations are correlated. Along the x-axis (Figure 79), the stream-wise length scale L_{11} is the largest, indicating that the flow remains correlated over longer distances in this direction. Conversely, the transverse and vertical length scales (L_{22} and L_{33}) are smaller, reflecting shorter spatial correlations due to the presence of recirculating flows and vortex interactions within the pores. The same trends are observed along the y- and z-axis, with L_{11} dominating the spatial correlations, while L_{22} and L_{33} show more pronounced fluctuations due to the complex interactions between the flow and the porous structure.
In Table 16 we resume the data obtained for the gyroid struct=1.20 showing the integral time- and length-scales, the rms fluctuating velocity $u' = \sqrt{\frac{2}{3}k}$ and the kolmogorov scales using an approximation

of the dissipation rate $\epsilon \propto \frac{(u')^3}{L_0}$.

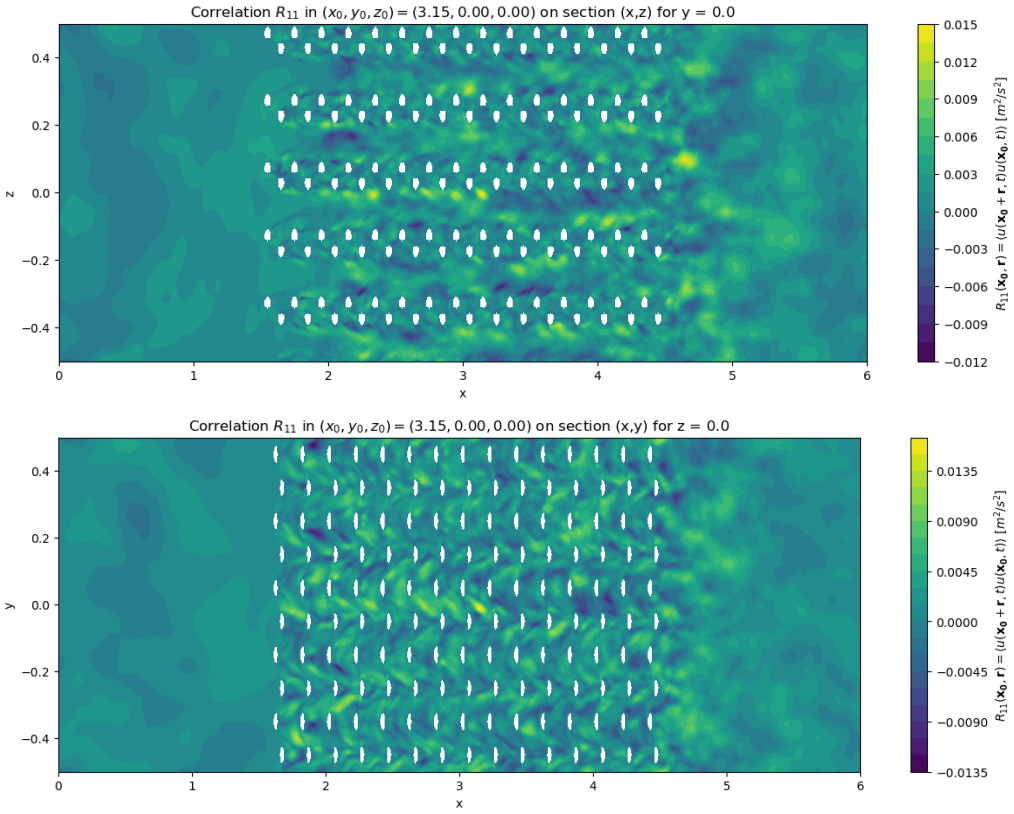

Figure 76: Gyroid with struct = 1.20: space-correlation R_{11} in $\mathbf{x_0} = (3.15, 0.0, 0.0)$ on the plane sections (x,z) at y=0.0 and (x,y) at z=0.0.

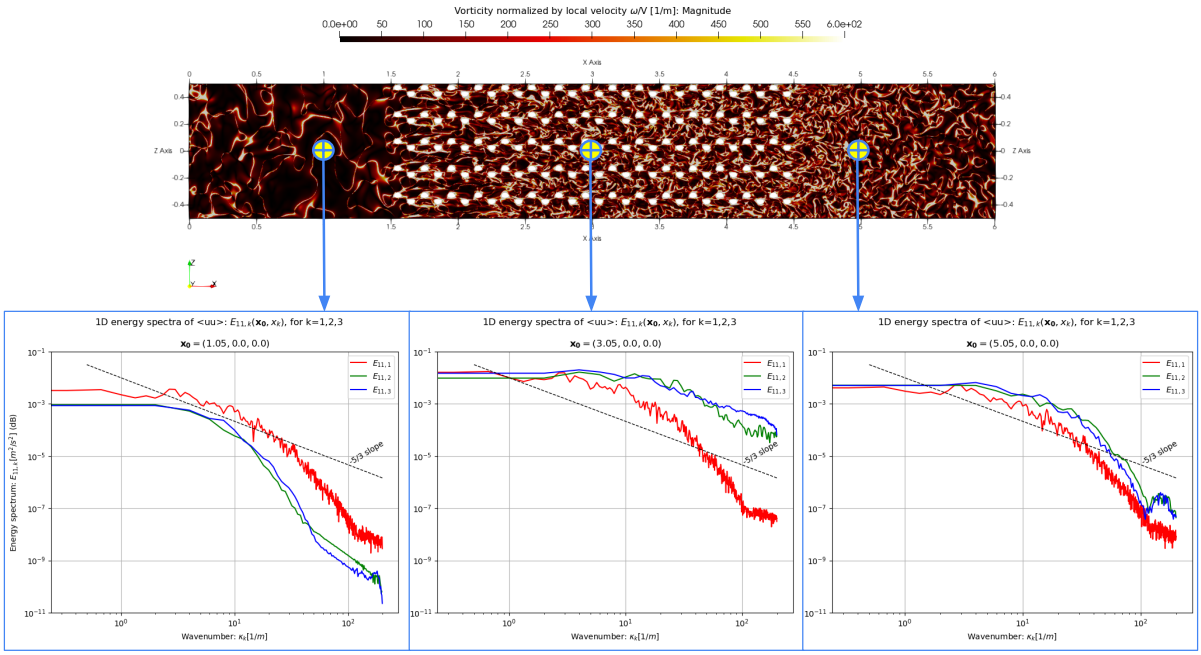

Figure 77: Gyroid with struct = 1.20: Spectra $E_{11,k}$ across different positions in the domain along the line (y,z)=(0.0, 0.0): just before the PM in $x = 1.0$, in the middle of the PM in $x = 3.0$ and after the PM in $x = 5.0$.

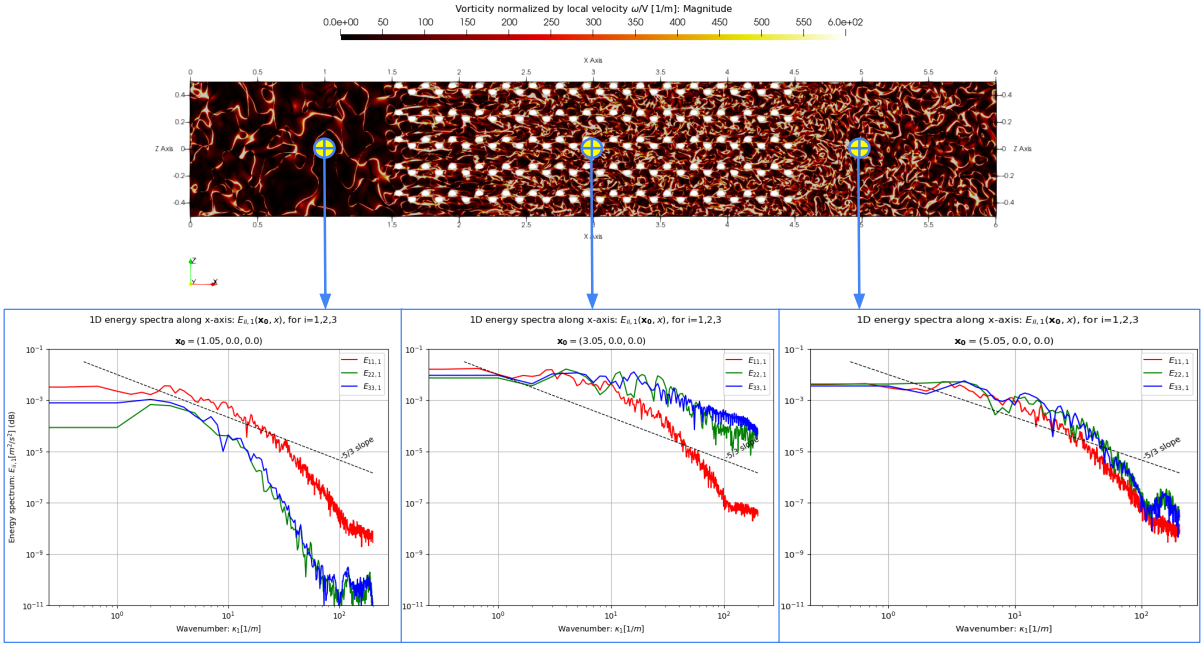

Figure 78: Gyroid with struct = 1.20: Spectra $E_{ii,1}$ across different positions in the domain along the line (y,z)=(0.0, 0.0): just before the PM in $x = 1.0$, in the middle of the PM in $x = 3.0$ and after the PM in $x = 5.0$.

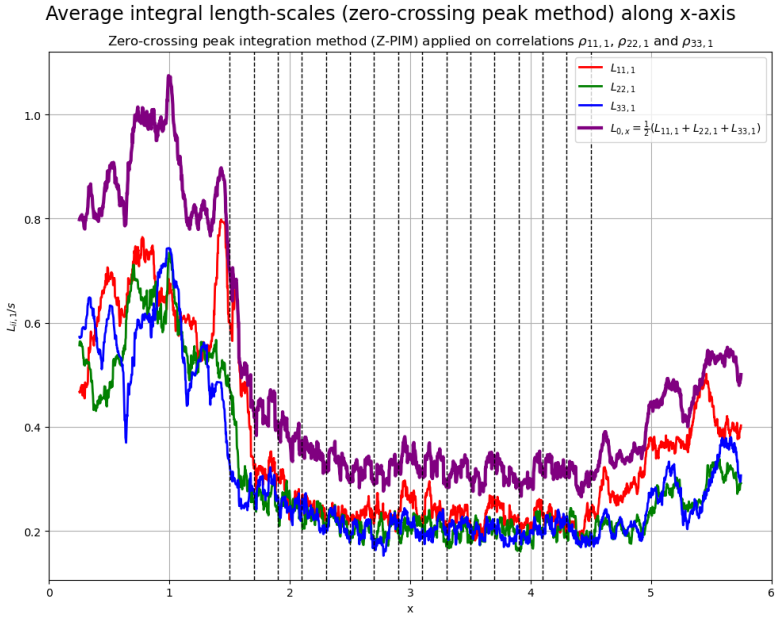

Figure 79: Gyroid with struct = 1.20: x-axis integral length-scales ($L_{11,1}$, $L_{22,1}$, $L_{33,1}$) and their trace $L_{0,x} = \frac{1}{2}(L_{11,1} + L_{22,1} + L_{33,1})$ averaged along the longitudinal axis x. The computation of the integral length-scales is done using the Z-PIM method, explained in Section 5.5.4. Length-scales are normalized by the pore size s (in this case $s = 0.2$).

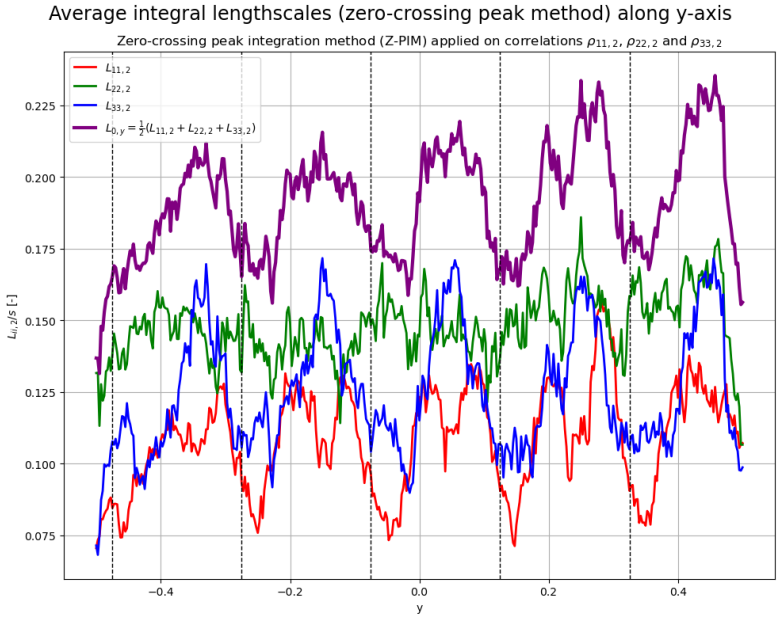

Figure 80: Gyroid with struct = 1.20: y-axis integral length-scales ($L_{11,2}$, $L_{22,2}$, $L_{33,2}$) and their trace $L_{0,y} = \frac{1}{2}(L_{11,2} + L_{22,2} + L_{33,2})$ averaged along the longitudinal axis y. The computation of the integral length-scales is done using the Z-PIM method, explained in Section 5.5.4. Length-scales are normalized by the pore size s (in this case $s = 0.2$). Only the PM domain is considered.

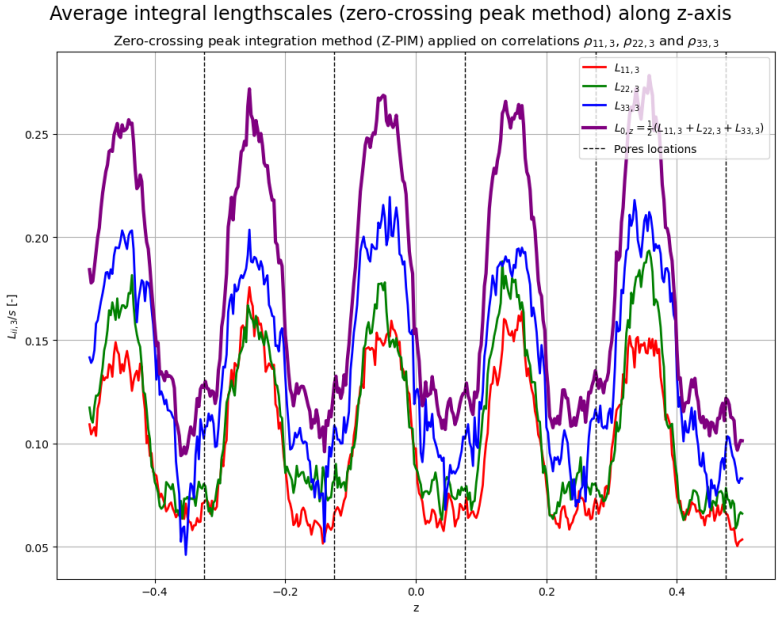

Figure 81: Gyroid with struct = 1.20: z-axis integral length-scales ($L_{11,3}$, $L_{22,3}$, $L_{33,3}$) and their trace $L_{0,z} = \frac{1}{2}(L_{11,3} + L_{22,3} + L_{33,3})$ averaged along the longitudinal axis z. The computation of the integral length-scales is done using the Z-PIM method, explained in Section 5.5.4. Length-scales are normalized by the pore size s (in this case $s = 0.2$). Only the PM domain is considered.

7.4 Turbulence analysis comparison: effect of the struct

In this section, we analyze the turbulence behavior in TPMS gyroid structures with two different values of the structural coefficient: $\text{struct}_a = 0.75$ and $\text{struct}_b = 1.20$. These values correspond to gyroid structures with distinct porosity ($\phi_a = 0.72$ and $\phi_b = 0.90$ respectively), influencing the flow and turbulence characteristics throughout the domain. We compare the velocity components,the turbulent kinetic energy (TKE) and the RST components, as well as the integral time-scales to understand the effect of varying the gyroid structural coefficient on the turbulence within the porous media.
In Figure 82 the mean velocity components ($\bar{U}, \bar{V}, \bar{W}$) and the mean velocity magnitude $\bar{V}_{mag}$ are averaged along the x-axis for both gyroid structures. It can be observed that the flow exhibits significant differences in all components between the two cases. The structure with struct = 0.75 shows higher velocity magnitudes (around +20%) compared to the struct = 1.20 case, as expected due to its lower porosity and more streamlined path for the fluid flow. Something interesting can be remarked for the velocity component along the z-axis, namely $\bar{W}$, where also the configuration with high porosity has an important increase through out the porous media if compared with the component $\bar{V}$, meaning that the gyroid has a preferential direction, that in this study case with $k_x = k_y = k_z = 2\pi \times 5$ is prone to the z-axis.
Similarly as for the velocity components, in Figure 83 we show the normal RST components and the TKE averaged along the x-axis. Significant variations between the two structures are observed, with the struct = 0.75 case presenting higher turbulence levels (around +65%) across the domain. TKE peaks at around 0.4 - 0.5$[m^2/s^3]$ for a $struct = 0.75$ with a first peak at after the first pore while the configuration with $struct = 1.20$ has lower peaks around $0.1 m^2/s^3$ with the first that happens only in the third pore following the stream-wise direction. This is due to the increased confinement of the fluid within the more porous struct = 1.20 structure, leading to less energetic turbulent fluctuations. A huge increase of the TKE and its components is observed near the inlet, followed by peaks localized periodically in the second half of each pore. A decaying behavior happens at the exit of the porous media, similarly to grid turbulence experiences. It is evident how porous media with smaller pore sizes are better turbulence generators, if the same turbulence spectrum is injected at the inlet, as in our case.
The integral timescales are computed for the three velocity components $\bar{\tau_x}, \bar{\tau_y}, \bar{\tau_z}$ and the turbulent kinetic energy $\bar{\tau_{TKE}} = \frac{1}{2}(\bar{\tau_x} + \bar{\tau_y} + \bar{\tau_z})$. The results are shown in Figure 84. It is observed that the integral timescales are generally higher for the struct = 1.20 case, particularly in the x- and z-directions. This reflects the lower turbulence intensity within the more porous structure, resulting in slower temporal variations in the flow field. It is interesting to remark that the lower porosity configuration does create a blocking effect in the first stream-wise pore leading to a peak in the time-scales $\bar{\tau_x}$ and $\bar{\tau_y}$, which is not observed in the higher porosity configuration. We are happy also to see that the injected turbulence match in both cases and that its time-scale is coherent with the user-defined spectrum through the SRFM.

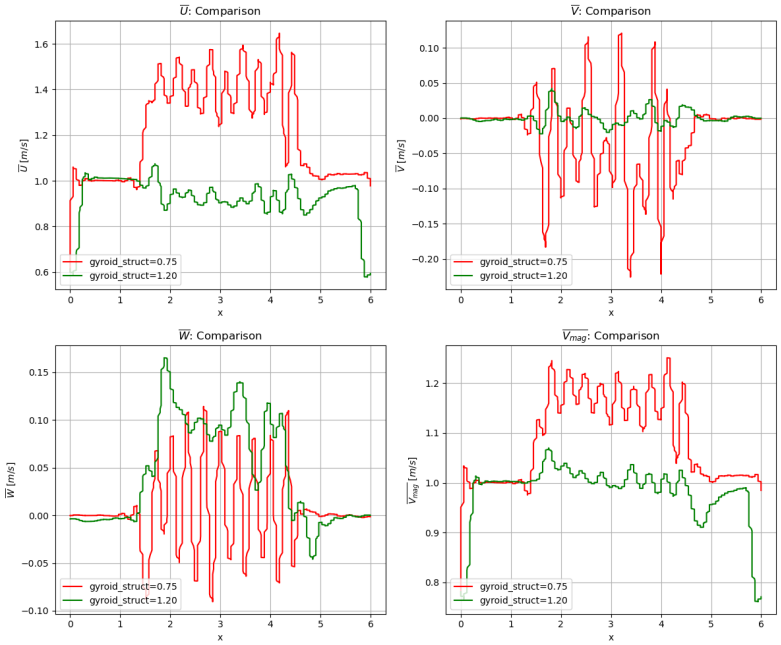

Figure 82: Gyroid $struct = 0.75$ vs Gyroid $struct = 1.20$ comparison: mean velocity components ($\langle U \rangle$, $\langle V \rangle$, $\langle W \rangle$) and mean velocity magnitude $V_{mag} = \sqrt{(\langle U \rangle)^2 + (\langle V \rangle)^2 + (\langle W \rangle)^2}$ averaged along the longitudinal axis x.

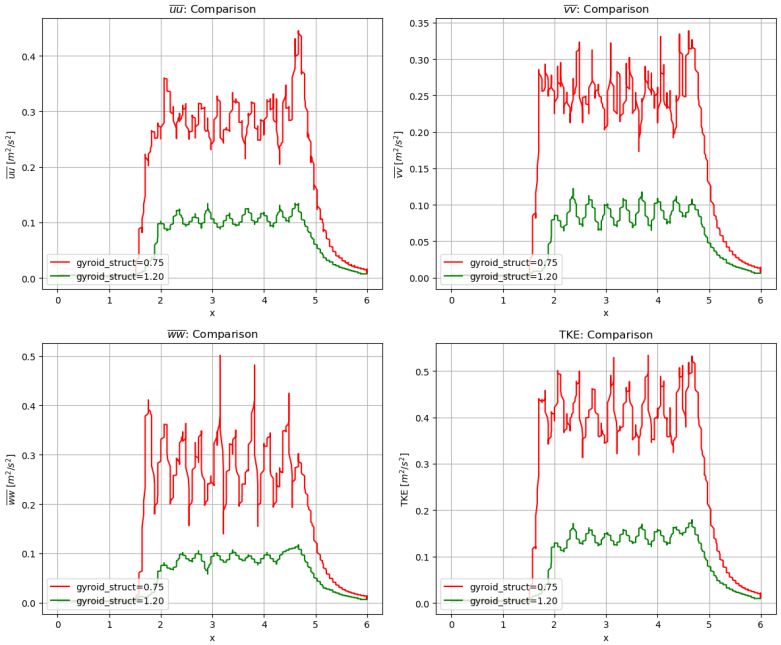

Figure 83: Gyroid $struct = 0.75$ vs Gyroid $struct = 1.20$ comparison: normal RST components $\langle uu \rangle$, $\langle vv \rangle$, $\langle ww \rangle$ and of their half-trace $TKE = \frac{1}{2}(\langle uu \rangle + \langle vv \rangle + \langle ww \rangle)$ averaged along the longitudinal axis x.

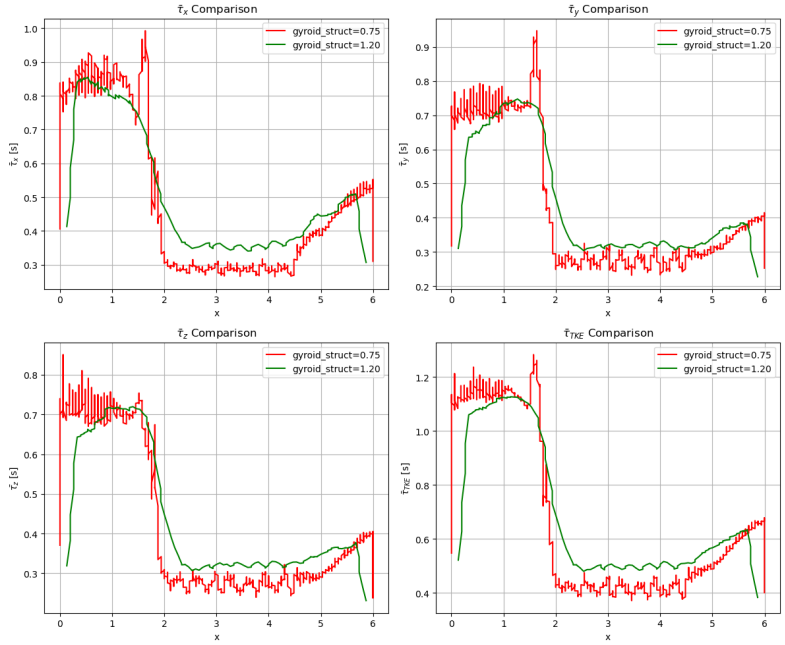

Figure 84: Gyroid $struct = 0.75$ vs Gyroid $struct = 1.20$ comparison: 1D integral time-scales τ_x, τ_y, τ_z and their half-trace $\tau_{TKE} = \frac{1}{2}(\tau_x + \tau_y + \tau_z)$ averaged along the longitudinal axis x.

For a complete comparison, in Figures 107, 108 and 109 we compare the FFT in frequency domain of the normal RST components and of its half-trace, the TKE, for three different locations along the computational domain: before, inside and after the porous media respectively. In general we prove the expected trend that the energy distribution over all the spectrum of eddies is higher for the struct=0.75 configuration if compared with the struct=1.20 in all cases: just before, inside and after the porous media. Moreover the local turbulence Reynolds in the lower porosity case is higher leading to lower Kolmogorov scales as well. In Tables 17 and 16 we resume the data, especially the time-scales, collected for the two configurations in three points (before, inside and after the PM). In order to have a more clear view about the time-scales in play and to underline the effect of the structural factor, in Table 18 we summarize the integral time-scales from Figure 84 and we add also an approximation based on the local $u_{rms} = u'$ of the Kolmogorov scales. As expected, for $struct = 0.75$ Kolmogorov scales are reduced by the PM of around -50% compared to the case $struct = 1.20$ as the local turbulent Reynolds number increases at low porosity. Moreover the dissipation is enormously enhanced of around 10 times more due to a consistent increase of the TKE (+66.7 %) that is reflected on an increase in the u_{rms} of +123.6%.

Table 16: **Gyroid struct 1.20**: $u_{\text{rms}} = \sqrt{\frac{2k}{3}}$, dissipation rate $\epsilon = \frac{u_{\text{rms}}^3}{L_0}$, integral time scales τ, length scales L, Kolmogorov scales, and Reynolds number $Re_0 = \frac{u_{rms} L_0}{\nu}$ at different x-positions. Kolmogorov scales are computed using $\eta = \left(\frac{\nu^3}{\epsilon}\right)^{1/4}$ and $\tau_\eta = \left(\frac{\nu}{\epsilon}\right)^{1/2}$, where $\nu = 4.0 \times 10^{-4}\,\text{m}^2/\text{s}$. Note that the isotropic integral length-scale L_0 is compute as: $L_0 = \sqrt{L_{0,x}^2 + L_{0,y}^2 + L_{0,z}^2}$. Lenght-scales are normalized by a constant pore size $s = 0.2$.

Quantity	**x = 1.0**	**x = 3.0**	**x = 5.0**
k **(m/s)**	5.0e-2	8.0e-2	4.0e-2
u_{rms} **(m/s)**	1.8e-1	2.3e-1	1.6e-1
ϵ **(m^2/s^3)**	4.2e-3	2.9e-2	6.5e-3
τ_{11} **(s)**	8.0e-1	3.5e-1	5.5e-1
τ_{22} **(s)**	7.0e-1	3.0e-1	3.5e-1
τ_{33} **(s)**	7.0e-1	3.0e-1	3.5e-1
τ_0 **(s)**	1.1e+0	5.0e-1	5.8e-1
$L_{0,x}/s$ **(-)**	8.5e-1	3.5e-1	4.5e-1
$L_{0,y}/s$ **(-)**	7.5e-1	2.0e-1	3.5e-1
$L_{0,z}/s$ **(-)**	7.5e-1	2.2e-1	3.5e-1
L_0/s **(-)**	1.4e+0	4.6e-1	6.7e-1
η **(m)**	1.2e-2	5.7e-3	8.7e-3
τ_η **(s)**	3.1e-1	1.2e-1	2.5e-1
Re_0	1.3e+2	5.3e+1	5.4e+1

Table 17: **Gyroid struct 0.75**: $u_{\text{rms}} = \sqrt{\frac{2k}{3}}$, dissipation rate $\epsilon = \frac{u_{\text{rms}}^3}{L_0}$, integral time scales τ, length scales L, Kolmogorov scales, and Reynolds number $Re_0 = \frac{u_{rms} L_0}{\nu}$ at different x-positions. Kolmogorov scales are computed using $\eta = \left(\frac{\nu^3}{\epsilon}\right)^{1/4}$ and $\tau_\eta = \left(\frac{\nu}{\epsilon}\right)^{1/2}$, where $\nu = 4.0 \times 10^{-4}\,\text{m}^2/\text{s}$. Note that the isotropic integral length-scale L_0 is compute as: $L_0 \approx u_{\text{rms}}\tau_0$. Lenght-scales are normalized by a constant pore size $s = 0.2$.

Quantity	**x = 1.0**	**x = 3.0**	**x = 5.0**
k **(m/s)**	5.0e-2	4.0e-1	2.0e-1
u_{rms} **(m/s)**	1.8e-1	5.2e-1	3.7e-1
ϵ **(m^2/s^3)**	4.2e-3	3.0e-1	9.7e-2
τ_{11} **(s)**	8.0e-1	3.0e-1	4.0e-1
τ_{22} **(s)**	7.0e-1	2.5e-1	3.0e-1
τ_{33} **(s)**	7.0e-1	2.5e-1	3.0e-1
τ_0 **(s)**	1.1e+0	4.3e-1	5.0e-1
$L_0/s \approx (u_{\text{rms}}\tau_0)/\text{s}$	1.4e+0	1.1e+0	9.1e-1
η **(m)**	1.2e-2	2.7e-3	4.4e-3
τ_η **(s)**	3.1e-1	3.6e-2	6.4e-2
Re_0	1.3e+2	2.8e+2	1.7e+2

Table 18: Comparison Gyroid *struct* = 1.20 vs *struct* = 0.75: macroscopic and Kolmogorov time-scales, macroscopic and Kolmogorov length-scales, u_{rms}, dissipation and turbulent Reynolds number Re_0 computed at 3 different x-positions: before the PM ($x = 1.0$), inside the PM ($x = 3.0$) and after the PM ($x = 5.0$). The relative difference is calculated as $\left(\frac{\text{value}_{0.75} - \text{value}_{1.20}}{\text{value}_{1.20}}\right) \times 100$, and is shown in parentheses next to the values for Gyroid struct 0.75. Red values indicate a reduction relative to Gyroid struct 1.20, while green values indicate an increase. Note that the isotropic integral length-scale L_0 is compute for both cases as: $L_0 \approx u_{\text{rms}}\tau_0$. Moreover, lenght-scales are normalized by a constant pore size $s = 0.2$.

Quantity	**Gyroid struct**	**x = 1.0**	**x = 3.0**	**x = 5.0**
u_{rms} **(m/s)**	1.20	1.8e-1	2.3e-1	1.6e-1
	0.75	1.8e-1 (0%)	5.2e-1 (+123.6%)	3.7e-1 (+123.6%)
ϵ **(m^2/s^3)**	1.20	4.2e-3	2.9e-2	6.5e-3
	0.75	4.2e-3 (0%)	3.0e-1 (+957.6%)	9.7e-2 (+1396.9%)
τ_{11} **(s)**	1.20	8.0e-1	3.5e-1	5.5e-1
	0.75	8.0e-1 (0%)	3.0e-1 (-14.3%)	4.0e-1 (-27.3%)
τ_{22} **(s)**	1.20	7.0e-1	3.0e-1	3.5e-1
	0.75	7.0e-1 (0%)	2.5e-1 (-16.7%)	3.0e-1 (0%)
τ_{33} **(s)**	1.20	7.0e-1	3.0e-1	3.5e-1
	0.75	7.0e-1 (0%)	2.5e-1 (-16.7%)	3.0e-1 (0%)
τ_0 **(s)**	1.20	1.1e+0	5.0e-1	5.8e-1
	0.75	1.1e+0 (0%)	4.3e-1 (-15%)	5.0e-1 (-13.8%)
L_0/s **(-)**	1.20	1.4e+0	2.3e+0	3.4e+0
	0.75	1.4e+0 (0%)	1.1e+0 (-52.3%)	9.1e-1 (-72.7%)
η **(m)**	1.20	1.2e-2	5.7e-3	8.7e-3
	0.75	1.2e-2 (0%)	2.7e-3 (-52.6%)	4.4e-3 (-49.4%)
τ_η **(s)**	1.20	3.1e-1	1.2e-1	2.5e-1
	0.75	3.1e-1 (0%)	3.6e-2 (-69.3%)	6.4e-2 (-74.2%)
Re_0	1.20	1.3e+2	5.3e+1	5.4e+1
	0.75	1.3e+2 (0%)	2.8e+2 (+428.3%)	1.7e+2 (+218.5%)

8 Conclusions

This manuscript successfully opens the way for a systematic analysis of turbulence in TPMS structures. As stated in the introduction, the main objectives of the work were:

1. Numerical approach validation for the PGS combined IBCc method;
2. Efficient post-treatment strategy of big-data from DNSs;
3. Turbulence analysis in a Gyroid structure with structural factor $struct = 1.20$, in order to start understanding the key aspects of the turbulence in a TPMS and the main turbulence analysis tools to use;
4. Comparative turbulence analysis Gyroid $struct = 0.75$ vs Gyroid $struct = 1.20$, in order to start having an idea of the influence of the geometrical variability of the TPMS over the flow, and its magnitude over the turbulence properties such as the length- and time-scales.

The simulations analyzed in this work are summarized in Tables 8.pt1 and 8.pt2, with their respective main numerical settings.
As you reach this conclusion, I invite you to revisit the preceding sections with fresh insights, if you feel the urge. It has been my goal to provide a comprehensive understanding, and I hope my efforts have contributed meaningfully to your knowledge.
In science, what may seem like the end of a journey is often just the opening of new doors, leading to further exploration and discovery. This is not an ending, but the beginning of new questions and challenges yet to be unraveled.

In the following section, we briefly go through all the listed objectives and discuss the key findings with their implications. Finally we conclude with some perspectives for the future.

Table 19: Simulation Parameters for TPMS Simulations (Part 1)

Simulation	**PGS factor** (α^{-2})	$L_{0,inj}$	Tu_{inj} **[%]**	Re_{inj}	Re_p	**CFL**	**Nb Iterations**	**Nb Sub-sampling**
Minigyroid struct=0.75	0.15	0.258	9.11	2500	≈ 1500	0.25	1200k	1k
Minigyroid struct=0.75	Any	0.258	9.11	2500	≈ 1500	0.25	2000k	2k
Gyroid struct=0.75	0.005	0.258	9.11	2500	≈ 300	0.25	205k	200
Gyroid struct=1.20	0.005	0.258	9.11	2500	≈ 275.5	0.25	205k	200

Table 20: Simulation Parameters for TPMS Simulations (Part 2)

Simulation	**Domain size:** (L_x, L_y, L_z)	**TPMS location:** $[x_1, x_2]$	**Cells:** (N_x, N_y, N_z)	**Order SDM polynomial: p**
Minigyroid struct=0.75	(8,1,1)	[2.0, 6.0]	120,16,16	3
Minigyroid struct=0.75	(8,1,1)	[2.0, 6.0]	120,16,16	3
Gyroid struct=0.75	(6,1,1)	[1.5, 4.5]	600,100,100	5
Gyroid struct=1.20	(6,1,1)	[1.5, 4.5]	600,100,100	5

8.1 Efficient post-treatment strategy of big-data from DNSs

The post-treatment strategy for handling large datasets generated by DNS (run using the JAGUAR code) has proven to be a crucial element for efficient data analysis, particularly in cases involving high DoF. The results show a substantial reduction in storage requirements—up to 93%—while maintaining the accuracy needed for both spatial and temporal analysis. By combining high temporal resolution probes with strategically sub-sampled spatial planes and volumes, extracted through a highly performant code (Section 7.1), we effectively balanced the need for detailed flow characterization with the constraints of storage and computational cost.
Our approach leveraged Python-based tools like Antares and `mpi4py` to handle data extraction and reduction in a scalable manner, optimizing the distribution of data across computational resources. This enabled the retention of essential flow features, particularly turbulence patterns, while significantly reducing the volume of raw data that needed to be stored and processed. The application of sub-sampling and selective extraction ensured that the computational load remained manageable without compromising the quality of the turbulence analysis. A preliminary analysis was performed to limit uncertainties in the skewness and kurtosis of the velocity field below 20% and 80% respectively. Specifically, uncertainty was evaluated with confidence intervals computed using the Jack-knife method [19] as detailed in Section 4.5.1.
In conclusion, the post-treatment strategy developed in this study offers a highly efficient solution for managing large-scale DNS data. When combined with high-performance computing resources, such as those available at GENCI, this strategy enables the extraction of valuable insights into turbulent flows within porous media, setting the stage for more comprehensive turbulence studies with minimal data overhead.

8.2 Validation of the numerical approach PGS method with IBCs

The validation of the PGS method with IBCs has provided a comprehensive assessment of the numerical approach applied to flow in complex porous media. The validation was carried out on a simplified "minigyroid" geometry, which allowed for efficient computational comparisons while maintaining sufficient complexity to challenge the numerical methods. The grid used consisted of a coarse mesh with $(16 \times 16 \times 120)$ cells, resulting in approximately two million degrees of freedom, ensuring the computational cost remained manageable during the validation process.
The solver configuration employed for this validation utilized a polynomial degree $p = 3$, a PGS factor of $\alpha_{PGS}^{-2} = 0.15$, and a $CFL = 0.25$.

- **Incompressibility validation:** A key prerequisite for the application of the PGS method is the validation of the incompressibility assumption, specifically the low pressure in-homogeneity assumption. This hypothesis was confirmed analyzing the pressure and density fields within the PM domain. Slight gradients are observed just at the IBC walls but the overall flow can be considered incompressible.

- **First-order statistics validation:** The first-order statistics, particularly mean velocity components, were effectively preserved with the PGS method with errors less than 4%, primarily localized near the IBC boundaries. This slight deviation is expected due to the interaction between the PGS and IBC, yet it does not significantly affect the overall flow dynamics.

- **Second-order statistics validation:** The second-order statistics, involving the RST components and the TKE, exhibited larger errors compared to first-order quantities. Near the boundaries, particularly in the regions close to the IBC cells, the PGS method under-predicted TKE by approximately 5-10%. This under-prediction is attributed to the damping of small-scale eddies near the porous walls, as the interaction between the IBC and PGS slightly suppresses the turbulent structures in these regions. However, in the bulk regions, away from the boundaries, the error in TKE was below 5%, indicating that the method reliably captures the main turbulent characteristics in the core flow. The second-order statistics show that while the PGS introduces some minor deviations, particularly near boundaries, it performs well in preserving the essential turbulence dynamics in the majority of the domain.

- **Computational efficiency and time scales:** A key advantage of the PGS method is its computational efficiency. The Kolmogorov time scales in the porous structure are of the order of the centiseconds, while the numerical time steps, constrained by the CFL condition, were significantly

smaller. The PGS method allowed a reduction in computational time by an increase of the simulation time-step by the PGS coefficient (in this case $\alpha \simeq 2.5$), while still capturing the critical turbulent features. This efficiency gain makes the method particularly useful for high-resolution simulations in porous media, where computational resources are often a limiting factor.

In conclusion, the validation of the PGS method with IBCs shows that it provides reliable and accurate results for both mean flow and turbulence statistics, with minor localized errors near the walls. The method offers significant computational savings without compromising the key features of the flow. Future work should focus on refining the interaction between PGS and IBC to further reduce errors in the near-wall turbulence predictions, particularly for high-fidelity simulations. This could help also in increasing safely the PGS coefficient α even more, allowing for even higher performances.
Overall, the PGS method is a powerful tool for simulating turbulent flows in porous media, offering a balance between accuracy and efficiency.

8.3 Turbulence Analysis for a TPMS Material: *Gyroid struct* = 1.20

A summary of the results for the gyroid with *struct* = 1.20 is presented in Table 16, while the main findings are schematized in the following points:

- **Mean Flow Characteristics:**
  - The analysis revealed that the maximum velocity at the center of the gyroid pores reached approximately **2.3 times** the inlet velocity, indicating **significant acceleration** due to the geometry's inherent jetting effects. This high velocity contributes to enhanced mixing and flow acceleration within the pore spaces.
  - A **preferential flow direction** was identified in the cross-direction of the material, particularly along the z-axis. This was evidenced by the higher mean value of W compared to V inside the porous medium, emphasizing the non-symmetrical nature of the flow within the gyroid.
  - Boundary layers formed along the pore walls, leading to **pronounced velocity gradients**. These gradients are crucial for understanding how the gyroid structure influences flow separation and re-circulation, suggesting localized regions of turbulence generation near the walls and especially behind them, where **vortex shedding** is observed.
- **Turbulent Kinetic Energy (TKE):**
  - TKE exhibited a **sharp increase at the PM inlet**, with a peak increase of around **40%** compared to the region before the media, underscoring the role of pore geometry in energy dissipation and turbulence amplification. This highlights the gyroid's **capacity to spatially modulate turbulence levels**.
  - **Inside the porous media the TKE increases constantly** until the exit with a rate of approximately **+3.6%** per pore.
  - The **periodic** structure of the gyroid played a fundamental role in shaping the **TKE distribution**, with local maxima corresponding to regions of flow acceleration and deceleration near the pore exits. This periodicity is directly linked to the formation and modulation of turbulent structures within TPMS materials.
  - The highest TKE levels were consistently observed at the transitions between stagnation zones and jet-like flows, suggesting that the interaction between these flow regimes is a key driver of turbulence within the porous structure.
  - A **delayed onset of turbulence** was observed, with significant TKE generation only occurring after the flow passed through the first **three pores**. This implies that the high porosity of *struct* = 1.20 reduces flow confinement, leading to a gradual build-up of turbulence as the flow progresses.
- **Energy Spectra:**

- **Initial anisotropy** was observed in the energy spectra, with larger turbulent structures concentrated in the stream-wise direction and smaller scales dominating the transverse and vertical directions. This anisotropy indicates that energy cascades differently along the main flow direction compared to the other axes, reflecting the influence of the gyroid geometry.
- The TPMS structure acts as an **"isotropizer" along the stream-wise direction**, gradually promoting isotropy through the diffusive action of the geometry, along with dissipation and TKE enhancement. This allows us the comparison with **grid turbulence** experiences.
- Length scales deduced from the spectra (peak of the pre-multiplied energy spectra) have not been fully utilized, as the simulations are not completely converged at low frequencies.

- **Integral time- and length- Scales:**
  - **Integral time-scales** where computed using the **classical methodology** where the velocity auto-correlations are integrated over the time-shift domain.
  - On the other hand, **integral length-scales** were computed using the **Z-PIM method**, that proved to be **highly effective** in cases where space-correlations were not fully converged. Its robustness in handling complex flow fields and incomplete data (e.g. not fully converged simulations at low frequencies) makes it an invaluable tool for identifying characteristic length scales in intricate porous geometries such as the gyroid. This method enhances the accuracy of turbulence analysis, particularly where traditional methods struggle with resolving spatial interactions.
  - **Inside the PM** the **integral length scales in the stream-wise direction** were found to extend up to **0.4 times** the characteristic pore size, while **transverse scales** were limited to **0.25 times**. This demonstrates, in **agreement with the PSPH**, how the pore size constrains turbulent structure development, particularly in the transverse directions, where vortex interactions are more prominent.
  - **Before the PM** there is a **region of adaption** to the pore size that in this case is smooth and takes around 3 pores in longitudinal direction.
  - **After the PM** there is a **region of merging and slowing down** of the eddies where both the length- and time- scales increase moderately.

8.4 4. Comparative Turbulence Analysis for TPMS materials: Effect of structural factor *struct* over a Gyroid

A summary of the results for the gyroid with $struct = 0.75$ is presented in Table 17, while a comparative analysis of the timescales and length scales between the gyroid structures with $struct = 1.20$ and $struct = 0.75$ is provided in Table 18. The main conclusions are:

- **Turbulent Kinetic Energy (TKE):**
  - In this comparative analysis, it was observed that **the structural factor** *struct* **(and so the porosity) significantly impacts the TKE levels** within the gyroid structures.
  - For $struct = 0.75$, TKE peaks at around 0.4 - 0.5 m^2/s^3 with the first peak occurring after the first pore. In contrast, the $struct = 1.20$ configuration exhibited lower TKE peaks around 0.1 m^2/s^3, with the first peak observed only in the third pore along the streamwise direction.
  - **The increase in structural factor leads to higher confinement of the flow, thus generating lower TKE.** This demonstrates the crucial role of structural complexity in regulating turbulent fluctuations.

- **Time-scales:**
  - The integral timescales τ in the gyroid structures also varied with the structural factor. For $struct = 0.75$, the timescales were shorter, indicating more frequent turbulent events and higher turbulence intensity as well as the smaller "real" pore size to be considered.

  - **At the PM inlet** we observe an **obstruction effect in the low porosity** configuration that makes increase significantly (+15% ÷ 20%) the time-scale before its sharp **adaptation to the pore, within one longitudinal pore**. On the other side, the blocking effect **is not observed in the high porosity** configuration where the time-scales **adapt smoothly within three pores** to the pore dynamics.

- **Kolmogorov scales (HIT assumption):**

  - The **Kolmogorov scales** η **and** τ_η, representing the smallest scales of turbulence, are computed through a HIT approximation and showed notable differences. For $struct = 0.75$, the Kolmogorov length scales were approximately half of those in the $struct = 1.20$ configuration reflecting the important increase of the u_{rms} ($\simeq +124$ %) and local turbulent Reynolds number Re_0 ($\simeq +428$ %).
  - This reflects that **lower-porosity structures**, like $struct = 0.75$, **promote higher turbulence Reynolds numbers and TKE production, increasing dissipation rates and facilitating a more rapid energy cascade to smaller scales.**

- **Dissipation Rate and Turbulent Reynolds Number (HIT assumption):**

  - **The dissipation rate** ϵ are computed through a HIT approximation. **In the** $struct = 0.75$ **gyroid showed an approximate increase of 10 times more compared to the** $struct = 1.20$ **case inside the PM.**
  - This is consistent with the significantly higher turbulence Reynolds numbers, with $struct = 0.75$ reaching values more than 4 times that of $struct = 1.20$. **These findings underscore how the structural factor directly modulates the intensity and nature of turbulence within the porous medium.**

In summary, the comparative analysis of gyroid structures with varying structural factors demonstrates that increasing the structural factor reduces both TKE and dissipation rates, while also lengthening the integral timescales, accordingly to the real pore size proportional to the porosity. The more confined flow of the $struct = 1.20$ **configuration leads to weaker turbulence and a slower energy cascade, as reflected in the larger Kolmogorov scales and lower dissipation rates. This analysis is vital for optimizing TPMS materials in applications requiring precise control over turbulence characteristics.**

8.5 Future perspectives

This study opens several pathways for further research, both in terms of enhancing our understanding of turbulence in porous media and extending the applicability of TPMS-based simulations. Future work could focus on the following areas:

- **Investigation on more TPMS topologies**: Expanding the analysis to other TPMS structures, such as the Diamond and Primitive configurations, will provide a more comprehensive understanding of how different topological features influence turbulence. Each topology presents unique interactions between flow and geometry, which could affect turbulent energy distribution and dissipation.

- **Deeper investigation on the structural factor (porosity)**: The impact of porosity on flow behavior warrants further investigation. It would be particularly insightful to explore the existence of a critical porosity threshold beyond which the Pore Scale Prevalence Hypothesis (PSPH) may no longer hold, as suggested by recent literature [148]. This could refine our understanding of flow transitions in porous media and the role of geometry in modulating turbulent structures.

- **Investigation of injected turbulence parameters**: The influence of the injected turbulence spectrum at the inlet, mainly defined by a turbulence intensity (Tu) and an injection integral length-scale for the energy-containing eddies (L_0), should be systematically studied. It would be intriguing to assess scenarios where the injected turbulence scale is smaller than the pore size, thereby challenging the assumptions of the PSPH. Such an approach may reveal novel flow regimes where external turbulence dominates over pore-scale effects.

- **Investigation over the effect of the inlet Reynolds number**
- **Investigation of multiscale TPMS structures**: Multiscale TPMS materials, with hierarchical structures at different length scales, offer a complex environment for turbulent interactions. Understanding how energy cascades through these scales, and how different length scales interact within the material, could lead to new insights into optimizing porous media for specific engineering applications, such as heat exchangers or reactors.
- **Influence of the IBCs on RST-trasport equation and TKE Budget**: Further analysis is required to assess how the IBC affects the RST tensor and the terms in the TKE budget. In particular, when using significant PGS factors to accelerate simulations, the influence of SP (IBC cells) near the walls should be minimized. Preliminary results indicate that reducing the number of wall-adjacent cells decreases the pressure correlations, which are crucial for accurate modeling of TKE transport equations, especially the pressure-strain correlation and pressure-diffusion terms. However, more detailed analysis is necessary to publish conclusive findings.
- **Detailed analysis of TKE Budget Terms**: Extracting and analyzing the individual terms in the TKE budget will provide deeper insights into energy transfer mechanisms within the TPMS structures. Understanding the relative contribution of production, dissipation, and transport terms could help refine turbulence models for porous media.
- **Development of a turbulence model** based on the system parameters: A robust turbulence model could be developed by systematically varying key parameters such as topology, structural factor, and inlet turbulence characteristics. The goal would be to establish a transfer function for the porous material, which describes its ability to modulate turbulence under various flow conditions.
- **Experimental validation** through PIV and wind-tunnel tests: To strengthen the validation of the numerical findings, experimental techniques such as **Particle Image Velocimetry (PIV)** and wind-tunnel testing should be employed. These methods would provide high-resolution, real-world flow data that can be directly compared with simulation results, thus enhancing the reliability of the computational models.
- **Validation using alternative solvers**: To ensure the robustness of the numerical approach, additional solvers, such as **Lattice Boltzmann Methods (LBM)**, should be used for comparison. LBM has been successfully applied in studies of porous media turbulence [72, 70, 175, 60, 61], and its inclusion in this work would provide an additional layer of validation for the DNS results obtained using the Jaguar code.
- **Incorporation of chemical reactions for combustion studies**: Extending the study to include reactive flows will allow for an investigation of flame stability, heat release, and pollutant formation in turbulent combustion within porous media. Such studies are critical for applications in energy production and environmental protection, where the efficiency of combustion processes and emissions control is paramount.

A Figures: PGS method validation

In this appendix, we provide additional figures and tables related to the results presented in Section 7.2.

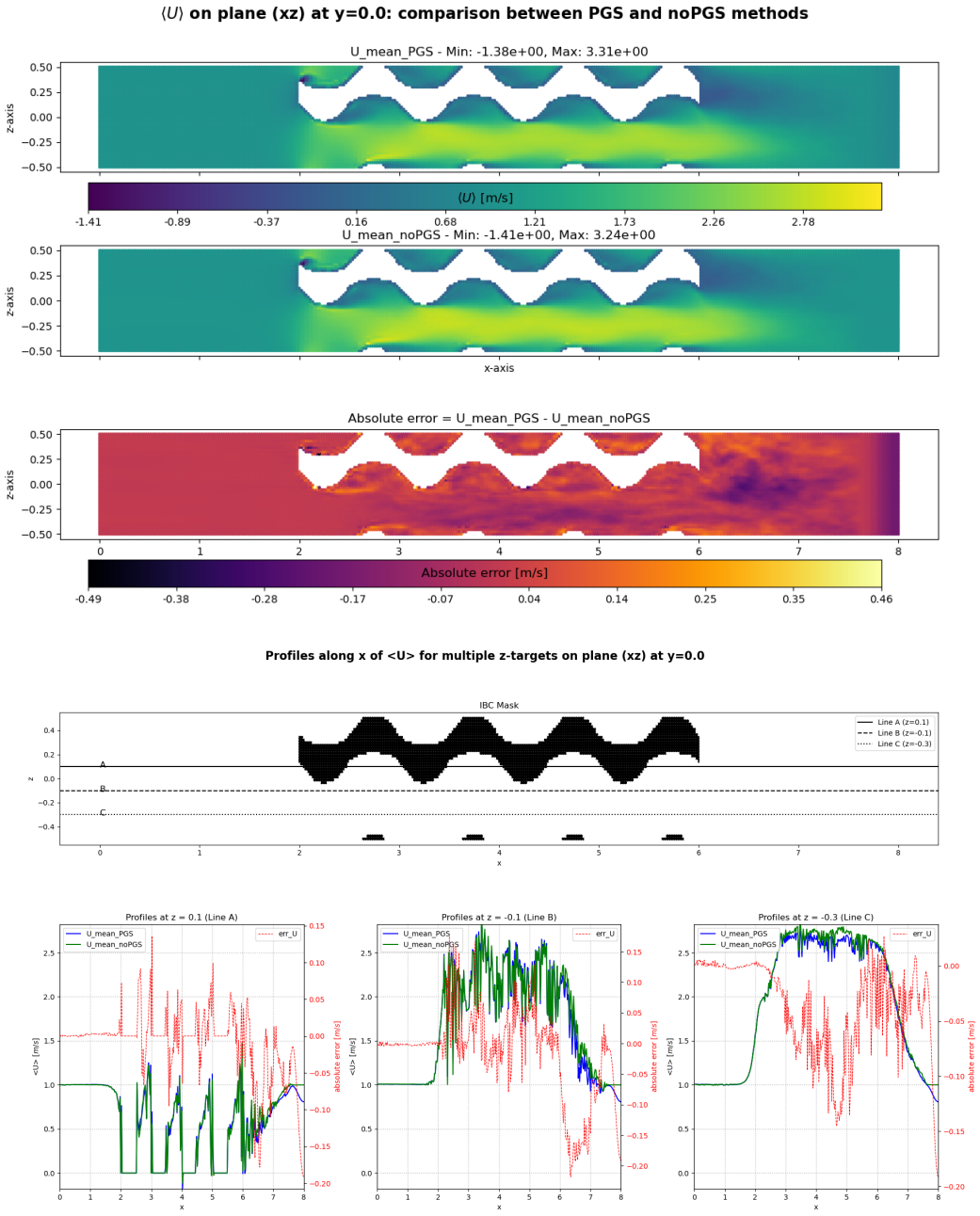

Figure 85: Comparison between PGS and no PGS methods for a one transversal pore configuration: $\langle U \rangle$.

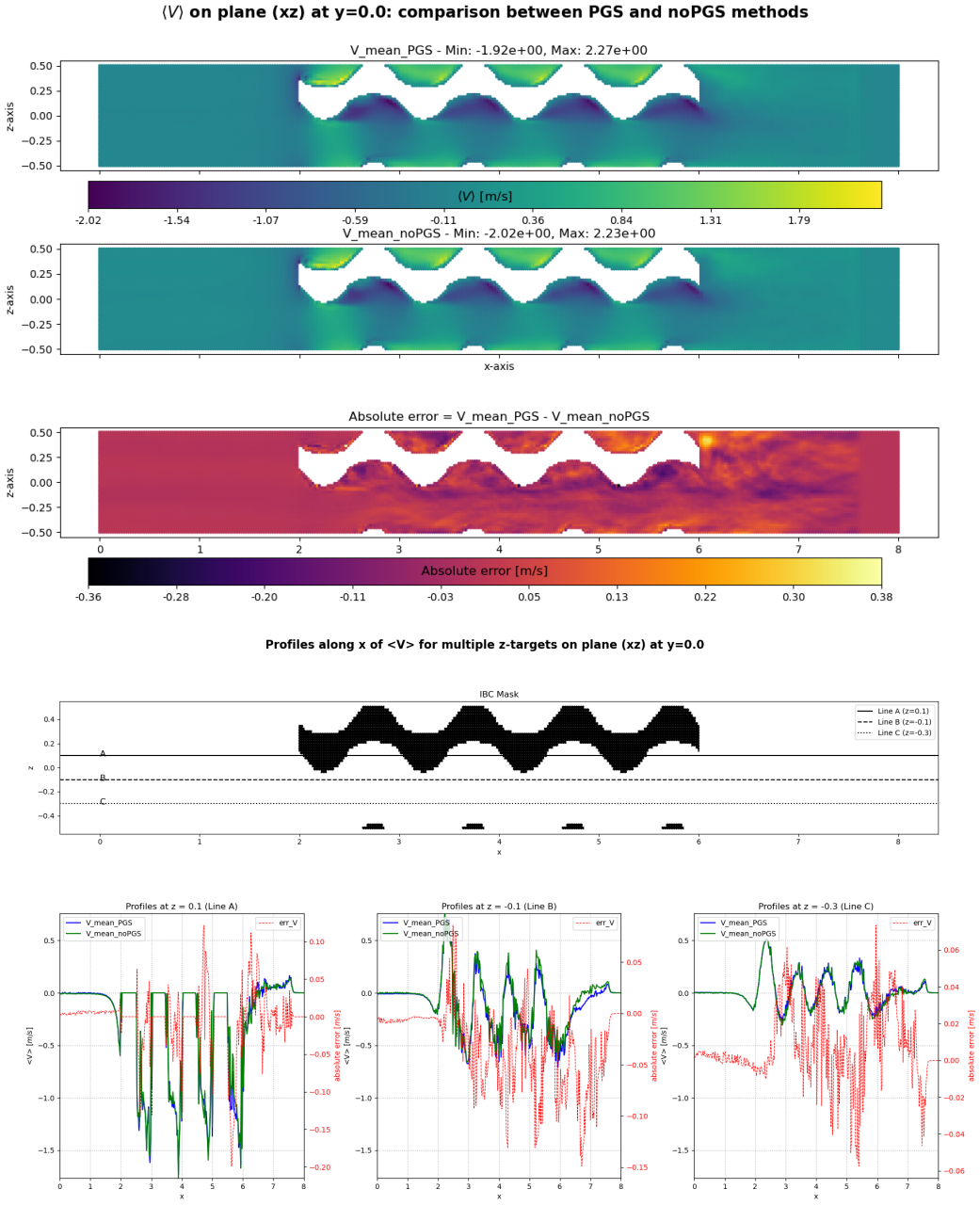

Figure 86: Comparison between PGS and no PGS methods for a one transversal pore configuration: $\langle V \rangle$.

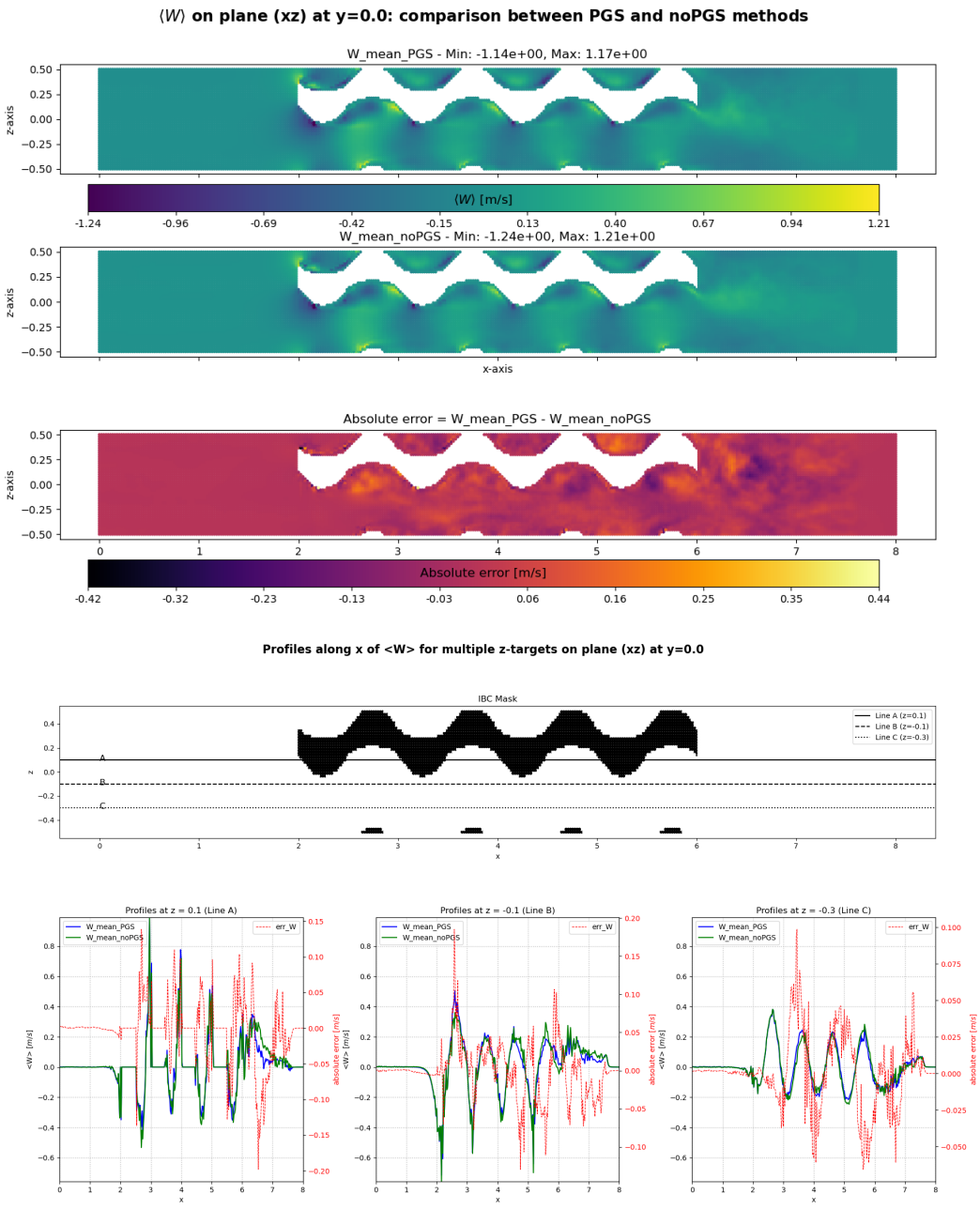

Figure 87: Comparison between PGS and no PGS methods for a one transversal pore configuration: $\langle W \rangle$.

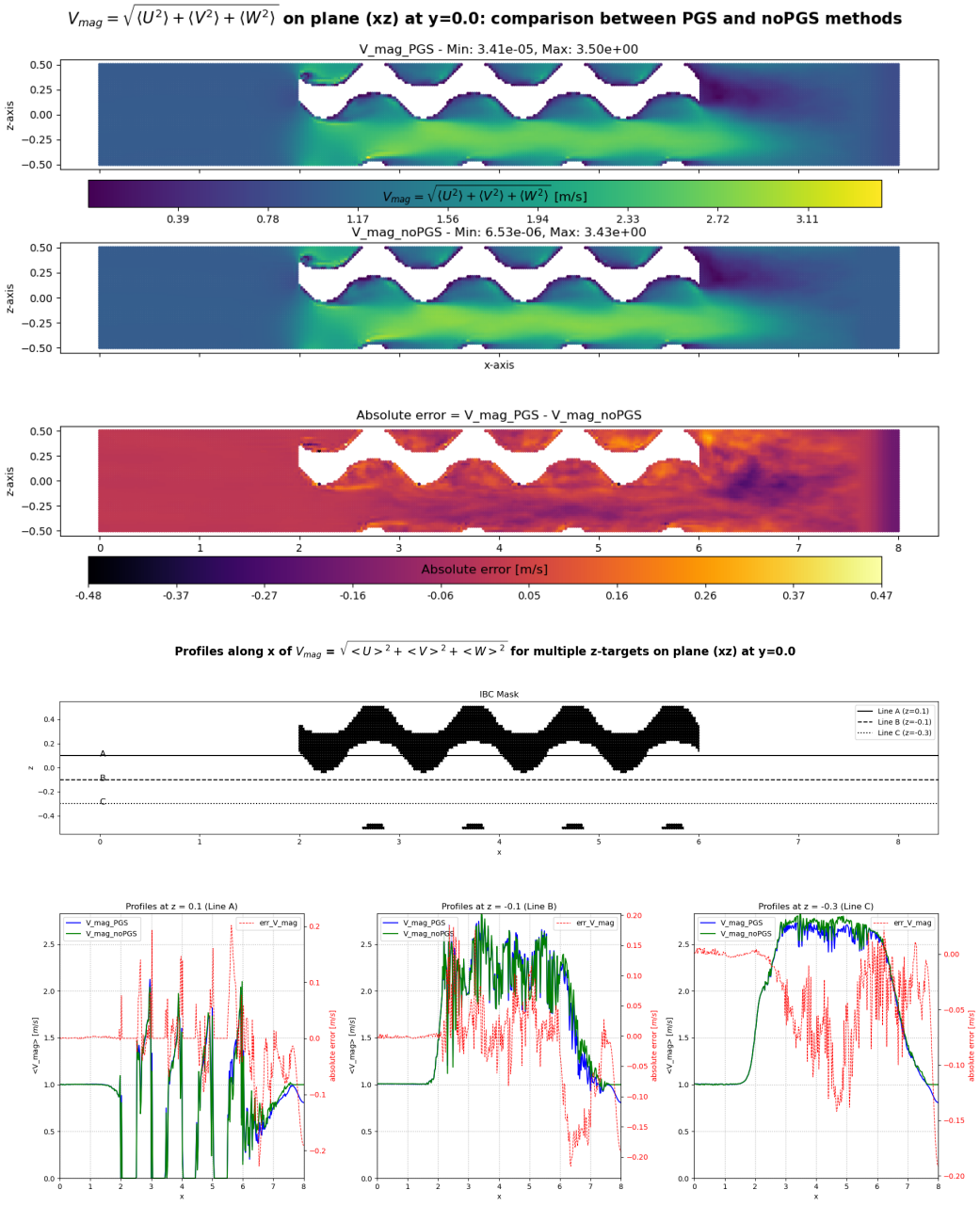

Figure 88: Comparison between PGS and no PGS methods for a one transversal pore configuration: mean velocity magnitude V_{mag}.

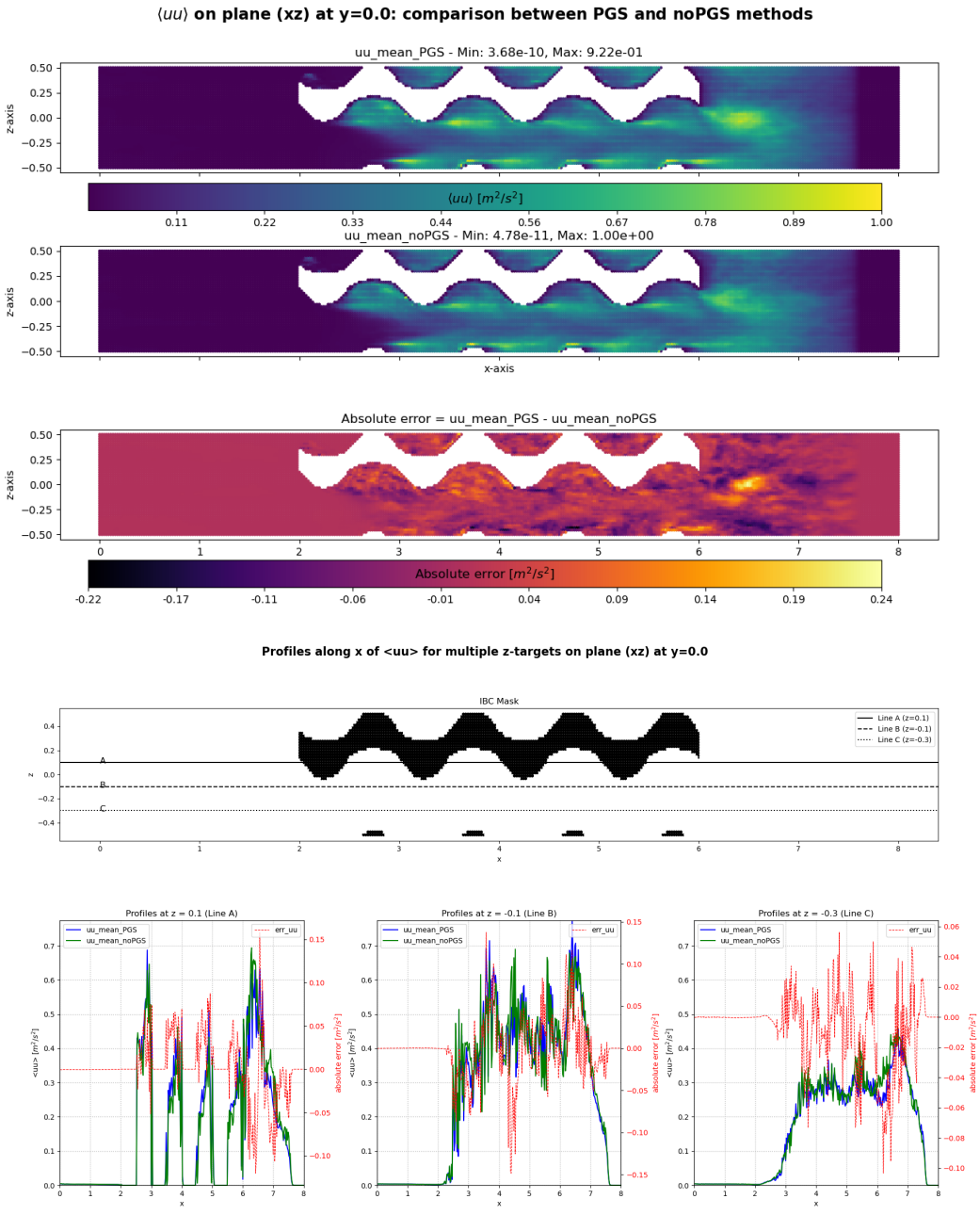

Figure 89: Comparison between PGS and no PGS methods for a one transversal pore configuration: $\langle uu \rangle$.

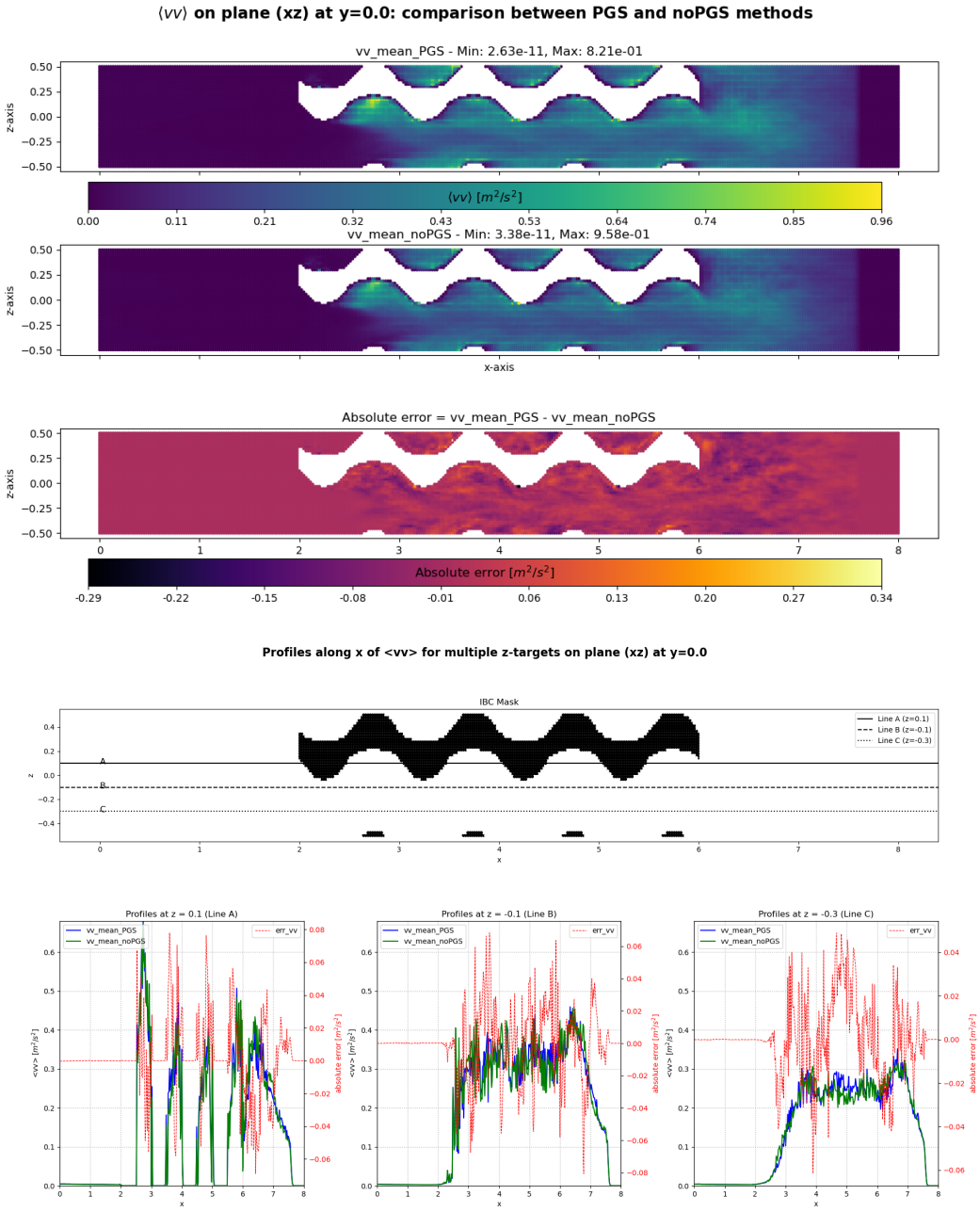

Figure 90: Comparison between PGS and no PGS methods for a one transversal pore configuration: $\langle vv \rangle$.

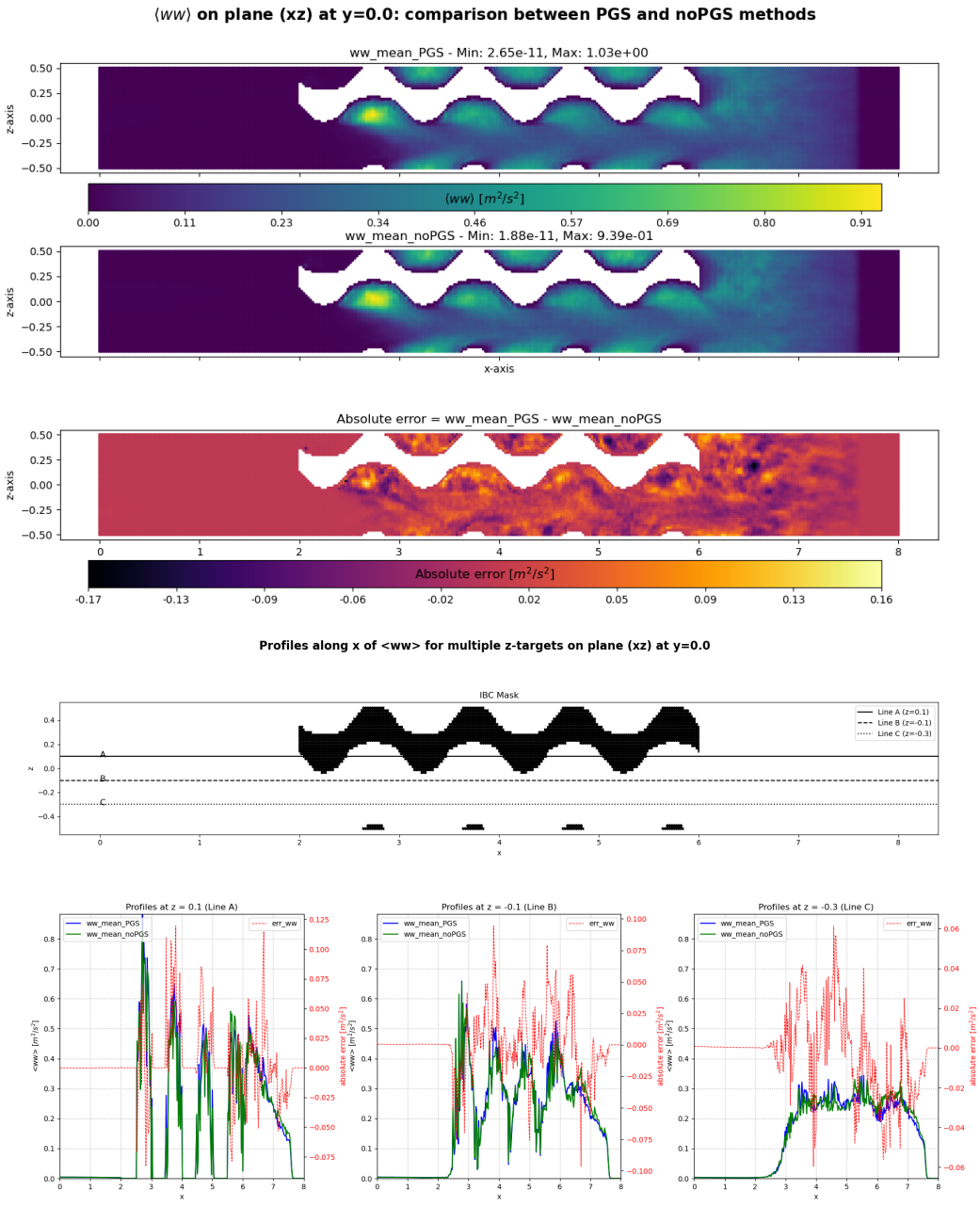

Figure 91: Comparison between PGS and no PGS methods for a one transversal pore configuration: $\langle ww \rangle$.

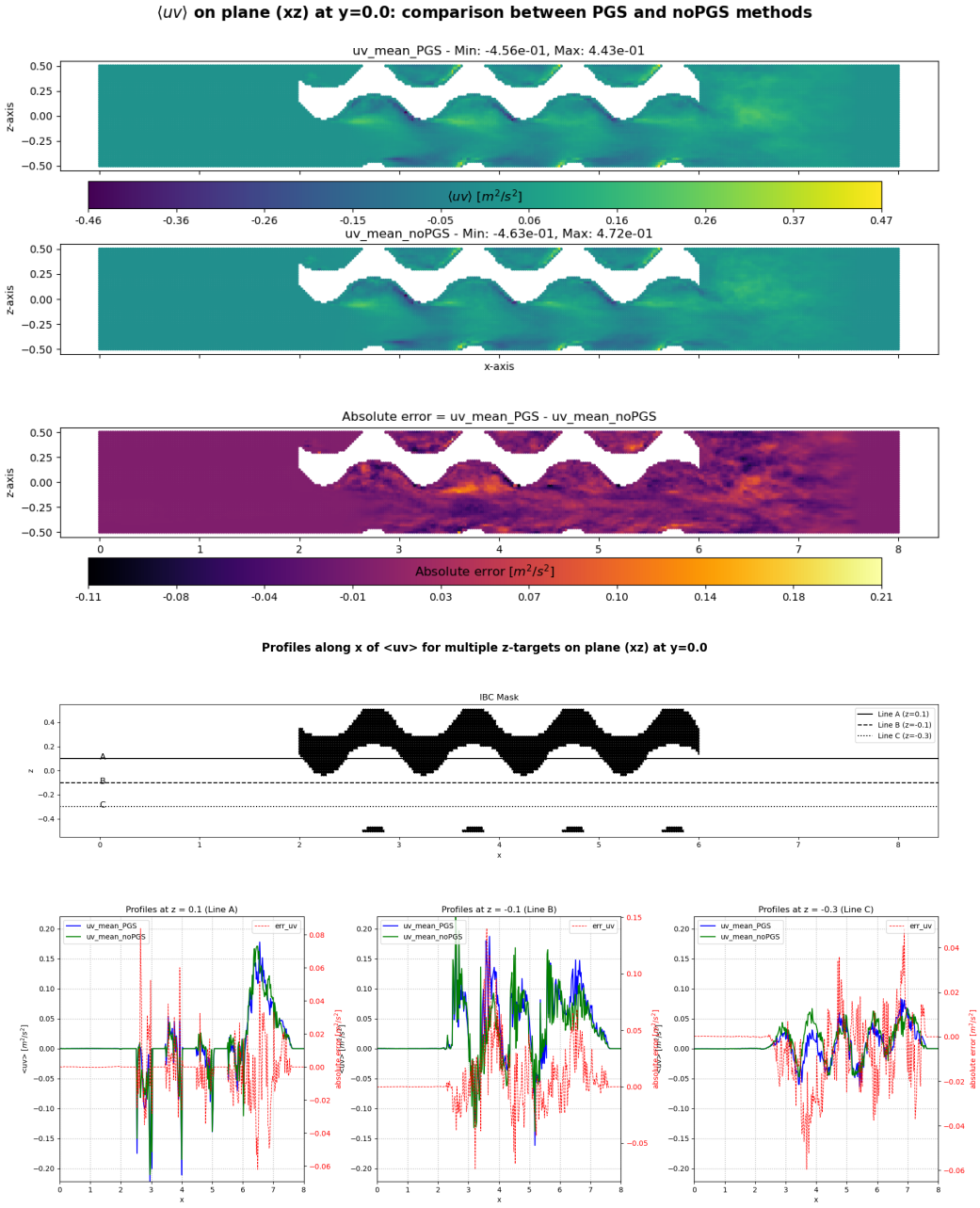

Figure 92: Comparison between PGS and no PGS methods for a one transversal pore configuration: $\langle uv \rangle$.

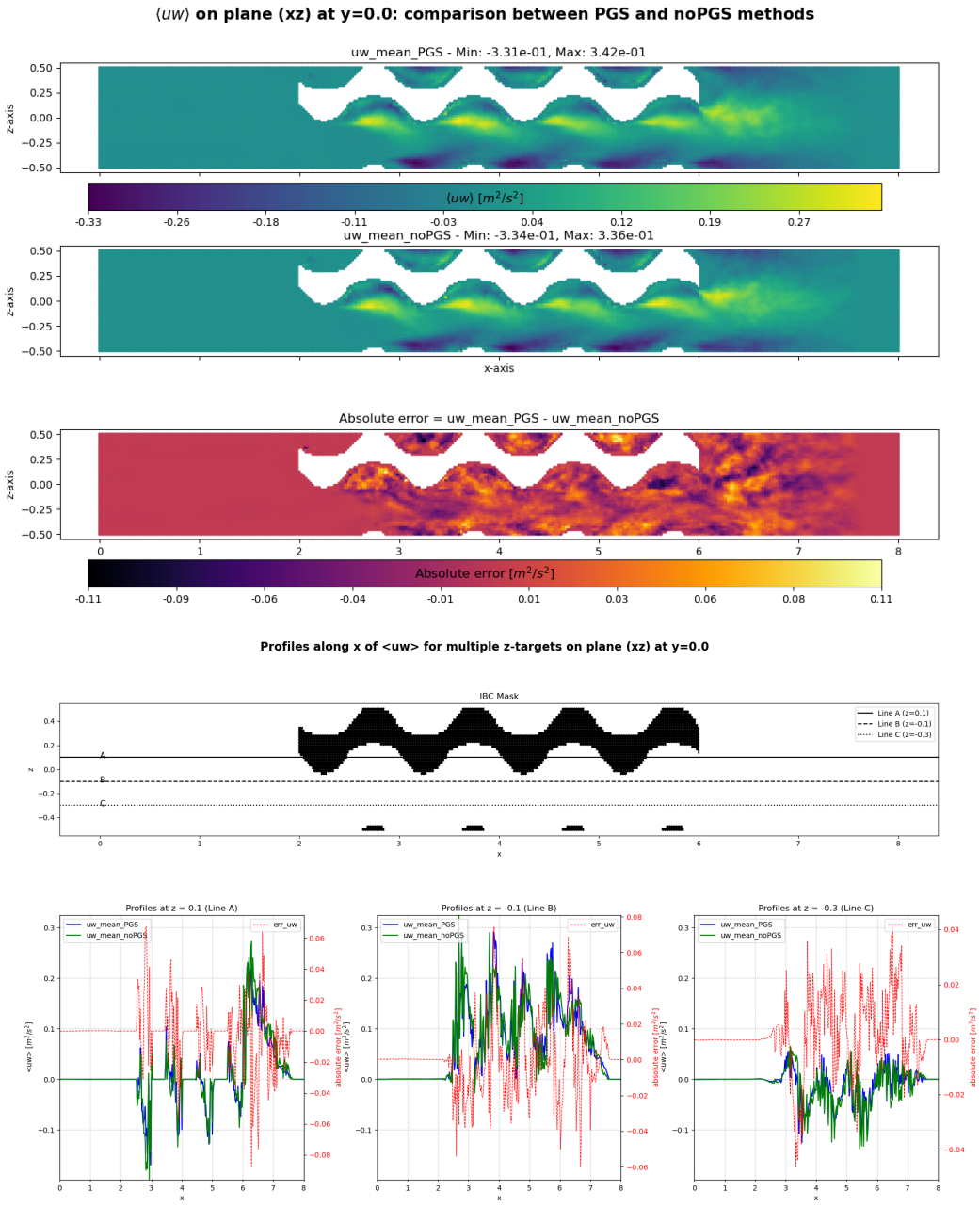

Figure 93: Comparison between PGS and no PGS methods for a one transversal pore configuration: $\langle uw \rangle$.

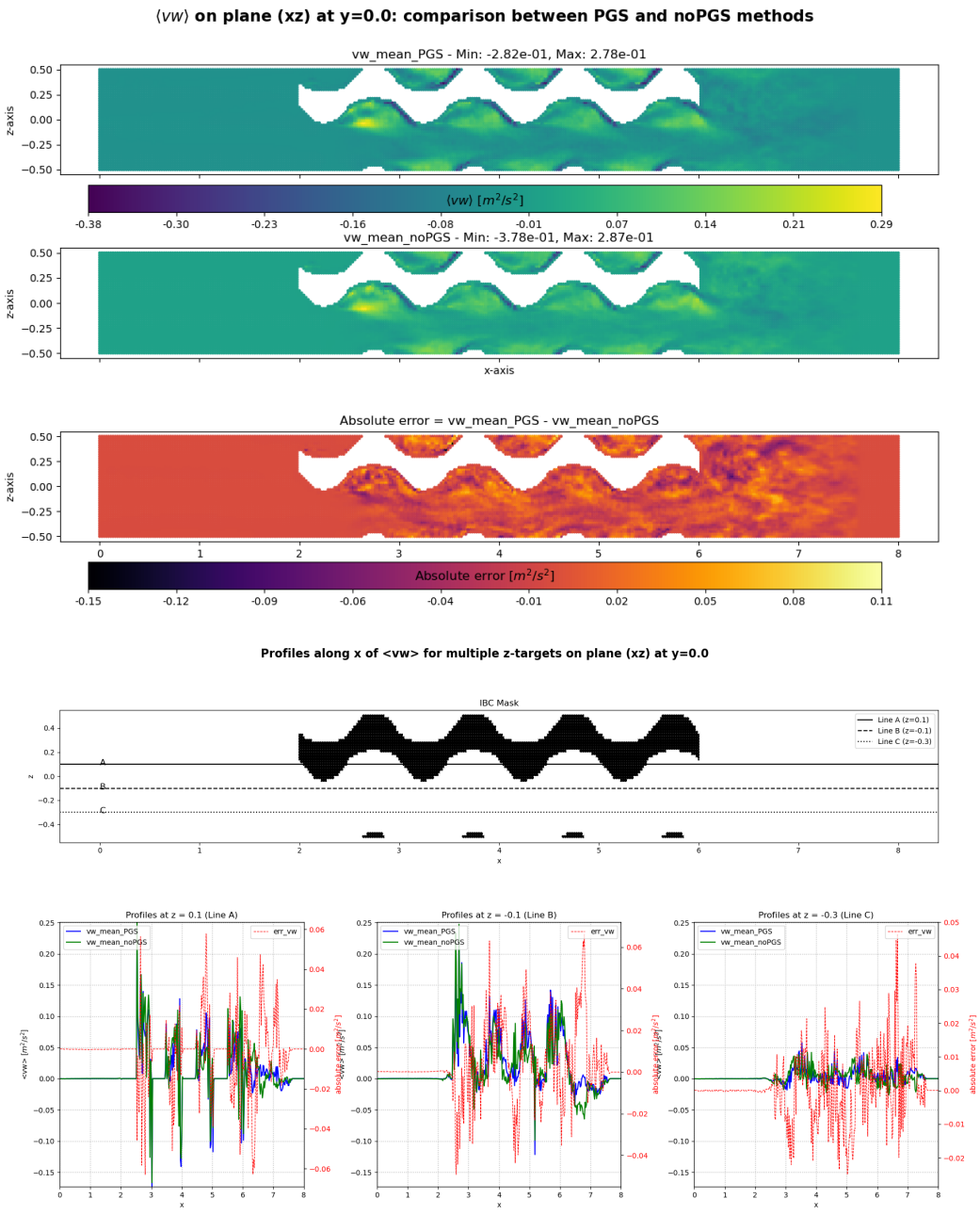

Figure 94: Comparison between PGS and no PGS methods for a one transversal pore configuration: $\langle vw \rangle$.

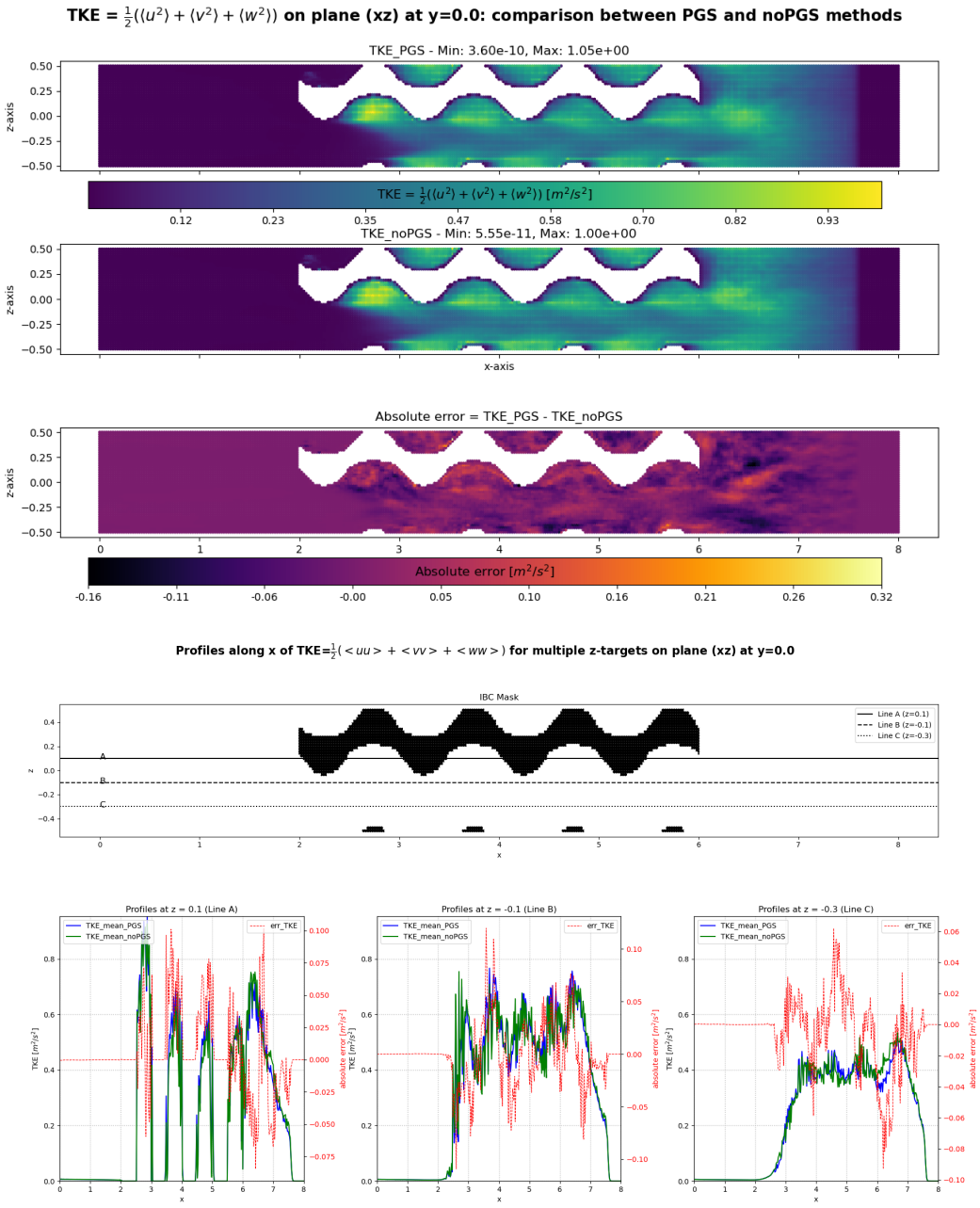

Figure 95: Comparison between PGS and no PGS methods for a one transversal pore configuration: TKE.

B Figures: Gyroid struct=1.20

In this appendix, we provide additional figures and tables related to the results presented in Section 7.3.

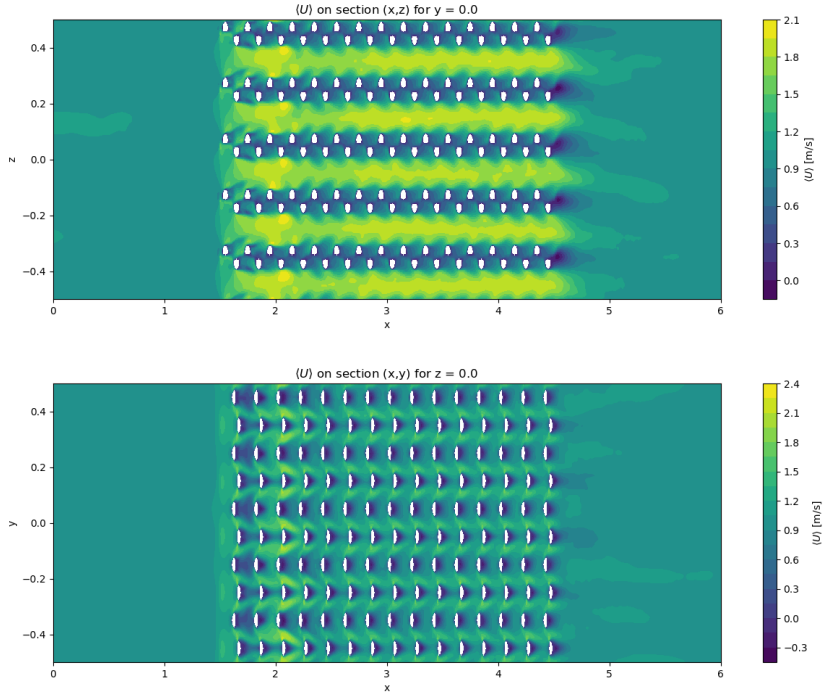

Figure 96: Gyroid struct=1.20: Mean velocity component $\langle U \rangle$ in the xz and xy planes.

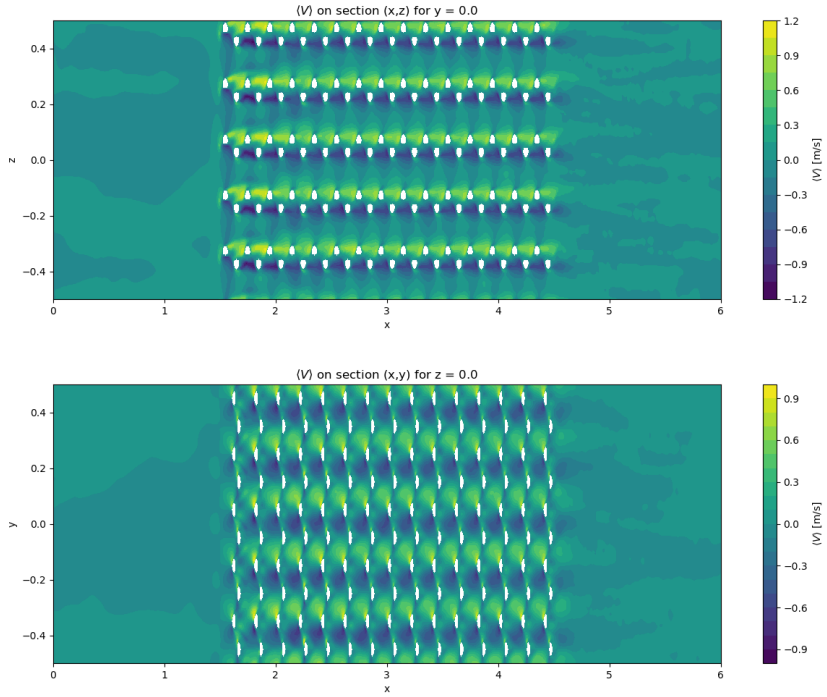

Figure 97: Gyroid struct=1.20: Mean velocity component $\langle V \rangle$ in the xz and xy planes.

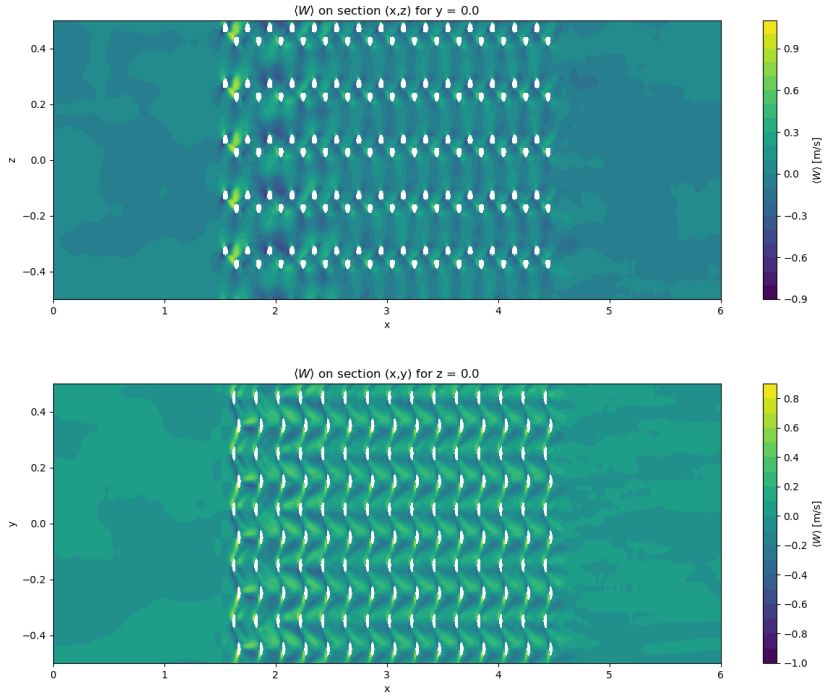

Figure 98: Gyroid struct=1.20: Mean velocity component $\langle W \rangle$ in the xz and xy planes.

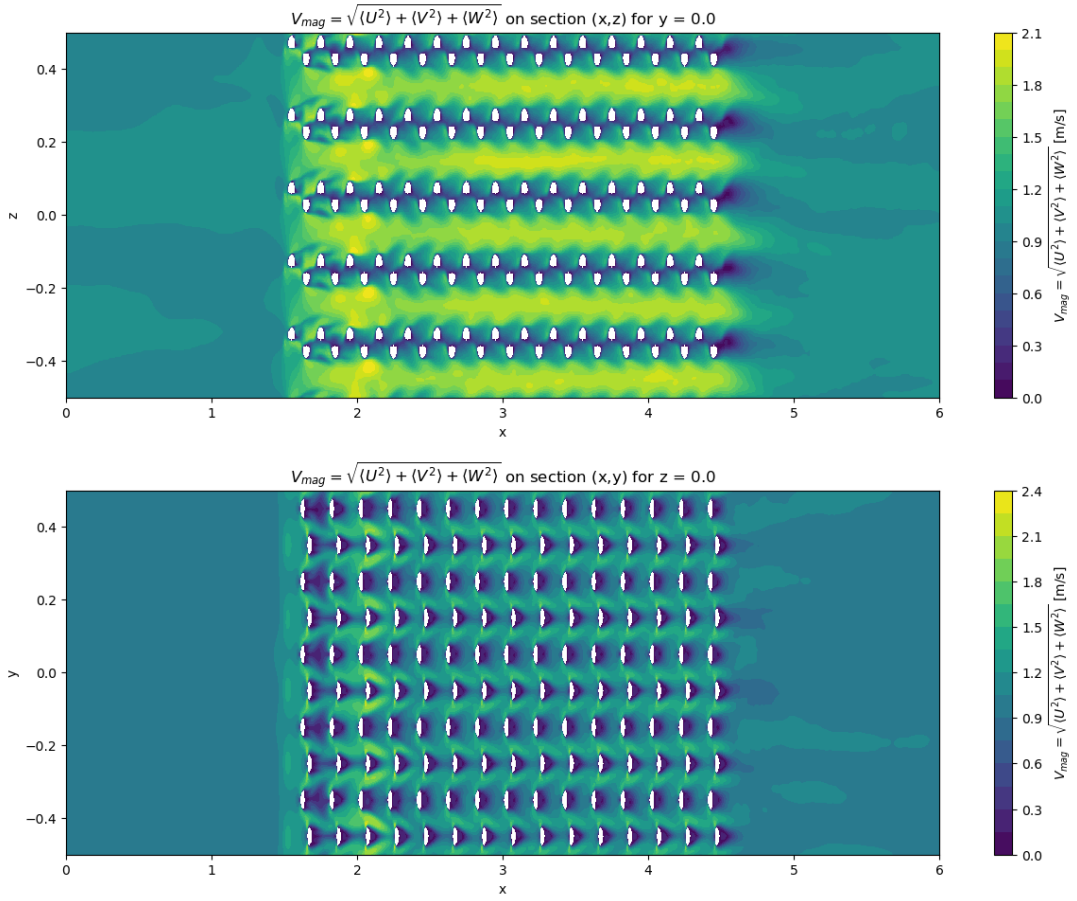

Figure 99: Gyroid struct=1.20: Mean velocity magnitude $V_{mag} = \sqrt{(\langle U \rangle)^2 + (\langle V \rangle)^2 + (\langle W \rangle)^2}$ in the xz and xy planes.

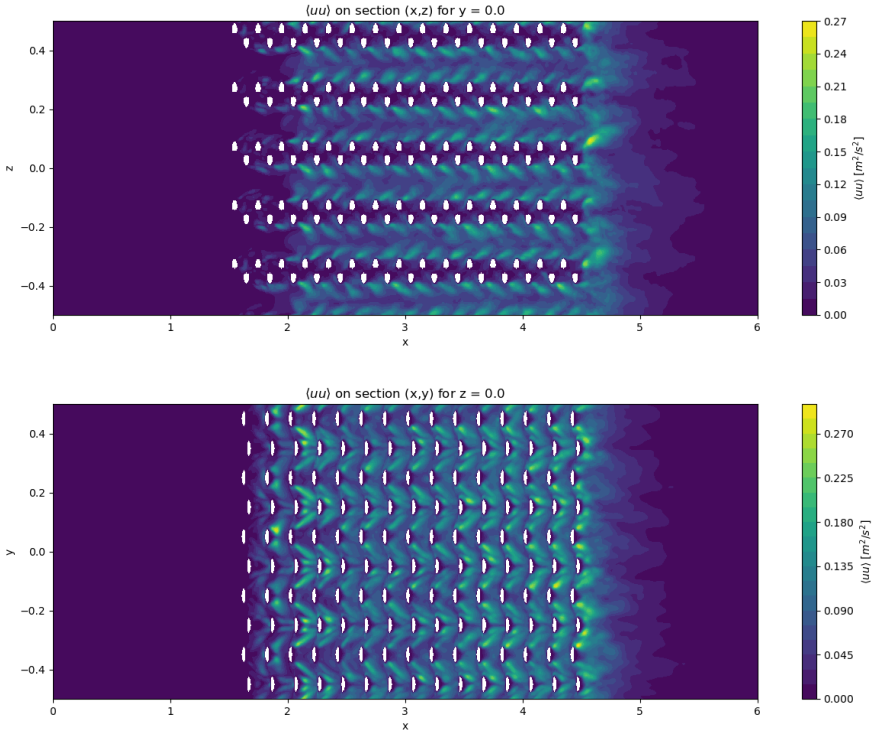

Figure 100: Gyroid struct=1.20: Mean velocity component $\langle uu \rangle$ in the xz plane at $y = 0.0$ and in the xy plane at $z = 0.0$.

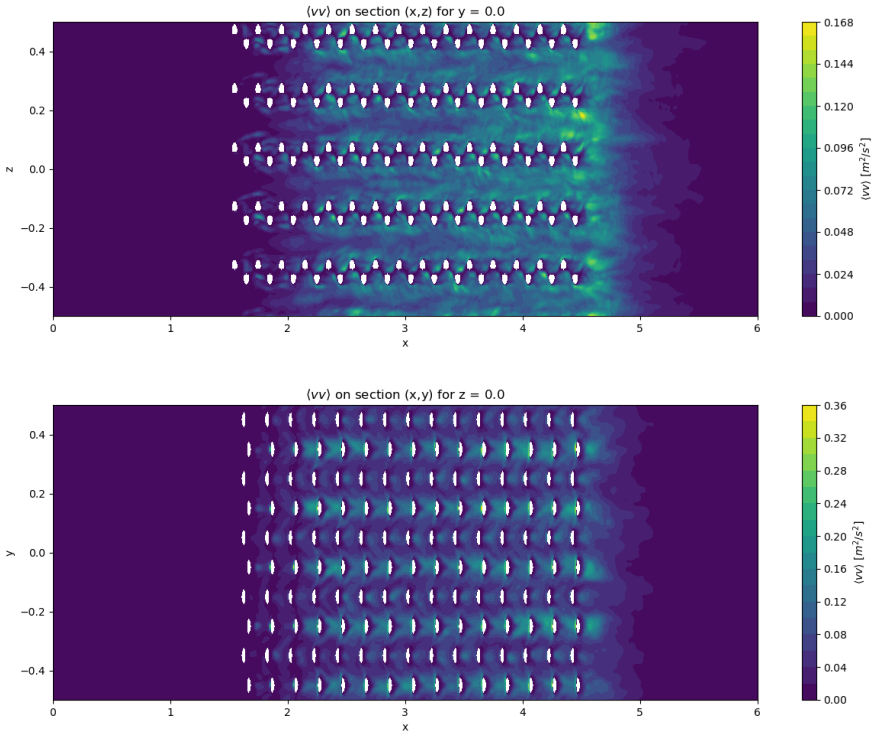

Figure 101: Gyroid struct=1.20: Mean velocity component $\langle vv \rangle$ in the xz plane at $y = 0.0$ and in the xy plane at $z = 0.0$.

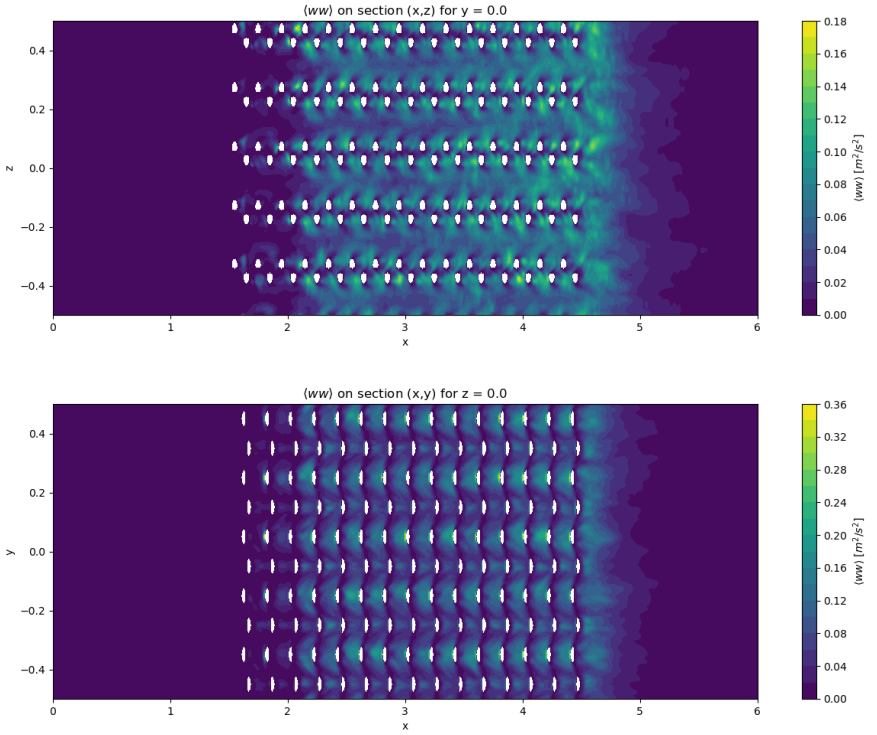

Figure 102: Gyroid struct=1.20: Mean velocity component $\langle ww \rangle$ in the xz plane at $y = 0.0$ and in the xy plane at $z = 0.0$.

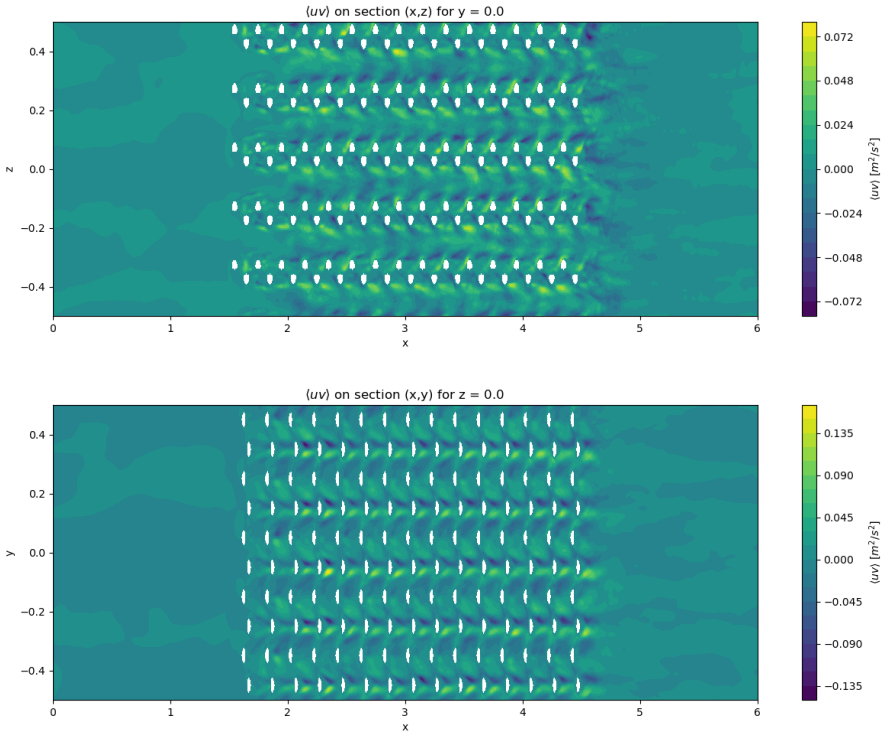

Figure 103: Gyroid struct=1.20: Reynolds stress $\langle uv \rangle$ in the xz plane at $y = 0.0$ and in the xy plane at $z = 0.0$.

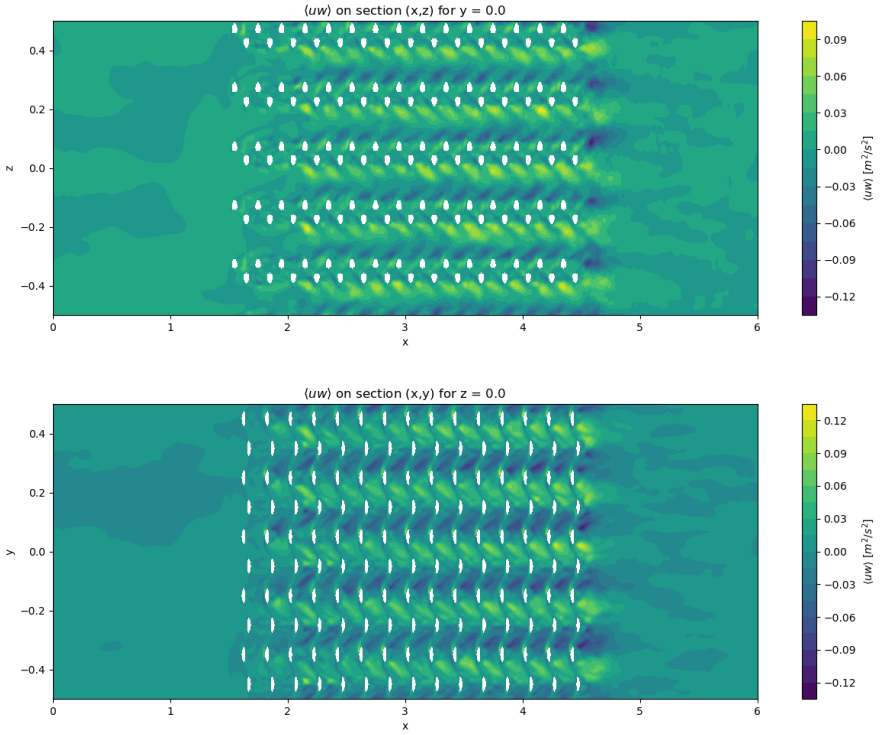

Figure 104: Gyroid struct=1.20: Reynolds stress $\langle uw \rangle$ in the xz plane at $y = 0.0$ and in the xy plane at $z = 0.0$.

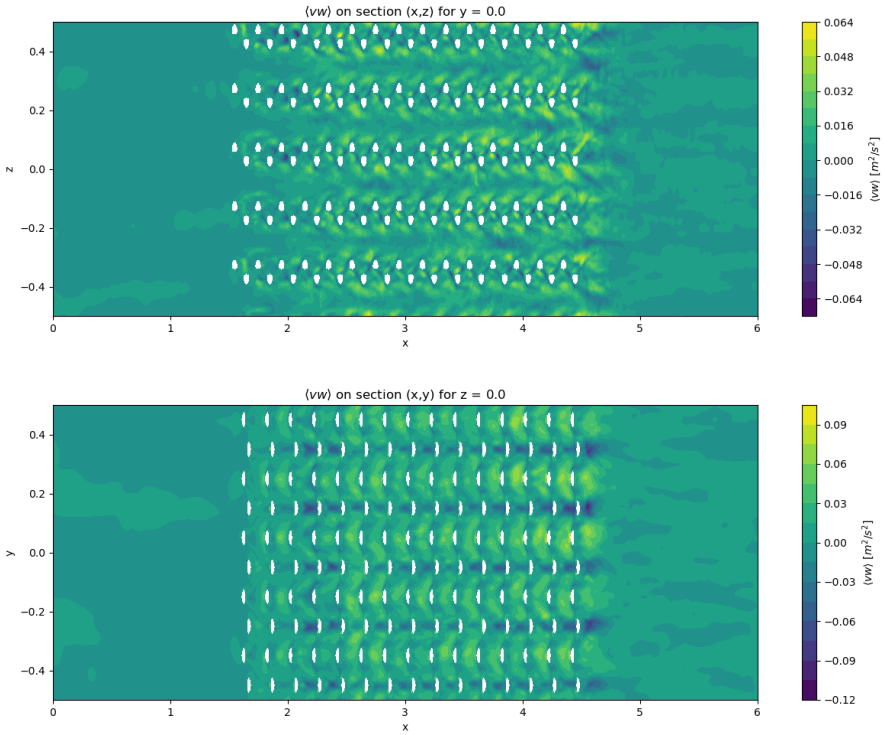

Figure 105: Gyroid struct=1.20: Reynolds stress $\langle vw \rangle$ in the xz plane at $y = 0.0$ and in the xy plane at $z = 0.0$.

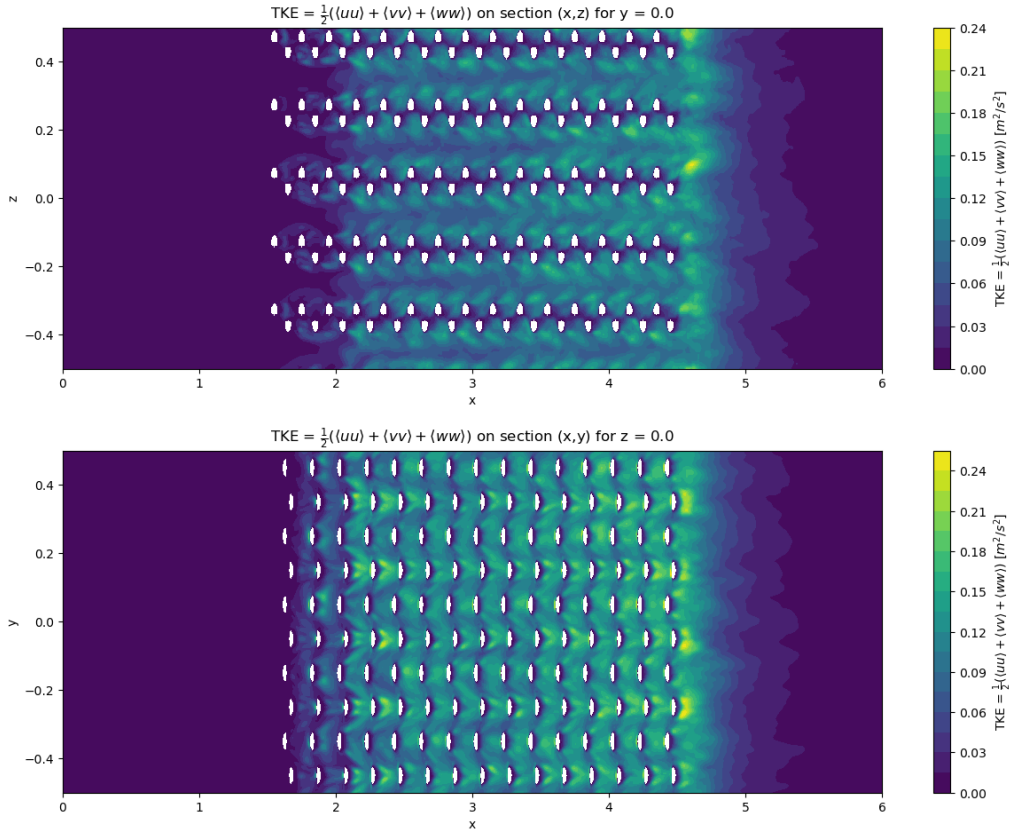

Figure 106: Gyroid with struct = 1.20: TKE visualization on the plane sections (x,z) at y=0.0 and (x,y) at z=0.0.

C Figures: Comparison Gyroid $struct = 1.20$ vs $struct = 0.75$

In this appendix, we provide additional figures and tables related to the results presented in Section 7.4.

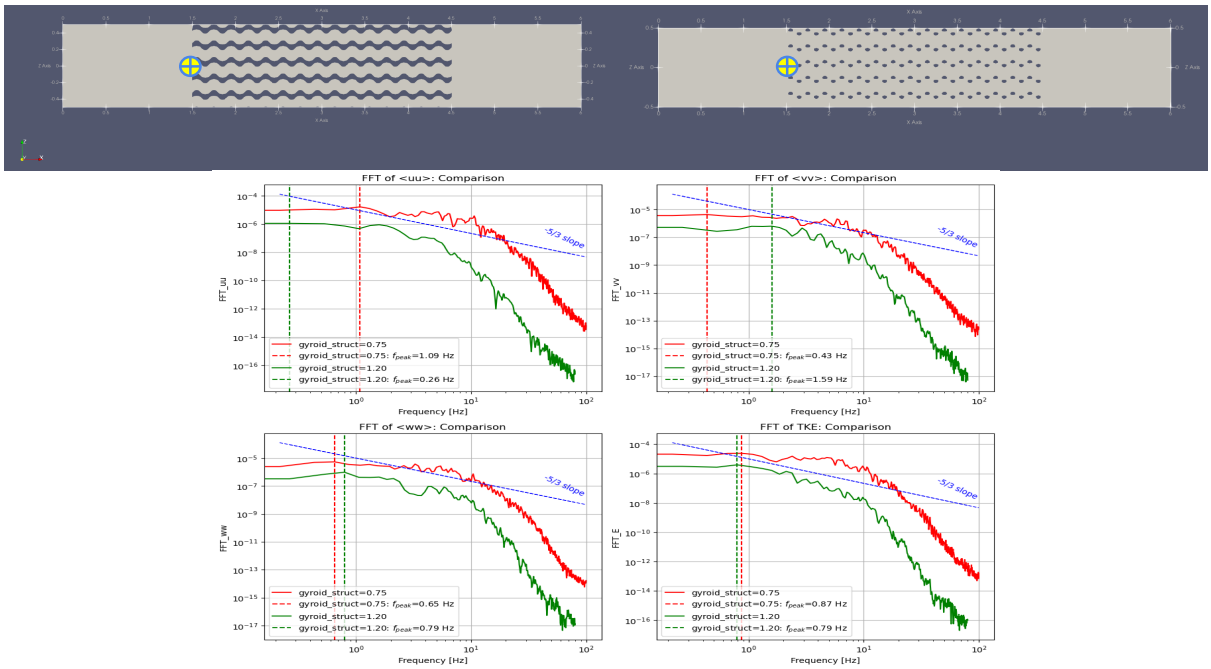

Figure 107: Gyroid $struct = 0.75$ vs Gyroid $struct = 1.20$ comparison: FFT of the time auto-correlations $\langle uu \rangle$, $\langle vv \rangle$, $\langle ww \rangle$ and of their half trace $TKE = \frac{1}{2}(\langle uu \rangle + \langle vv \rangle + \langle ww \rangle)$ in $(x_0, y_0, z_0) = (1.5, 0.0, 0.0)$ (just before the porous media).

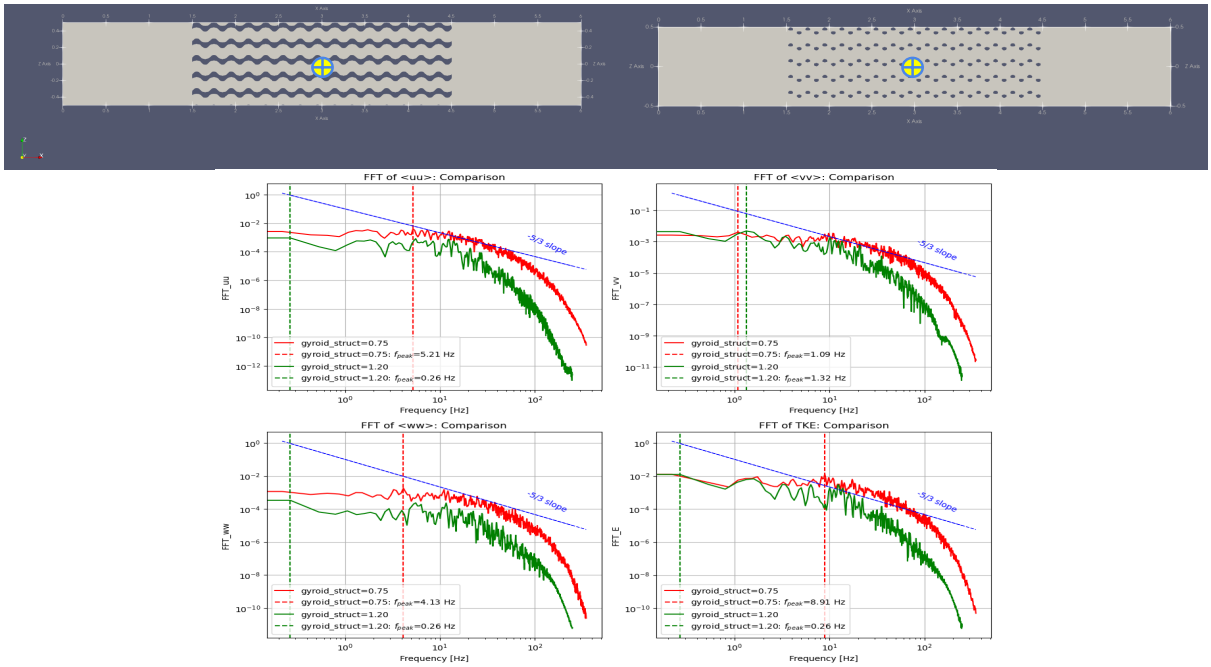

Figure 108: Gyroid $struct = 0.75$ vs Gyroid $struct = 1.20$ comparison: FFT of the time auto-correlations $\langle uu \rangle$, $\langle vv \rangle$, $\langle ww \rangle$ and of their half trace $TKE = \frac{1}{2}(\langle uu \rangle + \langle vv \rangle + \langle ww \rangle)$ in $(x_0, y_0, z_0) = (3.0, 0.0, 0.0)$ (in the middle of the porous media).

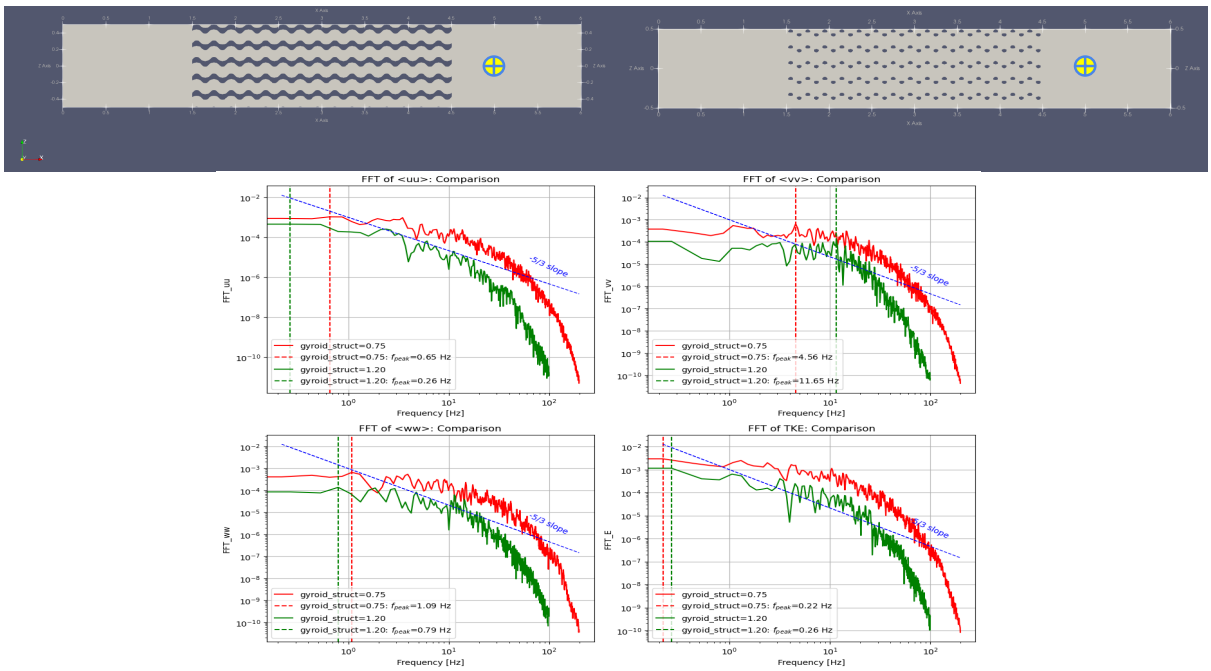

Figure 109: Gyroid *struct* = 0.75 vs Gyroid *struct* = 1.20 comparison: FFT of the time auto-correlations $\langle uu \rangle$, $\langle vv \rangle$, $\langle ww \rangle$ and of their half trace $TKE = \frac{1}{2}(\langle uu \rangle + \langle vv \rangle + \langle ww \rangle)$ in $(x_0, y_0, z_0) = (5.0, 0.0, 0.0)$ (after the porous media).

References

[1] Abdul Salam Abd and Ahmad S Abushaikha. "Reactive transport in porous media: a review of recent mathematical efforts in modeling geochemical reactions in petroleum subsurface reservoirs". In: *SN Applied Sciences* 3.4 (2021), p. 401.

[2] *ADIGMA - A European Initiative on the Development of Adaptive Higher-Order Variational Methods for Aerospace Applications*. Vol. 113. Notes on Numerical Fluid Mechanics and Multidisciplinary Design. Berlin, Heidelberg: Springer Berlin Heidelberg, 2010. ISBN: 978-3-642-03706-1 978-3-642-03707-8. DOI: 10.1007/978-3-642-03707-8.

[3] Davar Ali et al. "Permeability and fluid flow-induced wall shear stress in bone scaffolds with TPMS and lattice architectures: A CFD analysis". In: *European Journal of Mechanics - B/Fluids* 79 (2020), pp. 376–385. ISSN: 0997-7546. DOI: https://doi.org/10.1016/j.euromechflu.2019.09.015. URL: https://www.sciencedirect.com/science/article/pii/S0997754619302213.

[4] John D. Anderson. *Fundamentals of Aerodynamics*. 6th. New York: McGraw-Hill Education, 2020.

[5] B. V. Antohe and J. L. Lage. "A general two-equation macroscopic turbulence model for incompressible flow in porous media". In: *Intl J. Heat Mass Transfer* 40.13 (1997), pp. 3013–3024.

[6] E. Arquis and J.-P. Caltagirone. "Sur les Conditions Hydrodynamiques au Voisinage d'une Interface Milieu Fluide-Milieu Poreux: Application à la Convection Naturelle". In: *Comptes Rendus de l'Académie des Sciences Paris, Série II* 299 (1984), pp. 1–4.

[7] Marco Atzori, Ricardo Vinuesa, and Philipp Schlatter. "Control effects on coherent structures in a non-uniform adverse-pressure-gradient boundary layer". In: *International Journal of Heat and Fluid Flow* 97 (2022), p. 109036. DOI: 10.1016/j.ijheatfluidflow.2022.109036.

[8] Marco Atzori et al. "Intense Reynolds-stress events in turbulent ducts". In: *International Journal of Heat and Fluid Flow* 92 (2021), p. 108802. DOI: 10.1016/j.ijheatfluidflow.2021.108802.

[9] Christophe Bailly and Daniel Juve. "A stochastic approach to compute subsonic noise using linearized Euler's equations". In: *5th AIAA/CEAS aeroacoustics conference and exhibit*. 1999, p. 1872.

[10] S. Banerjee et al. "Presentation of anisotropy properties of turbulence, invariants versus eigenvalue approaches". In: *Journal of Turbulence* 8 (2007), N32. ISSN: 1468-5248. DOI: 10.1080/14685240701506896.

[11] G. K. Batchelor. *The Theory of Homogeneous Turbulence*. Cambridge: Cambridge University Press, 1953.

[12] G. K. Batchelor. *An Introduction to Fluid Dynamics*. Cambridge: Cambridge University Press, 1967.

[13] P. Batten et al. "On the Choice of Wavespeeds for the HLLC Riemann Solver". In: *SIAM Journal on Scientific Computing* 18.6 (1997), pp. 1553–1570.

[14] Andrew B. Bauer. "Impedance Theory and Measurements on Porous Acoustic Liners". In: *Journal of Aircraft* 14.8 (Aug. 1977), pp. 720–728. ISSN: 0021-8669, 1533-3868. DOI: 10.2514/3.58844. (Visited on 09/30/2024).

[15] Thomas Bayes. *An Essay towards solving a Problem in the Doctrine of Chances*. London: Royal Society, 1763.

[16] C. W. Bechara and J. M. M. "Synthetic turbulence generation and its applications". In: *Computers & Fluids* 21.4 (1992), pp. 643–657.

[17] S. Belcher. "Turbulence and transport in rough boundary layers". In: *Boundary-Layer Meteorology* 114 (2005), pp. 339–360.

[18] S. Belcher, I. Harman, and J. Finnigan. "Turbulence and transport in urban canopies". In: *Annual Review of Fluid Mechanics* 44 (2012), pp. 379–404.

[19] L. H. Benedict and R. D. Gould. "Towards better uncertainty estimates for turbulence statistics". In: *Experiments in Fluids* 22.2 (1996), pp. 129–136. DOI: 10.1007/s003480050030.

[20] Gregory P. Bewley et al. "On integral length scales in anisotropic turbulence". In: *Physics of Fluids* 24.6 (2012), p. 061702. ISSN: 1070-6631, 1089-7666. DOI: 10.1063/1.4726077.

[21] M. A. Biot. "Mechanics of Deformation and Acoustic Propagation in Porous Media". In: *Journal of Applied Physics* 33.4 (Apr. 1, 1962), pp. 1482–1498. ISSN: 0021-8979, 1089-7550. DOI: 10.1063/1.1728759.

[22] Gianluca Blois et al. "The influence of bed roughness on hyporheic exchange flow". In: *Water Resources Research* 50 (2014), pp. 2649–2660.

[23] C. Bogey and C. Bailly. "A Family of Low Dispersive and Low Dissipative Explicit Schemes for Flow and Noise Computations". In: *Journal of Computational Physics* 194.1 (2004), pp. 194–214.

[24] Emeric Boigné et al. "X-ray computed tomography for flame-structure analysis of laminar premixed flames". In: *Combustion and Flame* 200 (Feb. 2019), pp. 142–154. ISSN: 00102180. DOI: 10.1016/j.combustflame.2018.11.015. (Visited on 09/30/2024).

[25] W. P. Breugem and B. J. Boersma. "Direct numerical simulations of turbulent flow over a permeable wall using a direct and a continuum approach". In: *Physics of Fluids* 17.2 (Feb. 1, 2005), p. 025103. ISSN: 1070-6631, 1089-7666. DOI: 10.1063/1.1835771.

[26] Eric Brown-Dymkoski, Nurlybek Kasimov, and Oleg V. Vasilyev. "A Characteristic Based Volume Penalization Method for General Evolution Problems Applied to Compressible Viscous Flows". In: *Journal of Computational Physics* 262 (2014), pp. 344–357. DOI: 10.1016/j.jcp.2013.12.060.

[27] John R. Burns et al. "Study of fluid dynamics in rotating packed beds for process intensification". In: *Chemical Engineering Science* 55 (2000), pp. 2407–2419.

[28] J. C. Butcher. *Numerical Methods for Ordinary Differential Equations*. John Wiley & Sons, 2016, p. 82.

[29] Pierre Carlotti and Philippe Drobinski. "Length scales in wall-bounded high-Reynolds-number turbulence". In: *Journal of Fluid Mechanics* 516 (2004), pp. 239–264. ISSN: 0022-1120, 1469-7645. DOI: 10.1017/S0022112004000667.

[30] M. H. Carpenter and C. A. Kennedy. *Fourth-order 2N-storage Runge-Kutta Schemes*. Tech. Rep. National Aeronautics and Space Administration, 1994, p. 82.

[31] Lara de Carvalho et al. "Oil–air separation in porous media: An experimental and numerical study". In: *Journal of Porous Media* 18 (2015), pp. 1021–1035.

[32] Luciano Castillo and W. Keith George. "Modeling uncertainty in turbulent flows". In: *Journal of Fluid Mechanics* 528 (2005), pp. 89–112. DOI: 10.1017/S0022112004003021.

[33] CERFACS. *Antares - A numerical tool for aerodynamics research.* 2024. URL: https://cerfacs.fr/antares/.

[34] M. Chandesris et al. "Direct numerical simulation of turbulent heat transfer in a fluid-porous domain". In: *Phys. Fluids* 25 (2013), p. 125110.

[35] X. Chu, B. Weigand, and V. Vaikuntanathan. "Flow turbulence topology in regular porous media: from macroscopic to microscopic scale with direct numerical simulation". In: *Phys. Fluids* 30 (2018), p. 065102.

[36] X. Chu et al. "Direct numerical simulation of convective heat transfer in porous media". In: *Int. J. Heat Mass Transfer* 133 (2019), pp. 11–20.

[37] R. Handler D. Goldstein and L. Sirovich. "Modeling a No-Slip Flow Boundary with an External Force Field". In: *Journal of Computational Physics* 105.2 (1993), pp. 354–366.

[38] Éloïse D'ayer. "Improving boundary layer models on a rough wall with high order numerical simulations using IBCs". Phs Thesis. Toulouse, ISAE, 2022.

[39] Narendra Dave et al. "Nuclear pebble bed reactor simulations using lattice Boltzmann method: Flow and heat transfer analysis". In: *Nuclear Engineering and Design* 338 (2018), pp. 37–46.

[40] N. Deen and M. van Sint Annaland. "Numerical simulation of fluidized beds: A review of recent advances". In: *Chemical Engineering Science* 87 (2012), pp. 186–203.

[41] Anthony Dixon. "Packed bed heat and mass transfer: How do we increase our understanding". In: *Applied Thermal Engineering* 39 (2012), pp. 104–116.

[42] J. A. Domaradzki. "Nonlocal triad interactions and the dissipation range of isotropic turbulence". In: *Phys. Fluids* 4 (1992), pp. 2037–2045.

[43] J. A. Domaradzki and R. S. Rogallo. "Local energy transfer and nonlocal interactions in homogeneous, isotropic turbulence". In: *Phys. Fluids A* 2 (1990), pp. 413–426.

[44] Jared Dunnmon et al. "An investigation of internal flame structure in porous media combustion via X-ray Computed Tomography". In: *Proceedings of the Combustion Institute* 36.3 (2017), pp. 4399–4408. ISSN: 15407489. DOI: 10.1016/j.proci.2016.06.188. URL: https://linkinghub.elsevier.com/retrieve/pii/S1540748916302504 (visited on 09/30/2024).

[45] Jiawei Feng et al. "Triply periodic minimal surface (TPMS) porous structures: from multi-scale design, precise additive manufacturing to multidisciplinary applications". In: *International Journal of Extreme Manufacturing* 4.2 (2022).

[46] L. Ferracina and M. Spijker. "An extension and analysis of the Shu-Osher representation of Runge-Kutta methods". In: *Mathematics of Computation* 74.249 (2005), pp. 201–219.

[47] U. Frisch. *Turbulence: The Legacy of A. N. Kolmogorov.* Cambridge University Press, 1995.

[48] D. N. Assanis G. C. Papageorgakis. "COMPARISON OF LINEAR AND NONLINEAR RNG-BASED k-epsilon MODELS FOR INCOMPRESSIBLE TURBULENT FLOWS". In: *Numerical Heat Transfer, Part B: Fundamentals* 35.1 (1999), pp. 1–22. DOI: 10.1080/104077999275983.

[49] *Gamma function.* Wikipedia. 2024. URL: https://en.wikipedia.org/wiki/Gamma_function.

[50] A. O. Gbadamosi et al. "An overview of chemical enhanced oil recovery: Recent advances and prospects". In: *Int. Nano Lett.* 9.3 (2019), pp. 171–202.

[51] William K. George and Hassan J. Hussein. "Locally axisymmetric turbulence". In: *Journal of Fluid Mechanics* 233 (1991), pp. 1–23.

[52] Samuel E. Ahmed et Al. Georgios A. Deskos Daniele Di Vita. "Reduced-Order Representation of Turbulence via the Lumley Triangle". In: *Fluids* 6.12 (2021), p. 431. DOI: 10.3390/fluids6120431.

[53] M. Ghisalberti and H. Nepf. "Shallow flows over a permeable medium: The hydrodynamics of submerged aquatic canopies". In: *Transp. Porous Media* 78 (2009), p. 385.

[54] S. A. Ghoreishi-Madiseh et al. "A transient natural convection heat transfer model for geothermal borehole heat exchangers". In: *J. Renewable Sustainable Energy* 5.4 (2013), p. 043104.

[55] James Gleick. *Chaos: Making a New Science.* New York: Penguin, 1988.

[56] S. K. Godunov. "A Difference Method for Numerical Calculation of Discontinuous Solutions of the Equations of Hydrodynamics". In: *Matematicheskii Sbornik* 89.3 (1959), pp. 271–306.

[57] S. Gottlieb and C.-W. Shu. "Total Variation Diminishing Runge-Kutta Schemes". In: *Mathematics of Computation* 67.221 (1998), pp. 73–85.

[58] S. Gottlieb and C.-W. Shu. "Total variation diminishing Runge-Kutta schemes". In: *Mathematics of Computation* 67.221 (1998), pp. 73–85.

[59] Lin He, S. Yi, and Yangzhu Zhu. "Flow Visualization of Hairpin Vortices in a Mach 3.0 Flat-Plate Boundary Layer". In: *Engineering, Physics* (2013).

[60] Xiaoliang He et al. "Angular multiscale statistics of turbulence in a porous bed". In: *Physical Review Fluids* 3.8 (Aug. 2, 2018), p. 084501. ISSN: 2469-990X. DOI: 10.1103/PhysRevFluids.3.084501.

[61] Xiaoliang He et al. "Characteristics of turbulence in a face-centred cubic porous unit cell". In: *Journal of Fluid Mechanics* 873 (Aug. 25, 2019), pp. 608–645. ISSN: 0022-1120, 1469-7645. DOI: 10.1017/jfm.2019.403.

[62] JP Herzig, DM Leclerc, and P Le Goff. "Flow of suspensions through porous media—application to deep filtration". In: *Industrial & Engineering Chemistry* 62.5 (1970), pp. 8–35.

[63] J. O. Hinze. *Turbulence*. 2nd. New York: McGraw-Hill, 1975.

[64] L. R. Howarth. "On the Analysis of Turbulence". In: *Journal of the Royal Aeronautical Society* 48 (1938), pp. 547–565.

[65] H. E. Huppert and J. A. Neufeld. "The fluid mechanics of carbon dioxide sequestration". In: *Annu. Rev. Fluid Mech.* 46 (2014), pp. 255–272.

[66] H. T. Huynh. "A Flux Reconstruction approach to high-order schemes including discontinuous Galerkin methods". In: *18th AIAA Computational Fluid Dynamics Conference*. 2007, p. 4079.

[67] H. T. Huynh. "A reconstruction approach to high-order schemes including discontinuous Galerkin for diffusion". In: *47th AIAA Aerospace Sciences Meeting Including the New Horizons Forum and Aerospace Exposition*. pages 59, 60, 61, 62, 64, 78. 2009, p. 403.

[68] G. Irvine et al. "Cooling characteristics of a produce cooling system using perforated bin liners". In: *Journal of Food Engineering* 20 (1993), pp. 177–193.

[69] Javier Jiménez. *Turbulence and vortex dynamics*. Edition 2001. Palaiseau: Ecole polytechnique, Département de mécanique, 2001. ISBN: 978-2-7302-0859-8.

[70] Y. Jin and A. V. Kuznetsov. "Turbulence modeling for flows in wall bounded porous media: An analysis based on direct numerical simulations". In: *Physics of Fluids* 29.4 (2017). DOI: 10.1063/1.4979062.

[71] Y. Jin, M.-F. Uth, and H. Herwig. "Structure of a turbulent flow through plane channels with smooth and rough walls: an analysis based on high resolution DNS results". In: *Computers & Fluids* 107.31 (2015), pp. 77–88. DOI: 10.1016/j.compfluid.2014.10.015.

[72] Y. Jin et al. "Numerical investigation of the possibility of macroscopic turbulence in porous media: a direct numerical simulation study". In: *Journal of Fluid Mechanics* 766 (2015), pp. 76–103. DOI: 10.1017/jfm.2015.9.

[73] Yan Jin and Andrey V. Kuznetsov. "Multiscale modeling and simulation of turbulent flows in porous media". In: *International Journal of Fluid Engineering* 1.1 (Mar. 1, 2024), p. 010601. ISSN: 2994-9009, 2994-9017. DOI: 10.1063/5.0190279.

[74] Lluís Jofre, Stefan P. Domino, and Gianluca Iaccarino. "A Framework for Characterizing Structural Uncertainty in Large-Eddy Simulation Closures". In: *Flow, Turbulence and Combustion* 100.2 (2018), pp. 341–363. ISSN: 1386-6184, 1573-1987. DOI: 10.1007/s10494-017-9844-8.

[75] J. Karweit, C. W. Bechara, and T. H. D. M. T. "A method for generating random Fourier modes". In: *Journal of Fluid Mechanics* 151 (1984), pp. 145–167.

[76] R. B. Kazerooni and S. K. Hannani. "Simulation of turbulent flow through porous media employing a v2f model". In: *Sci. Iranica Trans. B Mech. Eng.* 16 (2009), pp. 159–167.

[77] Oraib Al-Ketan et al. "Functionally graded and multi-morphology sheet TPMS lattices: Design, manufacturing, and mechanical properties". In: *Journal of the Mechanical Behavior of Biomedical Materials* 102 (2020).

[78] J. Kim, P. Moin, and R. Moser. "Turbulence statistics of a fully developed channel flow at low Reynolds number". In: *Journal of Fluid Mechanics* 177 (1987), pp. 133–166.

[79] Donald L. Koch and Reghan J. Hill. "Inertial Effects in Suspension and Porous-Media Flows". In: *Annual Review of Fluid Mechanics* 33.1 (2001), pp. 619–647.

[80] Douglas L. Koch. "Uncertainty analysis in turbulence measurements". In: *Experiments in Fluids* 43.6 (2007), pp. 791–802. DOI: 10.1007/s00348-007-0332-2.

[81] A. N. Kolmogorov. "A refinement of previous hypotheses concerning the local structure of turbulence in a viscous incompressible fluid at high Reynolds number". In: *Journal of Fluid Mechanics* 13.1 (1961), pp. 82–85. DOI: 10.1017/S0022112062000518.

[82] Andrey N. Kolmogorov. *The Local Structure of Turbulence in Incompressible Viscous Fluid for Very Large Reynolds Numbers*. Moscow: Akademiia Nauk SSSR, 1941.

[83] D. A. Kopriva. "A staggered-grid multidomain spectral method for the compressible Navier-Stokes equations". In: *Journal of Computational Physics* 143 (1998), pp. 125–158.

[84] M. Kozuka, Y. Seki, and H. Kawamura. "DNS of turbulent heat transfer in a channel flow with a high spatial resolution". In: *Proc. of 7th Int. Symp. on Engineering Turbulence Modelling and Measurements (ETMM7)* 1 (2008), pp. 163–168.

[85] R. H. Kraichnan. "Diffusion of a passive scalar in homogeneous turbulence". In: *Physics of Fluids* 10 (1967), pp. 1417–1423.

[86] P. Kundu, V. Kumar, and I. M. Mishra. "Numerical modeling of turbulent flow through isotropic porous media". In: *Int. J. Heat Mass Transfer* 75 (2014), pp. 40–57.

[87] F. Kuwahara, T. Yamane, and A. Nakayama. "Large eddy simulation of turbulent flow in porous media". In: *International Communications in Heat and Mass Transfer* 33.4 (2006), pp. 411–418. DOI: 10.1016/j.icheatmasstransfer.2005.12.011.

[88] J. L. Lage, B. V. Antohe, and D. A. Nield. "Two types of nonlinear pressure-drop versus flow-rate relation observed for saturated porous media". In: *J. Fluids Eng.* 119.3 (1997), pp. 700–706.

[89] J. L. Lage, M. J. S. de Lemos, and D. A. Nield. "Modeling turbulence in porous media". In: *Transport Phenomena in Porous Media II*. Ed. by D. B. Ingham and I. Pop. Oxford: Elsevier, 2002, pp. 198–230.

[90] Pierre-Simon Laplace. *Théorie analytique des probabilitées*. Paris: V. Courcier, 1812.

[91] Per Larsson et al. "Enhanced mass transfer in rotating packed beds for intensified processes". In: *Chemical Engineering Science* 161 (2017), pp. 114–122.

[92] D. Lasseaux and F. J. Valdes-Parada. "Macroscopic model for unsteady flow in porous media". In: *Journal of Fluid Mechanics* 862 (2019), pp. 283–311.

[93] P. D. Lax. *Hyperbolic Systems of Conservation Laws and the Mathematical Theory of Shock Waves*. SIAM, 1973.

[94] K.-B. Lee and J. R. Howell. "Theoretical and experimental heat and mass transfer in highly porous media". In: *Int. J. Heat Mass Transfer* 34 (1991), pp. 2123–2132.

[95] M. Lemesle. *Analysis of Several Extensions for the Spectral Difference Method to Handle Discontinuity*. Tech. rep. CERFACS, 2014.

[96] M. J. S. de Lemos. *Turbulence in Porous Media, Modeling and Applications*. 2nd. Oxford, UK: Elsevier, 2012.

[97] M. J. S. de Lemos and E. J. Braga. "Modeling of turbulent natural convection in porous media". In: *Int. Commun. Heat Mass Transfer* 30 (2003), pp. 615–624.

[98] Marcelo de Lemos et al. "Porous burners for efficient combustion". In: *Journal of Porous Media* 12 (2009), pp. 1085–1100.

[99] Jan M. Link et al. "Flow dynamics and structure formation in dense fluidized beds". In: *Chemical Engineering Science* 60 (2005), pp. 5985–5995.

[100] Guansheng Liu et al. "Transport of engineered nanoparticles in porous media and its enhancement for remediation of contaminated groundwater". In: *Critical Reviews in Environmental Science and Technology* 50.22 (2020), pp. 2301–2378.

[101] Haihu Liu et al. “Pore-Scale Modeling of Spontaneous Imbibition in Porous Media Using the Lattice Boltzmann Method”. In: *Water Resources Research* 57.6 (June 2021), e2020WR029219. ISSN: 0043-1397, 1944-7973. DOI: 10.1029/2020WR029219.

[102] Qianlong Liu and Oleg V. Vasilyev. “A Brinkman penalization method for compressible flows in complex geometries”. In: *Journal of Computational Physics* 227.2 (2007), pp. 946–966. DOI: 10.1016/j.jcp.2007.07.037.

[103] Wei Liu, Liang Shi, and Haihu Liu. “Numerical study of the impact of geometrical parameters on the rarefied gas transport in porous media”. In: *Gas Science and Engineering* 110 (Feb. 2023), p. 204855. ISSN: 29499089. DOI: 10.1016/j.jgsce.2022.204855.

[104] Y. Liu, M. Vinokur, and Z. J. Wang. “Spectral Difference method for unstructured grids I: Basic formulation”. In: *Journal of Computational Physics* 216 (2006), pp. 780–801.

[105] Edward N. Lorenz. “Deterministic non-periodic flow”. In: *J. Atmos. Sci.* 20 (1963), pp. 130–141.

[106] Francesco Lucci et al. “Comparison of geometrical, momentum and mass transfer characteristics of real foams to Kelvin cell lattices for catalyst applications”. In: *International Journal of Heat and Mass Transfer* 108 (2017), pp. 341–350. DOI: 10.1016/j.ijheatmasstransfer.2016.11.073.

[107] John L. Lumley. *Computational Modeling of Turbulent Flows*. New York: Academic Press, 1979.

[108] John L. Lumley and H. A. Panofsky. “The Structure of Atmospheric Turbulence”. In: *Annual Review of Fluid Mechanics* 9 (1977), pp. 53–80. DOI: 10.1146/annurev.fl.09.010177.000413.

[109] Aleksandr Lyapunov. “Nouvelle forme du théorème sur la limite des probabilités”. In: *Mémoires de l’Académie Impériale des Sciences de Saint-Pétersbourg* 12 (1901), pp. 1–24.

[110] M. Matsumoto and T. Nishimura. *Subroutine to Generate Random Numbers*. http://www.math.sci.hiroshima-u.ac.jp/m-mat/MT/VERSIONS/FORTRAN/mt95.f90.

[111] Thomas Marchal. “Extension de la méthode des Différences Spectrales à la combustion”. PhD thesis. Université de Toulouse (France), 2023.

[112] Thomas Marchal, Hugues Deniau, and Guillaume Puigt. “Entropy-Stable Spectral Difference and Flux Reconstruction Methods for Discontinuous Flows”. In: *SSRN* (2023).

[113] Pierre-Alexandre Masset. “Modelling challenges of stationary combustion in inert porous media”. PhD thesis. IMFT - Institut de mécanique des fluides de Toulouse, 2022.

[114] Laura M McDowell-Boyer, James R Hunt, and Nicholas Sitar. “Particle transport through porous media”. In: *Water resources research* 22.13 (1986), pp. 1901–1921.

[115] Joseph Meadows and Ajay K. Agrawal. “Time-resolved PIV of lean premixed combustion without and with porous inert media for acoustic control”. In: *Combustion and Flame* 162.4 (Apr. 2015), pp. 1063–1077. ISSN: 00102180. DOI: 10.1016/j.combustflame.2014.09.028.

[116] C. Meneveau and K. R. Sreenivasan. “The multifractal nature of turbulent energy dissipation”. In: *J. Fluid Mech.* 224 (1991), pp. 429–484.

[117] L. Ménez et al. “Assessment of Volume Penalization and Immersed Boundary Methods for Compressible Flows with Various Thermal Boundary Conditions”. In: *Journal of Computational Physics* 493 (Nov. 2023), p. 112465. DOI: 10.1016/j.jcp.2023.112465. URL: https://doi.org/10.1016/j.jcp.2023.112465.

[118] R. N. Meroney. “Fires in porous media: Natural and urban canopies”. In: *Flow and Transport Processes with Complex Obstructions*. Ed. by Y. A. Gayev and J. C. Hunt. Vol. 236. Springer, 2007.

[119] Rajat Mittal and Gianluca Iaccarino. “Immersed boundary methods”. In: *Annual Review of Fluid Mechanics* 37 (2005), pp. 239–261. DOI: 10.1146/annurev.fluid.37.061903.175743.

[120] A.A. Mohamad. “COMBUSTION IN POROUS MEDIA: FUNDAMENTALS AND APPLICATIONS”. In: *Transport Phenomena in Porous Media III*. Elsevier, 2005, pp. 287–304. ISBN: 978-0-08-044490-1. DOI: 10.1016/B978-008044490-1/50015-6. URL: https://linkinghub.elsevier.com/retrieve/pii/B9780080444901500156.

[121] J. Mohd-Yusof. “Combined Immersed-Boundary/B-Spline Methods for Simulations of Flow in Complex Geometries”. In: *Annual Research Briefs NASA Ames Research Center*. Ed. by Stanford University Center of Turbulence Research. Stanford University Center of Turbulence Research, 1997, pp. 317–327.

[122] Abraham de Moivre. *The Doctrine of Chances: or, a Method of Calculating the Probabilities of Events in Play*. London: W. Pearson for the author, 1738.

[123] F. C. Moon. *Chaotic and Fractal Dynamics: An Introduction for Applied Scientists and Engineers*. New York: Wiley, 1992.

[124] D. O. Mora and M. Obligado. "Estimating the integral length scale on turbulent flows from the zero crossings of the longitudinal velocity fluctuation". In: *Experiments in Fluids* 61.9 (2020), p. 199. ISSN: 0723-4864, 1432-1114. DOI: 10.1007/s00348-020-03033-2.

[125] R. D. Moser, J. Kim, and N. N. Monsour. "DNS of turbulent channel flow up to $R_\tau = 590$". In: *Physics of Fluids* 11 (1999), pp. 943–945.

[126] M. Abdul Mujeebu et al. "Applications of porous media combustion technology – A review". In: *Applied Energy* 86.9 (Sept. 2009), pp. 1365–1375. ISSN: 03062619. DOI: 10.1016/j.apenergy.2009.01.017.

[127] L. Mydlarski and Z. Warhaft. "Passive scalar statistics in high Péclet number grid turbulence". In: *J. Fluid Mech.* 358 (1998), pp. 135–175.

[128] A. Nakayama and F. Kuwahara. "A macroscopic turbulence model for flow in a porous medium". In: *J. Fluids Eng.* 121 (1999), pp. 427–433.

[129] Edvard Neovius. "On the Theory of Minimal Surfaces". PhD thesis. University of Helsinki, 1833.

[130] D. A. Nield. "The limitations of the Brinkman-Forchheimer equation in modeling flow in a saturated porous medium and at an interface". In: *Int. J. Heat Fluid Flow* 12 (1991), pp. 269–272.

[131] H. Nimvari et al. "Numerical simulation of porous radiant burners". In: *Applied Thermal Engineering* 71 (2014), pp. 391–398.

[132] P.L. O'Neill et al. "Autocorrelation Functions and the Determination of Integral Length with Reference to Experimental and Numerical Data". In: *Proceedings of the Fifteenth Australasian Fluid Mechanics Conference: 13-17 December 2004, the University of Sydney, NSW 2006, Australia* (2004).

[133] A. M. Obukhov. "Some specific features of atmospheric turbulence". In: *J. Fluid Mech.* 13 (1962), pp. 77–81.

[134] C. Odenthal et al. "The CellFlux storage concept for cost reduction in parabolic trough solar thermal power plants". In: *Energy Procedia* 46 (2014), pp. 142–151.

[135] Aaron I. Packman et al. "Hyporheic exchange and stream-subsurface interaction in streambeds with partially mobile sediment beds". In: *Water Resources Research* 40 (2004), W08304.

[136] Y.-H. Pao. "Structure of turbulent velocity and scalar fields at large wavenumbers". In: *The Physics of Fluids* 8.6 (1965), pp. 1063–1075.

[137] Chang Min Park et al. "Environmental behavior of engineered nanomaterials in porous media: a review". In: *Journal of hazardous materials* 309 (2016), pp. 133–150.

[138] T. Passot and A. Pouquet. "Numerical simulation of compressible homogeneous flows in the turbulent regime". In: *Journal of Fluid Mechanics* 181 (1987), pp. 441–466.

[139] Bogdan I. Pavel and Abdulmajeed A. Mohamad. "An experimental and numerical study on heat transfer enhancement for gas heat exchangers fitted with porous media". In: *International Journal of Heat and Mass Transfer* 47.23 (2004), pp. 4939–4952. ISSN: 00179310. DOI: 10.1016/j.ijheatmasstransfer.2004.06.014.

[140] Charles S. Peskin. "The Immersed Boundary Method". In: *Acta Numerica* 11 (2002), pp. 479–517. DOI: 10.1017/S0962492902000077.

[141] A. Piquet, O. Roussel, and A. Hadjadj. "A Comparative Study of Brinkman Penalization and Direct-Forcing Immersed Boundary Methods for Compressible Viscous Flows". In: *Computers & Fluids* 136 (2016), pp. 272–284. DOI: 10.1016/j.compfluid.2016.06.001.

[142] Stephen B. Pope. *Turbulent Flows*. 1st ed. Cambridge University Press, Aug. 10, 2000. DOI: 10.1017/CBO9780511840531.

[143] P. J. Prescott and F. P. Incropera. "The effect of turbulence on solidification of a binary metal alloy with electromagnetic stirring". In: *J. Heat Transfer* 117 (1995), pp. 716–724.

[144] Alejandro J. Puga and John C. LaRue. "Normalized dissipation rate in a moderate Taylor Reynolds number flow". In: *Journal of Fluid Mechanics* 818 (2017), pp. 184–204. ISSN: 0022-1120, 1469-7645. DOI: 10.1017/jfm.2017.47.

[145] Na Qiu et al. "Experimental and numerical studies on mechanical properties of TPMS structures". In: *International Journal of Mechanical Sciences* 261 (2024). DOI: 10.1016/j.ijmecsci.2023.108657.

[146] J.D. Ramshaw, P.J. O'Rourke, and L.R. Stein. "Pressure gradient scaling method for fluid flow with nearly uniform pressure". In: *Journal of Computational Physics* 58.3 (1985), pp. 361–376. ISSN: 00219991. DOI: 10.1016/0021-9991(85)90168-8.

[147] F. Rao, A. V. Kuznetsov, and Y. Jin. "Numerical modeling of momentum dispersion in porous media based on the pore scale prevalence hypothesis". In: *Trans. Porous Med.* 133 (2020), pp. 271–292.

[148] Feixiong Rao and Yan Jin. "Possibility for survival of macroscopic turbulence in porous media with high porosity". In: *Journal of Fluid Mechanics* 937 (2021), A17. ISSN: 0022-1120, 1469-7645. DOI: 10.1017/jfm.2022.87.

[149] Sonia Rashidian and Mohamad Reza Tavakoli. "Using Porous Media to Enhancement of Heat Transfer in Heat Exchangers". In: *International Journal of Advanced Engineering, Management and Science* 3.11 (2017), pp. 1051–1064. ISSN: 24541311. DOI: 10.24001/ijaems.3.11.5.

[150] W. H. Reed and T. Hill. *Triangular Mesh Methods for the Neutron Transport Equation*. Technical report. Los Alamos Scientific Lab., N. Mex. (USA), 1973.

[151] L. F. Richardson. *Weather Prediction by Numerical Process*. Cambridge: Cambridge University Press, 1922.

[152] P. L. Roe. "Approximate Riemann solvers, parameter vectors, and difference schemes". In: *Journal of Computational Physics* 43.2 (1981), pp. 357–372.

[153] E. Saiki and S. Biringen. "Numerical Simulation of a Cylinder in Uniform Flow: Application of a Virtual Boundary Method". In: *Journal of Computational Physics* 123.2 (1996), pp. 450–465.

[154] Alan H. Schoen. *Infinite Periodic Minimal Surfaces without Self-Intersections*. Tech. rep. NASA Technical Note D-5541, 1970.

[155] Hermann Amandus Schwarz. "On Some Mapping Tasks". In: *Journal for Pure and Applied Mathematics* 70 (1865), pp. 105–120.

[156] Ammar Shams et al. "Large eddy simulation of a randomly stacked nuclear pebble bed". In: *Computers & Fluids* 96 (2014), pp. 302–321. DOI: 10.1016/j.compfluid.2014.03.016.

[157] Mehrzad Shams and John Dixon. "Large eddy simulation of fluid dynamics in pebble bed reactors". In: *Nuclear Engineering and Design* 263 (2013), pp. 383–398.

[158] Jafar Shayegan and Mahmood Alavi. "Modeling of catalytic steam reforming of methane". In: *Energy & Fuels* 22 (2008), pp. 3552–3561.

[159] C.-W. Shu and S. Osher. "Efficient implementation of essentially non-oscillatory shock-capturing schemes". In: *Journal of Computational Physics* 77.2 (1988), pp. 439–471.

[160] Sadaf Sobhani et al. "Investigation of Lean Combustion Stability, Pressure Drop, and Material Durability in Porous Media Burners". In: *Volume 5C: Heat Transfer*. ASME Turbo Expo 2017: Turbomachinery Technical Conference and Exposition. Charlotte, North Carolina, USA: American Society of Mechanical Engineers, June 26, 2017, V05CT17A001. ISBN: 9780791850893. DOI: 10.1115/GT2017-63204.

[161] R. J. Spiteri and S. J. Ruuth. "A new class of optimal high-order strong-stability-preserving time discretization methods". In: *SIAM Journal on Numerical Analysis* 40.2 (2002), pp. 469–491.

[162] K. R. Sreenivasan and P. Kailasnath. "An update on the intermittency exponent in turbulence". In: *Phys. Fluids A* 5 (1993), pp. 512–514.

[163] V. Srikanth et al. "Symmetry breaking of turbulent flow in porous media composed of periodically arranged solid obstacles". In: *J. Fluid Mech.* 929 (2021), A2.

[164] K. Suga. "Understanding and modelling turbulence over and inside porous media". In: *Flow, Turbulence and Combustion* 96.3 (2016), pp. 717–756. DOI: 10.1007/s10494-015-9673-6.

[165] Y. Sun, Z. J. Wang, and Y. Liu. "High-Order Multidomain Spectral Difference Method for the Navier-Stokes Equations". In: *44th AIAA Aerospace Sciences Meeting and Exhibit* (2006). AIAA Paper 2006-301.

[166] Y. Sun, Z. J. Wang, and Y. Liu. "High-Order Multidomain Spectral difference method for the Navier-Stokes equations on unstructured hexahedral grids". In: *Communications in Computational Physics* 2 (2007), pp. 310–333.

[167] Y. Tanino and H. M. Nepf. "Lateral dispersion in random cylinder arrays at high Reynolds number". In: *J. Fluid Mech.* 600 (2008), pp. 339–371.

[168] G. I. Taylor. "Statistical Theory of Turbulence". In: *Proceedings of the Royal Society A* 151 (1935). Reprinted in "The Science of Fluid Dynamics", pp. 421–444.

[169] C. Teruna et al. "Noise reduction mechanisms of an open-cell metal-foam trailing edge". In: *Journal of Fluid Mechanics* 898 (Sept. 10, 2020), A18. ISSN: 0022-1120, 1469-7645. DOI: 10.1017/jfm.2020.363.

[170] C. Teruna et al. "Numerical analysis of a 3-D printed porous trailing edge for broadband noise reduction". In: *Journal of Fluid Mechanics* 926 (Nov. 2021), A17. ISSN: 0022-1120, 1469-7645. DOI: 10.1017/jfm.2021.704.

[171] E. F. Toro. *Riemann Solvers and Numerical Methods for Fluid Dynamics: A Practical Introduction*. Springer Science & Business Media, 2013.

[172] Arsenii Trush, Stanislav Pospíšil, and Hrvoje Kozmar. "Comparison of turbulence integral length scale determination methods". In: *AFM* (2020), pp. 113–123. DOI: 10.2495/AFM200111.

[173] MPI Tutorial. *MPI Scatter, Gather, and Allgather*. 2024. URL: https://mpitutorial.com/tutorials/mpi-scatter-gather-and-allgather/.

[174] Engineering Sciences Data Unit. *Low-fin staggered tube banks: Heat transfer and pressure drop for turbulent single phase cross flow*. ESDU Data Item No. 84016. London: ESDU, 1984.

[175] M.-F. Uth et al. "A direct numerical simulation study on the possibility of macroscopic turbulence in porous media: Effects of different solid matrix geometries, solid boundaries, and two porosity scales". In: *Phys. Fluids* 28 (2016), p. 065101.

[176] K. Vafai. *Handbook of Porous Media*. 2nd. Boca Raton: Taylor and Francis Group, 2005.

[177] C. W. Van Atta and R. A. Antonia. "Reynolds number dependence of skewness and flatness factors of turbulent velocity derivatives". In: *Physics of Fluids* 23 (1980), pp. 252–257.

[178] C. W. Van Atta and W. Y. Chen. "Structure functions of turbulence in the atmospheric boundary layer over the ocean". In: *Journal of Fluid Mechanics* 44 (1970), pp. 145–159.

[179] R. Van Haren. *Optimised Runge-Kutta Time Integration for the Spectral Difference Method*. https://cerfacs.fr/wp-content/uploads/2018/12/CFD_AIAA2017_VANHAREN.pdf. Accessed: 2024-10-02. 2017.

[180] Adèle Veilleux. "Extension of the Spectral Difference method to simplex cells and hybrid grids". PhD thesis. Institut National Polytechnique de Toulouse (INPT), 2021.

[181] Roberto Verzicco. "Immersed Boundary Methods: Historical Perspective and Future Outlook". In: *Annual Review of Fluid Mechanics* 55.1 (2023), pp. 129–155. DOI: 10.1146/annurev-fluid-120720-022129. URL: https://doi.org/10.1146/annurev-fluid-120720-022129.

[182] C. Vigneault et al. "Application of porous media models to forced-air produce cooling systems". In: *Postharvest Biology and Technology* 33 (2004), pp. 163–172.

[183] J. M. Wallace and R. S. Brodkey. "Reynolds stress and joint probability density distributions in the u-v plane of a turbulent channel flow". In: *Physics of Fluids* 20 (1977), pp. 351–355.

[184] J. M. Wallace, R. S. Brodkey, and H. Eckelmann. "The wall region in turbulent shear flow". In: *Journal of Fluid Mechanics* 54 (1972), pp. 39–48.

[185] James M. Wallace. "Quadrant Analysis in Turbulence Research: History and Evolution". In: *Annual Review of Fluid Mechanics* 48 (2016), pp. 131–158. DOI: 10.1146/annurev-fluid-122414-034550.

[186] Jinghan Wang et al. "Investigation on flow and heat transfer in various channels based on triply periodic minimal surfaces (TPMS)". In: *Energy Conversion and Management* 283 (2023). DOI: 10.1016/j.enconman.2023.116955.

[187] W. Wang et al. "Information transfer between turbulent boundary layers and porous media". In: *J. Fluid Mech.* 920 (2021), A21.

[188] W. Wang et al. "Spatial and spectral characteristics of information flux between turbulent boundary layers and porous media". In: *J. Fluid Mech.* 949 (2022), A16.

[189] Z. J. Wang. "Spectral (Finite) Volume Method for Conservation Laws on Unstructured Grids: Basic Formulation". In: *Journal of Computational Physics* 178.1 (2002), pp. 210–251.

[190] Z. J. Wang. *Adaptive High-Order Methods in Computational Fluid Dynamics*. Vol. 2. World Scientific, 2011.

[191] Z. J. Wang. "High-order CFD methods: current status and perspective". In: *International Journal for Numerical Methods in Fluids* 72.8 (2013), pp. 811–845. ISSN: 0271-2091, 1097-0363. DOI: 10.1002/fld.3767. URL: https://onlinelibrary.wiley.com/doi/10.1002/fld.3767.

[192] David C. Wilcox. *Turbulence Modeling for CFD*. 3rd. DCW Industries, 2006.

[193] Brian D. Wood. "Inertial effects in dispersion in porous media". In: *Water Resources Research* (2007). DOI: 10.1029/2006WR005790.

[194] Brian D. Wood, Xiaoliang He, and Sourabh V. Apte. "Modeling Turbulent Flows in Porous Media". In: *Annual Review of Fluid Mechanics* (2020). ISSN: 0066-4189, 1545-4479. DOI: 10.1146/annurev-fluid-010719-060317.

[195] Huijin Xu et al. "Analytical considerations of local thermal non-equilibrium conditions for thermal transport in metal foams". In: *International Journal of Thermal Sciences* 95 (Sept. 2015). DOI: 10.1016/j.ijthermalsci.2015.04.007.

[196] Tokuo Yamamoto and Altan Turgut. "Acoustic wave propagation through porous media with arbitrary pore size distributions". In: *The Journal of the Acoustical Society of America* 83.5 (1988), pp. 1744–1751.

[197] Min Yang and Ping Sheng. "Sound Absorption Structures: From Porous Media to Acoustic Metamaterials". In: *Annual Review of Materials Research* 47.1 (July 3, 2017), pp. 83–114. ISSN: 1531-7331, 1545-4118. DOI: 10.1146/annurev-matsci-070616-124032.

[198] Kirttayoth Yeranee and Yu Rao. "A Review of Recent Investigations on Flow and Heat Transfer Enhancement in Cooling Channels Embedded with Triply Periodic Minimal Surfaces (TPMS)". In: *Energies* 15.23 (2022). DOI: 10.3390/en15238994.

[199] M. Yu, Z. J. Wang, and Y. Liu. "On the accuracy and efficiency of discontinuous Galerkin, Spectral Difference and Correction Procedure via Reconstruction methods". In: *Journal of Computational Physics* 259 (2014), pp. 70–95.

[200] Shixiang Yu, Jinxing Sun, and Jiaming Bai. "Investigation of functionally graded TPMS structures fabricated by additive manufacturing". In: *Materials Design* 182 (2019).

[201] Amir Zamani and Brij Maini. "Flow of dispersed particles through porous media—deep bed filtration". In: *Journal of Petroleum Science and Engineering* 69.1-2 (2009), pp. 71–88.

[202] Yong Zhang et al. "Catalytic methane steam reforming in packed bed reactors: A review of approaches and results". In: *Chemical Engineering Journal* 348 (2018), pp. 692–713.

[203] Y. Zhou. "Interacting scales and energy transfer in isotropic turbulence". In: *Phys. Fluids* 5 (1993), pp. 2511–2524.